Investigation of Advanced Back Contacts for CdTe Thin Film Solar Cells

Zur Erlangung des akademischen Grades Doktor-Ingenieur (Dr.-Ing.)
genehmigte Dissertation von

Alireza Barati

August 2020 — Darmstadt — D 17

TECHNISCHE UNIVERSITÄT DARMSTADT

Surface Science

Fachbereich Material- und Geowissenschaften
Fachgebiet Oberflächenforschung

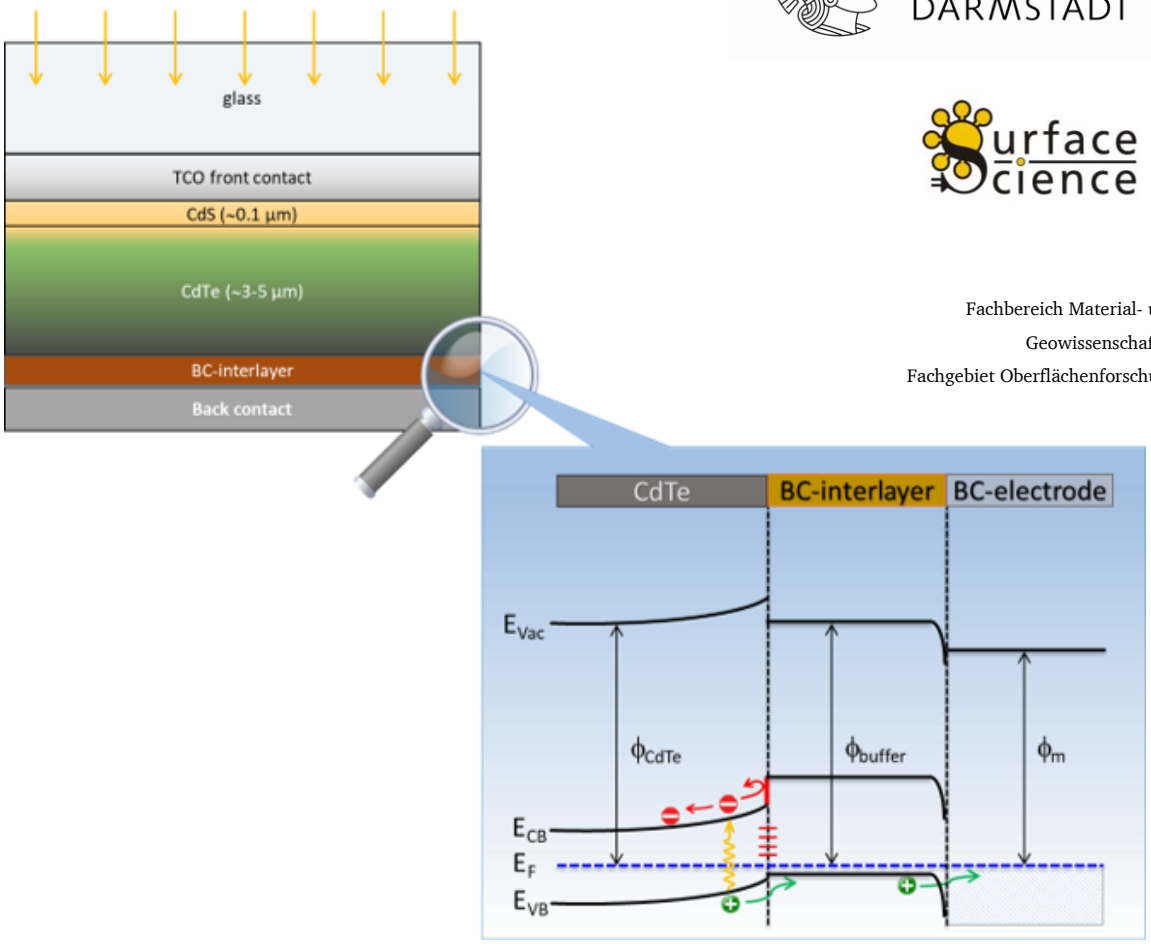

Investigation of advanced back contacts for CdTe thin film solar cells

Untersuchung verbesserter Rückkontakte für CdTe-Dünnschichtsolarzellen

Doktorarbeit vom Fachbereich Material- und Geowissenschaften
der Technischen Universität Darmstadt

Eingereicht von Alireza Barati

1. Gutachter: Prof. Dr. Wolfram Jaegermann
2. Gutachter: Prof. Dr. Lambert Alff

Tag der Einreichung: 7. September 2020
Tag der Prüfung: 1. Dezember 2020

Darmstadt 2020 – D 17

Bitte zitieren Sie dieses Dokument als:
URN: urn:nbn:de:tuda-tuprints-191929
https://tuprints.ulb.tu-darmstadt.de/id/eprint/19192

Dieses Dokument wird bereitgestellt von TUprints,
E-Publishing-Service der TU Darmstadt
http://tuprints.ulb.tu-darmstadt.de
tuprints@ulb.tu-darmstadt.de

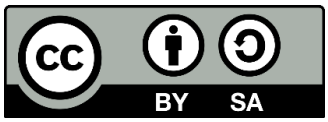

Erklärung zur Dissertation

Hiermit versichere ich, die vorliegende Dissertation ohne Hilfe Dritter nur mit den angegebenen Quellen und Hilfsmitteln angefertigt zu haben. Alle Stellen, die aus Quellen entnommen wurden, sind als solche kenntlich gemacht. Diese Arbeit hat in gleicher oder ähnlicher Form noch keiner Prüfungsbehörde vorgelegen.

Darmstadt, den 20. August 2020

_____

(Alireza Barati)

Abbreviations and Symbols

AFM	Atomic Force Microscopy
AM1.5G	Air-Mass 1.5 Global solar radiation (1000 W/m^2)
BC	Back Contact
BM	Bromine-Methanol
CAE	Constant Analyzer Energy
C-AFM	Conductive Atomic Force Microscopy
CBD	Chemical Bath Deposition
CBM	Conduction Band Minimum
CFC	Chlorofluorocarbon
CPE	Constant Phase Element
CSS	Close Space Sublimation
C-V	Capacitance-Voltage
DAISY-SOL	DArmstadt Integrated SYstem for SOLar cell research
E_B	Binding Energy
EBSD	Electron Back-Scatter Diffraction
E_{CBM}	Energy of the Conduction Band Minimum
EDX	Energy Dispersive X-ray
E_F	Fermi level
E_g	Energy gap
e-h	electron-hole
EQE	External Quantum Efficiency
E_{VBM}	Energy of the Valence Band Maximum
FF	Fill Factor
FPP	Four-Point Probe
FTO	Florine-doped Tin Oxide
GB	Grain Boundary
HRT	Highly Resistive Transparent
HST	High Substrate Temperature
HVE	High Vacuum Evaporation
IQE	Internal Quantum Efficiency
IS	Impedance Spectroscopy
ITO	Indium-doped Tin Oxide
J_L	Light current density
J_{sc}	Short Circuit current density
LST	Low Substrate Temperature
MOCVD	Metal Organic Chemical Vapor Deposition
N_A	Acceptors Density
N_D	Donors Density
PES	Photoelectron Spectroscopy
PV	Photovoltaic
PVD	Physical Vapor Deposition

QE	Quantum Efficiency
RF	Radio Frequency
R_H	Hall coefficient
RMS	Root Mean Square
R_p	Parallel Resistance
R_s	Series Resistance (solar cells)
R_s	Sheet Resistance/ Surface Resistance (thin films)
RT	Room Temperature
SEM	Scanning Electron Microscope
SIMS	Secondary Ion Mass Spectroscopy
SR	Spectral Response
T_A	Annealing Temperature
TCO	Transparent Conducting Oxide
UHV	Ultra-High Vacuum
UPS	UV Photoelectron Spectroscopy
VB	Valence Band
VBM	Valence Band Maximum
V_H	Hall Voltage
V_L	Vacuum Level
V_{oc}	Open Circuit Voltage
VTD	Vapor Transport Deposition
XP	X-ray Photoelectron
XPS	X-ray Photoelectron Spectroscopy
XRD	X-ray Diffraction
Z	Impedance
μ	carrier mobility
μ_e	electron mobility
μ_h	hole mobility
μ_H	Hall mobility
η	Solar cell efficiency
λ	wavelength
ϕ	work-function
ρ	resistivity
σ	conductivity
ω	angular frequency
χ	electron affinity

Contents

Zusammenfassung

Ein Schlüsselproblem für die Herstellung von CdTe-Solarzellen ist die Bildung von stabilen und nieder-ohmigen Kontakten. Bei der Deposition typischer Metalle auf CdTe-Oberflächen bilden sich Barrieren durch nicht angepasste Bandenergie-Positionen. Die Anpassung der Bänder ist bestimmt durch die Austrittsarbeit des Metalls, Oberflächenzustände und Metall-induzierte Grenzflächenzustände, die zu "Fermi level pinning" nahe der Bandmitte führen. Die Hauptaufgabe dieser Doktorarbeit war die grundlegende Untersuchung der Parameter, die eine verlässliche Bildung ohmscher Kontakte zu CdTe ermöglichen. Dazu wurde eine multifunktionale Vakuum-Kammer, die mit einer Plasma-Ionen-Quelle sowie unterschiedlichen Magnetron- und PVD-Quellen ausgerüstet war, an DAISY-SOL integriert. Die Solarzellen wurden durch die sequentielle Deposition von CdS und CdTe Schichten auf TCO-Glas durch "close-space-sublimation" (CSS) präpariert. Danach wurden die Zellen durch eine $CdCl_2$ Behandlung und durch die Abscheidung des Rückkontakts fertiggestellt. Nach jedem Depositions- oder Behandlungsschritt konnten die Proben zu dem Escalab Spektrometer für die XPS/UPS Charakterisierung im Ultra-Hoch-Vakuum transferiert werden.

Das Ziel war die Eliminierung von Cu für den Rückkontakt (aufgrund von Stabilitätsproblemen) und die Herstellung des Kontakts ohne chemischen Ätzschritt. Dazu musste die $CdCl_2$ Aktivierung in einer nichtoxidativen Atmosphäre durchgeführt werden, wofür ein in-situ $CdCl_2$ Aktivierungsreaktor entwickelt und für die Aktivierung im Vakuum integriert wurde. Dieser Aufbau ergab neben den Vorteilen in der trockenen Herstellung der Zellen die Möglichkeit, die Effekte der Aktivierung auf die CdS und CdTe-Schichten mittels Photoelektronen-Spektroskopie zu untersuchen. Zusätzlich wurden keine Oxid-Schicht gebildet, die die elektrische Vermessung der Leitfähigkeit der Proben mit AFM (c-AFM) in nano-Auflösung ermöglichte. Die Effekte die durch typische Behandlungsschritte wie $CdCl_2$ Aktivierung and chemisches Ätzen vor Bildung des Rückkontakts verbunden sind, konnten damit zusätzlich untersucht werden.

Die elektrischen Eigenschaften der fertiggestellten Zellen wurden durch Strom-Spannungs-, externe Quanteneffizienz- und Kapazitäts-Spannungs-(C-V) Messungen charakterisiert. Die Oberflächenmorphologie und Struktur der Schichten wurde mittels AFM, SEM und XRD untersucht. Die Leitfähigkeit und Ladungsträgerkonzentration einiger Filme wurden mit 4-

Punkt oder Hall-Effekt –Messungen bestimmt.

Drei unterschiedliche Rückkontaktansätze wurden in dieser Arbeit untersucht:

Der erste Ansatz war auf die Anwendung einer Zwischenschicht (oder kombinierten Schichtstruktur) zwischen CdTe und dem Metallkontakt ausgerichtet. Verschiedene Zwischenschichten wie ZnTe, Sb_2Te_3, Sb and Te wurden verwendet und die damit notwendigen Herstellungsparameter optimiert. Zelleffizienzen vergleichbar zu der Standard-Nasschemischer Prozessierung wurden erreicht, ohne dass chemische Ätzschritte, Waschvorgänge oder Cu verwendet wurden. Basierend auf früheren Ergebnissen wurde auch ZnTe (ZnTe:N) als vielversprechender Kandidat für den Rückkontakt getestet; da eine hohe p-Dotierung für ohmsche Kontakte und ein vernachlässigbarer Valenzband-Versatz für die CdTe/ZnTe Grenzflächen gemessen wurden. Leider wiesen die Zellen mit ZnTe:N/Au Rückkontakt relative kleine Wirkungsgrade auf, was auf die Degradierung der Zellen während der ZnTe:N Schichtabscheidung zurückgeführt wird. Als eine Alternative wurde Sb als p-Dopand für ZnTe verwendet. Nach Testung unterschiedlicher Prozesse wurde ein 4-Stufen-Prozess für hoch p-dotierte ZnTe (ZnTe:Sb) Dünnschichten mit Leitfähigkeiten von 31 S/cm (Widerstände von 0.03 Ω.cm) entwickelt. Obwohl der Kontakt zwischen ZnTe:Sb und den Metallen (Mo oder Au) ebenfalls ohmschen Charakter aufwies, war der erreichte Wirkungsgrad der damit hergestellten Solarzellen ebenfalls nur klein.

Ein weiterer Ansatz war die direkte Sb-Dotierung der CdTe Oberflächen zur Bildung von Tunnelkontakten. Dafür wurde eine effiziente Methode entwickelt, die mit einigen Änderungen der Sb Dotierung von ZnTe entsprach. Solarzellen mit einer Sb-dotierten CdTe Oberflächen zeigten einen sehr kleinen Serien-Widerstand (3-5 Ω/cm^2) und die Effizienz der Zelle war um 20% zur Standard-Zelle erhöht. Zelleffizienzen von 12.8% und Füll-Faktoren bis zu 69.3 % mit V_{oc} und J_{sc} von 770 mV und 24 mA/cm^2 wurden hergestellt. Dies waren zu der Zeit unsere Rekord-Wirkungsgrade.

Der letzte Ansatz war die Untersuchung von reduziertem Molybdän-oxid (MoO_x) als Rückkontakt-Zwischenschicht. MoO_x Schichten wurden durch RF reaktives Sputtern und PVD abgeschieden. Durch Änderung der Abscheideparameter und kontrolliert durch XPS und UPS, wurden die optimalen Bedingungen für die Deposition von MoO_x Schichten mit Austrittsarbeiten über 6 eV bestimmt.

CdTe Solarzellen mit MoO_x Rückkontakt-Zwischenschichten wiesen bessere Leistungsdaten als ohne Schicht auf, aber die Performanz war nicht besser als mit dem Standard-Rückkontakt (i.e. NP-Ätze mit gesputtertem Au). Drei Grenzflächenexperimente wurden

vorgenommen, um die Phasengrenze zwischen CdTe und MoO_x Schichten nach Sputter-Deposition und PVD-Abscheidung zu untersuchen. Die Grenzfläche wurde schrittweise durch Deposition von MoO_x Schichten auf die CdTe Oberfläche aufgebaut, wobei XPS und UPS Messungen nach jedem Schritt vorgenommen wurden. Das resultierende Energieband-Diagramm zeigte, dass MoO_x Zwischenschichten trotz der niedrigen Leitfähigkeit und der großen Austrittsarbeit kein niederohmigen Kontakt zu CdTe aufweisen können. Es zeigt sich, dass die große Austrittsarbeits-Differenz durch einen großen Grenzflächendipol kompensiert wird, und das Fermi-Niveau von CdTe immer 0.9 eV oberhalb des Valenzbands gepinnt wird. Deshalb muss CdTe hoch p-dotiert sein, um einen Rückkontakt mit kleinem Widerstand als Tunnelkontakt realisieren zu können; ansonsten ergibt sich eine große Barriere an der Phasengrenze.

Die meisten der hier untersuchten Cu-freien Rückkontakte zeigten keine Degradation nach 1 Jahr Lagerung im Labor.

Chapter 1

Introduction

Considering the limited reserves of fossil and nuclear (fission) fuels and the grave effects of fossil and nuclear power stations on the environment, their substitution with clean renewable-energy sources has become an increasingly important and vital research topic. This is important, because it will not only support the growth of industries and civilization on the whole, but it will result in a much cleaner atmosphere and improvement of the health and living standards on the planet earth.

Of the several renewable energy sources (e.g. solar, wind, hydroelectric, geothermal, biomass, and wave energy), only the solar energy has the capacity of meeting the energy demands of the countries on a large and sustainable scale. However, the problem with conversion of this energy is that it is spread over a large area, as well as over a wide wavelength spectrum; and of course, it is available only in the day times. On the other hand, it is practically an endless source of energy and its conversion to electrical energy produces no pollution.

Solar energy conversion can be done in two ways: photothermal and photovoltaics, each of which has its specific characteristics and advantages. The most important advantage of the photovoltaics is that it directly converts the sun light into the electrical energy, which is one of the most useful forms of energy, since it can be used for almost everything.

There are several photovoltaic (PV) technologies; e.g. single-crystal Si and GaAs cells, amorphous and microcrystalline Si cells, CdTe, CIS and CIGS cells, organic material cells, and Perovskite cells. Currently, of the second generation PV solar cells, i.e. single junction thin film solar cells, the CdTe cells have the highest large-area module efficiencies, the lowest cost of PV solar panels, and the highest industrial production worldwide [1]. Another advantage of the CdTe material is that it can be uniformly deposited at high rates (e.g. several μm/min) over large-area substrates. This in turn reduces the manufacturing costs. Furthermore, a very thin film ($\sim 2\,\mu$m) of CdTe absorbs almost all of the solar photon in its absorption range.

1.1 Motivation and scope of the project

One of the key challenges in manufacturing of CdS/CdTe solar cells is the formation of a stable and low-barrier ohmic contact to the CdTe layer. For the cell to function efficiently, the interface between the CdTe layer and the back contact (BC) should not present a barrier for transferring of holes to the metal electrode. Since p-type CdTe has a high work-function of about 5.7 eV, typical metals do not have work-functions large enough to build an ohmic contact. Even when a high work-function metal (like Au or Pt) is applied, a barrier height is formed due to an unfavorable energy-band alignment [2]. This alignment is determined by the work-function of the metal, interface states, and metal-induced gap states at the interface, which leads to pinning of the CdTe Fermi-level close to the middle of its energy gap. Some approaches such as creating a highly p-doped surface with copper and/or introducing an appropriate intermediate layer have been developed to overcome this problem; but there are still limitations concerning the stability, and in most cases a chemical etching is needed (which is not favorable for the mass production).

The main subject of this PhD project was an academic investigation of the parameters involved in the formation of a reliable ohmic back contact to the CdTe layer. The objectives were (1) to eliminate the use of copper (due to stability concerns), and (2) to make back-contacts without using the etching process. In order to meet these goals, the $CdCl_2$ activation had to be performed in a non-oxidizing atmosphere. Therefore, an in-situ $CdCl_2$ activation reactor was designed, fabricated, and integrated to the to the DAISY-SOL[1] to perform the activation process in vacuum. This facility, besides its benefits in fabrication of solar cells in an all-dry process, enabled us to study effects of the $CdCl_2$ activation on CdTe and CdS layers with photoelectron spectroscopy (PES). The PES investigation results along with other characterization of the completed solar cells, such as external quantum efficiency (EQE) and C-V measurements, will be presented in chapter 5. By an appropriate heat treatment, the CdTe surface was cleaned and does not contain any oxide or $CdCl_2$ deposition after the in-situ activation. Therefore, it was possible to study effects of the activation process on electrical properties of the cells by conductive AFM studies (chapter 6).

In previous studies in our group, a valence-band offset of 0.1 eV was measured at the CdTe/ZnTe interface [3]. Therefore, ZnTe could be a good candidate as a BC interlayer. If

[1] DArmstadt Integrated SYstem for SOLar cell research

ZnTe is used as an interlayer, it has to be p-type doped to form a low-resistance ohmic contact between p-ZnTe and the metal back contact. Copper-doped ZnTe layers have already been used as interlayer in CdTe solar cells, but they were not stable due to the copper diffusion [4].

As an alternative, p-type nitrogen-doped ZnTe (ZnTe:N) layers have successfully been deposited by RF sputtering and thermal evaporation of ZnTe (in presence of nitrogen ions created by a plasma source) [5, 6]. However, CdTe solar cells with ZnTe:N BC-interlayer did not show good performances. This could be due to a large lattice-mismatch between CdTe and ZnTe [5] and/or defects created by the ions at the CdTe/ZnTe interface during deposition of the ZnTe:N layer.

In this work, in order to improve the efficiency (η) of solar cells with ZnTe interlayers, we tried to modify the CdTe/ZnTe interface with an appropriate heat-treatment step, after deposition of the ZnTe:N layer. Another approach was to use a new method for p-type doping of ZnTe. For this purpose, antimony (Sb) was used and an efficient method for deposition of highly p-type antimony-doped ZnTe (ZnTe:Sb) layers was developed [7]. However, cells with ZnTe:Sb back contact interlayer did not show a good performance; therefore, we decided to use a similar method to dope the CdTe surface with antimony.

An effective procedure for doping of CdTe surface was developed that improved our CdTe solar cell efficiency by about 20%. Other BC-interlayers such as Te and Sb_2Te_3 were also studied, which will be discussed in chapter 7.

An additional back contact strategy was application of reduced molybdenum oxide (MoO_x) as the BC-interlayer, which will be investigated in chapter 8. The MoO_x layers with work-function larger than 6 eV and good conductivity were deposited by reactive RF-magnetron sputtering and thermal evaporation. The MoO_x layers and their interface with CdTe were analyzed by X-ray and UV-photoelectron spectroscopy. Solar cells with MoO_x/Mo back contact without any etching step were prepared that had better performance as compared with the cells without the MoO_x interlayer (when no chemical etching was involved in fabrication of the cells).

Chapter 2

CdTe Thin Film Solar Cells

Cadmium telluride with a direct bandgap of E_g = 1.45 eV and high absorption coefficient is an ideal candidate for production of thin film solar cells. The primary design for thin film CdTe solar cells is often based on n-type CdS and p-type CdTe layer structures. These cells can be produced in both substrate and superstrate configurations, as shown schematically in Fig. 2-1. In superstrate structure (which is the most common and efficient method of fabrication of CdS/CdTe solar cells) the CdS and CdTe layers are sequentially deposited onto a transparent-conducting oxide (TCO) coated glass substrate as shown in Fig. 2-1 (left). In this configuration, the light must pass through the substrate in order to reach the cell. In the superstrate configuration with this layer structure, conversion efficiencies of 19.6% (in the laboratory scale), and 16.1% (at industrial scale) have already been reported [8, 9]. In recent years, the energy conversion efficiency in CdTe PVs has bordered to 22%, mostly due to CdS removal, application of group V p-type doped graded CdSeTe/CdTe absorbers and ZnTe back contacts [10].

In the substrate configuration, the CdTe, CdS and TCO layers are sequentially deposited onto a substrate, which does not need to be transparent since the light does not need to pass through it.

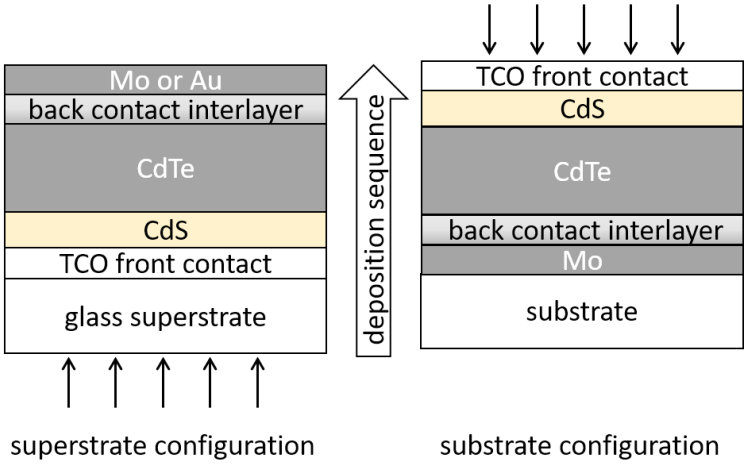

Fig. 2-1: Superstrate and substrate configurations of CdS/CdTe solar cells.

2.1 Substrate material

The substrate for CdTe solar cells with superstrate configuration has to be transparent and withstand high process temperatures (up to 620 °C). Glass is the most economical material that can be used in fabrication of CdTe solar cells. Low-cost soda-lime glasses are not suitable since they are not stable at high temperatures and some impurities may diffuse from the glass substrate to the CdS and CdTe layers during the fabrication process. In fabrication of high efficiency cells, highly transparent borosilicate glasses are used, which are stable to temperatures as high as 650 °C. Using a multi-layer antireflective coating may reduce the reflection of these glasses from 4% to 1% across the useful wavelength range of CdS/CdTe solar cells (400–850 nm) [11], but due to economic considerations, antireflection coatings usually are used for the laboratory champion cells.

2.2 Front contact material

For the superstrate CdS/CdTe solar cell, the first step is to deposit a TCO layer on the glass substrate as the front contact, in order to collect electrons from the CdS layer and transfer them to the metal electrode. The TCO layers should be highly transparent (visible transparency more than 80%) and have a sheet resistance less than 15 ohm per square. In addition, the TCO layer has to be stable at high process temperatures needed for fabrication of the cell.

Fluorine-doped tin-oxide (FTO) and indium-tin-oxide (ITO) are the two most common TCOs used as front contact material in CdS/CdTe solar cells, due to their electro-optical and chemical properties as well as their thermal stability. The choice between FTO and ITO depends on the deposition temperatures of the CdS and CdTe layers. For low deposition temperatures, ITO is preferred, since it has a higher optical transmission for a given sheet resistance. For high deposition temperatures, FTO is normally preferred, since it is more stable.

ITO with a buffer layer of SnO_2 can also be used for high deposition temperatures. The SnO_2 layer in this case acts as a barrier to prevent indium diffusion from ITO to the CdS and CdTe layers. In high efficiency CdTe solar cells with a very low CdS thickness (<50 nm), a high-resistance transparent (HRT) layer is used as a buffer layer between the TCO and CdS layers. When the CdS thickness is very low, some pinholes may be created in the CdS layer. This formation of pinholes leads to a short of the CdTe with the TCO layer,

leading to the formation of micro-diodes (which are not as efficient as the CdTe/CdS diode) and act as micro-shunts reducing the overall efficiency of the device.

Using an HRT buffer layer can help to maintain the device performance by limiting the leakage tunneling current of weak micro-diodes. The HRT buffer layer also reduces the surface roughness of the TCO and therefore, provides a suitable condition for deposition of pinhole-free CdS layers (with thicknesses below 100 nm). Intrinsic SnO_2 is the most commonly used HRT buffer layer, and its effect on performance of CdTe solar cells has already been studied [12-15].

2.3 CdS window layer

In conventional CdTe solar cells, CdS with a direct band-gap of 2.4 eV is used as the n-type part of the heterojunction diode. Since the light should pass through the CdS layer first (before it can be absorbed by the CdTe layer), the CdS film is usually referred to the "window layer". Due to the very low lifetime of holes and high recombination rates in the CdS layer, all photo-generated carriers in this layer recombine and do not contribute to the cell photocurrent. Hence, all the photons with wavelengths shorter than 520 nm (i.e. the wavelength corresponding to the bandgap of CdS) are effectively lost. Therefore, the CdS window layer should be as thin as possible (typically < 50 nm) and also uniform and pinhole-free, to prevent formation of micro-shunts between the CdTe and TCO. Such a thin film CdS layer can be deposited with several methods including chemical-bath deposition (CBD) [16, 17], physical-vapor deposition (PVD)[17], magnetron sputtering [18, 19], and close-space sublimation (CSS)[18, 20].

An approach to reduce the photocurrent loss in the short-wavelength region is incorporation of oxygen into the CdS window layer that increases its optical band-gap. The oxygenated CdS (CdS:O) window layers can be deposited by a reactive sputtering of a CdS target in an oxygen mixed Argon environment [21-23].

In the high-efficiency CdTe cells, the photocurrent loss in the CdS window layer has been considerably reduced by replacing the CdS layer by a bi-layer window material consists of CdS:O and CdSe thin films [24]. The bi-layer structure is formed from of an ultra-thin CdS:O layer (~10-15 nm) onto a TEC15 TCO coated glass substrate (section 4.2), followed by sputter deposition of a CdSe layer with thickness of ~100 nm. The external quantum efficiency (EQE) of completed CdTe solar cell with combined window layer appears to be

limited only by optical absorption at the FTO-coated glass substrate at the short-wavelengths region. EQE of the solar cells with CdS:O/CdSe window layer showed improvements in both short and long wavelength regions as compared with the standards CdS/CdTe solar cells. The improvement at the red region is due to a stronger intermixing at the CdSe/CdTe interface that leads to formation of a $CdSe_xTe_{1-x}$ alloy, which has a smaller energy gap, as compared with the formation of CdS_xTe_{1-x} at the CdS/CdTe interface. This is due to a higher solubility of Se in CdTe and lower activation energy for intermixing of Se into the CdTe, as compared with the sulfur [25]. The EQE improvement at the blue region is due to a much lower CdS thickness in the bi-layer window structure compared with the standard cells. The short circuit current (J_{sc}) of solar cells with a pure CdSe window layer (without CdS) were slightly higher than those with the combined window layer but the open circuit voltage (V_{oc}) and therefore the overall performance of these cells was lower. This is related to the contact between SnO_2 and CdSe that produces a larger band offset (compared with the SnO_2/CdS) that leads to a lower V_{oc} [26].

In the state-of-the-art CdTe cells with the layer structure presented in Fig. 2-3, the external quantum efficiency appears to be limited only by the short wavelengths absorption in the TCO-coated glass substrate [10]. Detailed information about the window layer structure is not clear; however, academic studies indicate that an ultra-thin CdS:O buffer layer and/or a CdSe window layer may have been used in these cells.

2.4 CdTe absorber layer

CdTe with a direct energy bandgap of 1.45 eV at room temperature [27] is within the optimum range of 1.2 to 1.5 eV for maximum photovoltaic energy conversion, as can be seen in Fig. 2-2 [28]. The theoretical maximum efficiency of CdTe-based solar cells is estimated to be around 30% [28, 29]. As a consequence of having a direct bandgap, CdTe has a high absorption coefficient of $>5\times10^5$ /cm for AM1.5 photons with energy larger than its bandgap [30]. Although more than 99% of the absorbable photons can be absorbed by a CdTe layer as thin as 2 μm [31], the CdTe thickness of conventional CdS/CdTe cells used to be more than ~3 μm. This is due to the difficulty in controlling of CdTe growth during its deposition and post-deposition treatment steps.

Cd and Te have a higher vapor pressure than the CdTe; therefore, the stoichiometric CdTe films are relatively simple to be prepared by physical vapor deposition (PVD) techniques, since the excess of each element re-evaporates from the substrate during deposition.

Polycrystalline thin film CdTe layers for solar cell applications have been deposited with several methods including CSS [20, 32], vapor transport deposition (VTD) [33], PVD [34, 35] and sputtering [35, 36]. Among these methods, the CSS and VTD are the most adapted methods for fabrication of high efficiency CdTe solar cells in laboratories and production lines.

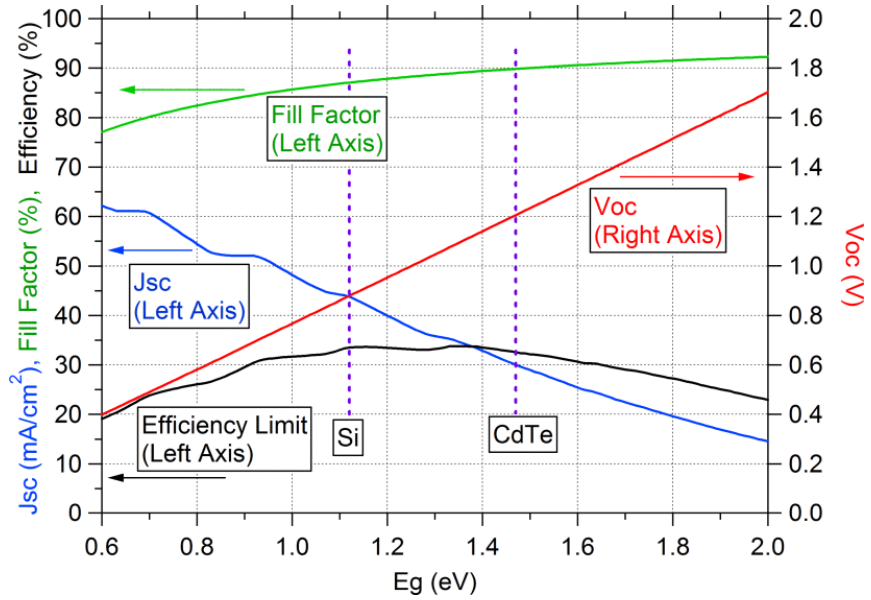

Fig. 2-2: Theoretical limits of V_{oc}, J_{sc}, fill factor and efficiency of solar cells as a function of the energy gap (E_g) of the absorber layer [28].

After decades of optimization of CdTe solar cells, the open-circuit voltage has remained limited to ~850 mV, which is far below the theoretical limit of ~1.2 V as shown in Fig. 2-2). V_{oc} can be improved by increasing both the acceptor density and minority carrier lifetime in the CdTe layer. For a long time, $CdCl_2$ treatment (chapter 5) and Cu doping were widely used to increase the carrier density and lifetime in CdTe layers to produce highly efficient solar cells; however, with these treatments p-type doping of the CdTe layer was always limited to ~10^{14} cm^{-3}. In a recent work [37], highly p-type arsenic doped CdTe layers with carrier densities as high as ~10^{16} cm^{-3} were deposited by MOCVD[1], however, the efficiency and V_{oc} of the solar cells produced with this method were relatively low (η=13.3%, V_{oc}=763 mV). This was due to a short carrier lifetime (~2 ns) that was related to a very small average grain size of the CdTe layer. In another work, in order to achieve both high hole density and long carrier lifetime, the Te lattice sites were replaced with

[1] Metal Organic Chemical Vapor Deposition

group V elements [38]. In this work, single-crystal CdTe wafers with high doping levels of $\sim 10^{17}$ cm^{-3} and very long carrier lifetime (on the order of 1 μs) were produced. To make solar cells, CdS:O/ZnO/ZnO:Al and Cu/Mo were sputter-deposited onto both sides of the CdTe wafer to form the front and back contacts, respectively. These cells had open-circuit voltage of 1.047 V and conversion efficiency of 15.2%, which are record values for single crystal CdTe solar cells with similar structure. In another study, polycrystalline CdTe films with hole density as high as 10^{16}–10^{17} cm^{-3} without compromising lifetime in the CdTe layer were produced by an in-situ Sb, As, and P doping and post-growth annealing [39]. In the state-of-the-art CdTe solar cell, which is shown schematically in Fig. 2-3, besides replacing the CdS with a buffer layer (CdS:O or MgZnO), arsenic doped CdSeTe/CdTe absorber prepared by VTD and a ZnTe/metal back contact were used [10]. Cu was replaced by substitutional As dopant in polycrystalline $CdSe_xTe_{1-x}$ and CdTe films to not only stabilize the energy states (and thus control the charge diffusion), but to substantially increase the majority-carrier density to 1×10^{16} - 1×10^{17} without lowering carrier lifetime. Within such modifications, photocurrent exceeded to 30 mA cm^{-2}, FF reached by ~80%, and device efficiency set to 20.8% high.

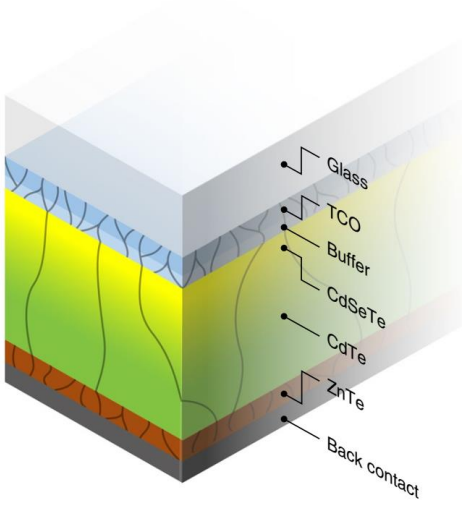

Fig. 2-3: Schematic of state-of-the-art CdTe solar cell [10].

2.5 Back contact material

In superstrate CdS/CdTe solar cells, the back contact is typically made by depositing a few nanometers of Cu onto the pre-treated CdTe surface followed by deposition of a metallic electrode (~100nm of Au or Mo) and an annealing step (at ~200°C). Another approach is

application of an appropriate layer between CdTe and the back electrode, to align the valence band for hole transport. In this PhD work, the back-contact has been intensively studied, which will be discussed with details in chapters 7 and 8.

Chapter 3

Basics

In this chapter, the working principle of p-n junction solar cells and some characterization techniques will be presented. SCAPS simulation program [40] was used to study the important parameters that affect the performance of CdTe solar cells. Most of the characterization methods that were used in this work will be introduced in this chapter except the conductive AFM measurements, which will be presented in chapter 6.

3.1 Operational details of p-n solar cells

The current density of a single junction solar cell in dark (J_D) is similar to the current density of a p-n diode and can be describe as

$$J_D = J_0 \left[\exp\left(\frac{qV}{nkT}\right) - 1\right] \tag{3.1}$$

The parameters in this equation are as following:

J_0: reverse saturation current density,

q: electric charge of electron,

V: voltage across the diode,

k: Boltzmann constant,

T: temperature in Kelvin (kT is called thermal voltage and is equal to 26 mV at room temperature,

n: diode quality factor [41].

When the solar cell is illuminated, light photons are absorbed in the cell and electron-hole (e-h) pairs are generated. The e-h pairs generated in the space-charge region of the cell (and some within the diffusion lengths in both sides of the depleted region) are separated by the electric field inside the depletion region and produce a light current (J_L) which is in opposite direction of the diode dark current. Therefore, the net current density under illumination is as following

$$J(V) = J_D(V) - J_L \tag{3.2}$$

J_L in this equation is the maximum current density of the solar cell under illumination that is equal to the short circuit current density (J_{sc}), therefore

$$J(V) = J_0\left[\exp\left(\frac{qV}{nkT}\right) - 1\right] - J_{sc} \tag{3.3}$$

J-V characteristics of this ideal solar cell in the dark and under illumination is shown in Fig. 3-1. When the solar cell is under open circuit condition, the net current density is zero (J=0) and the potential difference has its maximum value, which is called the open circuit voltage (V_{oc}). From equation 3.3, the open circuit voltage can be determined as follows

$$V_{oc} = \frac{nkT}{q}\ln\left(\frac{J_{sc}}{J_0} + 1\right) \tag{3.4}$$

This equation shows that V_{oc} increases logarithmically with J_{sc} or the light intensity.

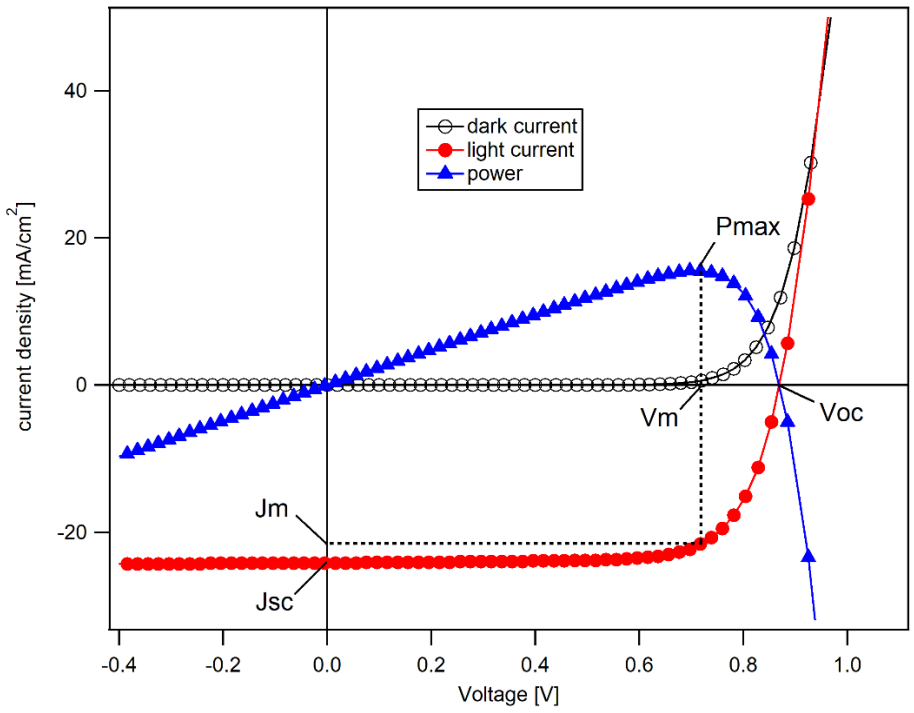

Fig. 3-1: J-V characteristics of an ideal solar cell in the dark and light.

The power density (P) is equal to the amount of product of the current density and voltage:

$$P = V \times J \tag{3.5}$$

When the voltage is between 0 and V_{oc}, the device generates power, but at $V < 0$ and $V > V_{oc}$ it consumes power. At the maximum power point, which is related to V_m and J_m in Fig. 3-1, the solar cell can produce its maximum power density which is equal to:

$$P_{max} = V_m \times J_m \tag{3.6}$$

The solar cell efficiency (η) is determined from the following equation:

$$\eta = \frac{P_{max}}{P_{in}} = \frac{V_m \times J_m}{P_{in}} = \frac{V_{oc} \times J_{sc} \times FF}{P_{in}} \tag{3.7}$$

In this equation, P_{in} is the incident power density and the Fill Factor (FF) of the solar cell is defined by the following equation:

$$FF = \frac{V_m \times J_m}{V_{oc} \times J_{sc}} \tag{3.8}$$

The FF represents the quality of the solar cell and its value is from 0.6 to 0.8 for good solar cells. In the J-V curve, the FF shows how similar the shape of the J-V curve is to a square.

3.1.1 Effect of R_s and R_p

In a simple single-diode model, the solar cell consists of a p-n junction diode in parallel with a current source. For the parasitic effects, a series resistance (R_s) and a shunt or parallel resistance (R_p) are considered in this model as shown in Fig. 3-2. The series resistance is due to the resistances of the layers and the electrical contacts to the cell and the shunt resistance is because of any shunts across the junction, which leads to a leakage current in the cell.

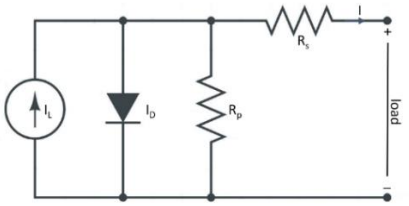

Fig. 3-2: equivalent circuit of a solar cell including R_s and R_p.

The J-V equation of a solar cell including R_s and R_p is [42]:

$$J = J_0 \left[\exp\left(\frac{q(V - JR_s)}{nkT}\right) - 1\right] + \frac{V - JR_s}{R_p} - J_L \tag{3.9}$$

SCAPS simulation program [40] was used to study the effect of the series and parallel (i.e. shunt) resistances on the parameters of a CdS/CdTe solar cell. The important parameters and J-V characteristics of solar cells with different series resistance are shown in Table 3-1 and Fig. 3-3, respectively. From this simulation, it can be concluded that the fill factor and efficiency are decreasing by increasing the series resistance. Since at V_{oc} the current is zero, the voltage does not drop across R_s, therefore the open circuit voltage is not affected by the series resistance, as can clearly be seen in Fig. 3-3. For highly efficient solar cells, R_s must be as low as possible. In highly efficient CdTe solar cells R_s is less than $\sim 5\ \Omega.cm^2$. The series resistance can be determined from the slope of J-V curve at V_{oc} using the following equation:

$$R_s = \left(\frac{\partial J}{\partial V}\right)^{-1} at\ \ V = V_{oc} \tag{3.10}$$

Table 3-1: parameters of CdS/CdTe solar cells with different series resistance.

R_s ($\Omega.cm^2$)	V_{oc} (V)	J_{sc} (mA/cm^2)	FF (%)	η (%)
0	0.87	24.19	76.18	16.04
2	0.87	24.17	71.63	15.07
5	0.87	24.13	65.00	13.67
10	0.87	24.07	54.64	11.46
20	0.871	23.88	37.94	7.89

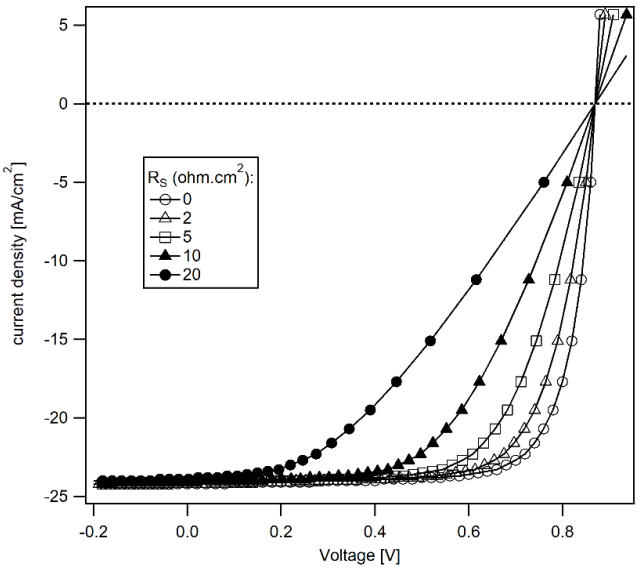

Fig. 3-3: effect of R_s on J-V curve of CdS/CdTe solar cells simulated using SCAPS.

Effect of the shunt resistance on performance of CdS/CdTe solar cells was also studied using SCAPS program. According to the results shown in Table 3-2 and Fig. 3-4, by decreasing the shunt resistance, fill-factor and efficiency of the cell significantly decrease while the short circuit current and open circuit voltage are almost constant. In order to produce an efficient solar cell, the shunt resistance must be as high as possible. In highly efficient CdTe solar cells R_p is larger than ~500 $\Omega.cm^2$. The shunt resistance can be determined from the slope of J-V curve at V=0 using the following equation:

$$R_p = \left(\frac{\partial J}{\partial V}\right)^{-1} at\ V = 0 \tag{3.11}$$

Table 3-2: effect of the shunt resistance on important parameters of a CdS/CdTe solar cell.

R_p ($\Omega.cm^2$)	V_{oc} (V)	J_{sc} (mA/cm^2)	FF (%)	η (%)
10^6	0.87	24.18	76.18	16.04
300	0.87	24.18	68.37	14.30
150	0.86	24.18	60.85	12.63
100	0.85	24.18	53.69	11.03
75	0.84	24.18	46.96	9.54

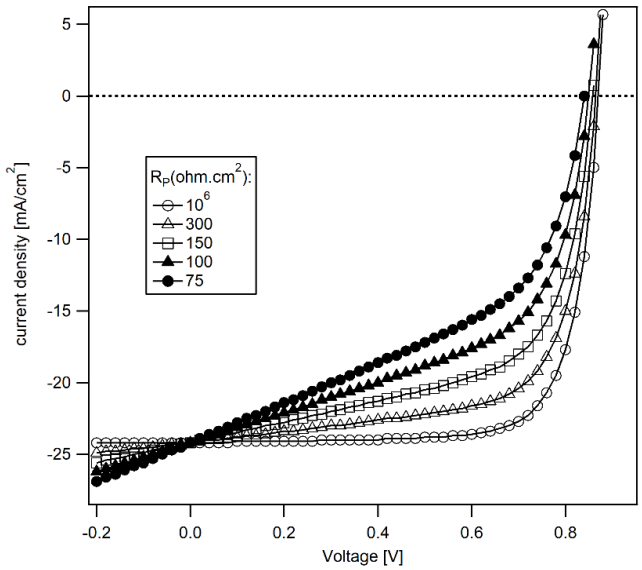

Fig. 3-4: effect of R_p on the J-V curve of CdS/CdTe solar cells simulated using SCAPS.

3.1.2 Two-diode model for CdTe solar cells

In CdTe solar cells, the contact between p-CdTe and the metal back contact is not ohmic and a Schottky diode forms, which is in opposite direction to the main junction as shown in Fig. 3-5. When a bias V is applied to the cell, the voltage is divided between the main junction diode (V_j) and back contact diode (V_b), as shown in Fig. 3-6 [43]. At low bias voltages (less than V_{oc}), the back diode does not affect the photocurrent since it is in forward bias. At bias voltages higher than V_{oc}, the V_j saturates and the voltage drops over the back contact; since the contact diode is in reverse bias, it blocks the photocurrent. As a consequence, the current at high bias voltages saturates at the contact saturation current that leads to a roll-over in the J-V curve (for example, see Fig. 7-24).

Another effect of the back-contact barrier is the intersection of the dark and light J-V curves at voltages higher than V_{oc}, which is called cross-over effect. As mentioned before, the junction voltage saturates for high forward biases. The saturation voltage under illumination is higher than its value in the dark [43]. This means that the total current under illumination saturates at a higher value than the dark current. Therefore, the dark and illuminated J-V curves are crossing at high voltages (see Fig. 7-29).

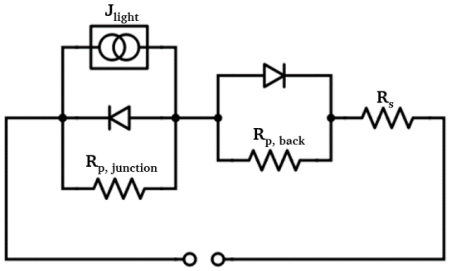

Fig. 3-5: two-diode equivalent circuit model for CdTe solar cell.

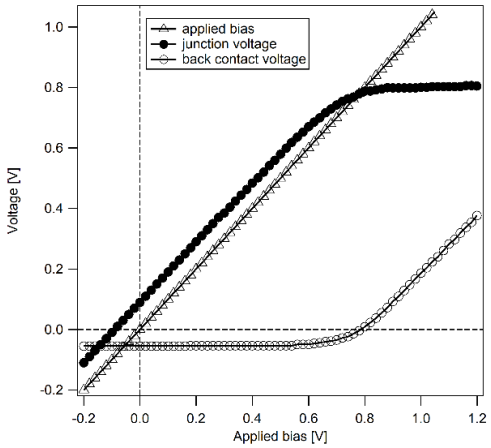

Fig. 3-6: junction voltage and contact voltage as a function of applied bias [43].

3.2 Electrical characterization of solar cells

The first characterization technique, which was performed on all completed solar cells, was J-V measurement. Some samples were also characterized by external quantum efficiency (EQE), impedance spectroscopy (IS) and C-V measurements. The details about these techniques are given in the following sections.

3.2.1 J-V measurement

Solar cells were characterized by J-V measurement in dark and light using a solar simulator model 81150 from LOT-Oriel GmbH. This setup was equipped with a 300 W Xenon lamp, filters, mirrors and lenses to simulate an AM1.5 global spectrum (see Fig. 3-9). The light intensity of the solar simulator was calibrated using a pyranometer model CMP11 each time before the measurement. The completed samples with 9 cells (see Fig. 4-6) were placed onto a sample holder and connected with nine parallel tips. Each tip was connected to the back contact of a cell. Another tip was also connected to the common front contact of the cells. A Keithley 2400 source meter was used for the current-voltage measurement. The source meter was controlled by a computer and the measurements were performed using a dedicated software from Antec Solar GmbH. In order to determine the solar cell parameters, i.e. efficiency, F.F., voltage and current at the maximum power (V_m and J_m), J_{sc}, V_{oc}, R_s and R_p, the cell area which in most cases was 16 mm^2 was given to the software and the program should be run twice. In the first run, in which the light shutter was closed and the cell surface was covered with a black cover, the dark J-V characteristics was measured. In the second run, the solar cell was exposed to the AM1.5 light and the light J-V characteristics was recorded. The measurements were performed by increasing the voltage from -1.0 V to +1.2 V by steps of 0.01 V and measuring the current passing through the cell.

3.2.2 Quantum efficiency measurement

A J-V measurement gives the absolute value of the J_{sc} produced by a solar cell, but it does not provide information about the source of J_{sc} losses. In order to find how photons with different wavelengths contribute to the current, the quantum efficiency (QE) of the cell has to be measured. QE measurement is tool to determine losses responsible for reducing the measured J_{sc} from its maximum theoretical value.

QE is defined as the ratio of the number of electrons (N_e) produced by a solar cell to the number of incident photons (N_{ph}) at each wavelength. Therefore, the QE equation can be written as following:

$$QE(\lambda) = \frac{N_e(\lambda)}{N_{ph}(\lambda)} = \frac{\frac{I_{SC}(\lambda) \cdot t}{e}}{\frac{E(\lambda)}{E_{ph}(\lambda)}} \tag{3.12}$$

Here $I_{sc}(\lambda) = J_{sc} \times A$ is the short-circuit current produced by the cell (A is the cell area), $E(\lambda)$ is the incident light energy and $E_{ph}(\lambda)=hc/\lambda$ is the photon energy. By substituting these in equation 3.12 it gives:

$$QE(\lambda) = \frac{hc}{\lambda} \cdot \frac{\frac{J_{SC}(\lambda)}{e}}{\frac{E(\lambda)}{A \cdot t}} = \frac{hc}{e\lambda} \cdot \frac{J_{SC}(\lambda)}{P(\lambda)} \tag{3.13}$$

which $P(\lambda) = \frac{E(\lambda)}{A \cdot t}$ is the light power intensity that irradiated to the solar cell. Spectral response (SR), which determines the spectral distribution of the short-circuit current, is defined as the ratio of the current generated by the solar cell to the light power incident on it, i.e.:

$$SR(\lambda) = \frac{J_{SC}(\lambda)}{P(\lambda)} \tag{3.14}$$

Therefore, the relation between QE and SR is as following:

$$QE(\lambda) = \frac{hc}{e\lambda} \cdot SR(\lambda) = \frac{1240}{\lambda(nm)} \cdot SR(\lambda) \tag{3.15}$$

The spectral response of solar cell, in units amperes per watt (A/W), can experimentally be measured for photons with different wavelengths and the result can be used to calculate the QE of the sample from equation 3.15. For measurement of the $SR(\lambda)$, the light intensity at each wavelength must be determined. In practice the light intensity $P(\lambda)$ is measured with the help of a reference detector with known spectral response. Therefore, in order to determine the QE of a sample, two measurements (J_{sc} vs λ measurement for sample and

reference) with the same parameters is performed and QE of the sample is calculated from the following equation:

$$QE^{sample}(\lambda) = \frac{hc}{e\lambda} \cdot \frac{J_{sc}^{sample}(\lambda)}{J_{sc}^{ref}(\lambda)} \cdot SR^{ref}(\lambda) = QE^{ref}(\lambda) \cdot \frac{J_{sc}^{sample}(\lambda)}{J_{sc}^{ref}(\lambda)} \quad (3.16)$$

In an ideal solar cell, for any incident photon with energy (E_{ph}) higher than the band gap (E_g) of the absorber layer, an electron will be produced; therefore, QE=1 when $E_{ph} \geq E_g$ and QE=0 for $E_{ph} < E_g$. However, in a real solar cell, QE < 1 even for $E_{ph} \geq E_g$ which is due to the optical and recombination losses. For example, in superstrate CdS/CdTe solar cells, the optical losses are mostly due to absorption of photons in TCO and glass substrate and also reflection of photons from the glass and interfaces. In addition, there are different recombination mechanisms, which lead to reduction of the QE. Electron-hole pairs generated in the CdTe layer may recombine at the CdS/CdTe interface, inside the CdTe layer or at the CdTe/back-contact interface for thin absorber layers.

SCAPS program was used to simulate the QE of a glass/FTO/CdS/CdTe solar cell. In Fig. 3-7(a) the simulated QE is illustrated and quantum efficiency of an ideal CdTe solar cell together with transmittance of a glass substrate are added to the figure to show different QE losses. QE losses related to the glass substrate and the TCO layer are shown in Fig. 3-7(b) and losses associated with the CdS and CdTe layers are also shown in Fig. 3-7(c). The QE losses of a CdS/CdTe solar cell in superstrate configuration can be explained as following:

- Reflection losses (~8-10%): incident photons may reflect from the glass surface and different interfaces before reaching to the CdTe absorber layer. Some of the photons are also reflected by the free electrons of the TCO layer. The glass reflection (which is about 7.6% at wavelength between 400 to 900 nm) can be reduced by applying an anti-reflection coating but this is only applied in “champion” cells;
- Absorption in the TCO (FTO) and glass substrate (about 5-10%): absorption/reflection in the visible wavelengths due to free electrons. The FTO absorption increases rapidly at short wavelengths due to the fundamental absorption at wavelengths correspond to the FTO energy gap (i.e. 320 nm);

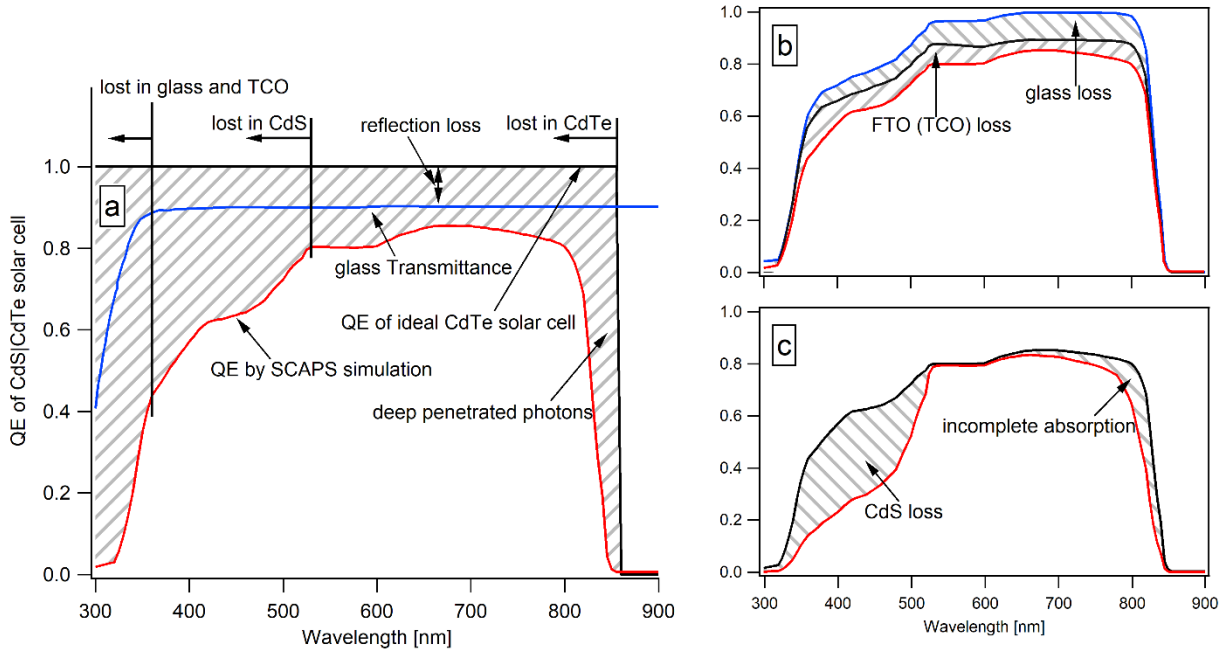

Fig. 3-7: (a) QE of glass/FTO/CdS/CdTe solar cell simulated by SCAPS program; QE of an ideal CdTe solar cell is also added to clarify different lost sources, (b) QE losses related to the glass and TCO layer, (c) QE losses related to the CdS and CdTe layers.

- Absorption in the CdS layer: due to a very high recombination rate, electron–hole pairs generated in the CdS layer cannot be collected. Therefore, photons with wavelength less than 520 nm (corresponding to the CdS bandgap of 2.4 eV) are lost, if they are absorbed in the CdS layer. Optical loss due to absorption in the CdS layer depicted in Fig. 3-8 (left). This figure shows how by increasing the CdS thickness, the quantum efficiency of the cell decreases. In practice, a very thin CdS layer (<30 nm) may lead to poor performance due to formation of shunt paths between the TCO and CdTe layer. In order to avoid shunting, a highly resistive transparent (HRT) buffer layer is applied on TCO [12, 44].
- Deep penetration loss: e-h pairs generated near to the back contact cannot be collected due to a very high interface recombination rate. Therefore, when the CdTe thickness decreases to less than ~2 μm, the quantum efficiency of the cell decreases, which is due to an incomplete absorption of photons, as shown in Fig. 3-8 (right). From this figure it can also be seen that by reducing the CdTe thickness from 4 μm to 3 μm, the QE loss (or J_{sc} loss) is very small; therefore, concerning J_{sc} of single junction CdS/CdTe solar cells, ~3 μm would be the optimum CdTe thickness for mass production.

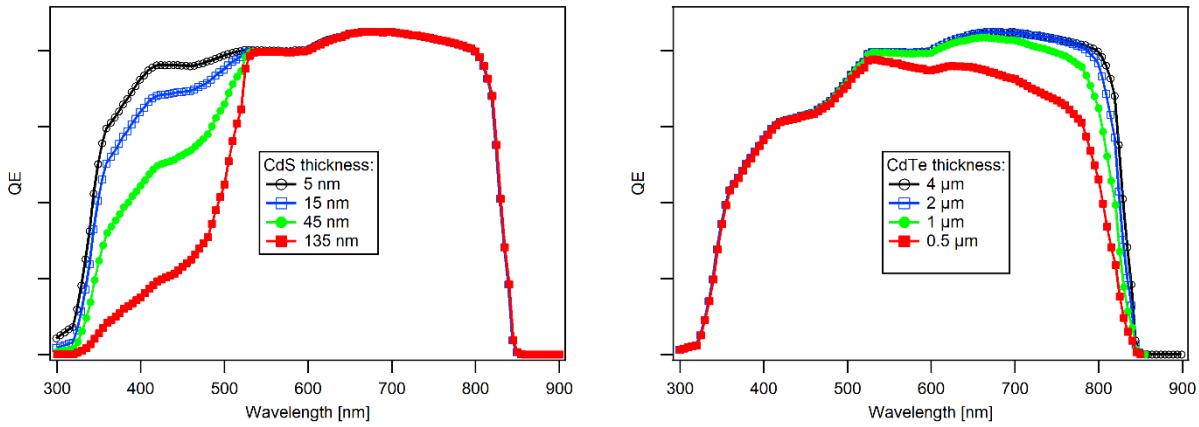

Fig. 3-8: effect of the CdS and CdTe thickness on the quantum efficiency.

The QE measurement may be reported in two ways, which are called external quantum efficiency (EQE) and internal quantum efficiency (IQE). In the EQE measurement (which is same as QE measurement), the spectral response of the sample is measured without applying any correction related to the optical losses (reflection and absorption of glass and TCO). But, for the IQE measurement, only transmitted photons to the cell are counted. Therefore, in order to measure the IQE of a glass/TCO/CdS/CdTe sample, in addition to its EQE measurement, transmittance (T) of a glass/TCO substrate has to be measured. Then, the IQE can be calculated from the following equation:

$$\mathrm{IQE}(\lambda) = \frac{\mathrm{EQE}(\lambda)}{1 - \mathrm{R}(\lambda) - \mathrm{T}(\lambda)} \tag{3.17}$$

$\mathrm{R}(\lambda)$ and $\mathrm{T}(\lambda)$ are the reflectance and transmittance of the substrate, respectively. The denominator in this equation is less than one, therefore the IQE of a solar cell is always larger than its EQE.

The short-circuit current of cell can be calculated from the QE measurement independently of J−V measurement. In order to do so, the QE must be multiplied by the photon flux $\mathrm{F}(\lambda)$, in units photons/m^2/nm/s), integrated over all measuring wavelengths (in units of nm) and multiplied by the elementary charge (e). The photon flux of the AM1.5G spectrum ($\mathrm{F_{AM1.5G}}$), which is shown in Fig. 3-9, is determined by dividing the AM1.5G power spectrum ($\mathrm{P_{AM1.5G}}$ based on ISO 9845-1) to the photon energy at each wavelength (i.e. hc/λ). Therefore, $\mathrm{J_{sc}}$ can be calculated as following:

$$J_{sc} = \int_{\lambda_1}^{\lambda_2} \frac{e\lambda}{hc} \cdot QE(\lambda) \cdot P_{AM1.5G}(\lambda) \cdot d\lambda \qquad (3.18)$$

$$= \int_{\lambda_1}^{\lambda_2} e \cdot QE(\lambda) \cdot F_{AM1.5G}(\lambda) \cdot d\lambda$$

This equation gives J_{sc} in units A/m^2. Hence the result must be multiplied by 0.1 to have the current density in mA/cm^2.

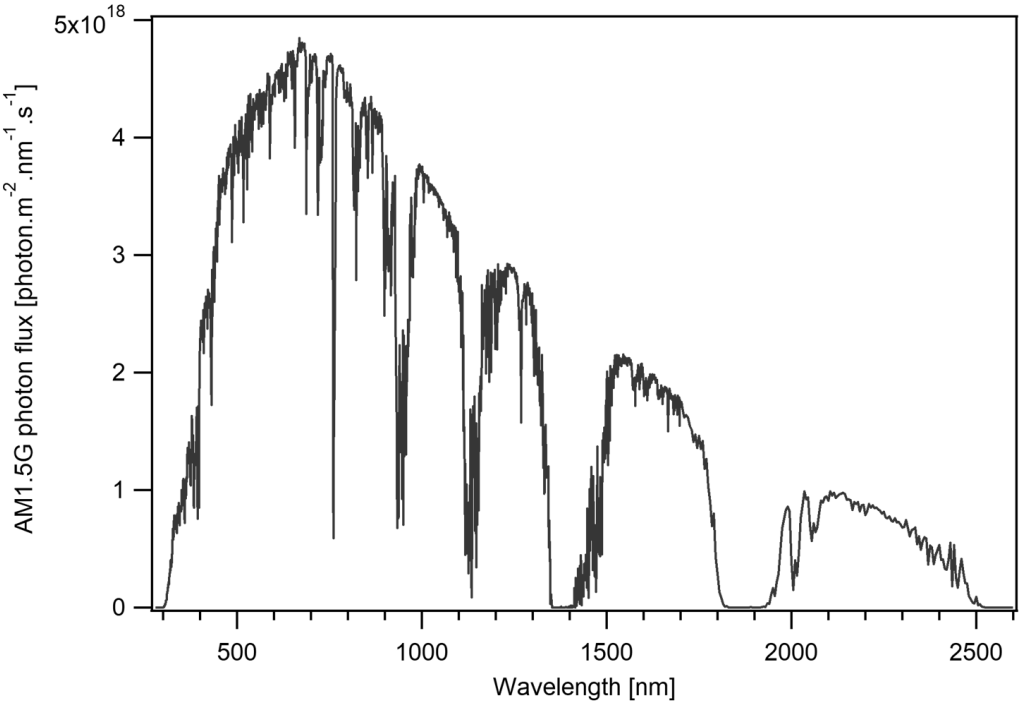

Fig. 3-9: Photon flux of AM1.5G solar spectrum ($F_{AM1.5G}$). The flux of high-wavelength photons (i.e. $\lambda > 2600$ nm) is not shown here.

The maximum current density (J_{max}) of an ideal CdTe solar cell under AM1.5G illumination can also be calculated from equation 3.18 by substituting the QE of an ideal CdTe solar cell (with E_g=1.45 eV corresponds to wavelength of 855 nm) in this equation. By doing the integration over relevant wavelength range (i.e. from 280 to 860 nm), J_{max} is calculated to be 32.2 mA/cm^2. When the QE shown in Fig. 3-7(a) is substituted in equation 3.18, it gives J_{sc}=22.9 mA/cm^2 which is 9.3 mA/cm^2 less than the J_{max}. This difference is related to the different loss mechanisms, which were discussed earlier.

QE measurement setup

The QE measurement in this work was performed in darkness (without additional light bias) using a home-made setup which is shown schematically in Fig. 3-10. In this setup, the light of a 150 W halogen lamp passes through a monochromator (made by HORIBA Jobin Yvon GmbH) equipped with a filter wheel with three filters that could produce monochromated light from 370 to 1200 nm with resolution of 5 nm. The monochromated light then passes through an optical chopper and optical lenses to produce a pulsed beam with size of about 2 mm by 2 mm on a beam-splitter, which splits it into two beams (a transmitted and a reflected beam to shine the sample and reference detector, respectively). The light intensity could be controlled by two slits, which were located at the entrance and exit of the monochromator. The monochromator (including filter wheel and slits) was controlled by a computer.

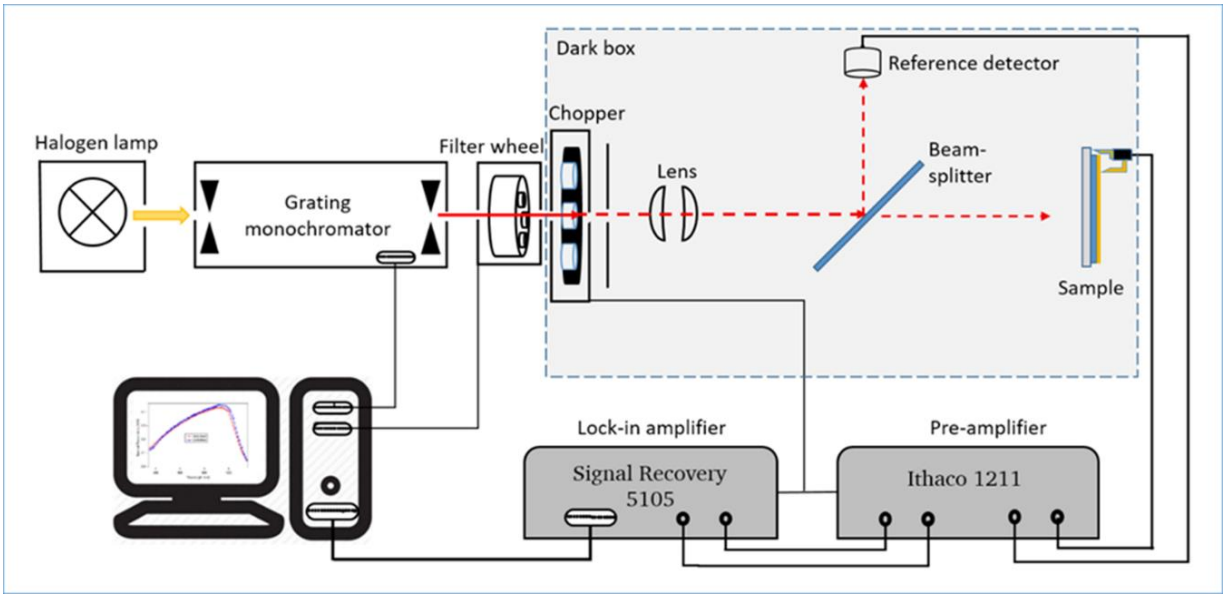

Fig. 3-10: experimental setup of the quantum efficiency measurement.

The photocurrent generated by the sample and reference cell were very small, therefore they had to be amplified to be measured correctly. The sample (which was mounted in a special sample holder with two spring contact probes) and the reference detector were connected to a current pre-amplifier (model Ithaco 1211) with BNC connectors. The pre-amplified signals were measured with a lock-in amplifier model 5105 from Signal Recovery.

The chopper with frequency of 37 Hz was used to pulse the signal; the lock-in amplifier was also set to that frequency. Since the lock-in will only amplify signals modulated at that specific frequency, it can separate the photocurrent from noises.

A LabView program was written in our group to control the experimental setup and measure the spectral response. The measured data were imported in the IGOR program to calculate the QE and J_{sc} of the solar cells.

Since the beam splitter in this setup did not split the beam with exactly equal intensities, a correction had to be applied when the sample and reference were measured simultaneously. It was found that if the halogen lamp had been turned on at least 20 minutes before starting the measurement, the light intensity remained stable; therefore, the QE measurements in this work were performed without using the beam splitter and the light intensity was determined by measuring a standard Si solar cell with known spectral response at the sample position.

3.2.3 Impedance Spectroscopy

Impedance spectroscopy (IS) is a powerful technique for electrical characterization of materials and their interfaces with conducting electrodes. In polycrystalline solids, transport properties are strongly affected by the microstructure, and impedance spectra usually contain features which can be related to that. In order to obtain useful information from the IS measurement of a solar cell, the measurement must be performed as a function of an experimental parameter such as DC voltage, temperature, illumination, layer thicknesses and electrical contacts.

Impedance spectroscopy is performed by applying an alternating voltage V(t) to a sample and measuring the current response I(t). V(t) and I(t) are sinusoidal functions that can be expressed as:

$$\begin{aligned} V(t) &= V_m \sin(\omega t) \\ I(t) &= I_m \sin(\omega t + \varphi) \end{aligned} \tag{3.19}$$

where V_m and I_m are the amplitude of the voltage and current signals, respectively, ω is the angular frequency ($\omega = 2\pi f$), φ is the phase difference between V(t) and I(t), and t is the time. For a purely resistive behavior $\varphi = 0$ and a pure capacitor $\varphi = 90$ degrees.

Impedance Z(t), which is the AC resistance of the sample, is defined as:

$$Z(t) = \frac{V(t)}{I(t)} \tag{3.20}$$

In a complex plane, Z can be written as:

$$Z = Z' + iZ'' = |Z|e^{i\varphi} \tag{3.21}$$

which Z′, Z″ and $|Z|$ are:

$$Z' = |Z|\cos\varphi \qquad Z'' = |Z|\sin\varphi \qquad |Z| = \sqrt{Z'^2 + Z''^2} \tag{3.22}$$

Z′ is the real component of the impedance (i.e. R or DC resistance of the device) and Z″ is the imaginary part of Z which is called reactance (X) and depends on the signal frequency. The reactance of a capacitor (C) and an inductor (L) in an AC circuit with angular frequency of ω is:

$$X_C = \frac{1}{C\omega} \qquad X_L = L\omega \tag{3.23}$$

A photovoltaic solar cell can be studied by impedance spectroscopy in terms of its ability to store and transfer charges (i.e. its capacitance and conductance). By means of impedance measurement, some important parameters of the cell, such as its capacitance, parallel and series resistances, can be determined. In a simple case, which is called RC model, the AC response of the solar cell can be modeled to an equivalent circuit which consists of a capacitor (C) in parallel with a resistor (R_p) and both are connected in series to another resistor (R_s) as shown in Fig. 3-11(left). The representation of the impedance spectrum in the complex plane is called Nyquist plot (also called the Cole-Cole plot or complex impedance plane plot). The Nyquist plot of the RC model is shown in Fig. 3-11(right). It should be noted that in this plot the frequency is increased towards the origin of the plot. At very high frequencies, impedance of the capacitor is very low ($X_c \approx 0$) and the capacitor behaves like a short circuit; therefore, the impedance of the whole circuit is equal to R_s. At very low frequencies, the impedance of the capacitor is very high and the capacitor behaves like an open circuit; therefore, the impedance of the circuit is equal to the sum of the parallel and series resistances (i.e. $Z = R_s + R_p$ at very low frequencies).

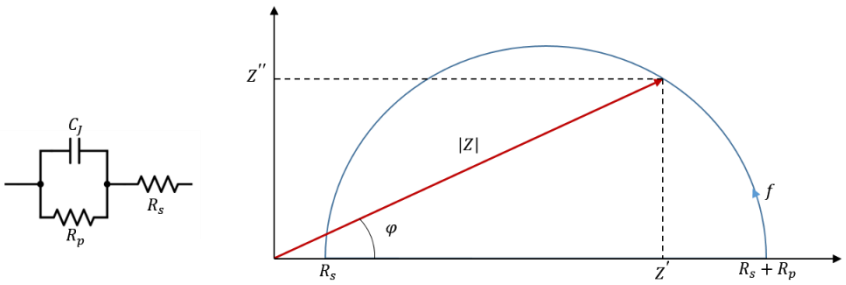

Fig. 3-11: The RC model (left), and resulting Nyquist plot (right). The arrow on the semicircle indicates that the frequency increases towards the origin of the plot [45].

The J-V curve of CdS/CdTe solar cells can be modeled by the two-diode as explained in section 3.1.2. The impedance spectra of the cell in this case can be simulated with a double RC-model, one RC for the junction diode and one for the back-contact diode, as illustrated in Fig. 3-12.

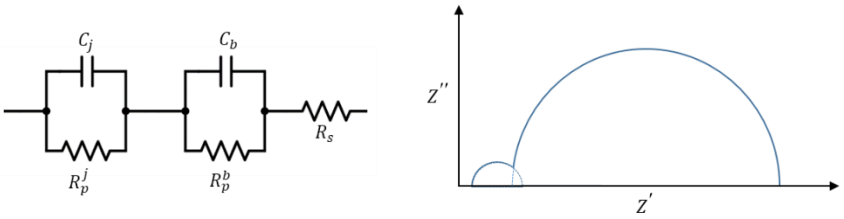

Fig. 3-12: The double RC model (left), and resulting Nyquist plot (right).

Although the two-diode model, in most cases, can explain the J-V behavior of CdS/CdTe solar cells, Friesen et al. found that the double-RC model cannot provide a good fit for impedance spectrum of these cells; therefore, they introduced another model based on a constant phase element (CPE) [45]. The CPE model has a similar structure as the RC-model, but the capacitor is replaced by a non-ideal frequency-dependent element, as shown in Fig. 3-13(left). The Nyquist plot of the CPE-model is a semicircle with its center below the Z′-axis as shown in Fig. 3-13(right).

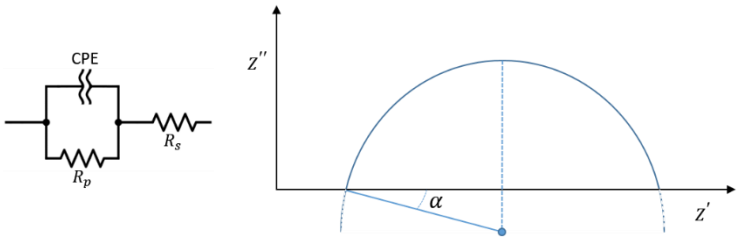

Fig. 3-13: The CPE-model (left), and resulting Nyquist plot (right).

This depressed semicircle shows a non-ideal capacitor which could be related to inhomogeneous distribution of grains and grain boundaries.

Capacitance-voltage measurement

Capacitance-voltage (C-V) measurement of a p-n junction is a well-established technique to get important physical information of semiconductor materials and devices including solar cells. Many useful information, such as doping concentration and profile, depletion width, defect densities and potential barriers, can be obtained from the C-V measurement. In order to perform this measurement, two simultaneous voltage sources are applied to the sample: an AC voltage with a fixed amplitude and a DC voltage which sweeps during the measurement. The AC signal is needed for measuring the capacitance and the DC bias is applied to probe the device at different depths.

In CdS/CdTe solar cells, it is well known that the n-CdS is much more heavily doped than the p-CdTe [43]; therefore, the width of the depletion region (W) is given by [46]:

$$W = \left[\frac{2K_s\varepsilon_0}{eN_A}\,(V_{bi} - V)\right]^{1/2} \tag{3.24}$$

where K_s is the dielectric constant of the CdTe, N_A is the uncompensated doping density in the CdTe layer, V_{bi} is the built-in voltage and V is the applied DC bias (which is positive in forward bias and negative in reverse bias). The capacity of the space charge region, which can be considered as a parallel plate capacitor, is as following:

$$C = \frac{K_s\varepsilon_0 A}{W} = A\left[\frac{K_s\varepsilon_0 eN_A}{2(V_{bi} - V)}\right]^{1/2} \tag{3.25}$$

therefore

$$\frac{1}{C^2} = \frac{2(V_{bi} - V)}{A^2 K_s\varepsilon_0 eN_A} \tag{3.26}$$

For a uniform carrier concentration, a plot of $1/C^2$ against V is a straight line that from its slope the doping density N_A can be determined, and an extrapolation of this line intersects the x-axis at V_{bi}. If the doping concentration in the CdTe layer is not uniform, the doping

profile $N_A(W)$, which is the free carrier density at the edge of the space charge region, is obtained from the following equation:

$$N_A(W) = \frac{2}{eK_s\varepsilon_0 A^2}\frac{-1}{d(C^{-2})/dV} \tag{3.27}$$

Fig. 3-14 shows the C-V and $1/C^2$ vs V curves of a CdS/CdTe solar cell simulated using the SCAPS program. At low forward bias, the applied voltage totally drops over the junction capacitance, as explained in section 3.1.2 ; therefore, the total capacitance of the cell equals the junction capacitance, which increases by increasing the DC bias.

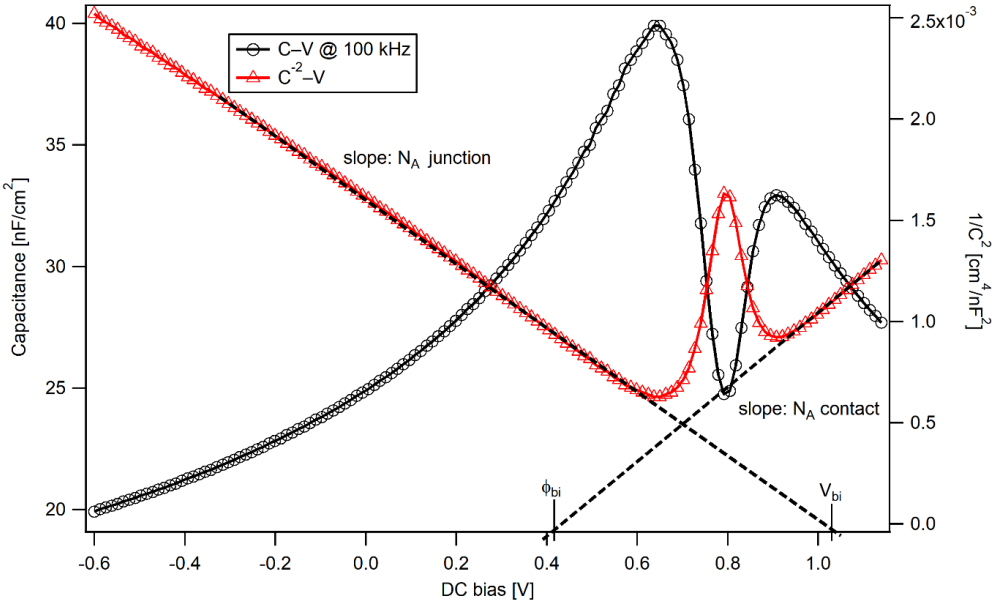

Fig. 3-14: C-V curve of a CdS/CdTe cell simulated using SCAPS.

From the slope of the $1/C^2$ vs V curve at low voltages, the carrier concentration near to the junction can be determined. At high DC voltages ($>\sim V_{oc}$), the junction voltage saturates and all additional applied voltages drop over the contact capacitance (C_c); therefore, any change of the total capacitance of the cell is related to the contact capacitance which decreases by increasing the applied DC voltage (because it is in the revers bias condition at high DC voltages). From the slope of the $1/C^2$ vs V curve at high voltages, the carrier concentration near to the back contact can be determined. At intermediate voltages, the applied voltage is divided between the C_j and C_c and both capacitors response to the AC

signal. In this case, total capacitance of the cell is changing from C_j to C_c and is equal to the equivalent capacitance of both which are connected in series, i.e. $C = C_j.C_c/(C_j+C_c)$.

Impedance measurement setup

Impedance measurements were performed using a Solartron 1260 frequency response analyzer. The CdS/CdTe solar cells were connected to the impedance analyzer in a shielded four-terminal configuration which is shown in Fig. 3-15. Four BNC cables with the same length were used for the connection and the outer shields of cables were connected together in both sides to reduce noises and induction effects. This configuration has a wide measurement range for impedances from 10 mΩ to 10 MΩ [47]. The measurements were performed in darkness at room temperature. The AC frequency was from 0.1 Hz to 4 MHz with a low amplitude of 20-25 mV and different DC bias voltages (-2 to 2V). In order to determine the series and shunt resistances of samples, the impedance spectra were fitted to appropriate equivalent circuits using the z-view V3.1 software from Scribner Associates Inc.

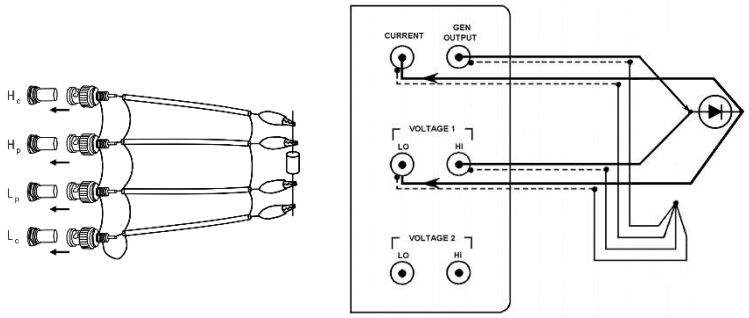

Fig. 3-15: shielded four-terminal connection setup for the impedance and C-V measurements.

C-V measurements were performed at a fixed frequency typically between 10 kHz and 100 kHz based on the sample. At low frequencies, the traps in the depletion region may respond to the AC signal which leads to a higher capacitance. Since the capacity related to the acceptors in the space charge region is important, the frequency should be high enough to avoid errors related to the traps. At very high frequencies, some artefacts may appear due to inductive resonances. In order to find the suitable frequency, a capacitance-frequency (C-*f*) measurement was performed for each sample before running the C-V measurement; then, a frequency from the high-frequency region (in which the capacitance does not change) was chosen. Another important parameter, which had to be correctly set, was the

delay time between different DC voltage steps. The delay time had to be long enough for the capacitance to be fully charged or discharged; otherwise, the recorded C-V curves were not the same for both DC sweep directions.

3.3 Photoelectron spectroscopy

The photoelectron spectroscopy (PES) is one of the most important techniques to study chemical composition and electronic structure of surface and interfaces of materials. This technique is based on the photoelectric effect, which is emission of electrons when high-energy photons hit the surface of a material; the emitted electrons (photoelectrons) are analyzed by a hemispherical electrostatic sector analyzer as shown schematically in Fig. 3-16 (left). A plot of electron counts or intensity vs binding energy (or kinetic energy) gives a spectrum. Each element has a unique spectrum, which acts as its fingerprint to be identified. Therefore, when several elements are present on the same surface, each element can be identified from its core electrons binding energies. The PES can be performed using monochromated UV photons or soft X-ray photons, which are called ultraviolet photoelectron spectroscopy (UPS) and X-ray photoelectron spectroscopy (XPS), respectively.

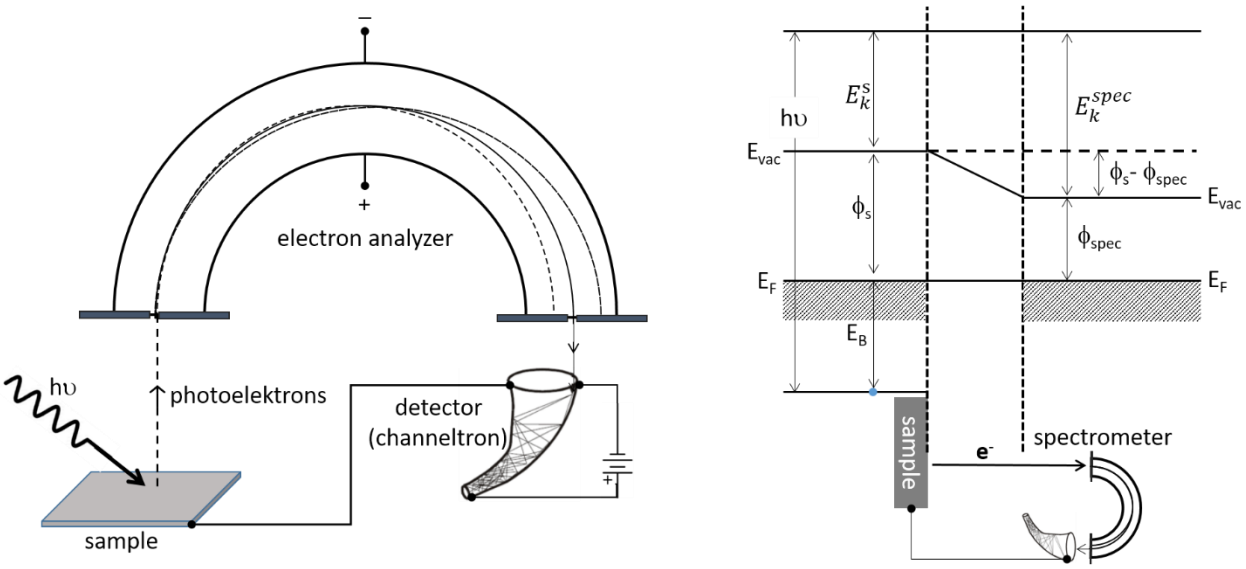

Fig. 3-16: Working principle of photoelectron spectroscopy.

When photons with energy of hυ hit a metallic sample with work-function of ϕ_s, the binding energy (E_B) of the emitted photoelectrons can be determined from the energy conversion equation, as following:

$$E_B = h\nu - \phi_s - E_k^s \tag{3.28}$$

where, E_k^s is the kinetic energy of the photoelectron at the sample surface. Usually, the sample is electrically connected to the spectrometer (channeltron) and their Fermi levels are balanced, as shown in Fig. 3-16 (right). When a photoelectron passes from the sample surface to the spectrometer, it feels a potential that is equal to the difference between the work-function of the sample (ϕ_s) and spectrometer (ϕ_{spec}). If ϕ_s is greater than ϕ_{spec}, the photoelectron accelerates and its kinetic energy would increase by ϕ_s-ϕ_{spec}, which means that the entire measured spectrum would shift to higher kinetic energy (lower binding energy) by ϕ_s-ϕ_{spec}. Therefore, the measured kinetic energy of photoelectron inside the spectrometer (E_k^{spec}) can be written as:

$$\begin{aligned} E_k^{spec} &= E_k^s + (\phi_s - \phi_{spec}) \\ &= h\nu - E_B - \phi_{spec} \end{aligned} \tag{3.29}$$

which shows that the measured kinetic energy of the photoelectrons is independent from the work-function of the sample. From equation 3.29, the binding energy of photoelectron is as following:

$$E_B = h\nu - \phi_{spec} - E_k^{spec} \tag{3.30}$$

which also is independent of the sample work-function. In a photoelectron spectrum, several peaks appear on a background. The main peaks are related to the photoelectrons that have not experienced inelastic collisions. These peaks are referred as core levels or Auger electrons and can be used to identify the elemental composition and chemical state of the sample. The electrons that have experienced inelastic collisions are called secondary electrons. These electrons have a continuous kinetic energy; therefore, they produce a background in the photoelectron spectrum. The excited photoelectrons then pass through an electrostatic input lens before entering the analyzer. The lens can decelerate or accelerate the electron beam to set its energy to a defined value before entering the hemispherical analyzer. In the analyzer, only electrons with energy very near to a defined pass energy (E_p) can pass through the exit slit and enter to the electron multiplier or channeltron to be counted. The passed electrons enter into a funnel-shaped detector (as

shown in Fig. 3-16) and generate secondary electrons by striking to the interior surface of the channel walls. The electrons then accelerate into the channel end and keep generating secondary electrons as they move towards the end. The resulting large shower of electrons are collected by the metallic anode at the end of the channel and produces an output pulse current from which value the number of photoelectrons can be determined.

3.3.1 Work-function measurement

One of the important parameters that can be measured by photoelectron spectroscopy is the work-function of metal and semiconductor samples. The work-function (ϕ) is the minimum energy required to remove an electron from the sample; therefore, it equals to the energy difference between the Fermi level and vacuum level (VL) as shown in Fig. 3-17 for metal and semiconductor materials. In metals, the work-function and ionization potential (I_p) are the same. In a non-degenerate semiconductor, the Fermi level is located within the bandgap and its position depends on the doping density; therefore, the work-function of semiconductor is also depending on the doping density and it may change from its electron affinity (χ), which is the energy difference between the conduction band minimum (CBM) and the vacuum level, to the ionization potential (I_p), which is the energy difference between the valence band maximum (VBM) and the vacuum level, as illustrated in Fig. 3-17.

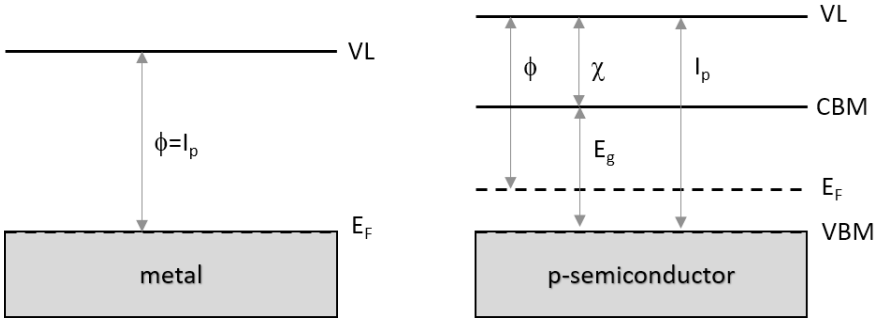

Fig. 3-17: schematic energy band diagram of a metal and a p-type semiconductor.

In order to measure the work-function with PES, the position of the secondary electrons cut-off is measured and its value is subtracted from the photon energy as shown in Fig. 3-18. For a correct measurement, the instrument needs to be calibrated in a way that the Fermi edge of a metallic sample (like Mo) is located at zero binding energy.

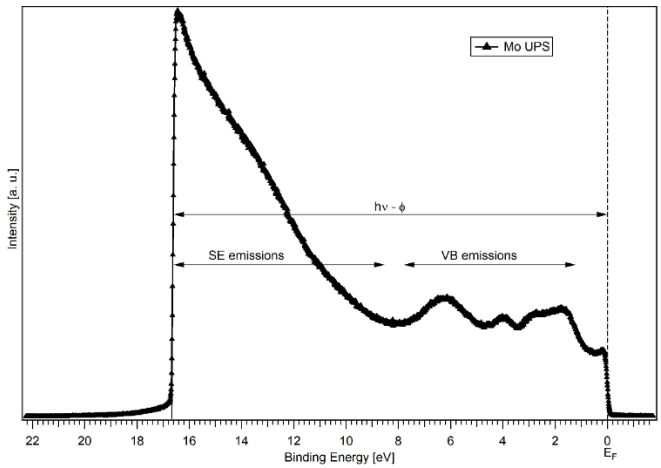

Fig. 3-18: UPS work-function measurement.

3.3.2 Interface experiment

The band alignment at the interface of two semiconductors or the barrier height for charge transport from a semiconductor to the contact material can be determined by photoelectron spectroscopy using stepwise deposition. The experiment begins with the PES measurement of a freshly deposited or cleaned substrate; then, the contact material is deposited onto the substrate in several steps followed by PES measurements after each step. By measuring the substrate and over-layer XPS core-level binding energies, the position of VBM of the substrate and over-layer can be determined. This process is repeated until the over-layer material covers the substrate completely and no signal from the substrate is visible in the PE spectra any more. This corresponds to an over-layer with total thickness of about 5-15 nm based on the materials and the substrate roughness. More information about this experimental procedure can be found in the literature [48, 49].

3.3.3 XPS depth profiling

Atomic depth-profiling uses an ion-beam to etch away layers of the surface or surface contaminations, revealing some subsurface information. Combining a sequence of ion-gun etch cycles with XPS analyses, provides quantified information as well as layer thicknesses. Before removing material from the sample surface, a spectrum (or set of spectra) was recorded from the surface of the sample. The surface was etched by parallel line scanning of an ion-beam over a rectangular area of the sample. After the etch cycle, the ion-beam

was shut down and another set of spectra was recorded. This sequence of etching and spectrum acquisition was repeated until profiling was proceeded to the required depth.

3.3.4 PES measurement setup

All XPS and UPS measurements in this work were performed on an Escalab 250 spectrometer from VG scientific, which was integrated to the Daisy-Sol for in-situ surface and interface characterizations in an ultra-high vacuum environment (see section 4.1). For the XPS measurements a monochromated Al-K_α X-ray source with photon energy of 1486.6 eV and for the UPS measurements a helium discharge UV lamp with He I emission line of 21.22 eV was used. The Escalab was equipped with an Ar ion sputter gun for sample cleaning and XPS depth profiling and an electron flood gun for charge compensation in non-conducting samples. Each XPS measurement was performed in a constant analyzer energy (CAE) mode with large area XL lens mode. In all measurements of this work, the pass energy for wide range XPS survey spectra was 50 eV and for the narrow range core-level, VB and Auger electrons measurements was set to 10 eV. The UPS measurements were performed with a pass energy of 0.5 eV and an acceleration voltage of 6 V was applied between the sample and analyzer to separate the secondary electrons of the sample from the secondary electrons generated in the channeltron. Since the accelerating voltage increases the kinetic energy of the sample photoelectrons by 6 eV, the UPS spectra must be shifted by 6 eV to higher binding energies (after the measurement) to cancel the effect of the accelerating voltage.

3.4 Other characterization techniques

Some individual thin films that were used as back contact interlayer were in addition studied by other characterization techniques such as Hall effect, AFM and XRD measurements.

3.4.1 Hall effect measurement

The Hall effect measurement technique has wide application in the characterization of semiconductor materials because it gives the resistivity, the carrier density, and the Hall mobility. A schematic diagram of the Hall effect measurement is shown in Fig. 3-19. A sample with thickness t and width W is located in a magnetic field B (in opposite of z-

direction) which is perpendicular to its surface. When a current (I) flow through the sample (in x-direction), a Hall voltage (V_H) is developed across the sample due to the electromagnetic force (F) which is in the y-direction for holes and opposite of the y-direction for electrons. The carrier type can be determined from the polarity of V_H, and the carrier density and Hall mobility from the magnitude of V_H.

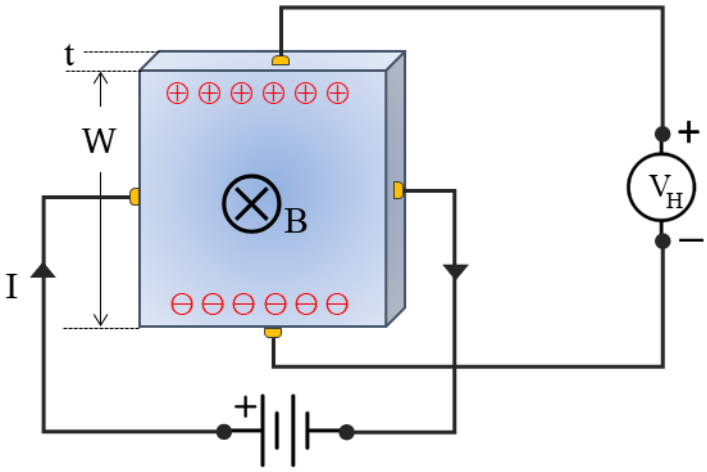

Fig. 3-19: Schematic design of the Hall effect measurement setup.

The Hall voltage is given by [50]

$$V_H = \frac{R_H B I}{t} \tag{3.31}$$

where R_H is the experimental Hall coefficient and is defines as

$$R_H = \frac{p\mu_h^2 - n\mu_e^2}{e(p\mu_h + n\mu_e)} \tag{3.32}$$

where μ_h and μ_e are the hole and electron mobility, respectively; p and n are the carrier concentration for p-type and n-type semiconductors, and e is the elementary charge.
The Hall mobility (μ_H) is defined as the product of the Hall coefficient divided by the resistivity (ρ):

$$\mu_H = \frac{R_H}{\rho} \tag{3.33}$$

The resistivity is related to the carriers' drift mobility as [50]

$$\rho = \frac{1}{e(n\mu_n + p\mu_p)} \tag{3.34}$$

In doped semiconductors, which the concentration of one carrier type is much larger than the other, p and n can be determined from the following equations

$$p = \frac{1}{eR_H} \qquad \text{for p-type semiconductor (when p >> n)} \tag{3.35}$$

and

$$n = -\frac{1}{eR_H} \qquad \text{for n-type semiconductor (when n >> p)} \tag{3.36}$$

Another simple method that was used to confirm the carrier type in a fast way was thermo-power measurement. In this method, a temperature gradient was applied across the sample and the potential difference between the hot and cold ends was measured. The carriers have a net flow from the hot end towards the cold end. If the carriers are holes, the cold end will be at a positive voltage relative to the hot end. In contrast, if the carriers are electrons, the hot end will be at a positive voltage relative to the cold end.

3.4.2 Four-point probe measurement

Sheet resistance or surface resistance (R_s) of a thin film can be measured by four-point probe (FPP) technique, which is shown schematically in Fig. 3-20. To perform the measurement, a DC current (I) is passed through the outer probes and the potential difference (V) between the inner probes is measured.

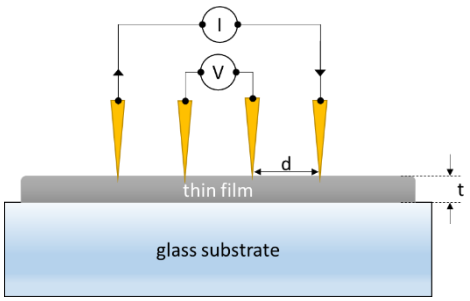

Fig. 3-20: schematic design of the FPP measurement.

When the probe distance (d) is much larger than the film thickness (t), R_s (in Ω/□) and resistivity (ρ) can be determined from the following equations:

$$R_s = \frac{\pi}{\ln 2}\frac{V}{I} \cong 4.53\ \frac{V}{I} \tag{3.37}$$

and

$$\rho = R_s.t \tag{3.38}$$

3.4.3 Morphology and structure characterizations

Morphology and structure of different layers were studied by atomic force microscopy (AFM), scanning electron microscopy (SEM) and X-ray diffraction (XRD) techniques. Basic information about these techniques can be found in textbooks [51-53].

The AFM measurements were performed using an Asylum research MFP-3D atomic force microscope. Crystalline properties of the films were investigated by Seifert XRD 3003 PTS diffractometer system using Cu K_α radiation (λ = 1.5406 Å). Some layers were characterized using a Siemens D5000 X-ray diffractometer with Cu K_α radiation.

Effects of the $CdCl_2$ activation and chemical etching on the electrical conductivity of the CdTe grains and grain boundaries were investigated using conductive AFM (c-AFM) measurement, which will be discussed with detail in chapter 6.

The cross section of a few completed solar cells was also investigated with a SEM setup which was equipped with EDX (energy dispersive X-ray) and EBSD (electron backscatter diffraction) detectors.

Chapter 4

Fabrication of CdTe Solar Cells

4.1 Experimental setup

Solar cells investigated in this work were prepared in the superstrate configuration using DAISY-SOL[1]. This system consisted of different preparation chambers that were integrated together via a distribution chamber and all were connected to an analyzing chamber through a transfer chamber, as shown schematically in Fig. 4-1. A picture of the system is also shown in Fig. 4-2.

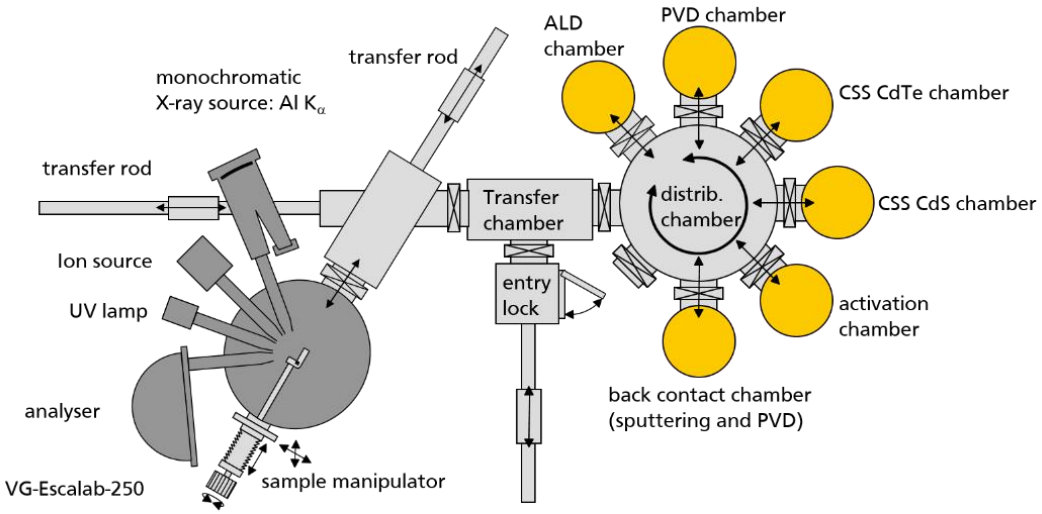

Fig. 4-1: DAISY-SOL configuration.

The samples could be transferred between the chambers without breaking the ultra-high vacuum (UHV) environment. The chambers were separated by UHV valves and could be evacuated with their dedicated pumps to pressures as low as $\sim 10^{-10}$ mbar. The substrates, which in most cases were 2 × 2 cm glass (coated with a TCO layer), were mounted in a special sample holder and were introduced into the system through an entry-lock chamber. Only this small chamber needed to be vented for loading and unloading of the samples.

[1] DArmstadt Integrated SYstem for SOLar cell research.

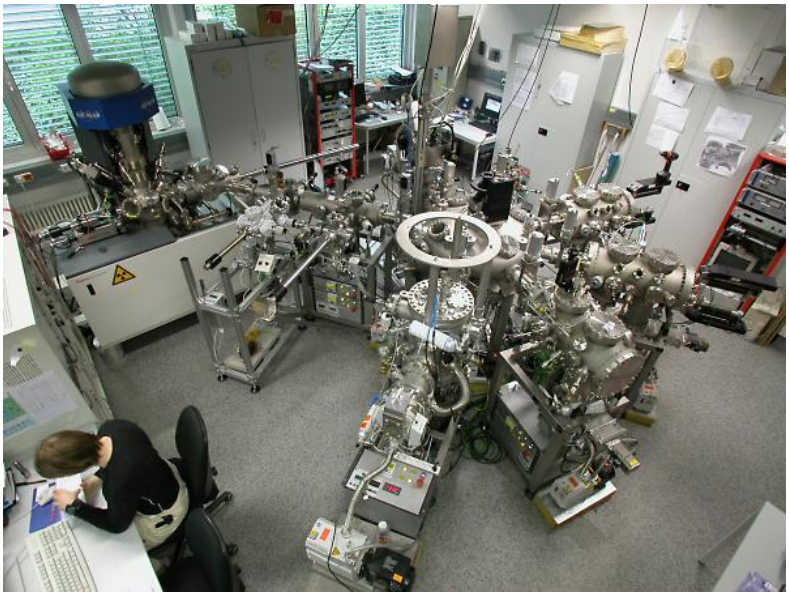

Fig. 4-2: DAISY-SOL picture.

4.2 Substrate preparation

In this work, three different TCO-coated glass substrates were used, as are listed in Table 4-1. The Antec substrate was made from a 4 mm glass coated with a 255 nm thick ITO layer and a buffer layer of intrinsic tin oxide (SnO_2) with a thickness of ~45 nm. The Pilkington substrate (TEC15) consisted of a 3.2 mm glass covered with ~300 nm FTO layer and an intrinsic SnO_2 buffer layer with thickness of ~25 nm. Some Pilkington substrates without the buffer layer were also used.

The surface resistances of the TCO-coated substrates were measured by four-point probe technique. For each sample the measurement was performed 5 times at different points. The average values of the sheet resistance are given in Table 4-1.

Table 4-1: Specifications of the substrates.

Sample supplier	TCO	Buffer layer	Sheet resistance (Ω/□)
Antec Solar	ITO	SnO_2 (~45 nm)	17
Pilkington (TEC15)	SnO_2:F	SnO_2 (~25 nm)	14
Pilkington	SnO_2:F	-	10

In order to transfer the substrates into the deposition chambers, they need to be cut as squares with dimensions of ~20 mm. After cutting, the samples were cleaned in three steps in ultrasonic baths with a soap solution (Edisonit powder mixed with deionized water),

followed by an isopropanol cleaning. After each ultrasonic bath, the samples were washed by deionized water. In the last step, the samples were cleaned in an ultrasonic bath with deionized water and then dried with a nitrogen gas and immediately were put in pre-cleaned sample holders.

4.3 Close-space sublimation deposition

Close-space sublimation (CSS) is one of the most efficient techniques in fabrication of CdS/CdTe solar cells. In this technique, the substrate is placed in a short distance (of the order of a few mm) on top of the source, and both are heated to a high temperature. Due to this configuration, deposition of the layers at rather high substrate temperatures (a few tens of degrees lower than the source temperature) with very high deposition rates (up to about 10 $\frac{\mu m}{min}$) is possible.

For deposition of the CdS and CdTe films, two CSS chambers were designed and fabricated for use in the Daisy-Sol system. The schematic diagram and a real picture of the CSS setup is shown in Fig. 4-3 [32]. In this setup, the distance between the source and the substrate holder was fixed but both could be moved in parallel. As deposition source, a special graphite crucible, which could be heated by halogen lamps, was used. The source temperature was controlled by Eurotherm controllers using type-K thermocouples that were inserted in the crucible body. On top of the crucible, a graphite aperture plate was placed. This plate had 25 holes, each with a diameter of 2 mm. The aperture plate could be heated with a tantalum heating wire, which was placed on top of the source just under the aperture. The substrate and its holder were also heated by halogen lamps and their temperatures could be independently controlled by the Eurotherm controllers. The substrate temperature was measured by a pyrometer through a window with a special filter that was calibrated for the glass substrates. The substrate holder temperature was measured by thermocouples. The substrate holder had two graphite shutters, one on the left and another on the right of the sample position. The source was kept under these shutters during the heating-up and cooling-down periods.

The CSS deposition of each layer consisted of the following steps:

1. Transferring the cleaned TCO-coated glass substrate to the CSS chamber and putting it in its position. In order to do this, the sample needed to be fixed into a special

holder, as shown in Fig. 4-3. The holder can be handled from outside of the vacuum chamber by wobble sticks that are installed in each chamber.

2. Moving the sample towards the pyrometer window and adjusting its position using a laser beam.
3. Moving the source under the right shutter.
4. Setting the deposition parameters in the deposition control software. The deposition parameters were the temperature profiles of the source, and the substrate.
5. Running the deposition program.

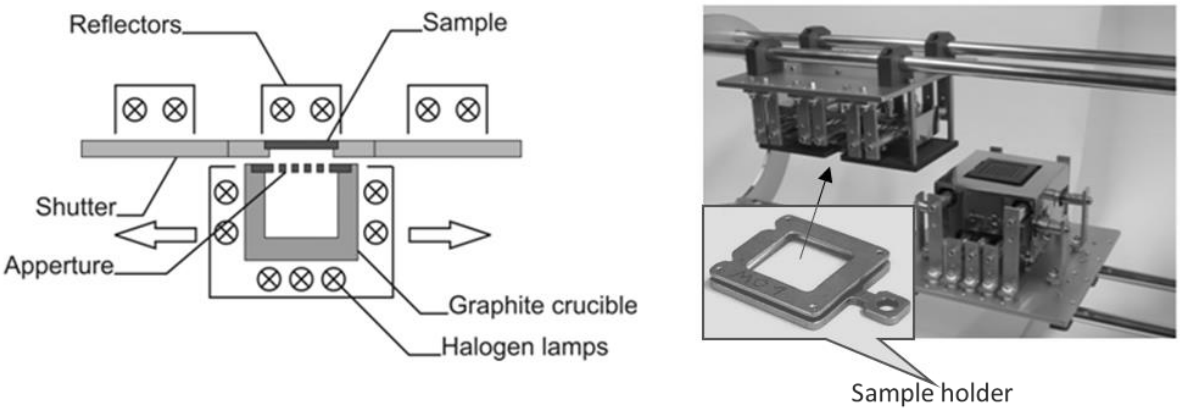

Fig. 4-3: Close-space sublimation (CSS) setup. Schematic configuration (left), and an actual picture of the instrument including the picture of a sample holder (right).

The deposition program had five steps as shown in Fig. 4-4. In the first step (which took 15 minutes), the source and the substrate temperatures (T_{source} and T_{sub}, respectively) were increased from room temperature to the deposition temperatures. In the second step (which took 5 minutes), these temperatures were kept constant. During these two steps the source was located under the right shutter. In the third step, the source was moved automatically in 10 seconds with constant speed to the substrate position with the help of an electromotor.

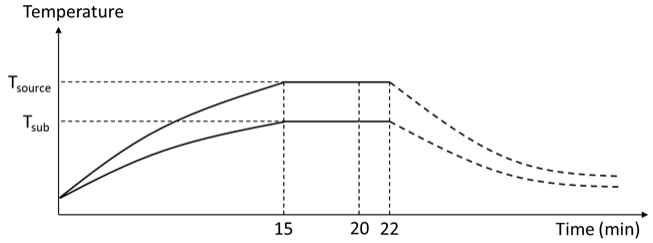

Fig. 4-4: The heating profile of the CSS deposition program.

In the fourth step, which was the deposition step, the source stayed under the substrate normally for 2 minutes. In the last step, the source and the substrate heaters were powered down and the source was moved to the left shutter position in 10 seconds time.

4.4 CSS deposition of CdS and CdTe layers

A CdS layer with a thickness of 200 nm was deposited onto the TCO-coated glass substrate using the procedure explained in the previous section. After deposition of the CdS layer and cooling down the sample temperature (to less than 150 °C), it was transferred to the CdTe chamber. Then, a CdTe layer with a thickness of about 5 μm was deposited on top of the CdS layer with a similar procedure. The deposition parameters of the CdS and CdTe layers are summarized in Table 4-2. The deposition rate depended on the amount of the material in the source (among other deposition parameters); therefore, when the source had less material, its temperature had to be increased to keep the deposition rate constant. Since the focus of this work was on the back contact, several samples with almost similar deposition parameters were prepared. These samples were used for further treatments, i.e. $CdCl_2$ activation and back contact investigations.

Table 4-2: CSS deposition parameters of the CdS and CdTe layers.

	T_{source} (°C)	T_{sub} (°C)	deposition time (min)	thickness (μm)	deposition rate (μm/min)
CdS	660-670	520	2	0.2	0.1
CdTe	590-610	520	2	5	2.5

4.5 $CdCl_2$ activation

One of the important steps in fabrication of CdS/CdTe solar cells was annealing of the samples in presence of chlorine, after deposition of the CdTe layer. This process, which is known as the "activation" step, will be discussed in chapter 5. The most common activation process is $CdCl_2$ treatment which can be performed in a wet or dry situation.

Our standard activation process was a wet treatment using a saturated solution made from $CdCl_2$ powder dissolved in methanol. In order to activate the samples, first a few drops of

the saturated $CdCl_2$-methanol solution was applied to the CdTe surface. After a few minutes, the solvent was evaporated in the air and a thin layer of $CdCl_2$ was formed on top of the CdTe surface. Then, the samples were annealed in a horizontal oven in air at 390 °C for 20 minutes.

Since the activation process was performed outside the vacuum chamber, this method is referred to as "ex-situ activation" in this work. A dry in-situ $CdCl_2$ activation was also developed which will be discussed in chapter 5.

4.6 Back contact formation

4.6.1 Wet back contact

During the ex-situ activation, an oxide layer was formed on the CdTe surface. This oxide layer (and also the remained $CdCl_2$ film) had to be removed by a chemical etching treatment, before deposition of the metallic back contact. A common etching solution was a mixture of HNO_3, H_3PO_4 and H_2O in a volume ratio of 1.3:70.5:28.2 (which is known as NP-etch solution).

The NP-etch in addition to removing the oxide layer, leaves a tellurium (or tellurium-rich) layer on the CdTe surface. This tellurium layer helps to make a low resistance contact to the CdTe.

Our standard back contact recipe was as following:

- Cleaning of the activated sample by a spray wash with deionized water (to remove some of the remained $CdCl_2$ from the surface).
- Drying of the samples with nitrogen gas followed by a short (30 sec) heating on a hot plate at 80 °C (or in front of the activation oven). We found that this was an important step for making reproducible cells.
- Immersing the sample (with a plastic tweezer) into the NP-etch solution until small bubbles were formed on the CdTe surface. This normally took about 15-25 seconds, until the entire CdTe surface was covered with the bubbles. At this time, the samples were taken out from the etching solution.

The CdTe surface color was changed from dark gray to silver gray after the etching. The sheet resistance of the sample before etching was too high (not possible to measure with our four-point probe setup), and after the etching it was significantly decreased (to about 40 kΩ/□).

If the etching time was too short (less than 7 seconds), the performance of the completed cells was poor (due to a high series resistance). On the other hand, when the etching time was too long (more than 40 seconds), most of the cells were not working (due to shortcuts); but some working cells had better performances as compared with the cells prepared with shorter etching times.

After the NP-etching step, the samples were washed with deionized water and dried with nitrogen gas. Then they were immediately transferred to a Balzers sputter coater (model SCD 050), which is shown in Fig. 4-5.

To form the TCO front and the CdTe back contacts, a gold layer with a thickness of about 100 nm was deposited onto the entire surface of the samples. The discharge current and deposition time were 40 mA and 400 s, respectively.

Fig. 4-5: Balzers SCD 050 sputter coater.

Then, the sample were mechanical scribed to define nine individual cells on each sample, as shown in Fig. 4-6. In order to have a better control on the cell area, a home-made structuring tool, which is shown in Fig. 4-6(left), was used. During this step, all of the

deposited layers, i.e. the gold, CdTe and CdS layers, were removed from the scratched region.

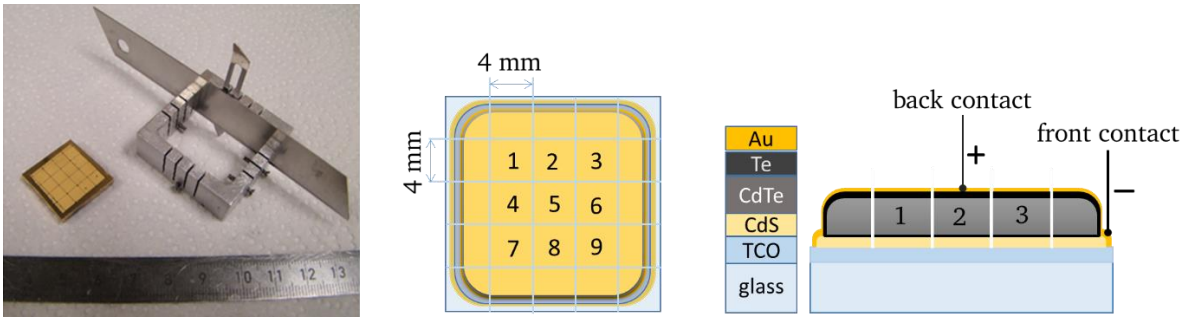

Fig. 4-6: The home-made structuring tool (left), and schematic images of a completed sample with 9 cells (right).

4.6.2 Dry back contacts

Back contact deposition chamber

A multi-purpose vacuum-deposition chamber (Fig. 4-7) was designed, fabricated and integrated with the DAISY-SOL, to investigate properties of various back contacts to the CdTe solar cells. This chamber was equipped with sputtering targets, PVD sources, and a plasma ion source. The chamber had special shutters to protect each source (from contamination) during deposition from other sources.

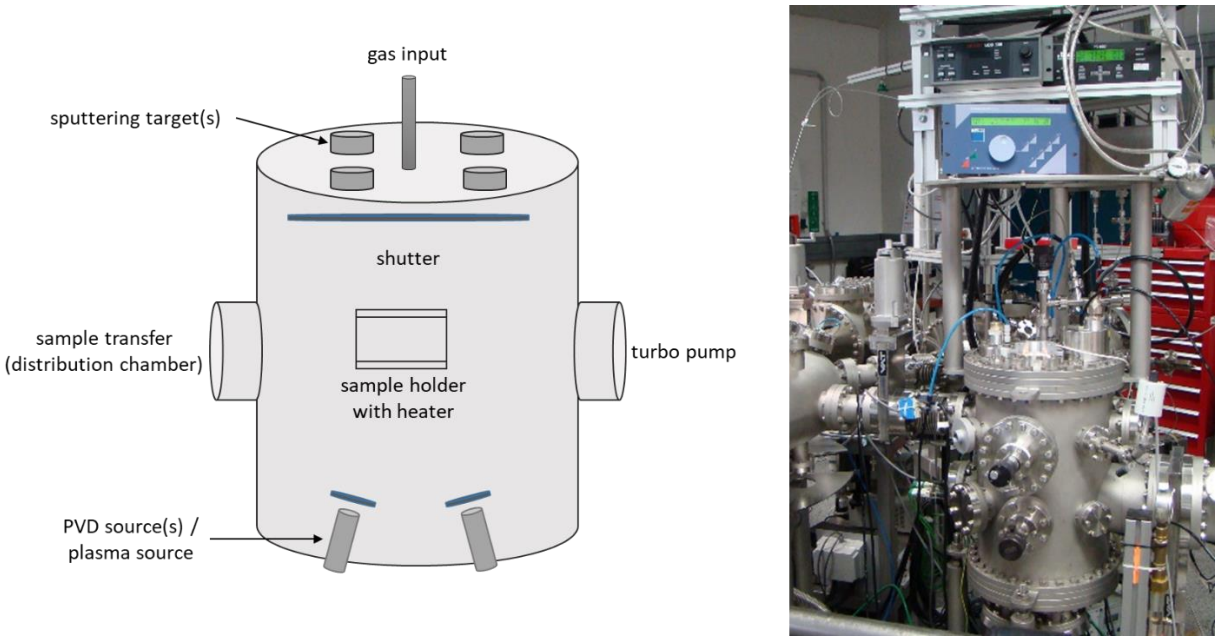

Fig. 4-7: Schematic (left) and a picture (right) of the back-contact chamber.

The base pressure of the chamber was in the range of 10^{-8} mbar. By closing the main vacuum valve and pumping through a bypass, it was possible to increase the chamber pressure when needed (e.g. during the sputtering process). The sputtering targets were located on top of the chamber (face down) while the PVD sources were located at the bottom (face up).

The substrate holder had two different positions: the top position was used during sputtering and the bottom position during PVD deposition. The substrates could be heated by halogen lamps mounted inside the substrate holder. The substrate-holder temperature was monitored by two thermocouples connected to the top and bottom positions. Since the electrical properties of some back-contact layers were very sensitive to the substrate temperature during deposition and/or post-deposition heat treatments, from time to time calibration experiments were performed for precise measurement of the substrate temperature.

Homemade effusion cells (Fig. 4-8) were used as PVD sources for deposition of different back contact layers. Each PVD source was calibrated every time after refilling (and after few depositions) for better control of the deposition rate. Calibration for high deposition rates (>5 nm/min) was performed by depositing a thick layer (>200 nm) and measuring the thickness of deposited film by a Dektak Profilometer.

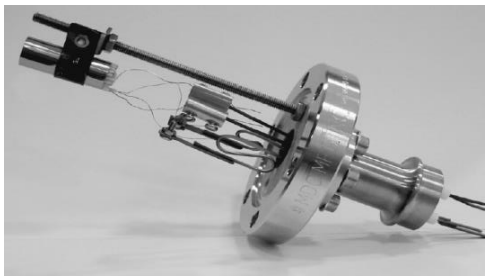

Fig. 4-8: A typical effusion cell with ceramic crucible (Al_2O_3) used for PVD deposition. Together with the heating wire, a thermocouple was mounted around the crucible for its temperature measurement. The crucible temperature was controlled by a Eurotherm controller.

For low deposition rates, the deposition rate and the deposited film thickness were monitored during deposition, by using an INFICON quartz-crystal microbalance film-thickness monitor. For some very thin layers such as Sb with thicknesses less than 10 nm deposited onto ZnTe, the top layer thickness was estimated by XPS measurements.

The chamber was also equipped with three MKS gas-flow controllers calibrated for Ar, N_2 and O_2 gases. DC and RF power supplies were available for sputtering deposition of the back contacts and interlayers.

Chapter 5

In-situ $CdCl_2$ Activation

An important step to reach high efficiency in CdS/CdTe solar cells is the activation process. This process consists of annealing of the samples in presence of $CdCl_2$ or a chlorine-containing atmosphere after deposition of the CdTe layer. The most common method for the activation is a $CdCl_2$ solution treatment [54-56]. In this method, a $CdCl_2$ film is deposited onto the CdTe surface using a solution of $CdCl_2$ dissolved in methanol, followed by a heat treatment in air at about 400 °C for 10-30 minutes. Other chloride solutions ($CdCl_2$:H_2O, $MnCl_2$:C_5H_5N and CsCl:H_2O) have also been used for the activation [57], but the best results have been obtained with the $CdCl_2$:CH_3OH solution. The $CdCl_2$ solution treatment is simple and efficient but it is not desirable for large-scale manufacturing, because it produces chemical waste containing Cd and also the uniformity is not good enough due to non-uniform $CdCl_2$ thickness. In order to have better control on the $CdCl_2$ thickness, the $CdCl_2$ layer can also be deposited by physical vapor deposition [58-60]. When the activation is performed by deposition of $CdCl_2$ followed by annealing, before processing the back contact, a washing or an etching step is needed to remove the remaining $CdCl_2$ and/or the oxide layer, which forms during the treatment.

Vapor treatment is another activation method in which the samples are annealed in the presence of $CdCl_2$ vapor in an oven [61, 62], or in a close spaced sublimation configuration [63-65]. This method needs shorter processing time and by using an appropriate heat treatment profile, residual $CdCl_2$ on the CdTe surface can be minimized.

Activation in non-oxidizing atmospheres such as HCl [66], chlorine[67] and CFC (Freon) gases [8, 68-72] have also been reported. Beside the benefit of non-oxidizing behavior of these gases, there are concerns about the corrosive behavior of HCl and chlorine and also environmental effects of the CFC gases.

The chlorine treatment has several effects on the samples including morphology, structure [73, 74] and electronic modifications [55, 75-78]. Morphological and structural changes strongly depend on the growth history of the CdTe and CdS layers [79]. Our previous investigation [20, 32, 80, 81] showed that $CdCl_2$ treatment on the samples prepared at low

sample temperature (< 350 °C) leads to loss of the (111) texture and the grain's orientation will be randomized after the treatment. For samples prepared at sample temperatures above ~500 °C, which already have random orientation, the activation treatment leads to a reduction of the structural defect density.

Another effect of the activation process is inter-diffusion of the CdS and CdTe layers at the interface [55, 75, 76, 82-84], which reduces the interface states and recombination velocity. This leads to a higher J_{sc} and improves the quantum efficiency of samples and changing the dominant current transport mechanism from interface recombination/tunneling to depletion region recombination [85-87].

Effects of the activation on the electronic properties of the layers and interface of the CdS/CdTe junction have already been studied by photoelectron spectroscopy [64, 88-90]. In this work we report about setting up a vacuum based in-situ $CdCl_2$ activation setup, integrated with the DAISY-SOL [76] to investigate effects of the activation process on electronic properties of CdS/CdTe samples without exposing them to air. The influence of the in-situ activation process on morphology and structure of the CdTe layer was investigated by atomic force microscopy (AFM) and X-ray diffraction (XRD). The electrical properties of the completed solar cells were characterized by current-voltage, external quantum efficiency (EQE), capacitance-voltage (C-V) and impedance spectroscopy measurements.

5.1 Experimental setup

The CdS and CdTe layers were deposited onto fluorine-doped tin-oxide (FTO) coated glass substrates by close-space sublimation (CSS) in vacuum using the DAISY-SOL. CdS and CdTe source temperatures were 680 and 610 °C respectively, while the substrate temperature was kept at 520 °C for both depositions. The CdS and CdTe thicknesses for a deposition time of 2 minutes for each layer were about 0.2 μm and 4-5 μm, respectively. After deposition of the layers, samples were in-situ transferred to the analyzer chamber and the activation chamber without breaking the ultra-high vacuum. X-ray photoelectron spectroscopy (XPS) of the samples was performed using a VG Escalab 250 spectrometer equipped with a monochromated Al anode X-ray source ($h\upsilon$ = 1486.6 eV).

An in-situ activation reactor (Fig. 5-1) was built up and integrated to the DAISY-SOL. The activation reactor consists of a graphite crucible filled with $CdCl_2$ powder and a sample

heater. The graphite crucible and the sample were heated by halogen lamps which were controlled by Eurotherm controllers. The $CdCl_2$ source temperature was measured by two thermocouples placed into the graphite crucible, while the substrate temperature was measured by a pyrometer.

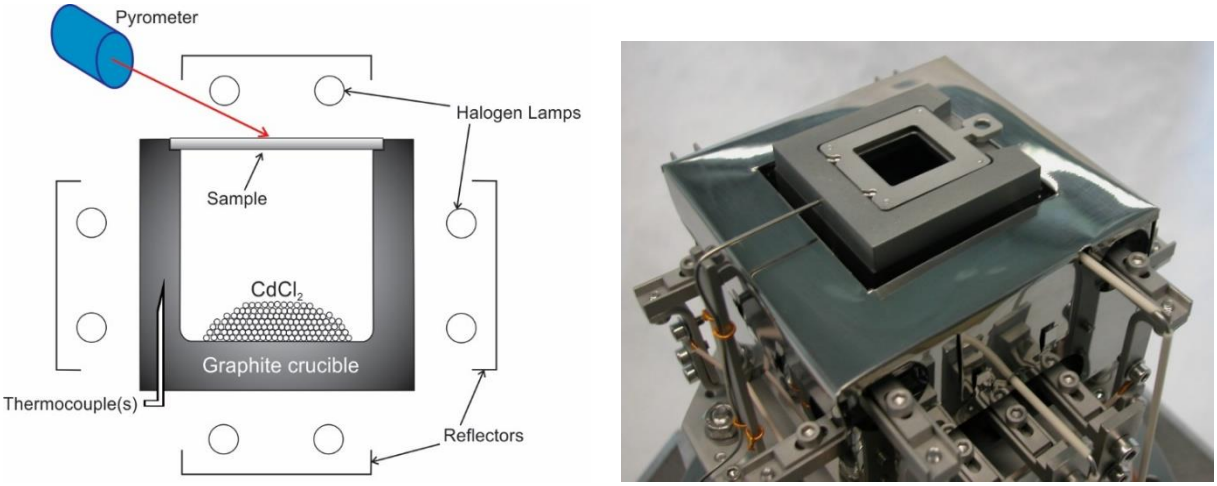

Fig. 5-1: (a) Schematic diagram of the in-situ activation system, (b) $CdCl_2$ activation reactor.

The glass/FTO/CdS/CdTe sample (2 cm × 2 cm) was mounted on a Mo holder which was placed face down on top of the $CdCl_2$ crucible and was heat treated. In this configuration, the most important parameters for the in-situ activation were: Substrate temperature (T_{sub}), $CdCl_2$ source temperature (T_{source}), and temperature profiles. A drawing of the temperature profiles is shown in Fig. 5-2.

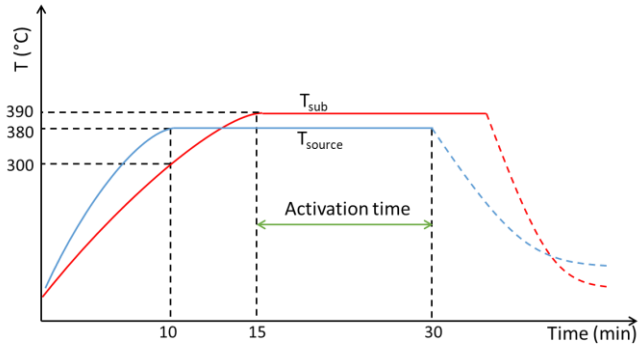

Fig. 5-2: Temperature profile of the in-situ $CdCl_2$ activation treatment. The optimum parameters are given in Table 5-1.

The substrate temperature was changed from 350 to 430 °C while the $CdCl_2$ source temperature was altered from 350 to 400 °C. The optimum activation parameters, which were obtained through a series of experiments, are shown in Table 5-1.

Table 5-1: Optimum heating programs for the in-situ $CdCl_2$ activation.

	Pre-heating (10 min)	Pre-heating (5 min)	Activation (15 min)	Post-activation annealing (5-15 min)
T_{sub}	Increasing from RT to 300 °C	Increasing from 300 to 390 °C	390 °C	390 °C
T_{source}	Increasing from RT to 380 °C	380 °C	380 °C	Cooling down (power off)

All samples which were used for the optimization experiments were non-activated glass/TCO/CdS/CdTe stacks which were prepared by CSS with the same deposition parameters. A post-activation annealing was performed to re-evaporate the $CdCl_2$ residue from the sample and provide a clean surface for the XPS analysis.

Surface morphology of the non-activated and activated samples was analyzed using an Asylum research MFP-3D atomic force microscope. XRD pattern of the samples were recorded in a θ:2θ geometry using a Siemens D5000 X-ray diffractometer with Cu K_α radiation.

In order to study the effect of activation on electrical properties of the samples, solar cells were completed by chemical etching using Nitric-Phosphoric (NP) acid followed by a gold sputtering from the non-activated and activated samples. An ex-situ activated sample was also prepared for comparison. The ex-situ activation was performed by depositing of 5 drops $CdCl_2$ dissolved in methanol on a 2 cm by 2 cm sample followed by annealing in air at 390 °C for 20 minutes. Before solar cell characterization, the samples were partitioned into nine 4 mm by 4 mm sized cells by mechanical scribing of the CdS/CdTe/Au layer stack. Current density-voltage (J-V) of the solar cells were measured under AM 1.5 illumination ($1000W/m^2$) using a solar simulator equipped with a Keithley 2400 SourceMeter. Spectral response of samples was measured using a setup consisted of a tungsten halogen lamp, monochromator, optical chopper, and a lock-in amplifier to determine external quantum efficiency of the samples. The measurement was performed from 350 to 950 nm with step size of 10 nm without additional light or voltage bias. A calibrated Si photodiode was used as reference for the EQE measurement. C-V profile of the solar cells was performed at room temperature in the dark at frequency of 50 kHz and AC amplitude of 20 mV, using a Solartron 1260 impedance analyzer.

5.2 XPS analysis of the in-situ activated samples

5.2.1 XPS analysis of non-oxidized samples

XPS measurement was performed on glass/FTO/CdS/CdTe samples before and after the in-situ activation without being exposed to air. A list of the samples that were measured is given in Table 5-2. XP survey spectra of the as-deposited and activated samples can be seen in Fig. 5-3.

Table 5-2: List of the samples that have been analyzed by XPS.

notation	treatment
as is	non-treated (as-deposited glass/FTO/CdS/CdTe)
act	in-situ activated
act+ann	in-situ activated followed by a vacuum annealing
act+spt	in-situ activated followed by an Ar sputtering
act+spt+ann	in-situ activated followed by an Ar sputtering and vacuum annealing

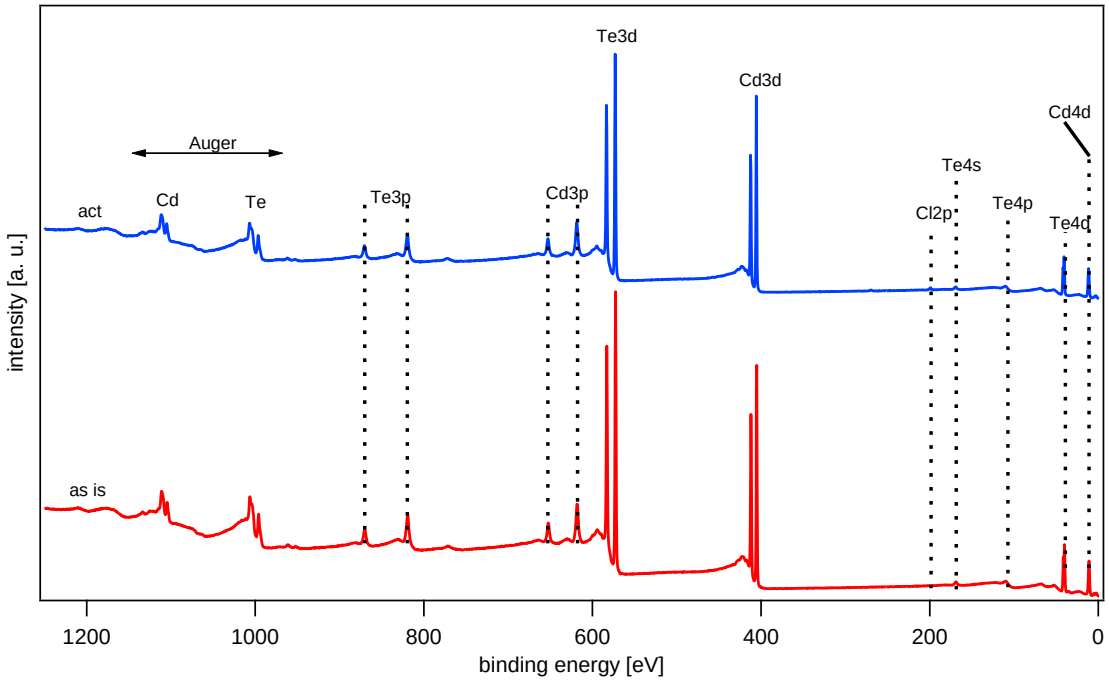

Fig. 5-3. XP survey spectra of the as-deposited and activated CdS/CdTe samples. The as-deposited sample shows only Cd and Te peaks while the activated sample shows extra signals that correspond to Cl.

The as-deposited sample shows only emissions of Cd and Te while for the activated sample, an additional small Cl 2p emission is observed. The high-resolution Cl 2p spectra of the treated samples are shown in Fig. 5-4. The Cl signal of the activated sample was significantly reduced after an annealing at 390 °C for 15 minutes in vacuum. This Cl signal

is attributed to a very thin $CdCl_2$ residue on the CdTe surface as it disappeared after only 1-minute sputtering by 1 keV argon ions.

Fig. 5-5 shows the Cd 3d and the Te 3d core levels of the samples that have been introduced in Table 5-2. A core-level shift ($\Delta E \sim 400$ meV) to higher binding energies was observed after the activation. After removing the topmost surface layer (which contains Cl) by Ar sputtering or vacuum annealing, the binding-energy of the core levels is shifted back to lower values ($\Delta E \leq 400$ meV).

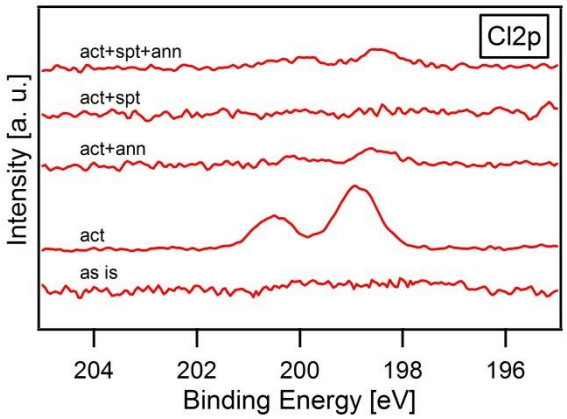

Fig. 5-4. High resolution Cl 2p spectra of the samples listed in Table 5-2. The Cl 2p emission is explained by $CdCl_2$ residues on the surface of the activated sample, which is significantly reduced after a post-activation annealing and vanishes completely after one-minute Ar ion sputtering.

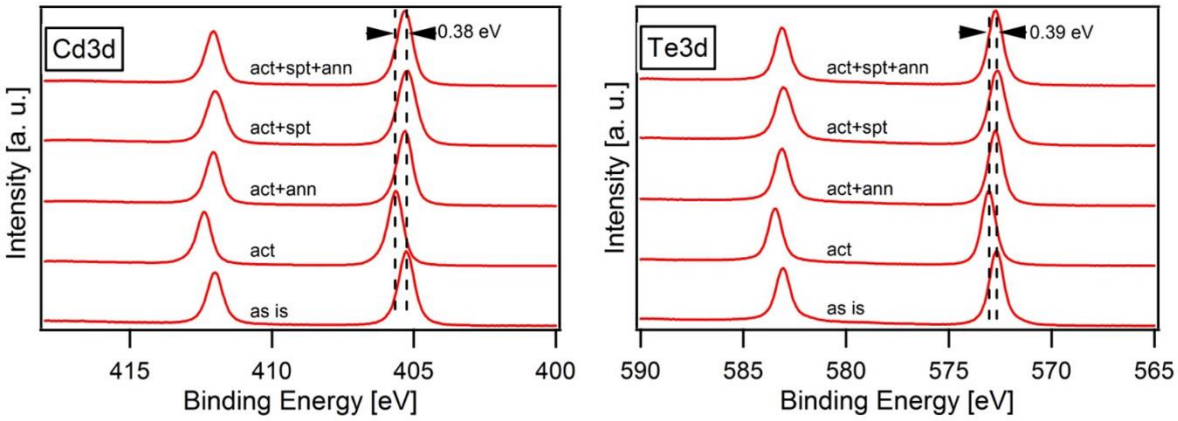

Fig. 5-5. Core levels of the Cd 3d (left), and the Te 3d (right). In both figures, the core-level binding energies were shifted to higher values after activation.

XPS measurement of the valence band region is shown in Fig. 5-6. The distance between the Fermi energy (E_F) and the valence band maximum (E_{VBM}), i.e. $E_F - E_{VBM}$, is indicated in the figure.

As the values of $E_F - E_{VBM}$ in Fig. 5-6 indicate, the Fermi level of the as-deposited sample is higher than midgap of the CdTe, which is about 0.75 eV, and it rises to even higher energies after the activation. Normally in CdS/CdTe solar cells, the CdTe should be p-type after activation; otherwise, the cells would not work. A Fermi level position near midgap may be explained by the Fermi-level pinning but moving of the Fermi level to higher binding energies means that the CdTe becomes more n-type after the activation, as was also found in our previous work [64].

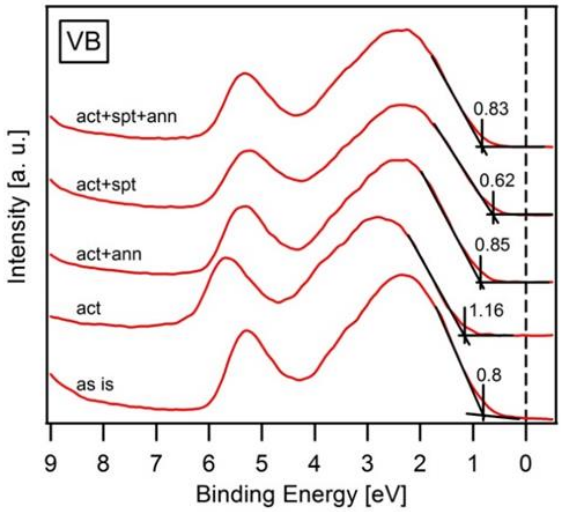

Fig. 5-6. XP spectra of the valence band region. The vertical lines show the valence band position with respect to the Fermi level which is at 0 binding energy. An upward shift of the Fermi level with respect to the valence band can be clearly seen after activation.

Possible explanations for this seemingly contradictory result are: (1) Some $CdCl_2$ still remains on top of the CdTe layer; (2) The surface of CdTe is n-type doped by chlorine (Cl_{Te}) or interstitial Cd (Cd_i).

In order to check the effect of possible remaining $CdCl_2$, the $CdCl_2$ residue was removed by a post-activation annealing as well as Ar ion sputtering. After the post-activation annealing, the Fermi level was shifted down to 0.85 eV which is slightly higher compared to the non-activated sample (Fig. 5-6). After surface cleaning by Ar ion sputtering, the Fermi level was shifted down to 0.62 eV which is lower compared to the non-activated sample, but it was shifted up again after a post-sputter annealing at 390 °C. The post-sputter annealing was performed for compensating of defects that may induced by the Ar ion sputtering.

Chlorine has two different impurity states in the band gap of CdTe [91-94]. One is an acceptor complex state with Cl in Te site (Cl_{Te}) and a vacancy of Cd (V_{Cd}) located at 0.1 eV

above the CdTe valence band and the other one is a donor Cl_{Te} level at 0.35 eV below the conduction band. Chlorine may diffuse to the bulk of CdTe and produce a p-type doping, but near to the surface, the possibility of n-type doping is higher. This is due to availability of more Cd at the surface region and lower possibility of the complex acceptor formation. On the other hand, at this region interstitial Cd may also lead to a surface n-type doping.
Another in principle possible reason for the shift of the Fermi level to higher energies could be surface photo-voltage or surface charging induced by the X-ray illumination during the photoemission process [95, 96]. Usually, the open circuit voltage of the CdTe solar cells increases more than 0.2 V after activation. Therefore, the CdTe surface of the activated sample has a higher positive voltage, which may lead to a shift of the Fermi level towards higher energies. In order to see whether this happens or not, a glass/Mo/CdTe sample, which should not produce any surface photo-voltage, was measured before and after the activation step. In this experiment also after activation, a shift of about 0.2 eV to higher binding energies was observed. A surface photovoltage can therefore be ruled out as origin of the binding energy shift after activation, according to previous investigations [64]. Therefore, these measurements clearly confirm that after the $CdCl_2$ treatment in vacuum, the surface of CdTe becomes n-type. This n-type region needs to be removed/compensated before/during back contact formation [97].

5.2.2 XPS analysis of oxidized samples

In order to study the effect of oxygen on the activation, samples which had been stored in air at room temperature for at least one month have been analyzed by XPS before and after the in-situ activation. For these samples, different contaminations might appear on the surface, which depend on many factors such as storage condition and the storage time. Most of the surface contaminations had to be removed before the in-situ activation; otherwise, the $CdCl_2$ source could become contaminated.
Fig. 5-7 shows the Te 3d core levels of non-cleaned and cleaned samples.

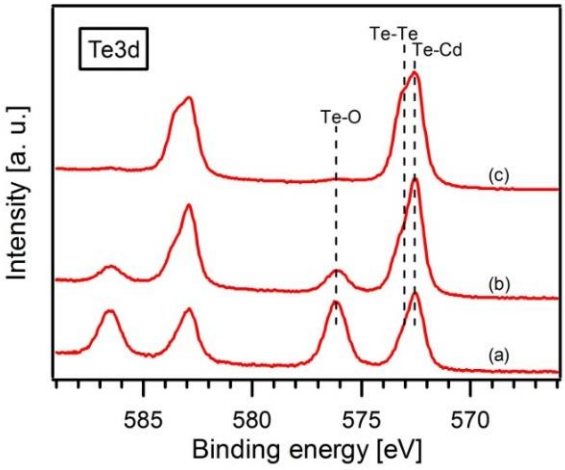

Fig. 5-7. Te 3d core levels of a non-cleaned (a), 5 min (b), and 20 min (c) ultrasonically cleaned samples before the activation. The ultrasonic cleaning leads to reduction of the oxide component and formation of an elemental tellurium layer on top of the CdTe surface.

The cleaning process was performed using an ultrasonic bath with deionized water. For the non-cleaned sample, two Te $3d_{5/2}$ emissions with a binding energy separation of 3.6 eV were observed, as can be seen in Fig. 5-7(a). The emission at lower binding energy (572.6 eV) corresponds to Te in CdTe and the one at higher binding energy (576.2 eV) corresponds to Te in $CdTeO_3$.

After the ultrasonic cleaning, the oxide component is significantly decreased and an extra emission at binding energy of 573 eV appeared, as shown in Fig. 5-7(b) and (c). From its binding energy, the additional species can be related to the formation of an elemental tellurium layer [98]. Longer ultrasonic washing time leads to an increased removal of the oxide component and also to the formation of a thicker elemental Te layer on the surface.

The oxidized sample, which was ultrasonically cleaned for 5 minutes, was measured by XPS before and after the in-situ activation also before and after Ar ion sputter cleaning. Fig. 5-8 shows the Cd 3d and Te 3d core levels of this sample. The O 1s spectra of the sample before and after the in-situ activation are also shown in Fig. 5-9.

The effect of the in-situ activation on the oxidized sample can be summarized as following:

- Core level binding energies are shifted by about 0.16 eV to higher values after the activation (Fig. 5-8), which correspond to an upward shift of the Fermi level. After removing of the residual species (Cl, C and O) from the surface by argon sputtering, a shift to lower binding energies was observed. Fermi level of the activated sample

after sputtering was also lower compared to the non-activated sample. However, E_F – E_{VBM} was still larger compared to the sputter-cleaned non-activated sample.

- The Te emission, which corresponds to $CdTeO_3$, was vanished after the activation, as can be seen in Fig. 5-8(right). The elemental tellurium, which had been created during the ultrasonic cleaning, was also disappeared.
- The O 1s emission shows two different components (Fig. 5-9). The emission at lower binding energy, which corresponds to $CdTeO_3$, vanished completely after the treatment. The emission at lower energy, which is due to the adsorbate, is significantly reduced.

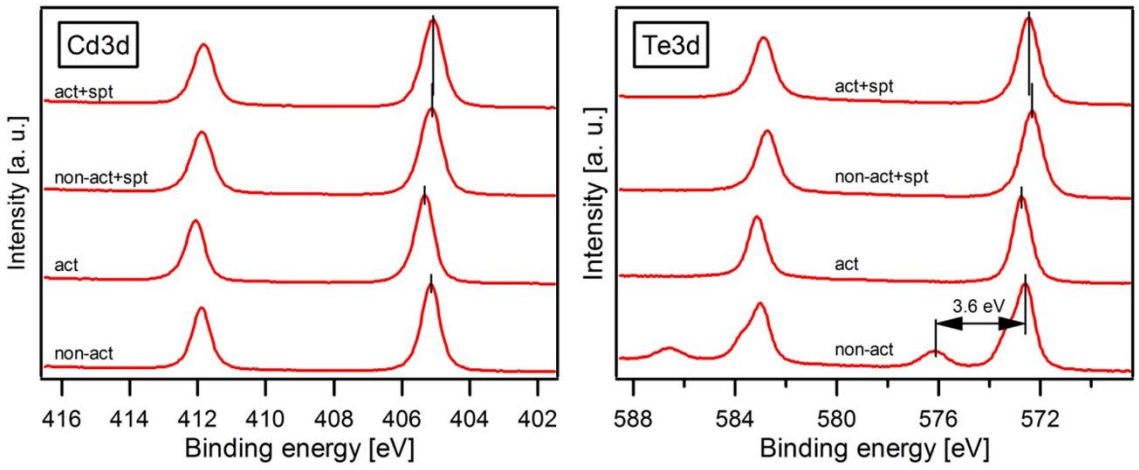

Fig. 5-8. Cd 3d (left) and Te 3d (right) core levels of the oxidized sample before and after the in-situ activation. Activation leads to vanishing of the oxide component and elemental tellurium from the surface and a shift of the core levels to higher binding energies.

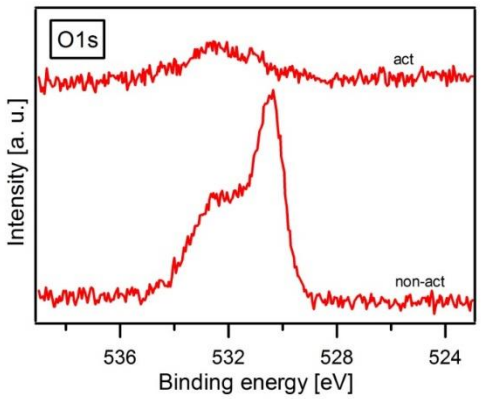

Fig. 5-9. O 1s core level spectrum of the oxidized sample before and after the in-situ activation. The oxide components are significantly reduced after the activation.

It was shown that CSS-CdS/CdTe solar cells, grown at high substrate temperatures and activated with $CdCl_2$ in an inert atmosphere have very similar cell performance to those cells treated with $CdCl_2$ in oxygen [99]; however, for the samples prepared at low substrate temperatures, through physical vapor deposition, increasing the oxygen concentration significantly improves the grain growth and sulfur diffusion [100]. On the other hand, it has been reported that for the MOCVD-CdS/CSS-CdTe samples, adding oxygen during the $CdCl_2$ treatment improves the solar cell performance [101]. The influence of oxygen upon optoelectronic properties of CdTe films has been investigated by Valdna [102]. They found that a small quantity of oxygen decreases the resistivity of the films caused by shallow acceptor complexes, whereas at higher concentrations it increases the resistivity of the films due to formation of isoelectronic complexes with cadmium vacancies. Introducing oxygen during CSS deposition of CdTe has also shown improvement in the solar cell performance [103, 104]. However, Komin et al. have shown that the presence of oxygen does not affect the electronic defects in CdTe [99, 105]. They also concluded that oxygen is not essential for the activation process, especially for samples prepared by high temperature CSS process. Our results clearly confirm this and also showed that the samples that were exposed to air before the vacuum activation have slightly better performance compared to the non-oxidized samples. However, adding oxygen to the chamber during the activation did not show any further improvement. It was also realized that sticking of the $CdCl_2$ to an oxidized CdTe surface is better than a cleaned sample. Therefore, we expect that the improvement in the performance could be due to a better $CdCl_2$ supply for diffusion to the layers.

5.3 Effects of the $CdCl_2$ activation on the morphology and structure

The surface morphology of the non-activated and in-situ activated glass/FTO/CdS/CdTe samples was studied by Atomic Force Microscopy. The deposition and activation parameters of both samples were similar to those explained in section 5.1. AFM images of the non-activated (a, b) and in-situ activated (c, d) samples are shown in Fig. 5-10.

The non-activated sample has a root mean square (RMS) surface roughness of 186 nm and consists of a mixture of small and large grains with diameters of about 1 to 5 μm. The in-situ activated sample has higher RMS surface roughness (278 nm) and larger average grain size compared to the non-activated sample.

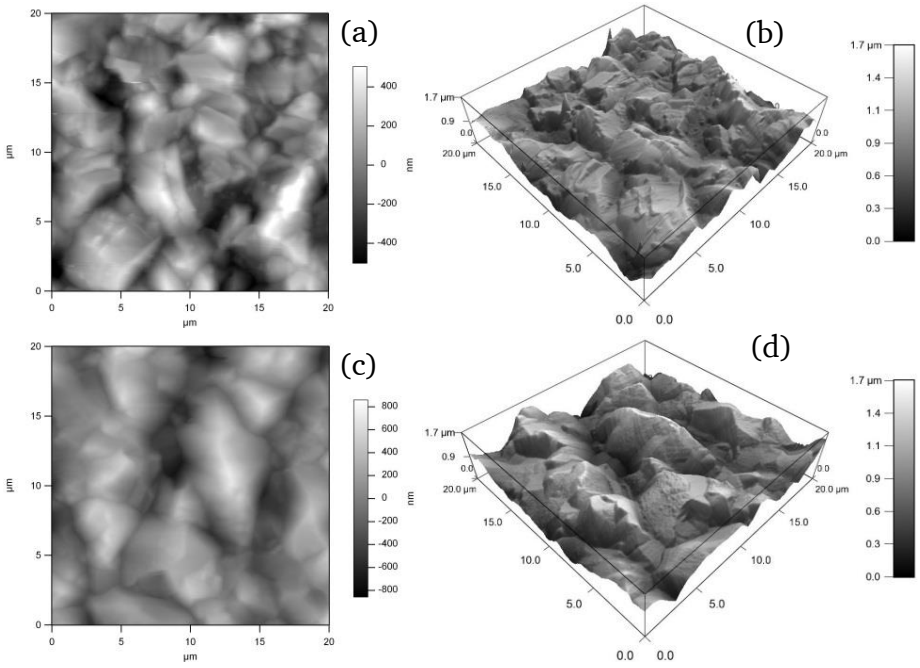

Fig. 5-10. AFM images of non-activated (a, b) and in-situ activated (c, d) glass/FTO/CdS/CdTe samples. The activated sample has higher RMS roughness and larger average grain size.

The density of the CdTe grains with diameter less than 2 μm is lower in the activated sample. This indicates that the activation leads to grain growth especially for the smaller grains. Our previous investigation showed that the ex-situ activation also results in grain growth but the RMS roughness decreased after the treatment [20]. One reason for the lower roughness could be due to $CdCl_2$ residue on the ex-situ activated sample, which may affect the AFM measurement. The grain growth and slight decrease in the surface roughness after $CdCl_2$ treatment has also been observed for samples prepared at low substrate temperature by sputtering [77].

In addition to the AFM morphological study, influence of the activation on crystallographic properties of the samples has been studied by XRD measurement. The XRD patterns, which have been normalized to the highest intensity, are shown in Fig. 5-11. As can be seen from this figure, the non-activated and in-situ activated samples have very similar XRD pattern. The reflection peaks of each sample can be indexed to cubic zincblende CdTe (JCPDS file No. 65-880) with a lattice constant of a = 6.48 Å. Harris analysis was performed to calculate the texture coefficient of the samples as explained in literature [20, 55]. The texture is almost random and it does not change significantly after the activation. This agrees with our previous work on ex-situ activated CdTe layers grown by CSS at high substrate temperatures [20, 32, 80, 81]. Table A1 (Appendix A) shows X-ray diffraction intensities

and the texture coefficient of the non-activated and activated samples along with the intensities of a powder sample (JCPDS file No. 65-880).

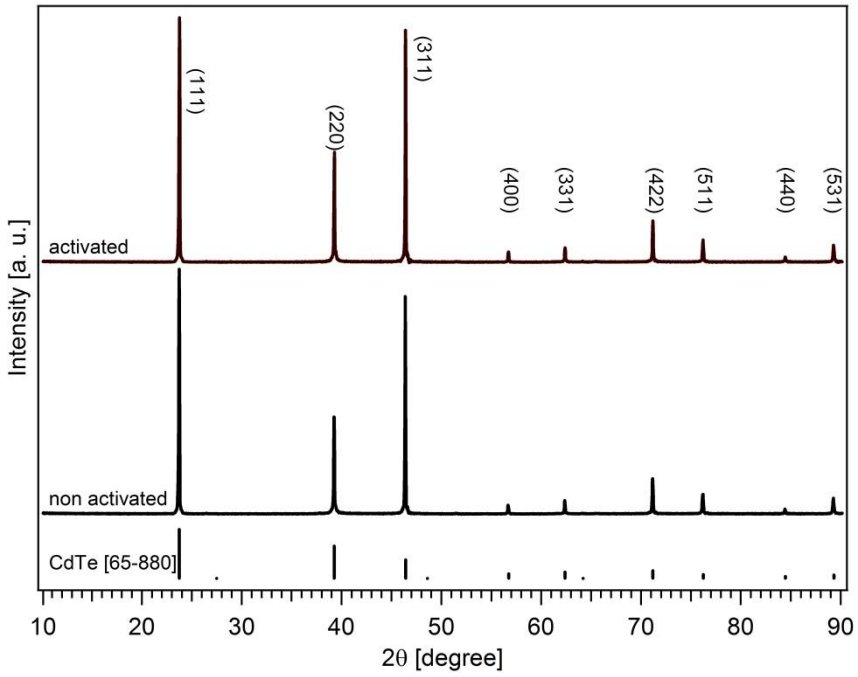

Fig. 5-11. XRD patterns of non-activated and in-situ activated glass/FTO/CdS/CdTe samples. Relative intensities of a CdTe powder with cubic structure are also shown as a reference.

5.4 Electrical characterization

5.4.1 J-V and EQE measurements

Fig. 5-12 shows the J-V characteristics of (a) non-activated, (b) ex-situ activated, and (c) in-situ activated solar cells. The average values for conversion efficiency (η), fill factor (F.F.), short circuit current density (J_{sc}), and open circuit voltage (V_{oc}) of the 3 best cells of every sample are also written on each diagram. As this figure indicates, both the ex-situ and in-situ activated samples show similar performance, but the in-situ activated cells have better uniformity. Potlog et al. have also observed a non-uniform performance in samples treated with $CdCl_2$ solution and they related the non-uniformity to the activation or back contact [57]. The rather low value of the photo-voltage in cells illustrated in Fig. 5-12, compared to our solar cells with Cu/Au back contact [20, 106] is attributed to an insufficient doping of the CdTe layer and to a high barrier height due to the use of a copper free back contact [107].

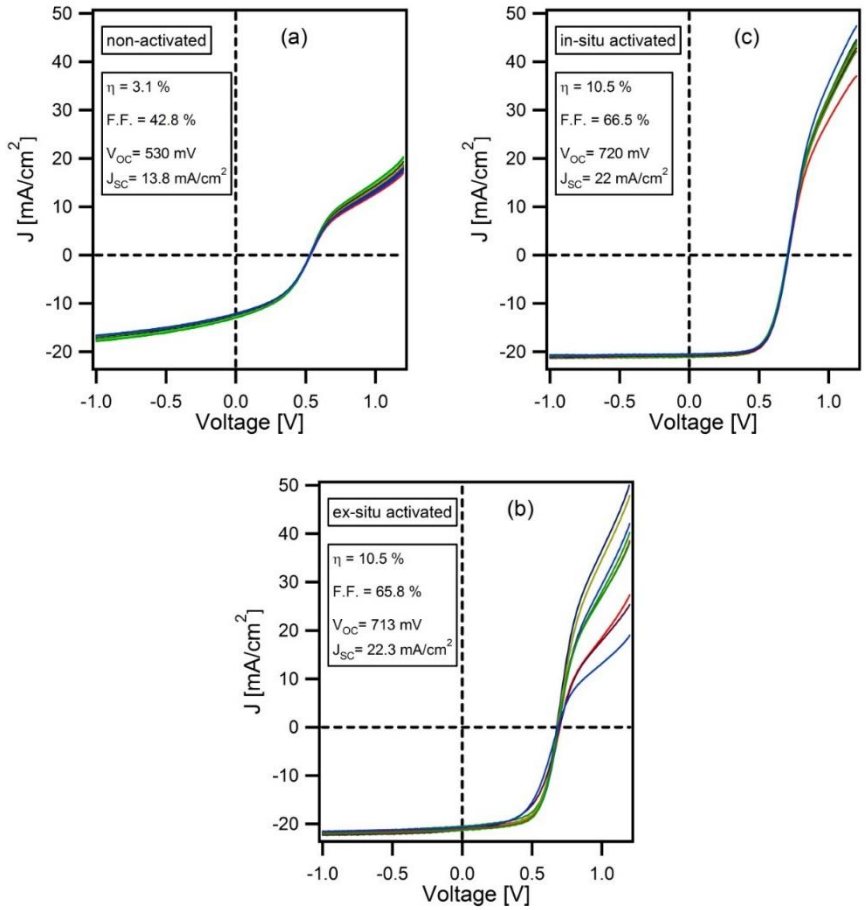

Fig. 5-12. J-V characteristics of (a) non-activated, (b) ex-situ wet activated, and (c) in-situ activated solar cells. Each graph shows the J-V characteristics of nine cells. Both the ex-situ and in-situ activated cells have similar performance but the uniformity of the in-situ activated cells is much better.

Fig. 5-13 shows EQE versus wavelength of the non-activated and activated solar cells. Maximum value of the EQE increased from 54% (at 550 nm) for the non-activated sample to 89% (at 600 nm) and 87% (at 670 nm) for the ex-situ and in-situ activated samples, respectively. The long wavelength cut-off is 851, 856 and 859 nm for the non-activated, ex-situ and in-situ activated samples, respectively. This shows that S diffusion to CdTe, which shifts the cut-off edge to higher wavelengths [94, 108], is more pronounced in the in-situ activated sample. On the other hand, Te diffusion into CdS is also higher for the in-situ activated sample which increases absorption of the window layer and therefore reduction of the EQE in the green region of the spectrum. XPS depth profiling was performed on a sample before and after the in-situ activation to study the inter-diffusion at the CdS/CdTe interface. Details of this experiment are given in Appendix A. From this measurement, it was found that the width of the inter-mixing region was increased from ~140 nm for the non-activated sample to ~200 nm after the activation (see Fig. A.3 in Appendix A). It

should be noted that, by extending the activation time or increasing the activation temperature, it is possible to enhance the inter-diffusion, but this may create shortcuts in some cells. Therefore, in our standard ex-situ activation, the annealing is performed at 390 °C for 20 minutes in which all the 9 cells on the sample were working. The EQE measurement shown in Fig. 5-13 was performed on a cell which had almost similar performance with the average performance of the 9 cells.

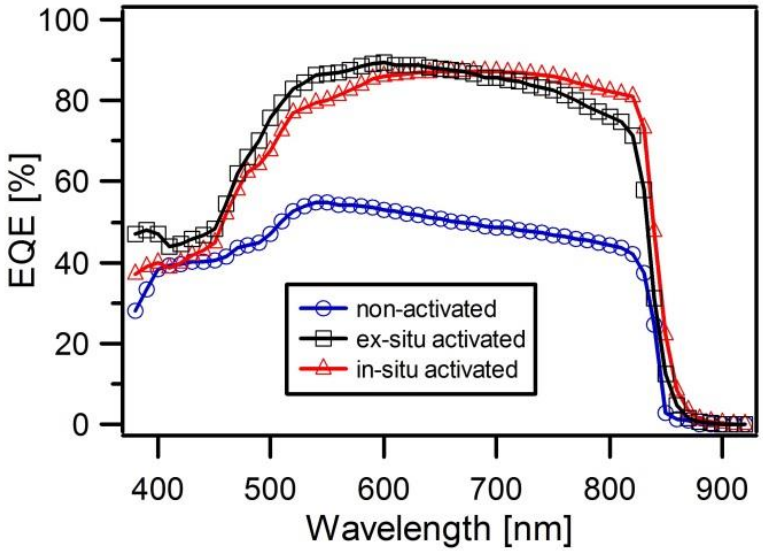

Fig. 5-13. External quantum efficiency of non-activated and activated samples.

5.4.2 C-V measurement

Other effects of the $CdCl_2$ treatment are redistribution of impurities [109, 110] and native atoms [78, 88, 111], which leads to a change in the doping profile of the CdTe and CdS layers. In order to compare effect of the activation on the carrier concentration and the doping profile in CdTe, C-V measurement was performed on the completed cells. The C-V characteristics of the non-activated and activated samples with their corresponding Mott-Schottky plot ($1/C^2$ versus V) and the doping profile are shown in Fig. 5-14. The doping profile is calculated from the slope of the Mott-Schottky plot based on the method presented by Hegedus and Shafarman [112]. By increasing the reverse bias voltage, the capacitance of the non-activated and ex-situ activated samples was decreased and it did not reach to a constant value even at -3 V, while for the in-situ activated sample it was almost constant at reverse voltages greater than 0.5 V (lower than -0.5 V) which means the CdTe layer is fully depleted. From the capacitance at zero bias, the width of the space charge layer was

calculated to be 1.7 μm, 2.1 μm and 2.5 μm for the non-activated, ex-situ and in-situ activated samples, respectively.

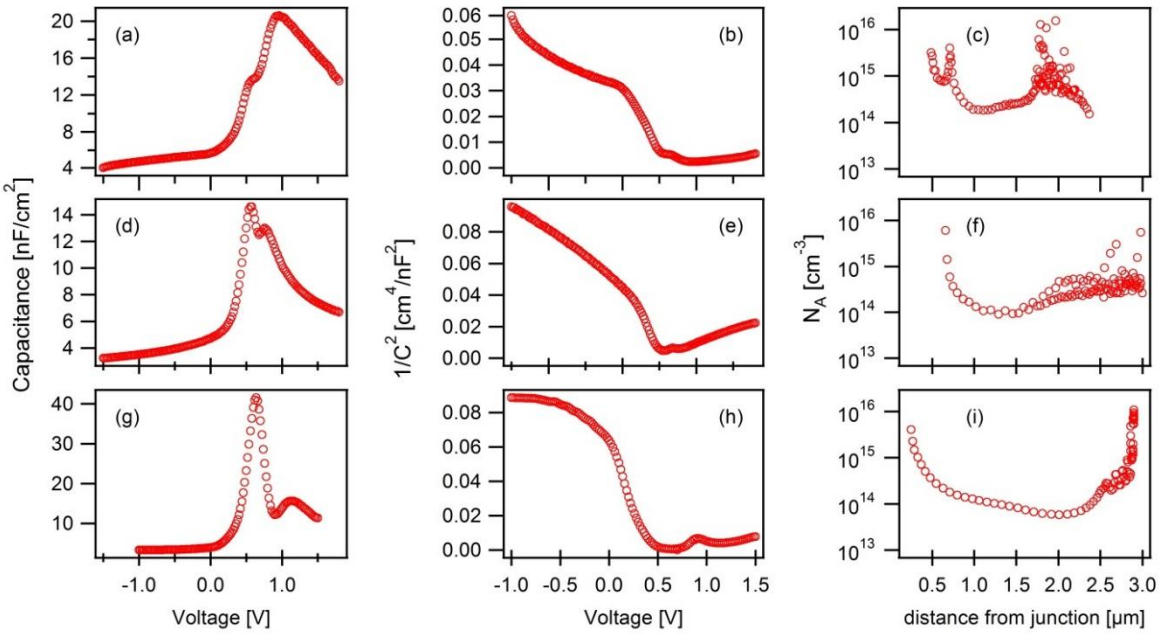

Fig. 5-14: Capacitance-Voltage (left), Mott-Schottky plot (middle) and p-type doping profile (right) of the non-activated (a, b, c), ex-situ activated (d, e, f) and in-situ activated (g, h, i) samples, respectively.

The maximum p-type carrier concentration near to the CdS/CdTe junction along with the minimum carrier concentration in the CdTe bulk are given in Table 5-3. According to this table, the carrier concentration at the CdTe bulk decreases after the activation while near to the junction it shows an increase. A decrease in the p-type carrier concentration after $CdCl_2$ treatment has also been reported by Britt and Ferekides [113]. It is expected that the cell with higher carrier concentration, should have higher V_{oc}, but the mentioned cells have almost similar V_{oc} and efficiency as shown in Fig. 5-12. There might be several reasons responsible for this, such as the doping of CdS and inter-diffusion at the junction, as has been discussed by Burgelman et al. [114]. Based on SCAPS simulation [115], the in-situ activated sample should have higher n-type doping in the CdS layer to compensate for the lower p-type carrier concentration in the CdTe layer.

Table 5-3: The carrier concentration in the CdTe layer calculated from the Mott-Schottky plot.

Carrier concentration (cm^{-3})	Junction	Bulk
non-activated	3.6×10^{15}	1.84×10^{14} @ 1.1 μm
ex-situ activated	5.8×10^{15}	9.43×10^{13} @ 1.5 μm
in-situ activated	3.9×10^{15}	5.78×10^{13} @ 2.1 μm

5.4.3 Impedance spectroscopy measurement

Another important effect of the $CdCl_2$ treatment is passivation of the defects, especially in the CdTe layer. In order to study this, the non-activated and activated solar cells were characterized by impedance spectroscopy. The measurement was performed on an impedance analyzer (Solartron 1260) and the results were fitted to appropriate equivalent circuits consisting of capacitors, resistors and a constant phase element (CPE) by using z-view V3.1 software (Scribner Associates, Inc) [7, 116, 117] .

The impedance spectrum (which is called Nyquist Plot) and the fitted equivalent circuit of an in-situ activated sample with gold back contact is shown in Fig. 5-15 (a) and (b), respectively. This measurement was performed in darkness under 400 mV forward bias in the frequency range from 0.1 Hz to 4 MHz. The equivalent circuit can be interpreted with the two-diode model that was introduced in chapter 3. For this sample, in order to have a better fitting, the junction capacitance was replaced with a CPE (CPE_j) as shown with the corresponding fitting parameters in Fig. 5-15. The CPE represents the spatial distribution of the junction capacitance originate from the grain boundaries, structural defects and a non-uniform doping (or impurities) within the absorber layer. There are two numbers for the parallel resistance, R_j for the junction and R_b for the back-contact. The sum of these numbers gives the parallel resistance of the cell, i.e., $R_p = R_j + R_b$. R_s and R_p were determined to be 7.3 $\Omega.cm^2$ and 7.07 $k\Omega.cm^2$, respectively. It should be noted that, the values of R_s and R_p from this experiment were different from those determined with the J-V measurement (i.e., $R_s = 6.4\ \Omega.cm^2$ and $R_p = 1.1\ k\Omega.cm^2$). The reason for such high deference (especially in R_p) could be due to the conditions of the measurements, since the J-V results were obtained under the light but the IS measurement was performed in darkness.

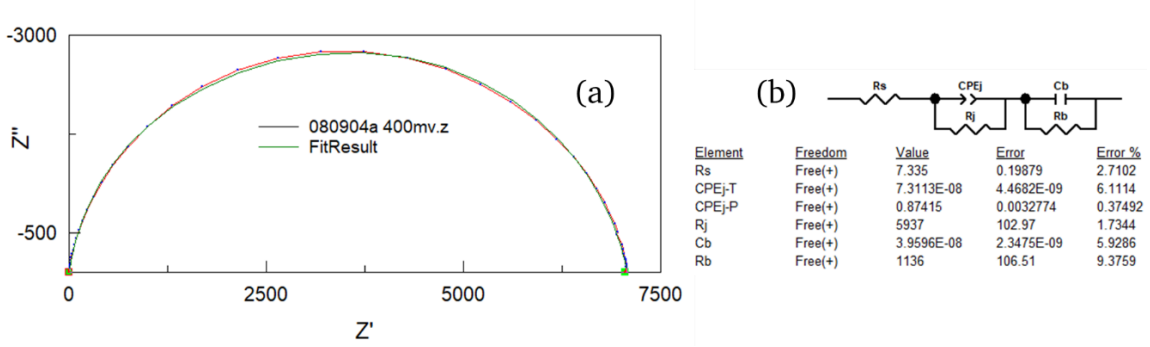

Element	Freedom	Value	Error	Error %
Rs	Free(+)	7.335	0.19879	2.7102
CPEj-T	Free(+)	7.3113E-08	4.4682E-09	6.1114
CPEj-P	Free(+)	0.87415	0.0032774	0.37492
Rj	Free(+)	5937	102.97	1.7344
Cb	Free(+)	3.9596E-08	2.3475E-09	5.9286
Rb	Free(+)	1136	106.51	9.3759

Fig. 5-15: (a) Measured and well fitted impedance spectra of an in-situ activated cell with gold back contact at room temperature in dark under 400 mV forward DC bias, and (b) Modeled equivalent circuit of the device.

For the non-activated cells, it was not possible to fit the impedance spectrum with a simple meaningful equivalent circuit, probably due to a large number of defects and inhomogeneity of these samples.

Further investigations (for example performing the measurement under illumination and/or various temperatures) is needed in order to get more information about the defect levels and to determine the back-contact barrier height as explained in literatures [116, 118, 119].

5.5 Summary and conclusion

An in-situ $CdCl_2$ activation setup was built and integrated with DAISY-SOL. By optimization of the in-situ activation process, efficiencies as high as ex-situ wet activated solar cells were obtained. CdS and CdTe layers were deposited onto FTO coated glass substrate by CSS in vacuum at high substrate temperature (T_{sub} = 520 °C). Non-activated and activated glass/FTO/CdS/CdTe samples were investigated by XPS, AFM and XRD. Influence of the activation on air-exposed samples has also been studied. Electrical properties of the completed solar cells were studied using J-V, EQE, C-V and IS measurements.

The results of this work can be summarized as following:

- XPS measurement showed that the activation leads to an n-type doping of the CdTe surface. Additionally, for the oxidized (air-exposed) samples, the oxide components were significantly reduced after the activation. The $CdCl_2$ residue can be removed with an appropriate post-activation annealing. Since no oxide layer was formed during the activation, the washing/etching steps to remove the $CdCl_2$ residue/oxide

layer were no longer necessary. Clearly, this is an important step towards producing very thin CdTe solar cells with an industrial friendly dry process.

- AFM measurement showed that the in-situ activation leads to increasing of the average grain size, and in contrast to the ex-situ activation, an increase in the surface RMS roughness.
- Both the non-activated and activated samples have very similar XRD pattern. Texture orientation of samples was almost random and it did not change significantly after the activation.
- Solar cells that were exposed to air before the in-situ activation showed better performance. However, adding oxygen to the chamber during the activation did not lead to further improvement.
- EQE measurement showed that the in-situ activated samples have better performance in the long wavelength region, while the ex-situ activated samples performed better at the green region of the solar spectrum.
- From the C-V measurement, it was understood that the carrier concentration in the bulk of the activated sample is lower, but near to the junction, it is slightly higher compared to the non-activated sample.
- It was previously found that the CdS layer became highly n-type after the activation [90, 120, 121]. This was also confirmed in this work by XPS measurement of glass/FTO/CdS layers before and after the activation (see Fig. A.4 in Appendix A). Therefore, the increase in the open circuit voltage of the cells after activation would be mostly due to an n-type doping of the CdS layer instead of the p-type doping of the CdTe, which is claimed in the literatures [122, 123].
- The impedance spectrum of the in-situ activated solar cell could be fit based on a modified double RC-model in which the junction diode was replaced with a CPE model.

Chapter 6

Conductive AFM Measurements

In CdS/CdTe solar cells, polycrystalline cells show higher performances, as compared with the cells made from single crystals. Therefore, there might be some beneficial effects related to the grain boundaries (GBs). In order to find a correlation between the CdTe morphology and solar cell performance, two sets of samples with different morphologies were investigated by the conductive Atomic-Force Microscopy (c-AFM). Effects of different post-deposition treatments on the samples were investigated by this technique.

6.1 Experimental

Samples were prepared by deposition of CdS (~0.2 μm) and CdTe (~5 μm) layers onto the TCO-coated glass substrates by closed-space sublimation (CSS) technique in vacuum at high substrate temperatures (T_{sub}= 500 - 520 °C). Two sample sets were studied by c-AFM. In one set, the CdS and CdTe layers were deposited onto the glass/ITO/SnO_2 substrates, while for the second set, the layers were deposited onto FTO-coated glass substrates. The samples received different post-deposition treatments (i.e. $CdCl_2$ activation and chemical etching), before being analyzed by the c-AFM. As a reference, a non-treated sample from each group was also measured. A list of the samples that were analyzed is given in Table 6-1.

The $CdCl_2$ activation was performed in vacuum in a closed-space configuration (chapter 5), followed by a vacuum annealing to re-evaporate any residual $CdCl_2$ from the CdTe surface. Therefore, the CdTe surface was cleaned after the treatment, as this was confirmed with X-ray photoelectron spectroscopy (XPS). The chemical etching of the CdTe surface was performed using Bromine/Methanol (BM) and Nitric/Phosphoric (NP) acid solutions.

Conductive AFM measurements were carried out using an MFP-3D atomic force microscope equipped with an ORCA module, shown in Fig. 6-1(left). The ORCA module consisted of a specially-designed cantilever holder that included a trans-impedance amplifier with a gain of 5×10^8 V/A. Doped diamond-coated conductive tips with nominal tip curvatures of 35 nm were used, which had good electrical conductivities and high wear resistances.

Table 6-1: List of the samples that were analyzed with the c-AFM.

Sample	Structure	Post-deposition treatment
A	glass/ITO/SnO_2/CdS/CdTe	-
B	glass/FTO/CdS/CdTe	-
C	glass/ITO/SnO_2/CdS/CdTe	$CdCl_2$ activation
D	glass/FTO/CdS/CdTe	$CdCl_2$ activation
E	glass/ITO/SnO_2/CdS/CdTe	$CdCl_2$ activation followed by BM etching
F	glass/FTO/CdS/CdTe	$CdCl_2$ activation followed by BM etching
G	glass/ITO/SnO_2/CdS/CdTe	Standard NP etching
H	glass/ITO/SnO_2/CdS/CdTe	$CdCl_2$ activation followed by standard NP etching
I	glass/ITO/SnO_2/CdS/CdTe	$CdCl_2$ activation followed by mild NP etching
J	glass/FTO/CdS/CdTe	$CdCl_2$ activation followed by mild NP etching

For glass/TCO/CdS/CdTe samples, one electrical contact was provided by placing a gold probe on the TCO layer, while the other contact was established by the conductive tip in contact with the sample surface, as illustrated in the schematic diagram in Fig. 6-1(right).

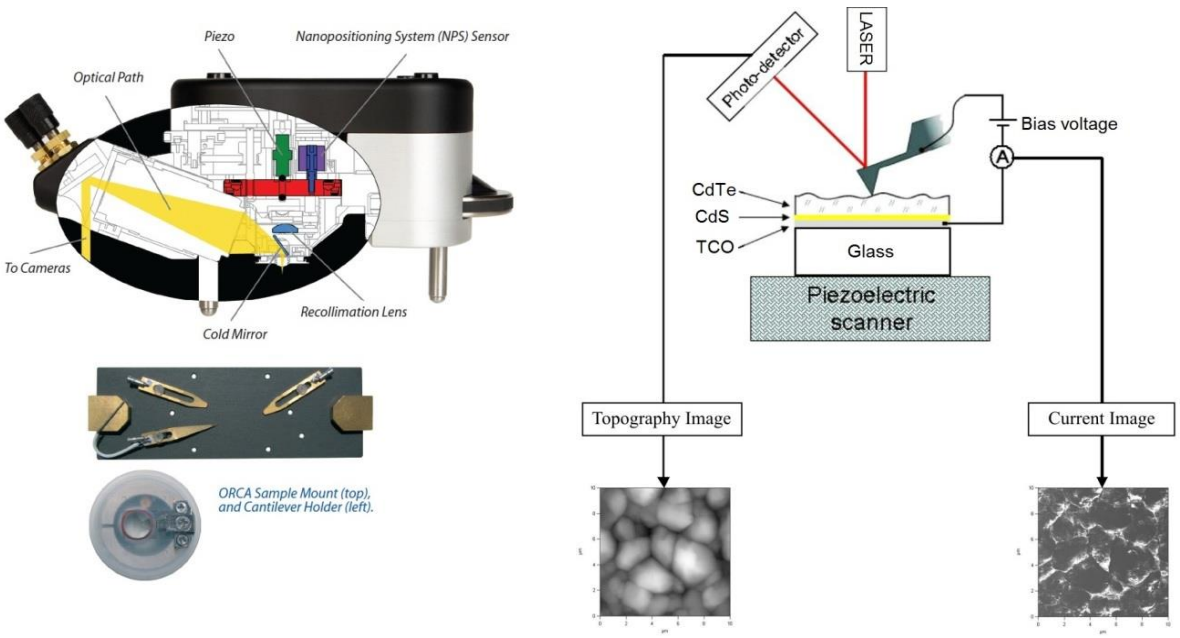

Fig. 6-1: MFP-3D setup with an ORCA module (left), and schematic diagram of the c-AFM (right).

In all measurements, the tip was grounded and the bias voltage was applied to the TCO. The measurements were performed in contact mode with a low scan rate (typically 0.5 - 1

Hz) and the topographic and current images were recorded simultaneously. Current-voltage (I-V) measurements were also performed on some specific points of each sample.

6.2 Results

6.2.1 As-deposited samples

Fig. 6-2 and Fig. 6-3 show the topographic and current images for two different non-treated samples (samples A and B), respectively. Sample A (and all other samples that were deposited onto glass/ITO/SnO_2 substrates) had isotropic grains with radii in the range of 2-4 μm. Sample B (and all other samples that were deposited onto glass/FTO substrates) had a very compact structure and the grains were merged together, as can be seen in the topographic images of these figures.

In the two-dimensional (2D) current images, the current is proportional to the brightness, i.e. the current passing through the sample/AFM-tip is higher at the white regions. For sample A, the current passing through the sample was higher at GBs, as clearly can be seen in the current image of Fig. 6-2, which was recorded at an applied bias of 1 V.

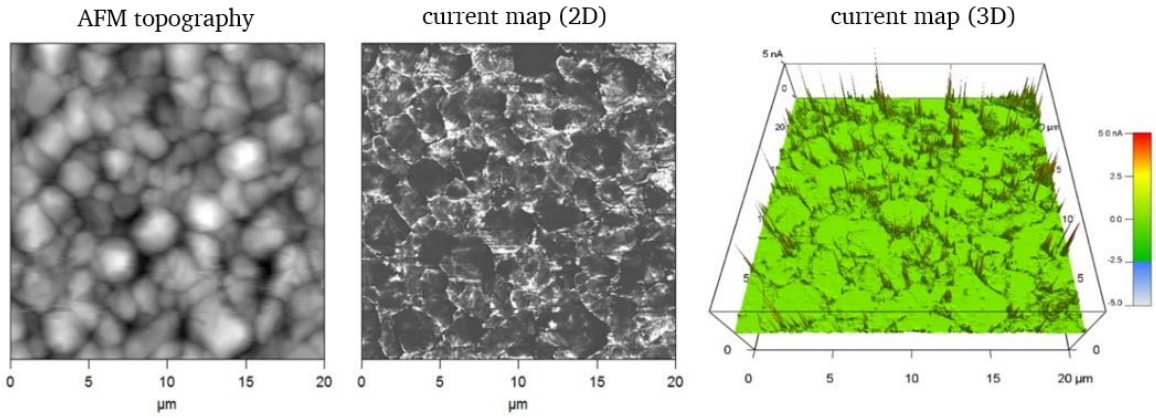

Fig. 6-2: AFM topography and current images of sample A (non-treated glass/ITO/SnO2/CdS/CdTe).

For sample B, the current was very low in all parts of the sample surface, and the current image had almost no contrast when it was measured with the bias voltage of 1 V. Therefore, the current image shown in Fig. 6-3 was recorded at a higher applied bias of 2.1 V; but still the contrast of the current image was lower, as compared with the sample A.

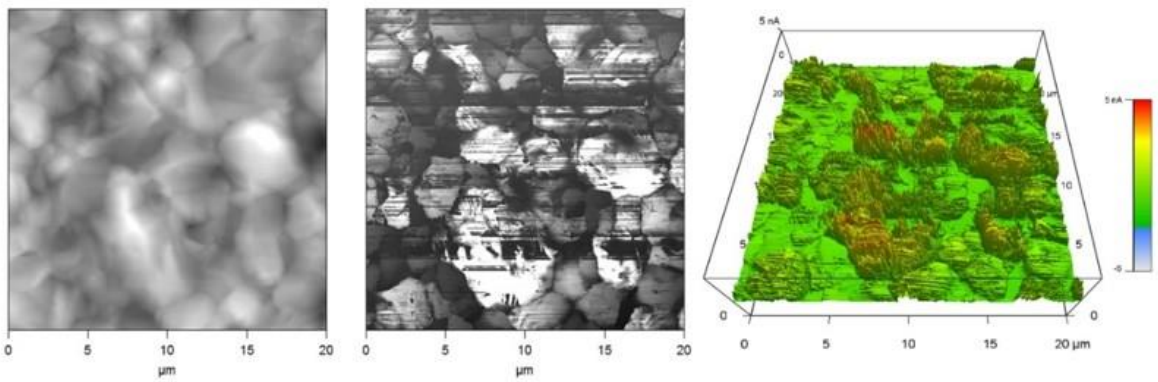

Fig. 6-3: AFM topography and current images of sample B (non-treated glass/FTO/CdS/CdTe).

6.2.2 $CdCl_2$ activated samples

The topography and the current images of the $CdCl_2$-activated samples (samples C and D) are shown in Fig. 6-4 and Fig. 6-5, respectively. The current image of sample C was recorded with applied bias of 0.5 V, while for sample D the applied bias was 1 V. Both samples were prepared at a high substrate temperature; therefore, as expected, after the $CdCl_2$-treatment no significant change in the morphology was observed. However, for both samples the current at most grain sites was significantly increased. Sample C still showed higher current at the grain boundaries and also there were few grains with much lower conductivities which appeared in black in the 2D current image. However, for sample D the difference between grains and grain boundaries was not noticeable. This is more obvious in Fig. 6-6, which shows local current-voltage measurements on some selected points on grain surfaces and at the grain boundaries. Except for point f, which was on a deep valley, the I-V characteristics on other points looked very similar. The rectifying shape of the I-V curves

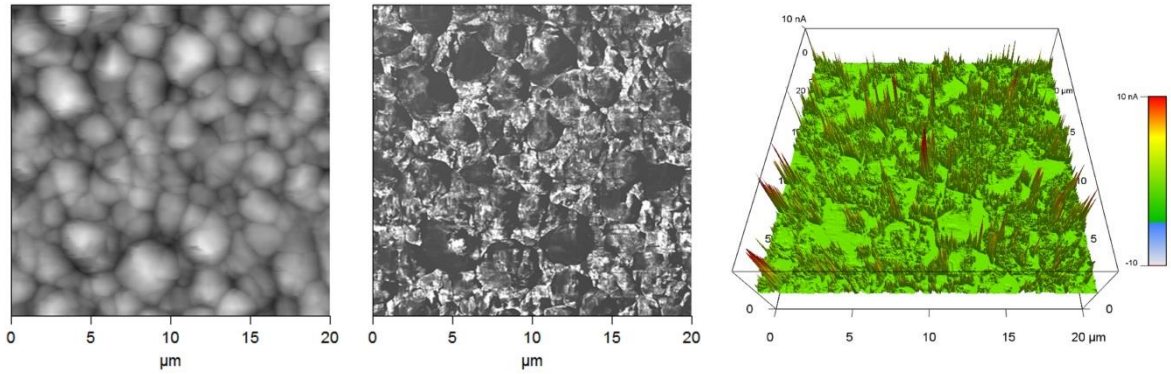

Fig. 6-4: AFM topography and c-AFM current map of sample C. The bias voltage was 0.5 V.

confirmed that the contact between the AFM tip and CdTe surface was not ohmic, which was expected for a non-etched CdTe surface.

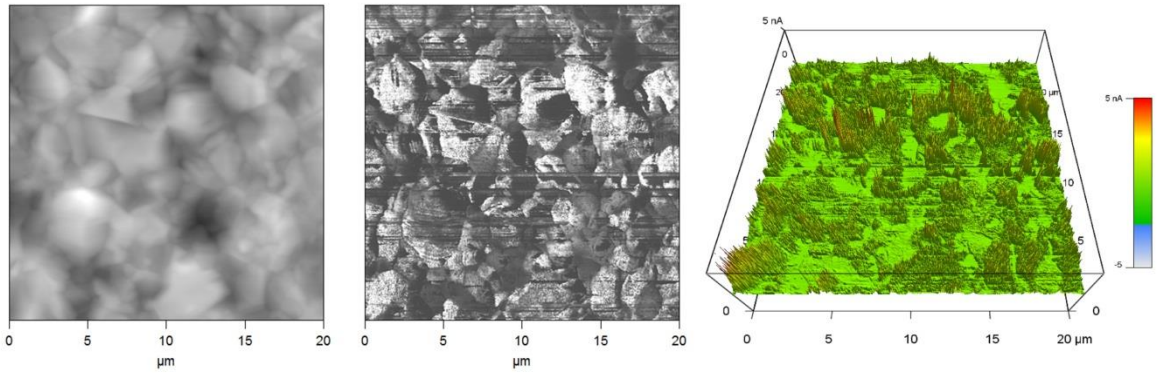

Fig. 6-5: AFM topography and c-AFM current map of sample D. The bias voltage was 1 V.

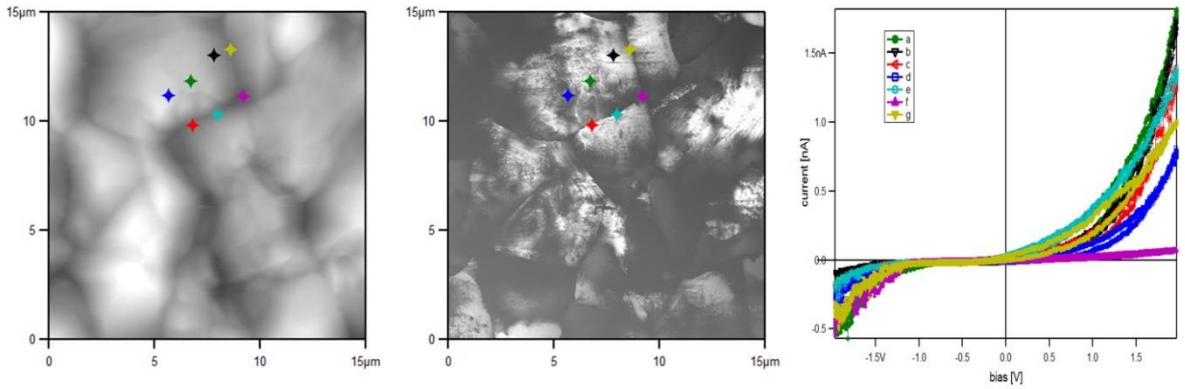

Fig. 6-6: local current-voltage measurement at different points on sample D.

An important step for recording the current images of the non-etched samples (both the non-activated and activated ones) was cleaning of them with deionized water in an ultrasonic bath. Without the cleaning step it was not possible to record good current images. This could be due to a very low conductivity of the CdTe surface before the cleaning (even for fresh deposited samples). After the cleaning, a very thin Te-rich layers is formed at the CdTe surface that improves its conductivity. This was confirmed by the XPS measurement that was discussed in section 5.2.2 (see Fig. 5-7).

6.2.3 BM-etched samples

Topographic and current images of BM-etched samples (sample E and F) are shown in Fig. 6-7 and Fig. 6-8. The etching time was 20 s. After the BM-etching step, the current at the

grain boundaries was much higher than at the grain surfaces, for sample E. However, for sample F, which had a compact structure, the current at most of the points was high and the conductivities of the grains and grain boundaries were almost similar.

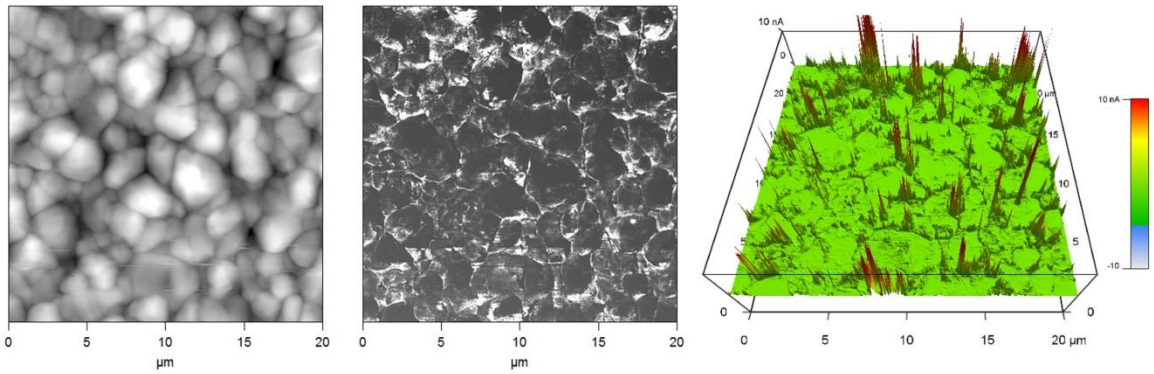

Fig. 6-7: AFM topography and c-AFM current map of sample E. The applied bias was 0.4 V.

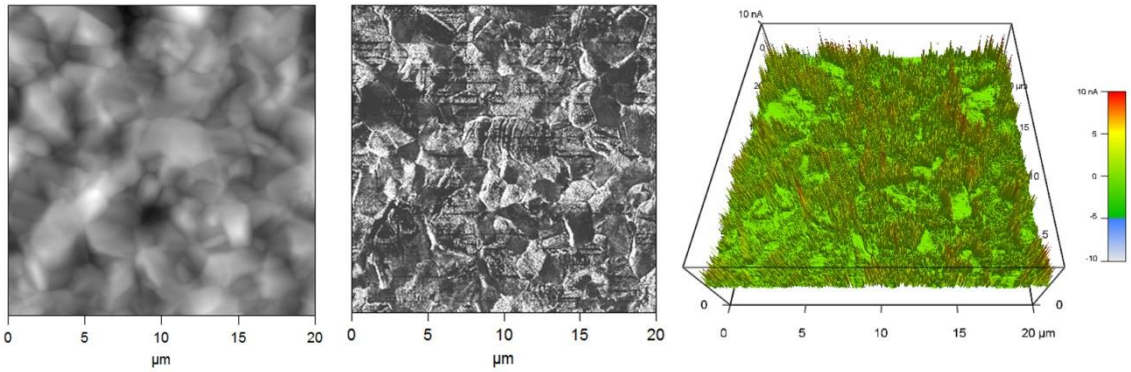

Fig. 6-8: AFM topography and c-AFM current map of sample F. The applied bias was 1 V.

It was also observed that with a constant bias voltage, the current passing through the tip-sample was degrading after each scan. This degradation was not related to the tip; because by measuring another place, again for the first scan the current was high, but after each scan it was diminished. One possibility for this degradation could be due to a local surface oxidation induced by the tip-surface electric field. In order to check this, another measurement was performed under nitrogen atmosphere but still the degradation was observed. Even after this measurement, we could not exclude the oxidation effect, because the AFM chamber was not completely sealed.

6.2.4 NP-etched samples

In our standard NP etching, the etching times were in the range of 20 - 30 s, when bubbles appeared on the whole surface of the CdTe layer. For the standard NP-etched samples, even without a bias voltage, the current (photo-generated current due to the AFM laser) was too high at all points, and it was not possible to record the current image with the standard ORCA holder. This could be due to formation of a conductive Te layer on the entire surface of the CdTe, which increases the contact area; therefore, it leads to a very large current collection. The formation of an elemental Te layer was confirmed EDX and XRD characterizations (see Fig. A.1 and Fig. A.2 in Appendix A).

In order to reduce the contact area and analyze individual grains, we tried to separate a small region by scanning around a small rectangular area, using a diamond tip. However, this was not successful; because during scratching out around the selected area, the layers were completely removed from the substrate. Another possible way for reducing the current was putting a resistor (R~20 MΩ) in series with the sample. With this configuration, it was possible to record the current image of the NP-etched samples. The current was still very high at all points of the surface and the current images had almost no contrast. Local current-voltage measurements were performed at different points (on grain surfaces and at the GBs). Fig. 6-9 shows the I-V characteristics of the non-activated and activated samples, after the NP-etching step (samples G and H).

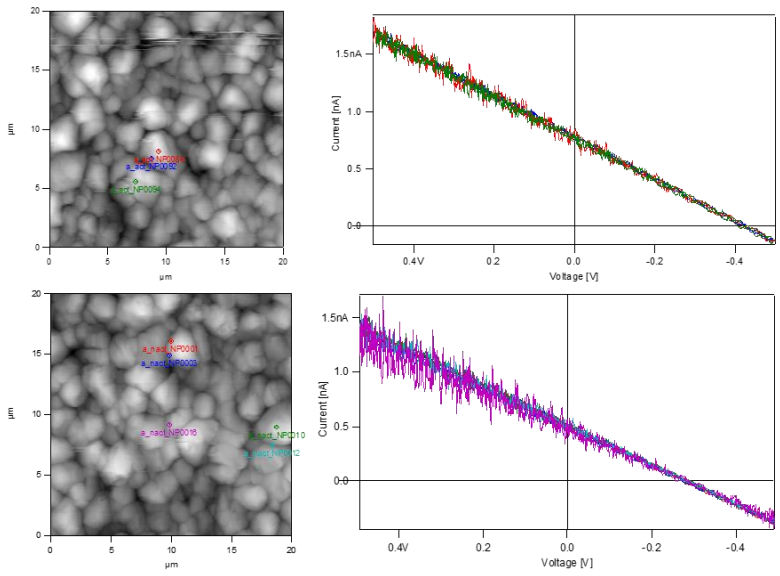

Fig. 6-9: I-V characteristics of non-activated NP-etched (bottom) and activated NP-etched (top) samples at different points.

The following results were obtained from these measurements:

- For both NP-etched samples and at all points, the contact between the tip and the sample surface showed an ohmic behavior.
- I-V characteristics of each sample at different points were almost the same.
- At zero bias voltage, there was a current passing through the tip. This was a photo-current produced by the sample under AFM's laser illumination.
- The bias voltage at which the current was zero was increased from ~0.3 V for the non-activated sample to ~0.5 V for the activated sample.

Effect of an external illumination on the I-V characteristics of the activated sample was investigated by shining the sample with an incandescent light bulb. The light intensity was about 0.5 W/cm^2. Illumination from the CdTe side did not have any detectable change on the I-V characteristics, but by illumination from the glass side, a parallel shift of the I-V to higher currents was observed, as shown in Fig. 6-10.

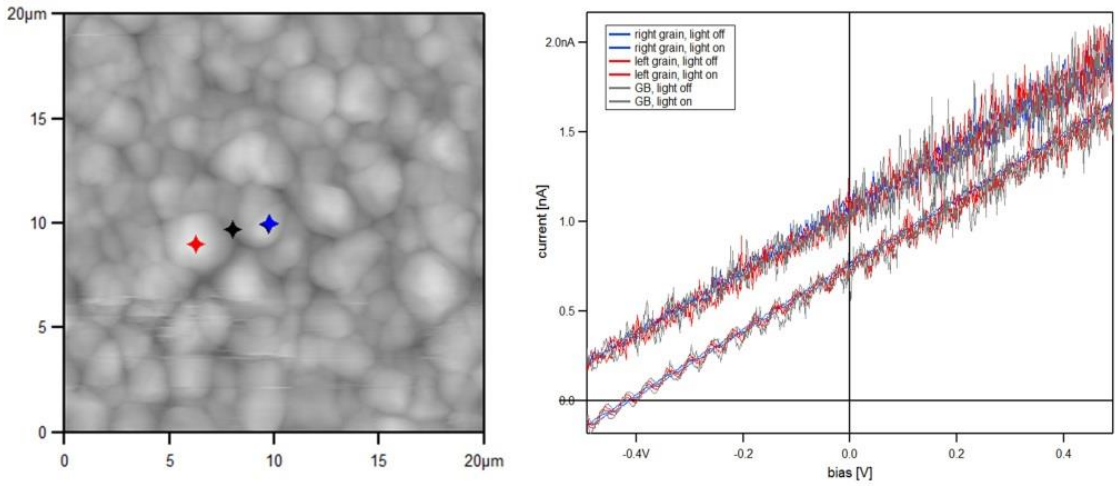

Fig. 6-10: Effect of an external illumination from the glass side on I-V characteristics of the activated NP-etched sample.

Mild NP-etched activated samples were also measured by c-AFM. For these samples, the etching time was reduced to 12 - 15 s, in which the bubbling started only at some points of the CdTe surface. Fig. 6-11 and Fig. 6-12 show the topography and current images of the mild NP-etched samples (I and J). The current images were recorded without applying any bias voltage. Therefore, the current in these figures is the photocurrent generated due to

illumination of samples with the AFM laser. As these figures clearly show, the current collection is more noticeable at the GBs.

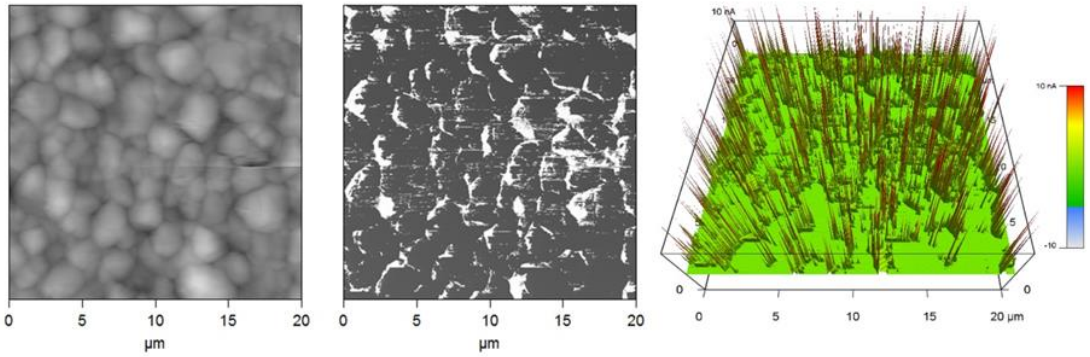

Fig. 6-11: AFM topography and c-AFM current map of sample I. Zero bias voltage was applied.

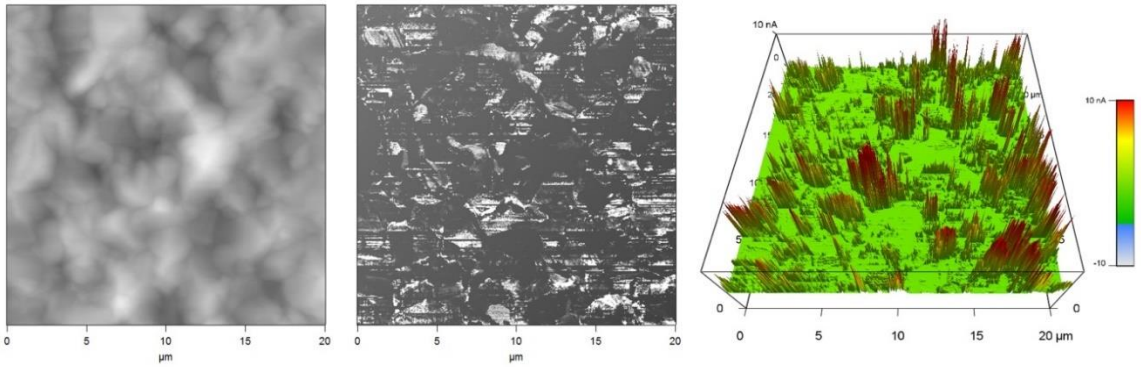

Fig. 6-12: AFM topography and c-AFM current map of sample J. No bias voltage was applied.

6.3 Discussions

During recording of the current images, the CdS/CdTe junction was in reverse bias, while the tip-surface diode was in forward bias; otherwise, there was no current or very small current even at high bias voltages (especially for the non-etched samples). The current passing through the tip spreads into the CdTe, so it can be concluded that the contact area in the CdS/CdTe junction was very large, as compared with the tip-surface contact area. The photocurrent from this area was high enough to exceed the tip-surface current. This means that, for the non-etched samples the current was controlled by the tip-surface contact (which was a Schottky contact in opposite direction to the CdS/CdTe junction). In should be mentioned that the dominant current routes did not change with the tip-pressure.

Therefore, any change in the current image could be related to a change in the tip-surface contact.

Based on the production method and structure of CdTe solar cell, there are different models to predict the band diagram at the GBs. The most reported models are downward [124-126] and upward [127] band-bending at the GBs. For samples that were examined in this work, the c-AFM current images can be explained by a downward band-bending, as schematically shown in Fig. 6-13 (middle). This figure indicates that at the GB the CdTe work-function was lower than at the grain surface. Therefore, the tip-CdTe barrier-height (Φ_B) was smaller that led to higher currents at the GBs, as compared with the current passing through the CdTe grains.

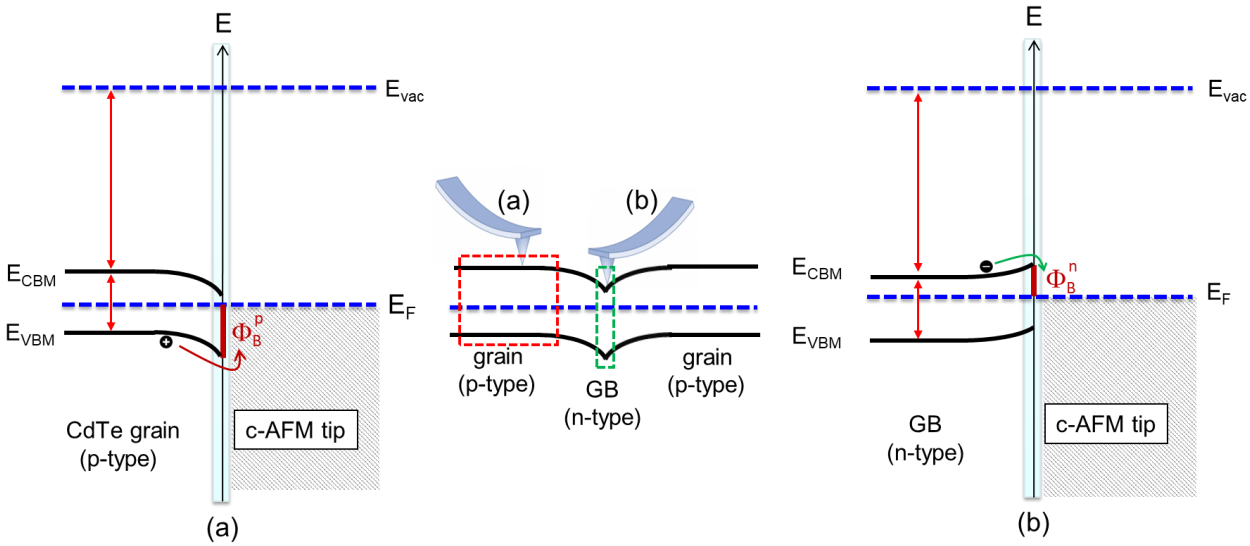

Fig. 6-13: Proposed energy-band diagram at the AFM-tip/CdTe interface. (a) on the p-CdTe grains a larger barrier for hole transport is formed, (b) on the n-CdTe GBs the barrier height for electrons is smaller.

The downward band-bending near the GBs produces a field that helps to separate the photogenerated electron-hole (e-h) pairs by creating two different routes for transport of the carriers, as schematically shown in Fig. 6-14. The electron is pulled into the GB core and transfers along the GB towards the front contact, while the hole transfers through the CdTe grain in the direction of the junction field towards the back contact. Therefore, the GBs improve the carrier collection (reduce the e-h recombination); however, when a GB crosses the junction, the open-circuit voltage is reduced, due to the formation of a weak junction (n-CdTe/n^+-CdS).

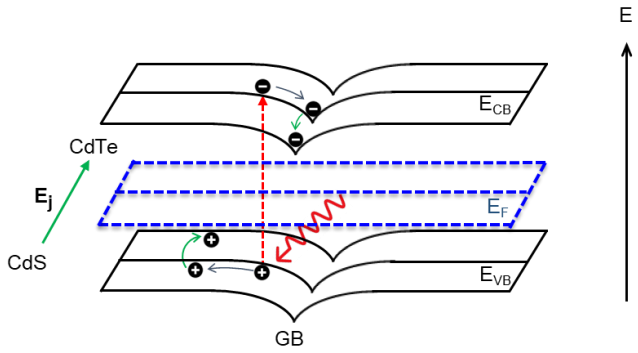

Fig. 6-14: Schematic drawing that shows how band-bending at GBs improves the carrier collection.

Electron backscatter diffraction (EBSD) images of two solar cells with different morphology are shown in Fig. 6-15. Cell B had larger grains, as compared with cell A; but cell A had a better performance. In cell A, the photo-generated carries would cross GBs to reach to the contacts; but in cell B at many places, they did not need to cross any GB. Therefore, solar cells with CdTe morphology similar to cell B have potential for a higher performance, if other factors especially the CdS thickness and $CdCl_2$ activation are optimized.

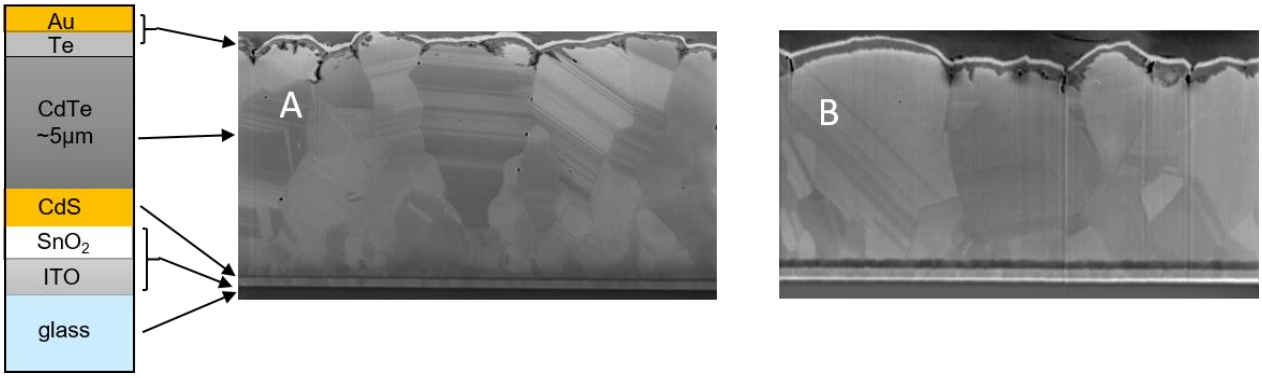

Fig. 6-15: EBSD images of solar cells with different morphologies.

Cell A: V_{oc}= 704 mV, J_{sc}=23.6 mA/cm^2, η=10.7 %

Cell B: V_{oc}=760 mV, J_{sc}=18 mA/cm^2, η=8.4 %

GBs play another important role by providing paths for diffusion of Cl towards the junction, during the $CdCl_2$ activation. Therefore, for solar cells with compact structures (like cell B), a special activation process (perhaps shorter activation time at a higher temperature) is needed. On the other hand, for solar cells with morphology similar to cell A, a high resistive buffer layer is necessary to prevent shunting at the points that the GBs cross the junction.

High resolution c-AFM images of the sample with isotropic grains are shown in Fig. 6-16. By comparing this figure (or Fig. 6-7) with Fig. 6-8, it can be concluded that this

morphology is not suitable for solar cells with thin absorber layers; because it can easily get shunted through the GBs.

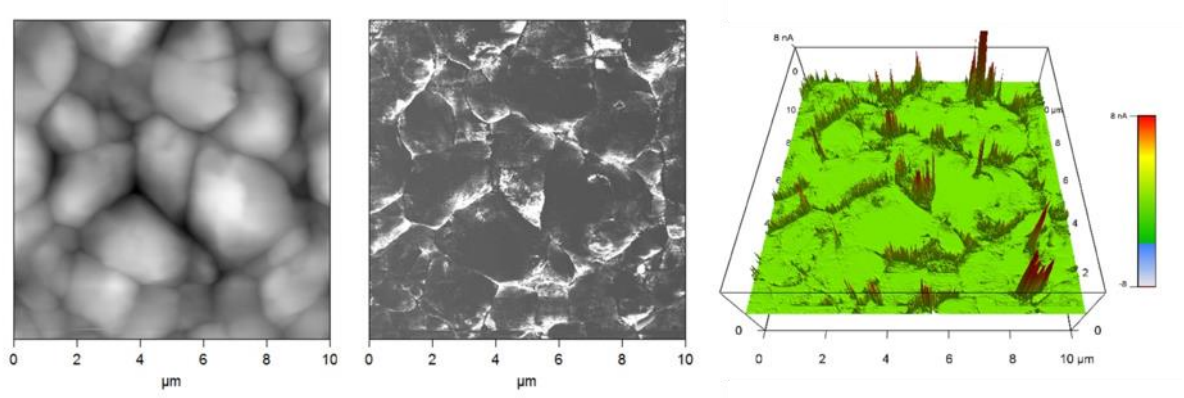

Fig. 6-16: High resolution c-AFM images of sample E.

6.4 Summary and conclusions

Effects of the activation and etching processes on the electrical conductivities and back contacts of CdTe/CdS solar cells were investigated using conductive AFM technique. For non-treated samples, the current passing through the sample was low and the GBs showed higher conductivities. After the activation, the current was higher for most of the points, but still the conductivities of the GBs were much higher than on the grains (especially for the samples with isotropic grains).

For BM-etched samples, the current at GBs was increased, and it was higher than the current through the grains. I-V measurements at different points on the samples showed that only for NP-etched samples the contact between the tip and the sample surface was ohmic. For other samples, and almost at all points, the contacts were rectifying, and a Schottky diode pointing in the opposite direction to the CdS/CdTe junction diode was formed.

Higher current at the GBs was due to a lower work-function at these regions, as compared with the grain surfaces. The band-bending near the GBs produced an electric field which is in the direction of the junction field. This field helped the electron collection and conduction along the GBs towards the junction. Therefore, the GBs improved the short circuit current of the cell by increasing the electron collection and reducing the recombination current. On the other hand, when a GB crosses the junction, the open-circuit voltage is reduced.

C-AFM measurements on BM-etched samples confirmed that the chemical etching was more pronounced at the GBs; therefore, it had to be avoided for CdTe solar cells with thin absorber layers (i.e. less than 2 μm), to reduce the shunting probability.

Consequently, it can be deduced that the $CdCl_2$ activation must be performed in a non-oxidizing atmosphere to provide a clean surface needed for dry back contacts, especially when no copper or copper-compound is used in the back contact.

Chapter 7

Back Contact Interlayers

The contact between a metal and p-type CdTe could be barrier-free for hole transport if the work-function of the metal was equal to (or larger than) the work-function of the p-CdTe, which is ~5.7 eV. Since typical metal electrodes do not have such high work-function, a barrier (Φ_B) is formed at the interface. CdTe is mostly covalent, therefore Φ_B is dominated by the interface states and weekly depends on the metals' work-function. In a study that was carried out previously in our group [128], it was found that when different metals are deposited onto the CdTe surface, a barrier height of ~1 eV (except for Te that was 0.6 eV) is formed at the interface, almost independent of the metals' work-function. This is mostly due to a reaction at the interface that leads to formation of a metal-telluride and elemental Cd^0, which pins the Fermi-level of CdTe near to the middle of its energy gap. The work-function of different metals deposited onto the CdTe surface along with the experimental barrier heights at the CdTe/metal interface, which were determined by photoelectron spectroscopy, are shown in Table 7-1.

Table 7-1: work-function and barrier height of different metals deposited on CdTe determined by photoelectron spectroscopy.

metal	work-function (eV)	Φ_B (eV)
Cd	4.20	1.18
Ti	4.30	1.15
V	4.30	1.07
Sb	4.55	0.97
W	4.55	1.05
Mo	4.60	0.95
Cu	4.65	0.95
Te	4.85	0.6
Ni	4.95	0.9
Au	5.10	0.86
Pt	5.60	1.03

This result confirms that it is not possible to make a low resistance contact with p-CdTe just by depositing a typical high work-function metal (like Au) onto its surface.
A common approach to overcome this problem is chemical etching of the CdTe surface with an appropriate etching solution (such as the NP- and BM-etch solutions), before deposition of the back electrode [129-132]. The etching process cleans the CdTe surface and creates a Te-rich layer, which is highly p-type and has much better conductivity compared with the non-treated CdTe surface [133]; therefore, a pseudo-ohmic contact can simply be formed by depositing a metal electrode (Au) onto the Te-rich CdTe surface [43]. This method is simple and effective but it is not suitable for mass production since it can only be used (in practice) for cells with a thick CdTe layer (>4 μm). For thinner films, the etching may produce conducting path through CdTe grain boundaries that may shunt the solar cell, as discussed in chapter 6.
Another approach to realize a low-resistance contact is application a layer between the CdTe surface and the back electrode. The intermediate layer should meet the following requirements:

- It should have a good electrical conductivity,
- it should be easy to make an ohmic contact with it,
- it should have a negligible valence-band offset with CdTe,
- it should have a negligible lattice mismatch with CdTe.

Several interlayers have already been introduced that can be categorized as following:

- interlayers like ZnTe [134-139] that have a negligible valence-band offset with CdTe to provide a low-barrier for hole transport,
- interlayers such as Cu or Cu_2Te [140, 141], Cu_2S [142], Cu_2O [143], Te [98, 144], Sb and Sb_2Te_3[145-150], which provide p-type doping of the CdTe surface that may lead to a tunneling contact,
- combined interlayers like ZnTe/Cu_xTe [151], which use the benefit of both layers (here ZnTe for the band alignment and Cu_xTe for p-type doping),
- high work-function materials including transition metal oxides (MoO_3 [152-162], V_2O_5 [158] and NiO [163]) that may provide a tunneling contact if applied as an ultra-thin layer on a highly doped CdTe surface. Thicker films of these oxides in

reduced form, which have a good conductivity, along with transition metal dichalcogenides (VSe_2 [2] and $TiSe_2$ [2, 164]) have also been studied.

Some alternative materials such as SnTe [165], CuI [166], BaCuSeF [167, 168], CdZnTe [134], HgTe [169, 170] and graphite paste doped with various materials [171, 172] have also been considered as back contact or BC-interlayer by various research groups.
In highly efficient CdTe solar cells always some copper (or copper compound) is presented, either intentionally (as dopant or a component of the contact material) or unintentionally due to the contamination and/or the materials' impurity. It is well known that the copper is a fast diffuser through grain boundaries in polycrystalline materials including CdTe. Cu diffusion in CdTe solar cells may lead to degradation of the cells in the following ways:

- back-contact degradation due to the migration of Cu from the back contact,
- segregation of Cu in GBs that leads to shunting,
- junction degradation: when the copper reaches the CdS layer it compensates the shallow donors in this layer by creating deep acceptor levels. This leads to a lower V_{oc} due to the degradation of the p-n junction.

In the state-of-the-art CdTe solar cell that was introduced in chapter 1, Cu was completely removed from the cell structure by doping the absorber layer (CdSeTe/CdTe) with group V elements and using ZnTe as the BC-interlayer [10].
In this work, copper-free BC-interlayers based on ZnTe, Te, Sb_2Te_3 and Sb and appropriate combinations of these layers were investigated. Most contacts were prepared in a dry procedure and without any chemical or physical etching. Optimization of different back contacts along with the XPS-analysis of some of the layers and interfaces are presented in this chapter. BC-interlayers based on molybdenum oxide will be discussed in chapter 8.

7.1 ZnTe back contact

7.1.1 Introduction

Zinc telluride with a direct band gap of 2.26 eV at room temperature [173], low electron affinity of 3.53 eV [174] and a high absorption coefficient of 10^5 cm^{-1} [175] has found many applications in CdTe and multi-junction tandem solar cells [176, 177]. There is a valence-band offset of less than 0.1 eV between CdTe and ZnTe, which provides a good hole-

transport [137]. On the metal contact side, ZnTe is usually doped to high levels ($p>10^{18}$ cm^{-3}) with Cu or group V elements (such as nitrogen) for realization of an ohmic contact. On the other hand, there is a conduction band offset of 0.9 eV between CdTe and ZnTe [137], which helps to reduce the back contact recombination by blocking the minority-carries; this plays an important role in p-i-n structures with a very thin CdTe absorber layer.

7.1.2 ZnTe/ZnTe:N back contact

In the work done by B. Späth [178], the best results were obtained by depositing a non-doped ZnTe layer (at a high substrate temperature) before deposition of the ZnTe:N layer. In that work, the following limitations in the performance of solar cells were observed:

- Defects at the CdTe surface induced by the previous processes, i.e., wet $CdCl_2$ activation and/or chemical etching,
- Interface states related to the lattice mismatch between CdTe and ZnTe, and
- Low doping of the CdTe layer.

In this research, the following experiments were performed to improve the performance of CdTe solar cells with a ZnTe interlayer:

- Deposition of ZnTe/ZnTe:N onto the in-situ activated samples (without any wet processing),
- Heat treatment/activation after deposition of the ZnTe for interface modification, and
- Using Sb and Cu-doped ZnTe interlayers.

The first investigation was deposition of a ZnTe:N layer onto the glass/TCO/CdS/CdTe substrates by thermal evaporation of the ZnTe in presence of nitrogen ions (which were produced by a Tectra ion source). A homemade effusion cell was used for evaporation of ZnTe. The most important deposition parameters were:

- ZnTe source temperature (affecting the evaporation rate),
- Substrate temperature, and
- Chamber pressure (i.e. nitrogen flow rate).

The optimum parameters for deposition of ZnTe:N layers on glass substrates were obtained in a previous project in our group [178]. In order to find the optimum substrate temperature on CdTe, the ZnTe:N layers were deposited on CdTe at substrate temperatures from 300 to

425 °C. The ZnTe source temperature and the chamber pressure were 600 °C and 5×10^{-5} mbar, respectively.

After deposition of the layers, their sheet resistances were measured by four-point probe technique. The results are given in Table 7-2. As this table shows, sample C that was prepared at 350 °C had the lowest sheet resistance.

Table 7-2: R_s of the ZnTe:N layers deposited onto CdTe at different substrate temperatures.

sample	T_{sub}(°C)	R_s (kΩ/□)
A	300	6.5
B	325	3.6
C	**350**	**1.9**
D	375	2.3
E	400	2.4
F	425	9

CdTe solar cells with ZnTe/ZnTe:N interlayers were prepared with the optimum film thicknesses obtained by B. Späth [178]. Using those results, a ZnTe layer (with a thickness of ~25 nm) was first deposited onto the in-situ-activated samples at 400 °C. Then, ZnTe:N layer (~200 nm) was deposited on the ZnTe layer at 350 °C. The back contact was completed by deposition of a Mo layer (with a thickness of ~150 nm) by DC sputtering.

After depositing the Mo layer, the sample was taken out of the chamber. Then, the Au front contact to the TCO was deposited and the sample structuring was performed (as is explained in section 4.6). A solar cell that was received a similar heat treatment, but without deposition of the ZnTe/ZnTe:N layer, was prepared for comparison. Another solar cell with wet back contact (NP-etching followed by Mo metallization) was also prepared to be used as a reference. All the samples were made with similar CdS and CdTe deposition and $CdCl_2$ activation parameters.

J-V characteristics of the completed solar cells were measured under AM 1.5 illumination. Performance parameters of the cells are given in Table 7-3 and the J-V curves are compared in Fig. 7-1.

The sample with ZnTe/ZnTe:N interlayer had a much better performance, as compared with the sample without BC-interlayer, but it had slightly lower performance as compared with the NP-etched sample. The ZnTe/ZnTe:N interlayer provided a contact with lowest series resistance (R_s = 4.8 Ω.cm^2) and highest FF, however, the V_{oc} and J_{sc} of this sample were smaller than the NP-etched sample, which led to a lower performance. The reason for

the low performance could be due to the CdTe/ZnTe interface, that will be discussed in the next section.

Table 7-3: Performance parameters of solar cells with ZnTe/ZnTe:N and without BC interlayer. As a reference, parameters of a NP-etched sample are also given.

Contact	V_{oc} (mV)	J_{sc} (mA/cm^2)	FF (%)	η (%)	R_s (Ω.cm^2)
ZnTe/ZnTe:N/Mo	717	20.3	67	9.8	4.8
Mo	670	19.5	25	3.3	140
NP-etched/Mo	750	21.5	64	10.3	10.4

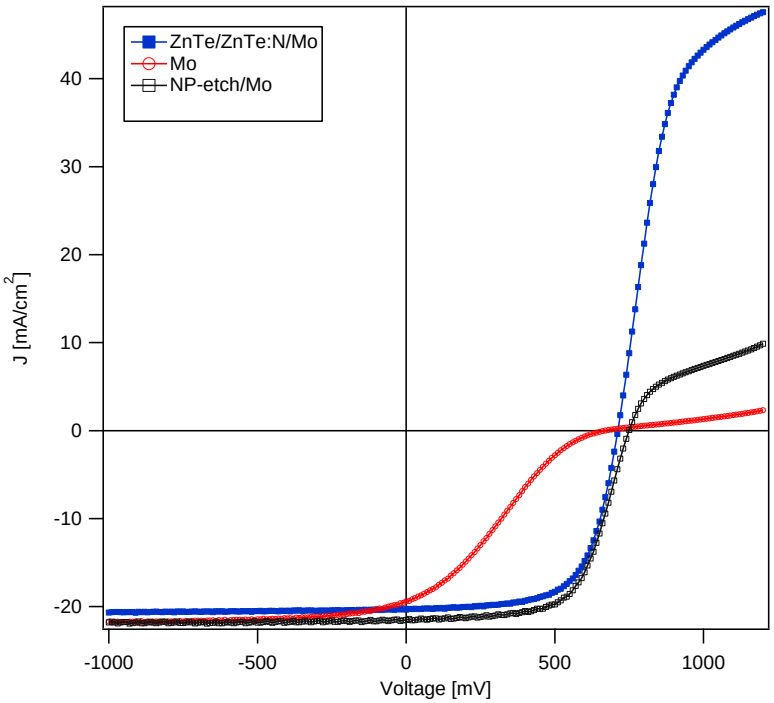

Fig. 7-1: J-V curves of solar cells with and without ZnTe/ZnTe:N BC-interlayer.

7.1.3 CdTe/ZnTe interface modification

In order to modify the CdTe/ZnTe interface, a post-deposition heat-treatment was necessary. If the heat-treatment was performed after the activation, the annealing temperature needed to be high (>400°C) to reach an effective inter-diffusion. At such high temperatures, it was found that the p-type ZnTe layers were not stable. Therefore, the idea was to activate the samples after the deposition of a thin ZnTe layer on the CdTe layer. For this purpose, a ZnTe layer (~50 nm) was deposited onto a non-activated glass/TCO/CdS/CdTe substrate, and then the activation was performed using the in-situ

activation setup. After the $CdCl_2$ activation, a 200nm thick ZnTe:N layer was deposited. Finally, a Mo layer was sputtered onto the ZnTe:N layer to complete the back contact. Solar cells prepared with this method had very weak performances (efficiencies less than 5%, see cell A in Fig. 7-2).

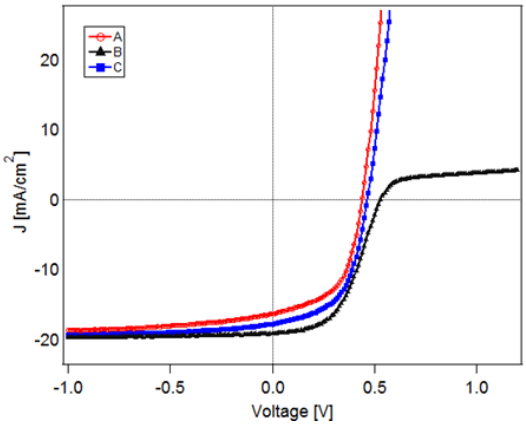

Fig. 7-2: J-V characteristics of solar cells with modified CdTe/ZnTe interface.

The following treatments were performed in order to improve the cell performance:

- Deposition of ZnTe onto pre-activated samples, followed by second activation and ZnTe:N/Mo deposition (cell B in Fig. 7-2),
- Deposition of a thin CdTe layer (~100nm) onto the pre-activated samples (at about 250 °C), followed by ZnTe deposition, second activation, and ZnTe:N/Mo deposition (cell C in Fig. 7-2).

None of the above treatments produced better performances compared to the primary cell with ZnTe/ZnTe:N BC-interlayer, as can be seen in the J-V curves in Fig. 7-2. The reason for the poor performance (i.e., very low V_{oc}) could be because of the following:

- The activation process was not efficient, which might be because of the production of $ZnCl_2$ that may affect the activation parameters (based on the XPS measurements that will be discussed in the following section),
- The ZnTe:N layer was deposited with the parameters that were optimized for glass substrates. It has been reported that the ZnTe:N layers which had been deposited onto activated CdTe surface had 200 times higher resistivity compare with the layers deposited onto glass or non-activated CdTe [179].

XPS study of the effects of activation on CdTe/ZnTe interface

In order to find the reason for the poor performance of the cells with modified CdTe:ZnTe interface, effects of the in-situ $CdCl_2$ activation on ZnTe and the CdTe/ZnTe interfaces were studied by XPS technique.

XP survey spectra of glass/TCO/CdS/CdTe/ZnTe sample before and after the activation are shown in Fig. 7-3. Before $CdCl_2$ activation, a pure ZnTe signal was observed which was Te-rich (Te to Zn atomic ratio was 1.25), and the Fermi-level of the ZnTe was at 0.83 eV above the valence band maximum (VBM).

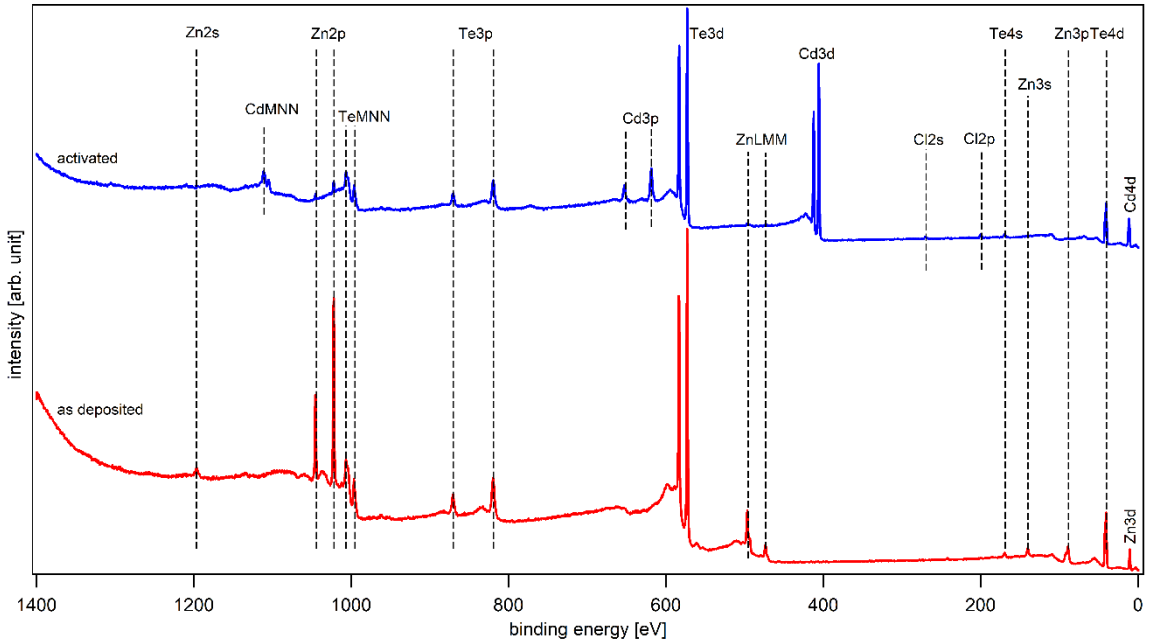

Fig. 7-3: XP survey spectra of the glass/TCO/CdS/CdTe/ZnTe sample, before and after the activation step.

After the activation, the Zn content reduced significantly, and the Cd and Cl emissions were also observed. The Cl emission was due to the deposition of a thin $CdCl_2$ on the surface during cooling down of the $CdCl_2$ source (the sample was not heated afterwards to re-evaporate the remaining $CdCl_2$). There were two Cd emissions (Cd $3d_{5/2}$ at 405.5 and 406.6 eV) which were related to $CdCl_2$ and CdTe, respectively (see Cd $3d_{5/2}$ spectra in Fig. 7-5).

XPS depth profiling was performed on the sample before and after the activation. Fig. 7-4 shows XP core-level spectra of Zn $2p_{3/2}$, Te $3d_{5/2}$ and Cd $3d_{5/2}$ of the non-activated sample during depth-sputtering across the CdTe/ZnTe interface. As expected, with increasing the sputtering time, a gradual decrease in the intensity of Zn $2p_{3/2}$ and increase in Cd $3d_{5/2}$

intensity was observed. By increasing the sputtering time, a slight shift of the Zn $2p_{3/2}$ core levels to lower binding energies was observed, while there was no detectible shift in the Cd $3d_{5/2}$ core levels. The Te $3d_{5/2}$ core levels were also gradually shifted from 572.96 eV in ZnTe to 572.64 eV in CdTe. These results are in contrast with the former measurement on stepwise deposited ZnTe onto CdTe substrate which showed a slight band bending in CdTe and very little chemical shift in Zn and Te core levels [180]. At the CdTe/ZnTe interface, the ZnTe valence-band maximum was above the CdTe valence band with an offset of about 0.16 eV.

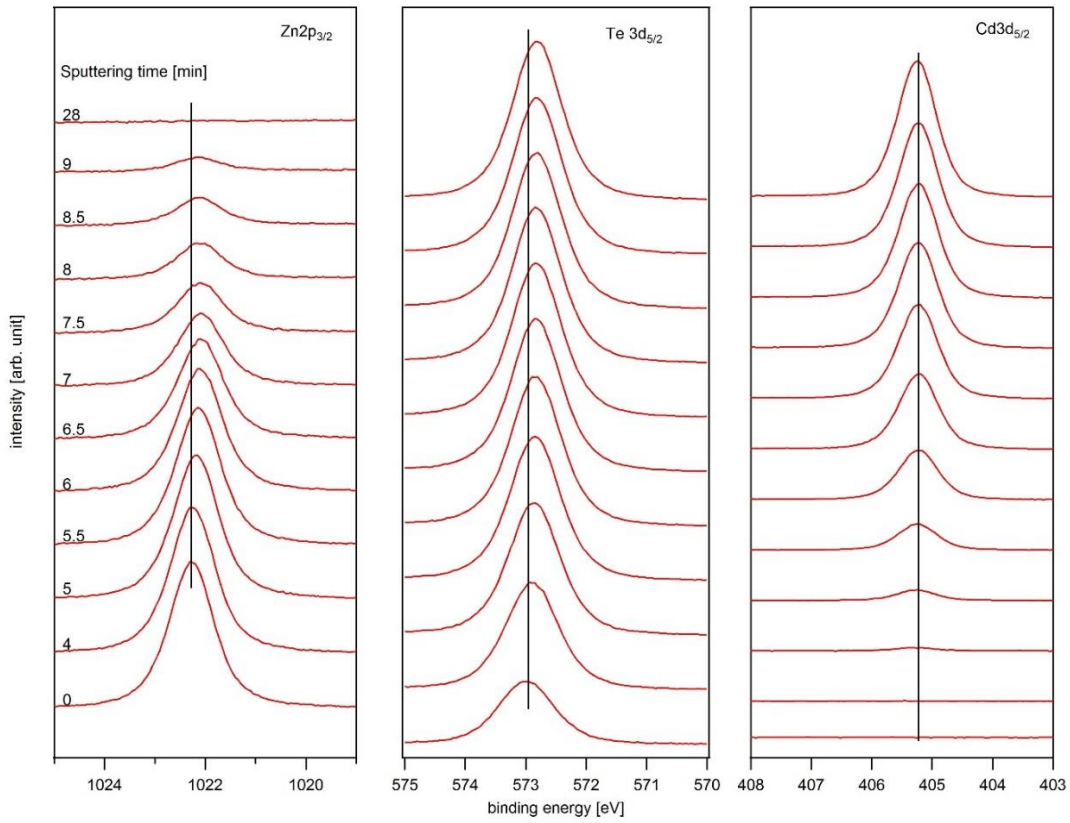

Fig. 7-4: XP core-level spectra of Zn $2p_{3/2}$, Te $3d_{5/2}$ and Cd $3d_{5/2}$ of the non-activated sample during depth sputtering across the CdTe/ZnTe interface.

XP core level spectra of Zn $2p_{3/2}$, Te $3d_{5/2}$ and Cd $3d_{5/2}$ of the activated sample during depth sputtering across the CdTe/ZnTe interface are shown in Fig. 7-5. The Zn content is very low on the surface and also through the whole ZnTe layer. This might be due to a chemical reaction between ZnTe and $CdCl_2$ which may lead to production of $ZnCl_2$. At the activation temperature of 380°C, the $ZnCl_2$ may evaporate from the surface and results in reduction of the Zn content. Therefore, a possible way to avoid the Zn deficiency might be activation

of the samples in presence of $ZnCl_2$ (instead of $CdCl_2$ activation) to modify the CdTe/ZnTe interface.

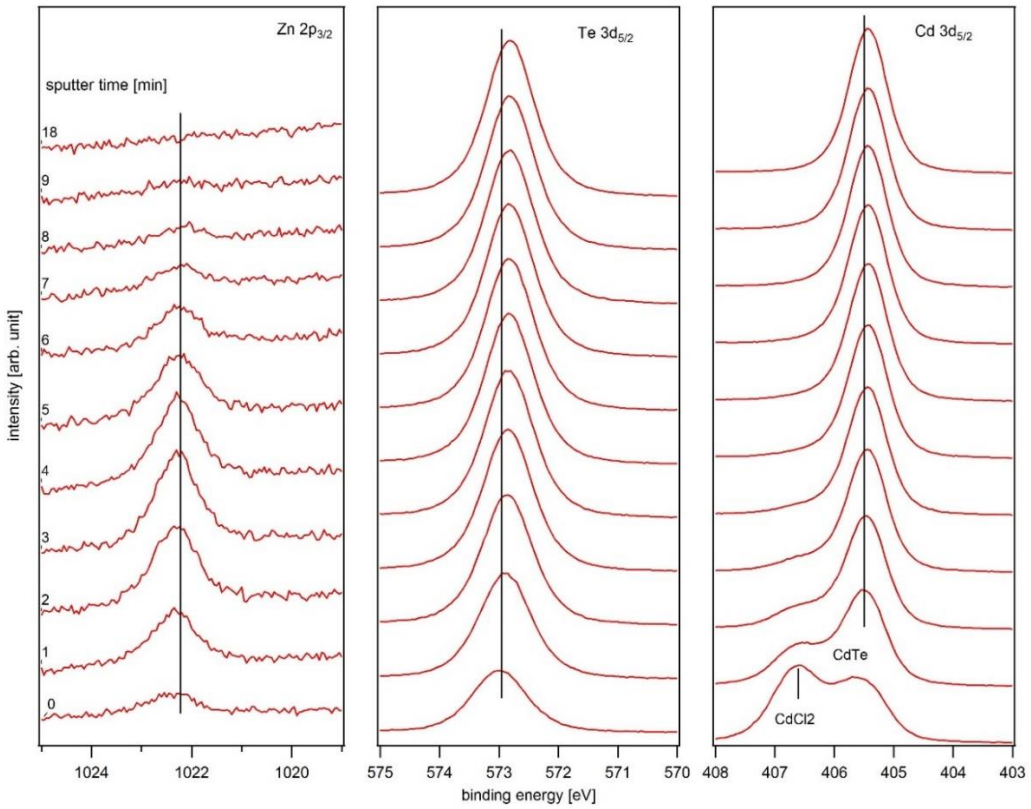

Fig. 7-5: XP core level spectra of Zn $2p_{3/2}$, Te $3d_{5/2}$ and Cd $3d_{5/2}$ of the activated sample, during depth sputtering across the CdTe/ZnTe interface.

7.2 Sb-doped ZnTe

Solar cells made by ZnTe:N as the BC-interlayer did not provide better performances, as compared with our standard NP-etched samples. Post-deposition annealing, which was performed to modify the CdTe/ZnTe interface, also did not improve performance of the cells. One reason for the low performance could be formation of defects at the CdTe/ZnTe interface induced by the plasma deposition of the ZnTe:N layer. Therefore, Sb was chosen to be used as an alternative dopant for deposition of p-type ZnTe layers by PVD method. An efficient procedure for producing highly p-type Sb-doped ZnTe layers (ZnTe:Sb) on glass substrates was developed [7], which will presented in the next section (including electrical and morphology characterization of the layers).

In another project we used the PVD deposited ZnTe layers to study the interface between BaCuSeF and ZnTe by photoelectron spectroscopy [167, 168]. The results of this work

showed that the BaCuSeF layers can be used to extract the holes from ZnTe (or CdTe), since the measured valence-band offset was negligible.

7.2.1 ZnTe:Sb on glass substrate

In this work, different methods have been tried, which were as following:

The first method was co-evaporation of ZnTe and Sb onto glass substrates at room temperature (RT) and higher substrate temperature followed by a post annealing step. The ZnTe source temperature (T_{ZnTe}) was 610 °C and the Sb source temperature (T_{Sb}) was varied from 380 to 470 °C. ZnTe deposition rate was ~ 7 nm/min and Sb deposition rate varied from less than 0.1 to ~1.5 nm/min, when the substrate temperature (T_{Sub}) was at RT. The substrate temperature during deposition was varied from RT to 300 °C. Deposition time for all samples was one hour. After deposition, the samples were annealed in vacuum and Ar atmosphere (at a pressure of 0.05 mbar) for one hour. The annealing temperature (T_A) was varied from 200 to 340 °C.

The second method was deposition of a thin Sb film between two ZnTe layers (sandwich structure) and post annealing of the samples. This method consisted of four steps. In the first step a 180 nm thick ZnTe film was deposited onto glass substrates at T_{Sub}= 420 °C. The second step was deposition of a thin Sb film (6-18 nm) at room temperature onto the ZnTe film. The third step was deposition of another 180 nm thick ZnTe film over the Sb layer at T_{Sub}= 240 °C. In the fourth step, the samples were annealed in Ar atmosphere (with pressure of 0.05 mbar). T_A was optimized to 320 °C and the annealing time was one hour.

Electrical measurements indicated that the co-evaporation method (at different substrate temperatures followed by a post annealing step) was not a suitable method for preparing highly Sb doped ZnTe films. The lowest sheet resistance (R_s) and resistivity (ρ) obtained with this method were 13.3 kΩ/□ and 0.5 Ω.cm, respectively. For this sample, evaporation rate ratio of Sb to ZnTe was ~5.5 % and T_{Sub} was 200 °C. After deposition, the sample was annealed in Ar atmosphere at T_A = 300 °C. For other samples prepared by the co-evaporation method with different evaporation rates and substrate temperatures, the samples were less conductive and it was not possible to measure their resistivity with our FPP setup.

Through a series of deposition experiments at various substrate and source temperatures, it was found that for deposition of a polycrystalline ZnTe film with large grain size (>200

nm) and without pinholes onto glass substrates, the substrate temperature and the deposition rate should be 420 °C and 6 -20 nm/min, respectively. On the other hand, it was possible to deposit ZnTe films with almost the same grain size at T_{Sub}=200-300 °C onto glass substrates covered with a ZnTe layer deposited at high substrate temperature (HST) of 420 °C (this will be explained with the AFM measurements). When we used a substrate temperature of 420 °C during co-evaporation, the XPS analysis showed that there was no Sb emission in the spectrum even when the Sb:ZnTe ratio of evaporation rates was 20%. This can be explained by the fact that at this temperature, the sticking coefficient of Sb atoms is very low and they re-evaporate from the surface due to high vapor pressure of Sb and UHV environment. By increasing the Sb evaporation rate, Sb atoms may only disturb the growth of the ZnTe film without any contribution in the film. Therefore, in order to have ZnTe:Sb films with large grain size and high concentration of Sb, the 4-step method was developed. It should be noted that deposition of the second ZnTe layer was done at low substrate temperature (LST) of 240 °C to avoid evaporation of Sb film from the surface of the first ZnTe layer.

Four-point probe measurement

Variation of R_s and ρ for samples prepared by the 4-step method as a function of Sb:ZnTe thickness ratio are shown in Table 7-4 and Fig. 7-6. The best result of the co-deposition method is also added to the table for comparison. The lowest R_s and ρ obtained with the 4-step method were 860 Ω/□ and 0.032 Ω.cm respectively, for a sample with Sb:ZnTe thickness ratio of 3.3%.

Hall effect measurement

Hall effect measurements at room temperature were performed to determine free hole concentration (p) and hole mobility (μ_p) of the Sb-doped films. The results are shown in Table 7-5 and Fig. 7-7. The highest carrier concentration measured was 3×10^{19} cm^{-3} for a sample which was prepared by the 4-step method with Sb:ZnTe thickness ratio of 3.3%. The hole mobility of this sample was 6.5 $cm^2/V.s$. The hole concentration was nearly constant at (2-3) $\times 10^{19}$ cm^{-3}, for Sb:ZnTe thickness ratio of larger than 3.3 %.

Table 7-4: Sheet resistance and resistivity of ZnTe:Sb films prepared by different methods.

Method	Sb:ZnTe Ratio (%)	Sheet Resistance (Ω/□)	Resistivity (Ω.cm)
co-evaporation	5.5	13300	0.5
4-step	1.7	2459	0.09
	2.5	1355	0.05
	3.3	860	0.032
	4.2	880	0.033
	5	930	0.034

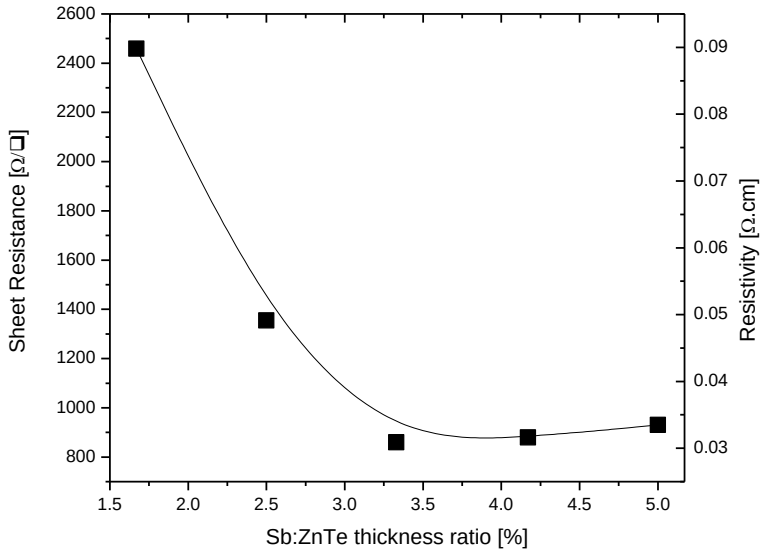

Fig. 7-6: Variation of R_S and ρ of ZnTe:Sb films versus Sb:ZnTe thickness ratio.

Table 7-5: Hole concentration and mobility of ZnTe:Sb films prepared by different methods.

Method	Sb:ZnTe ratio (%)	Hole concentration (cm^{-3})	Hole mobility ($cm^2/V.s$)
co-evaporation	5.5	7.8×10^{17}	15.6
4-step	1.7	8.4×10^{17}	69.4
	2.5	5×10^{18}	24.9
	3.3	3.1×10^{19}	6.5
	4.2	2.5×10^{19}	5.8
	5	3×10^{19}	5.3

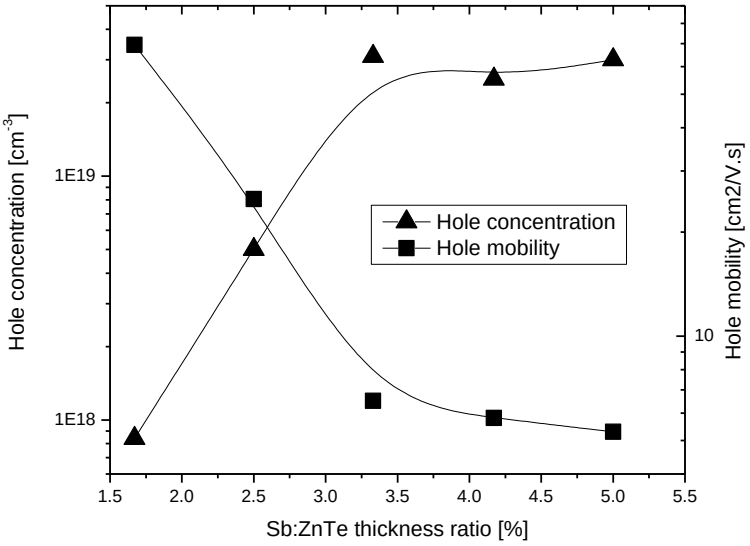

Fig. 7-7: Dependence of the hole concentration and mobility of 4-step ZnTe:Sb films on Sb:ZnTe thickness ratio.

AFM and SEM measurements

The AFM images of the ZnTe and ZnTe:Sb films are shown in Fig. 7-8. The film thickness, RMS roughness (R_q), and the average grain size (d_g) of the films are given in Table 7-6. From Fig. 7-8(a) and Fig. 7-8(b), it can be seen that the HST ZnTe layer has significant bigger grains as compared with the LST ZnTe layer, when both were deposited on glass substrates. However, the morphology of an LST ZnTe layer deposited on an HST ZnTe is almost similar to the HST ZnTe layer and it seems to be more compact, as shown in Fig. 7-8(c).

The AFM images of a 4-step ZnTe:Sb film with thickness of 360 nm is shown in Fig. 7-8(d). SEM micrographs of surface and cross-section of a 4-step ZnTe:Sb layer are shown in Fig. 7-9. For making ZnTe:Sb films, we need to put a thin Sb layer between the HST and LST ZnTe layers. This Sb film might change the morphology of the LST ZnTe film; however, for a thin Sb film (less than 20 nm), the AFM and SEM measurements showed that it did not affect the morphology.

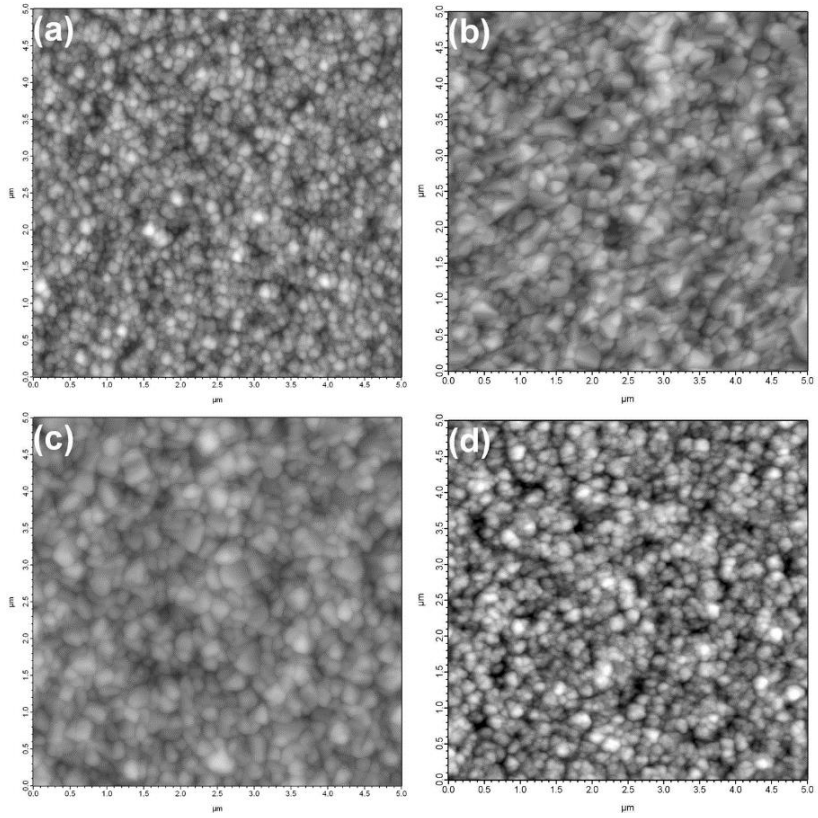

Fig. 7-8: AFM images (5×5 μm^2) of ZnTe and ZnTe:Sb films. (a) 1000 nm LST ZnTe onto glass, (b) 1000 nm HST ZnTe onto glass, (c) 500 nm LST ZnTe onto 500 nm HST ZnTe, and (d) 360 nm ZnTe:Sb prepared by 4-step method.

Table 7-6: The RMS roughness, and the average grain size of ZnTe and ZnTe:Sb films

Sample	Thickness [nm]	RMS roughness (R_q) [nm]	Average grain size (dg) [nm]
LST ZnTe	1000	13	160
HST ZnTe	1000	28	250
LST ZnTe on HST ZnTe	1000	19	250
4-step ZnTe:Sb	360	5	180

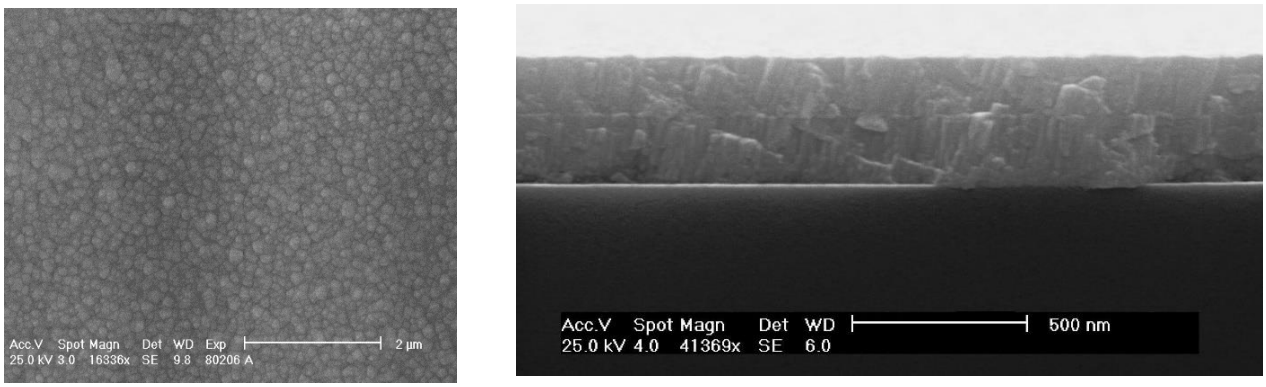

Fig. 7-9: SEM images of the surface and cross-section of a 4-step ZnTe:Sb layer.

XRD measurement

The XRD patterns of HST ZnTe and ZnTe:Sb films with Sb:ZnTe thickness ratio of 3.3 % are shown in Fig. 7-10. As is indicated, all the peaks belong to cubic ZnTe with a preferred orientation along the (111) plane. Other planes such as (200), (220), (311) and (400) were also observed. No major Sb or other compound diffraction line was observed in doped films.

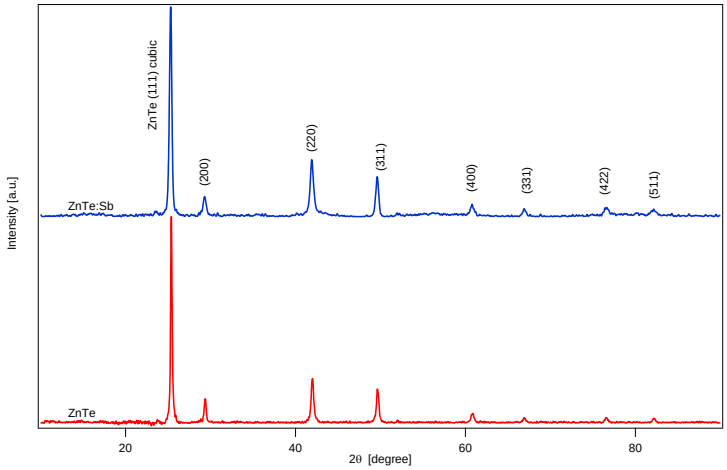

Fig. 7-10: XRD pattern of HST ZnTe and 4-step ZnTe:Sb films.

The XRD pattern of ZnTe and ZnTe:Sb films were very similar; and there was only a minor difference between the intensity of the peaks. The observed relative intensities are compared with the JCPDS values (65-385). The lattice constant (a) of the films were determined by using Bragg's formula for the cubic systems. The lattice constant was found to be 6.09 Å that is in good agreement with the value reported in literatures [181, 182]. There is no detectable difference between lattice constants of ZnTe and ZnTe:Sb films.

7.2.2 ZnTe:Sb on CdTe

A similar procedure (with some modifications) was used to deposit the ZnTe:Sb layers onto the in-situ-activated glass/TCO/CdS/CdTe substrates. XPS analysis was performed on the sample after each step. The XP survey spectra in Fig. 7-11 does not show any Sb emission before the annealing step. After the annealing step, a small Sb emission was observed on the surface (see inset in Fig. 7-11 which is the high-resolution Sb signal with 100x magnification). After two-minute sputtering by 1 kV Ar ions, there was no detectible Sb on the sample surface. XPS depth profiling does not show any Sb signal in the ZnTe:Sb layer and at the ZnTe:CdTe interface.

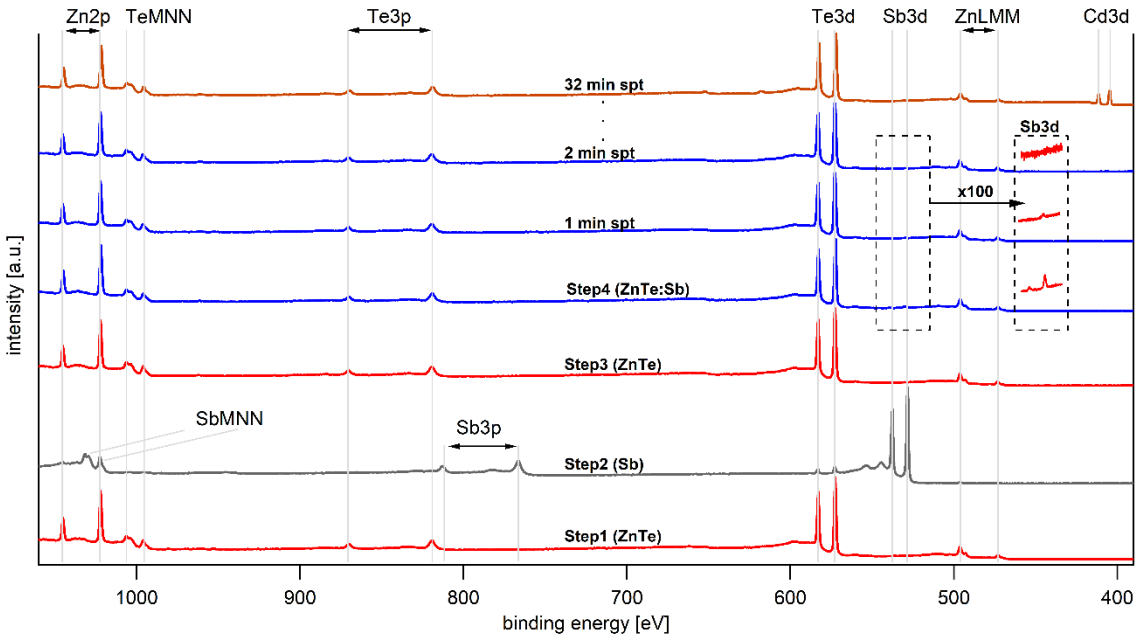

Fig. 7-11: XP survey spectra of ZnTe and ZnTe:Sb prepared by the 4-step method.

7.2.3 ZnTe:Sb/Mo back contact

The procedure for preparing solar cells with ZnTe:Sb/Mo back contacts are summarized as follows:

- Deposition of an HST-ZnTe layer with a thickness of about 150 nm onto the CdTe surface at T_{Sub}= 420 °C;
- Deposition of a thin Sb film (with a thickness of about 15 nm) onto the HST-ZnTe at room substrate temperature;
- Deposition of an LST-ZnTe layer (150 nm thick) over the Sb layer at T_{Sub}= 240 °C.
- Deposition of a molybdenum layer over the LST-ZnTe at room substrate temperature by DC sputtering.
- After the Mo deposition, the samples were taken out of the back-contact chamber and the gold front contacts deposition and sample structuring was performed, as is explained in section 4.6.

J-V characteristics of the completed solar cells were measured under AM 1.5 illumination after different annealing times. The annealing was performed at 320°C in Argon atmosphere from 20 to 80 minutes. Values of V_{oc}, J_{sc}, η and FF of the samples as function of the annealing times are shown in Fig. 7-12. Cells that were annealed for 60 minutes

showed the best results; but still no gain in the solar cells performances was achieved (as compared with our standard wet process.

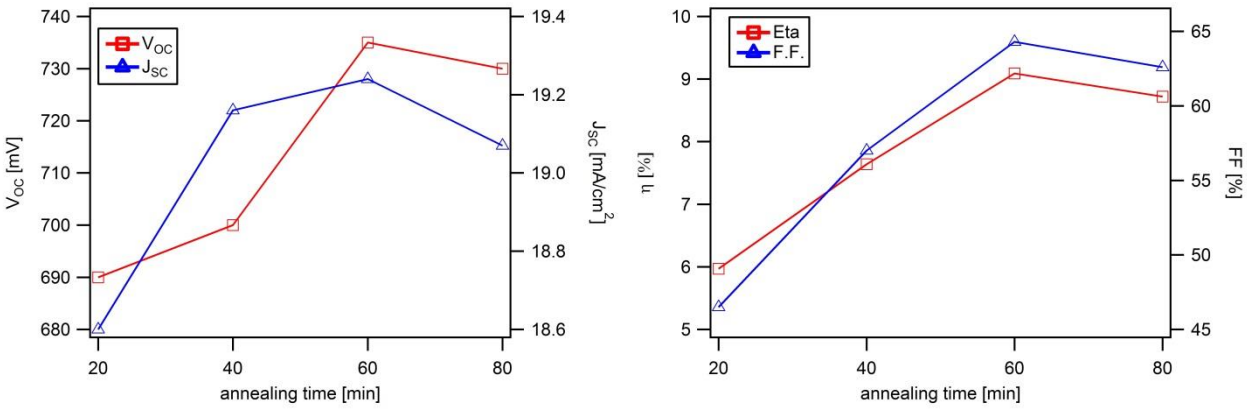

Fig. 7-12: Performance of the solar cells with ZnTe:Sb back contact interlayers.

7.3 Copper-doped ZnTe

The aim of this work was to investigate copper-free back contacts; but for comparison purposes, a few solar cells with copper-doped ZnTe (ZnTe:Cu) back contacts were also prepared.

The ZnTe:Cu layers were deposited onto the activated samples with a similar method which was used for deposition of the ZnTe:Sb layers.

In the first attempt, after the deposition of the HST-ZnTe layer (150 nm) and the copper film (15 nm), an LST-ZnTe layer (with thickness of 150 nm) was deposited at 250 °C, followed by a Mo-deposition at room temperature. Solar cells prepared with these parameters did not show acceptable performances, even before the post-deposition heat treatment. This might have been due to the diffusion of copper to the front contact during the LST-ZnTe deposition.

In order to have a better control on the copper diffusion, the LST-ZnTe layer was deposited at room temperature (RT). Since the RT-ZnTe had a poor conductivity (was not possible to be measured by four-point probe), its thickness was reduced to 50 nm (to avoid a high series-resistance). J-V characteristics of this sample was measured before and after the annealing process at 320 °C in Ar-atmosphere for 20 to 60 minutes.

Fig. 7-13 shows values of V_{oc}, J_{sc}, η, and FF of the sample, as a function of the annealing time. The optimum annealing time was found to be 20 min.

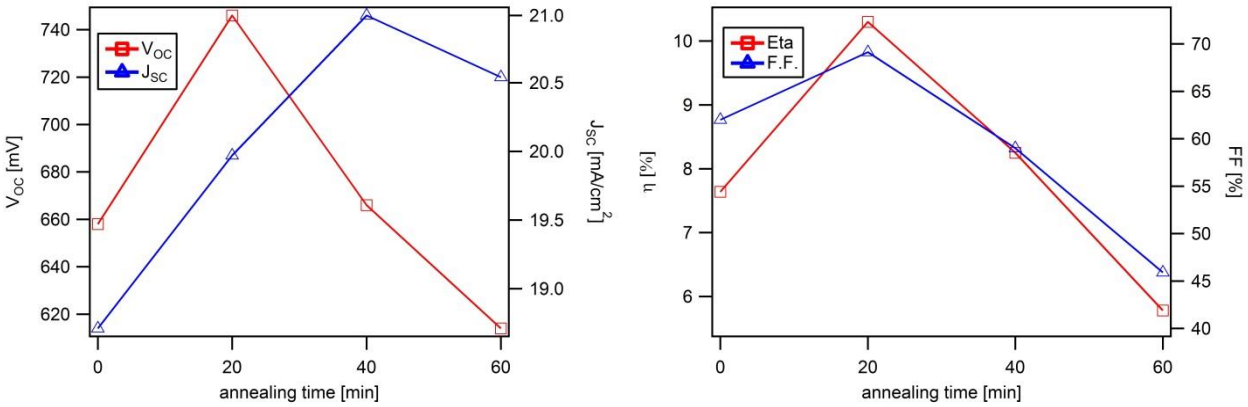

Fig. 7-13: Performance of the solar cells with ZnTe:Cu back contact interlayers.

J-V characteristics of the best cells with ZnTe:Sb/Mo and ZnTe:Cu/Mo back contacts together with a standard sample (with NP-etching/Au back contact) are compared in Table 7-7 and Fig. 7-14.

Table 7-7: Typical parameters of solar cells with different ZnTe interlayers in the back- contact. For comparison, a solar cell with NP-etched/Au is added.

Back contact	V_{oc} (mV)	J_{sc} (mA/cm^2)	FF (%)	Efficiency (%)	R_s (Ω.cm^2)
NP-etched/Au	720	22	66.5	10.5	9
ZnTe:Sb/Mo	735	19.2	64.3	9.1	7.9
ZnTe:Cu/Mo	741	20.4	68.1	10.3	6.3

Solar cells with ZnTe:Cu back contacts showed the highest fill factor of 68.1%, highest open-circuit voltage of 741 mV, and lowest series-resistance of about 4 Ω.cm^2, and almost no roll-over at high bias voltages, as can be seen in Fig. 7-14. However, the short-circuit current of these cells were lower than the standard cells with NP-etched/Au back contacts. Since the aim of this project was to investigate the copper-free contacts, the ZnTe:Cu back contact was not optimized in this work. However, in another project with copper-doped back contact we have developed a method for producing solar cells with very thin CdTe absorber layer thickness (1.5 – 3 μm) and efficiencies as high as 12.5 % without any chemical or physical etching [106].

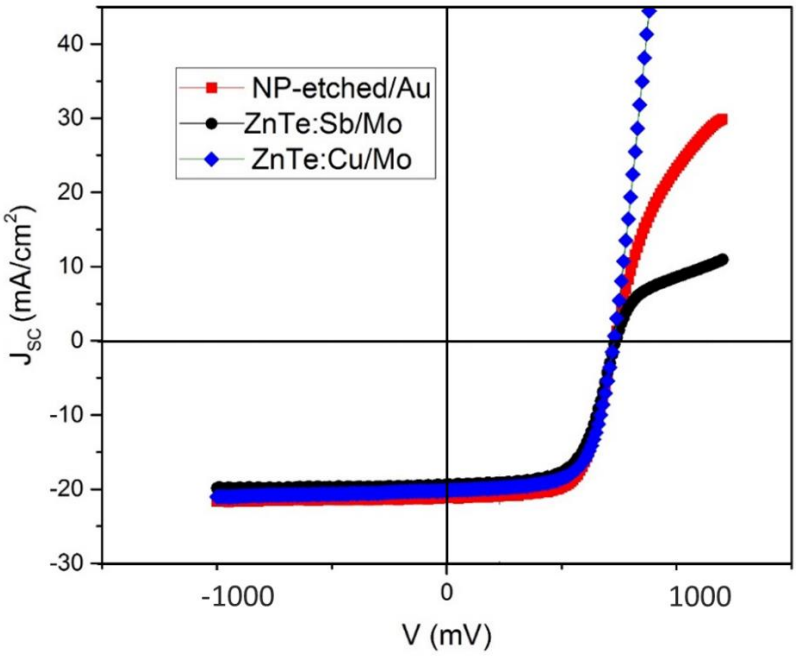

Fig. 7-14: J-V characteristics of solar cells with ZnTe:Sb/Mo and ZnTe:Cu/Mo back contact. J-V of a standard cell is also shown, as a reference.

Solar cells with ZnTe:Sb/Mo back contacts did not show promising results; although a lot of effort was done for optimization of this contact. In another experiment, the benefit of Sb-doping was used to improve the efficiency of CdTe solar cells, which is explained in the next section.

7.4 Sb doping of CdTe surface

In order to investigate the effect of Sb doping of CdTe on the solar cell performance, four identical pre-activated samples (glass/TCO/CdS/CdTe without back contact) were used. Sample A was completed by a standard etching process (25 seconds NP etching) followed by a gold sputtered back contact.
Sample B was treated by the following procedure:

- Rinsing with deionized water and drying.
- Deposition of a thin Sb film (~2 nm) by thermal evaporation onto CdTe at room temperature.

- Annealing in Ar atmosphere (P_{Ar}= 5×10^{-2} mbar, annealing temperature=380 °C, annealing time=60 min).
- Re-activation (ex-situ activation, wet $CdCl_2$ deposition and air annealing at 400 °C for 20 minutes).
- NP-etching.
- Rinsing with deionized water and drying.
- Deposition of the back contact (~100 nm sputtered Au).

Sample C was treated like sample B, but without the deposition of Sb on the CdTe surface. Sample D was re-activated by wet $CdCl_2$ process and completed by washing, NP-etching and a gold sputtering back contact. Samples C and D were prepared to realize the individual effect of $CdCl_2$ activation and annealing in order to find out the effect of the Sb doping process. J-V characteristics of these samples are compared in Table 7-8 and Fig. 7-15.

Table 7-8: J-V characteristics of a non-treated, a Sb-doped, and two reference samples.

Sample	Treatment	V_{oc} (mV)	J_{sc} (mA/cm^2)	FF (%)	Efficiency (%)	R_s (Ω.cm^2)
A	-	660	22.7	57.4	8.7	6.8
B	Sb doped	770	23	65.8	11.7	6.6
C	annealed and re-activated	730	21.7	62	9.3	9.7
D	re-activated	730	21	59.6	9.1	11.8

Sample A has rather low open circuit voltage. The re-activated sample has higher V_{oc}, FF and efficiency but slightly smaller J_{sc}, as compared with the pre-activated sample. By comparing the J-V characteristics of these samples, it can be concluded that the improvement in performance of the cells is related to both the activation and Sb doping treatments.

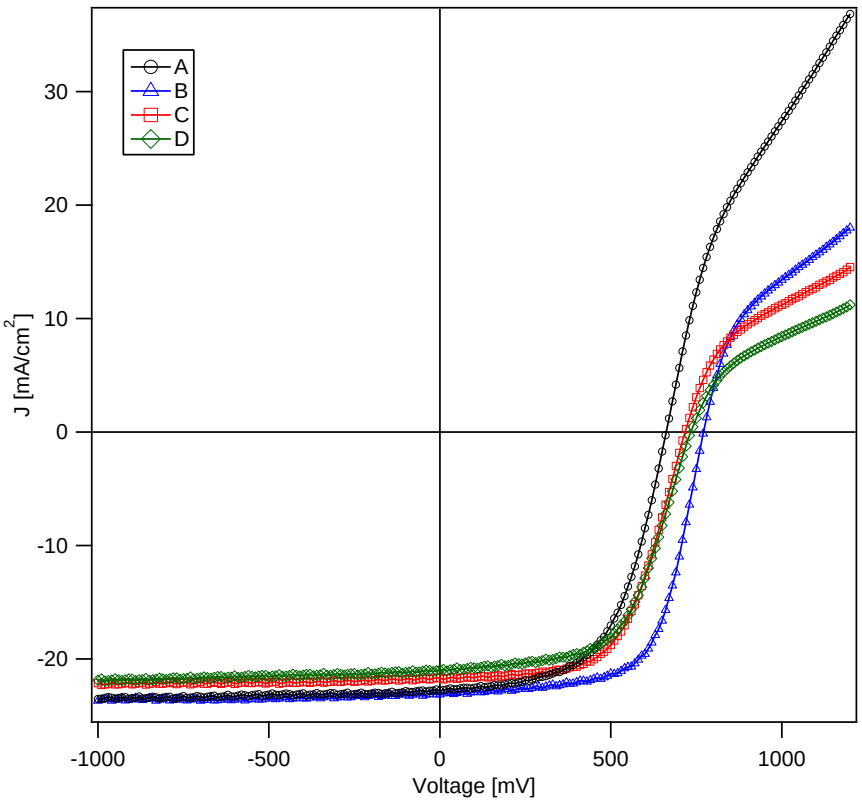

Fig. 7-15: J-V curves of the Sb doped solar cell (sample B) and the control samples as listed it Table 7-8.

In order to optimize the Sb thickness, another four samples with Sb thicknesses of 4, 6, 10 and 20 nm were prepared. J-V curves of these samples and the sample with Sb thickness of 2 nm are compared in Table 7-9 and Fig. 7-16. From the results of this experiment, the optimum Sb thickness was found to be 4 nm.

Table 7-9: Effect of the Sb thickness on performance of solar cells with Sb doped back contact.

Sample	Sb thickness (nm)	V_{oc} (mV)	J_{sc} (mA/cm^2)	FF (%)	Efficiency (%)	R_s (Ω.cm^2)
B	2	770	23	65.8	11.7	6.6
E	4	770	24	69.3	12.8	4.2
F	6	740	24.5	67.6	12.2	4.8
G	10	730	24	57.1	10	11.1
H	20	700	23.5	54.2	8.9	7.7

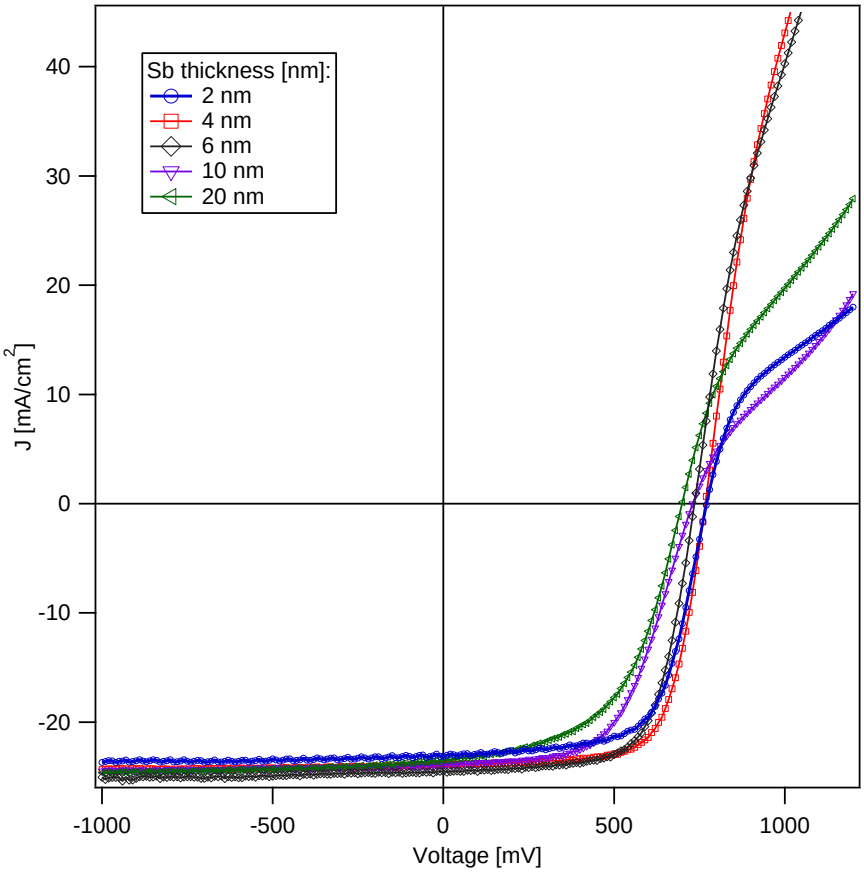

Fig. 7-16: Effect of the Sb thickness on the J-V curve of solar cells with Sb doped back contact.

The best solar cell (sample E) has efficiency of 12.8 % and fill factor as high as 69.3 % with V_{oc} and J_{sc} of 770 mV and 24 mA/cm^2, respectively. The series resistance of this sample was only 4.2 Ω.cm^2, which is as low as the R_s of solar cells with Cu/Au back contact. The Sb-doped sample had the record efficiency in our group at the time when this experiment was completed. No stress test was performed on these samples, but our measurements showed that they were stable after about one-year storage in the lab. Since no copper was used in fabrication of these cells, we expect them to be stable. An innovative procedure based on Sb doping of CdTe was developed in our group, which we have filed a patent on this procedure [183].

7.4.1 XPS measurements of Sb-doped CdTe

Effect of Sb doping on CdTe was investigated using photoelectron spectroscopy. XP survey spectra of an in-situ activated glass/TCO/CdS/CdTe sample before and after deposition of

the Sb layer and after annealing are illustrated in Fig. 7-17 and all the signals were identified as shown in the figure.

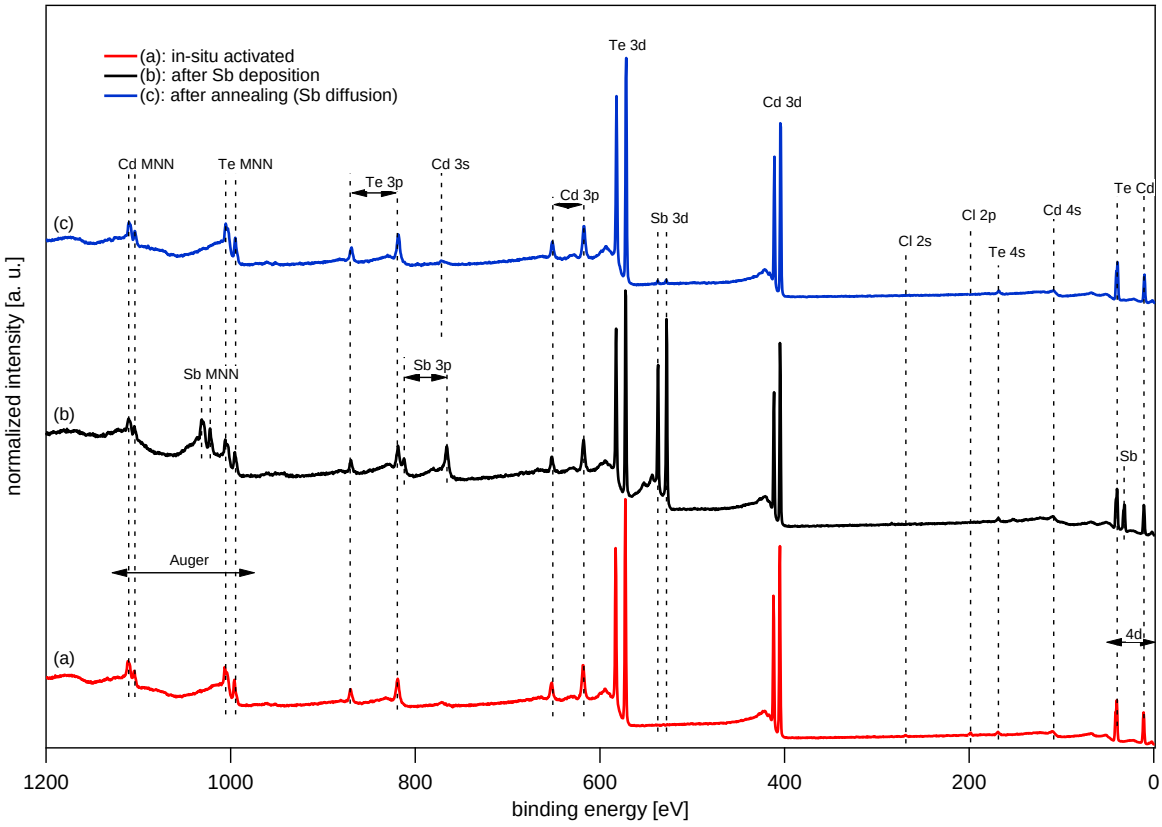

Fig. 7-17: XP survey spectra of a $CdCl_2$ activated sample before and after the Sb doping.

Since the sample was prepared in-situ and it was measured immediately after preparation, only signals corresponding to Cd, Te and Cl were detected on this sample, as shown in Fig. 7-17(a). After deposition of a thin Sb layer (~5 nm) on the CdTe surface, beside the Sb signals, Cd and Te signals were still visible in the spectrum as can be seen in Fig. 7-17(b). After the annealing, the intensities related to Sb were significantly decreased as can be seen in Fig. 7-17(c). Since the annealing was performed at 380 °C in an Ar atmosphere with pressure of 0.05 mbar, the reduction in the Sb would be related to the diffusion of the Sb atoms to the CdTe layer. The evaporation of Sb atoms from the CdTe surface is negligible since it has a very low vapor pressure under these conditions [184].

High-resolution XP spectra of Cd 3d and Te 3d core levels and XPS valence band spectra of the sample before and after the Sb doping are shown in Fig. 7-18. This measurement showed a parallel shift of spectra to lower binding energies by 0.37 eV after the Sb doping. The binding energy of the valence band maximum (E_{VBM}) with respect to the Fermi level

(E_F – E_{VBM}) was shifted from 1.1 eV to 0.74 eV after the Sb doping. This shows an effective p-type doping of the CdTe surface, although the Fermi level is still located near to the middle of the CdTe band-gap. A similar experiment was performed on a non-activated sample, but since the XPS results were almost similar to the results of the in-situ activated sample, they were not shown here. For the non-activated sample, a parallel shift of binding energies to lover values was measured and E_F – E_{VBM} was shifted from 0.9 eV for the non-doped sample to 0.7 eV after the Sb doping.

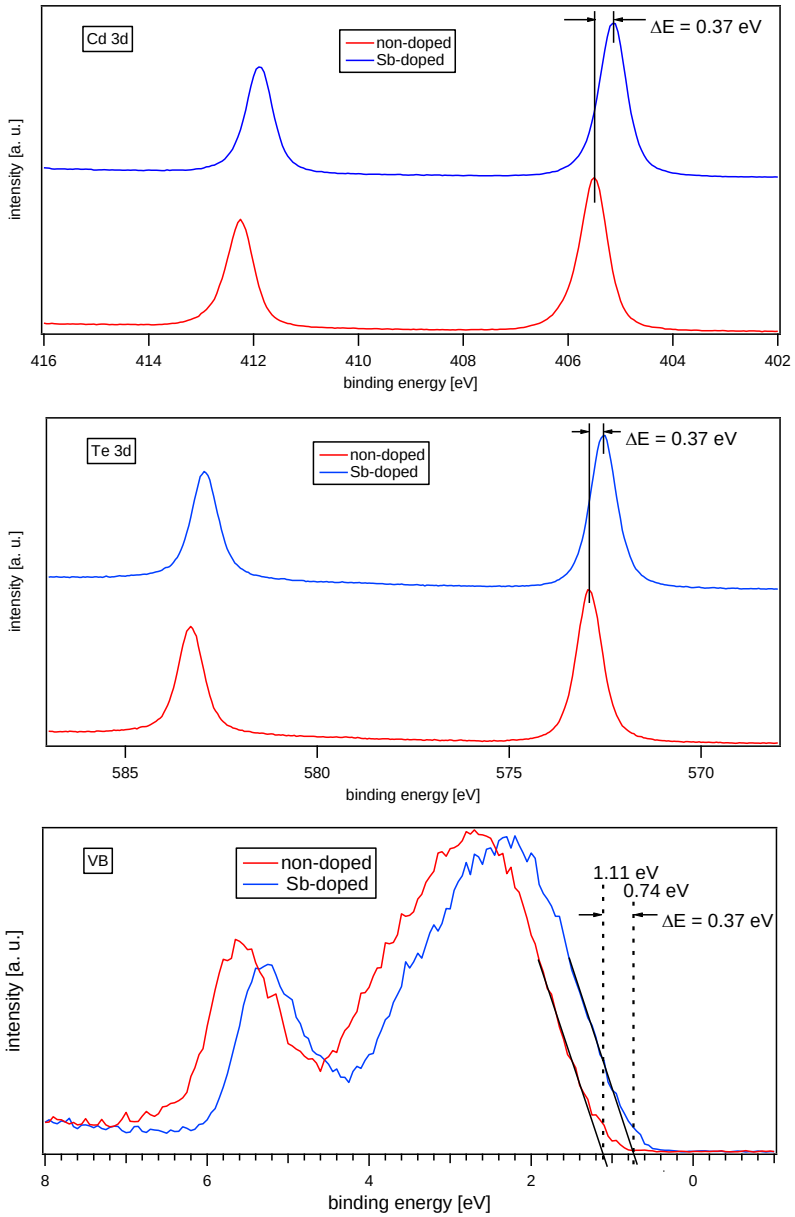

Fig. 7-18: XP core level of Cd 3d, Te 3d and VB spectra of an in-situ activated sample before and after the Sb doping.

7.5 Sb_2Te_3/Mo back contact

A Sb_2Te_3 layer (~100 nm) was deposited by sputtering (at different substrate temperatures, from room temperature up to 350 °C) onto the in-situ-activated samples. The back contact was completed by deposition of a molybdenum layer (~100 nm) onto the Sb_2Te_3 layer (at room substrate temperature).

J-V characteristics of the samples were measured before and after a post deposition annealing treatment. The values of cell efficiency, FF, and V_{oc} of these samples are shown in Fig. 7-19 (before annealing) and Fig. 7-20 (after annealing). The annealing was performed at 300 °C for 30 min in an inert atmosphere (Ar or N_2).

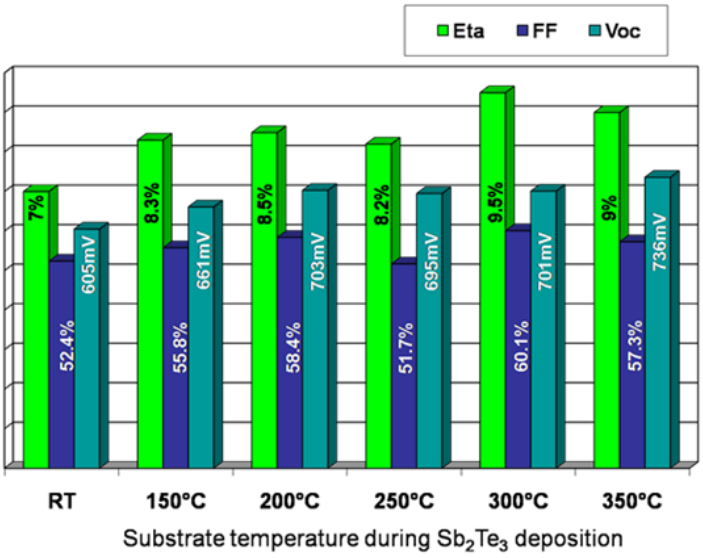

Fig. 7-19: η, FF and V_{oc} of the samples with Sb_2Te_3/Mo back contact before annealing.

Before the post-deposition annealing, the optimum substrate temperature during the Sb_2Te_3 deposition was found to be 300 °C. After the annealing, the samples, which were prepared at lower substrate temperature of 150 °C, delivered the best performances. J-V characteristics of the sample prepared at substrate temperature of 300 °C is shown in Fig. 7-21. In this sample, the open-circuit voltage was slightly lower (20-30 mV), as compared with the samples prepared with our standard back contact (chemical etching followed by gold sputtering), but the values of the FF and J_{sc} were almost similar.

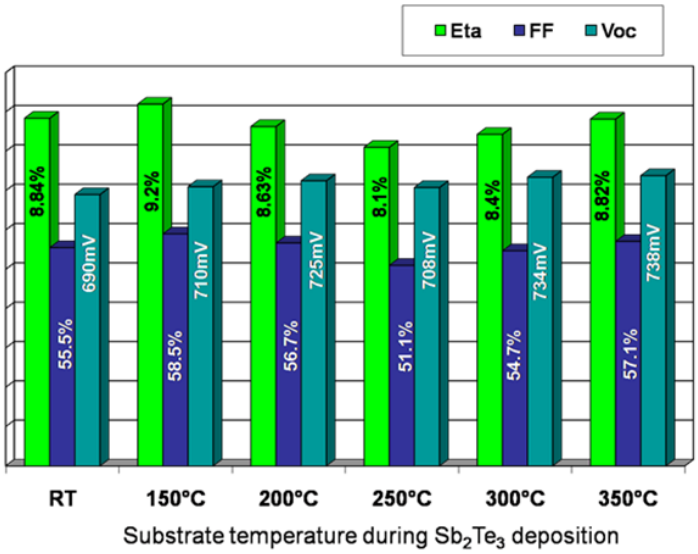

Fig. 7-20: η, FF and V_{OC} of the samples with Sb_2Te_3/Mo back contact after annealing.

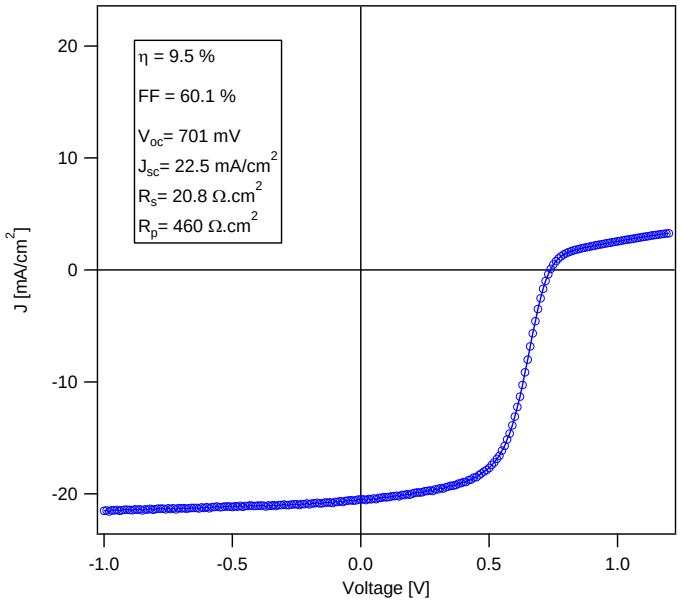

Fig. 7-21: J-V characteristics of CdTe solar cells with Sb_2Te_3/Mo back contact. The Sb_2Te_3 layer was deposited at the optimized temperature of 300 °C.

7.6 Sb/Sb_2Te_3/Mo back contacts

In order to improve the open-circuit voltage of the samples with Sb_2Te_3/Mo back contacts, a thin Sb layer was deposited onto the CdTe layer (before deposition of the Sb_2Te_3), in order to increase the p-type doping of CdTe. 1-15 nm Sb, 100 nm Sb_2Te_3 and 150 nm Mo layers were deposited onto the in-situ-activated samples at room temperature.

In order to optimize the post-annealing temperature, four samples (with Sb thickness of ~4 nm) were prepared and annealed for 30 min at 200, 250, 300, and 350 °C. Efficiency and

fill-factor of these samples as a function of the annealing temperatures are shown in Fig. 7-22. From this experiment, the optimum annealing temperature was found to be between 250-300 °C.

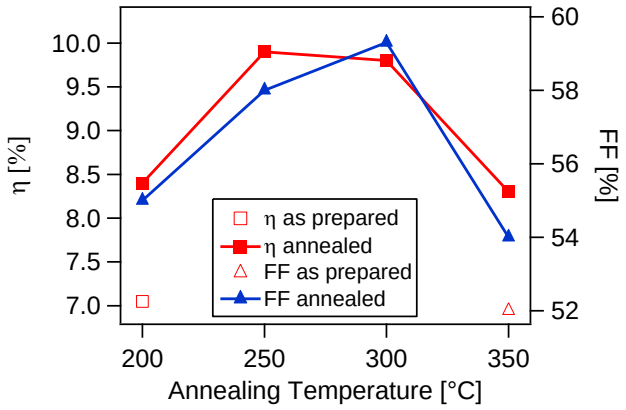

Fig. 7-22: Optimization of the post-deposition annealing temperature in CdTe solar cells with Sb/Sb_2Te_3/Mo back contact.

In order to optimize the Sb thickness, five samples with different Sb thicknesses (1-15 nm) were prepared and annealed at 250 °C for 30 min. V_{oc}, J_{sc}, η, and FF of these samples as a function of the Sb thickness are shown in Fig. 7-23. From this experiment, the most suitable Sb thicknesses were in the range of 2 - 7.5 nm.

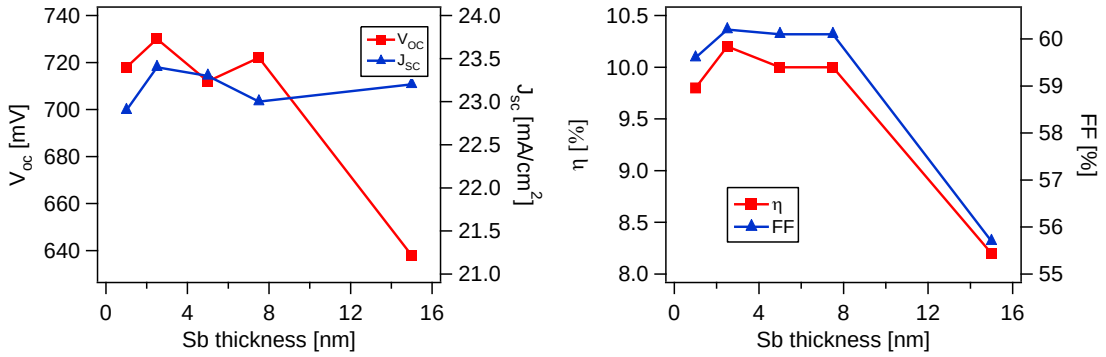

Fig. 7-23: Optimization of the Sb thickness in CdTe solar cells with Sb/Sb_2Te_3/Mo back contact.

Effect of the post-deposition annealing on J-V characteristics of the samples with different Sb thicknesses are shown in Fig. 7-24. In all samples, the open-circuit voltage was improved by at least 140 mV, however, J-V curves of most samples showed a very strong roll-over that was related to a very large series resistance. This indicates that the p-type doping of CdTe surface was not sufficiently high (or the highly doped area was not thin) to form a tunneling contact.

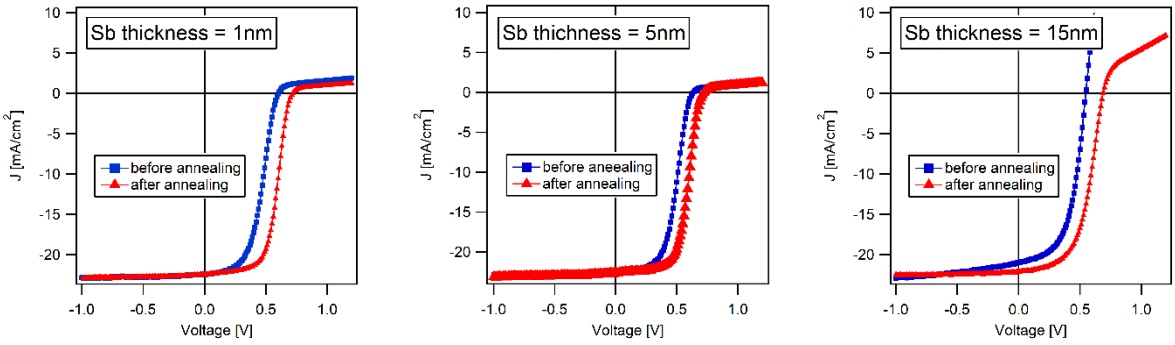

Fig. 7-24: Effect of the annealing on J-V characteristics of CdTe solar cells with Sb/Sb_2Te_3/Mo back contacts and for different Sb thicknesses.

7.7 Te/Mo back contacts

20 nm Te and 150 nm Mo layers were deposited onto an in-situ-activated sample at room temperature. The sample was annealed in an inert atmosphere at 250 °C for 30 min. J-V characteristics of this sample under AM 1.5 illumination (before and after the post-deposition annealing) are shown in Fig. 7-25.

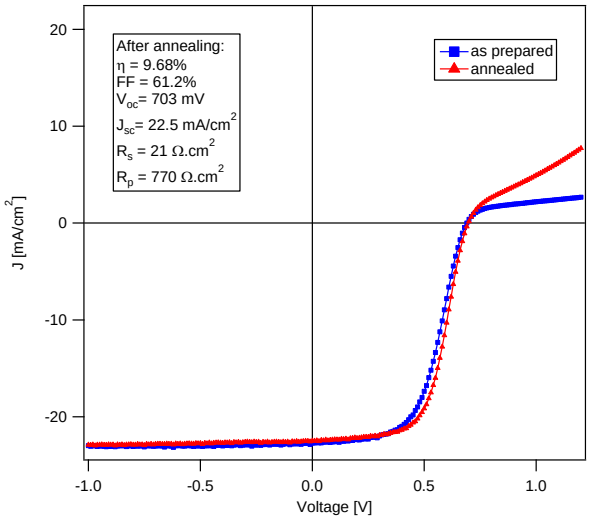

Fig. 7-25: J-V characteristics of CdTe solar cell with Te/Mo back contact, before and after the post-deposition annealing.

7.7.1 PES study of CdTe/Te/Mo interface

The CdTe/Te and Te/Mo interfaces were investigated by photoelectron spectroscopy of stepwise deposited Te layer onto CdTe and Mo substrates, respectively. First a freshly deposited CdTe (or Mo) layer was measured by XPS and UPS, then the measurement was repeated several times after each step of the Te deposition.

The BEs of Te $3d_{5/2}$ and Cd $3d_{5/2}$ as a function of Te deposition time onto the CdTe surface are shown in Fig. 7-26. The results for Te deposition on Mo substrate can be find in Appendix A. The BE of Te $3d_{5/2}$ started from 572.5 eV, which was related to Te in CdTe, and increased to 573 eV, which was related to elemental Te, as can be seen in Fig. 7-26(left). The BE of Cd $3d_{5/2}$ was shifted slightly (0.15 eV) to higher values at low Te coverage; however, after longer deposition time it returned to its initial value of 405.15 eV, which corresponds to Cd in the CdTe substrate.

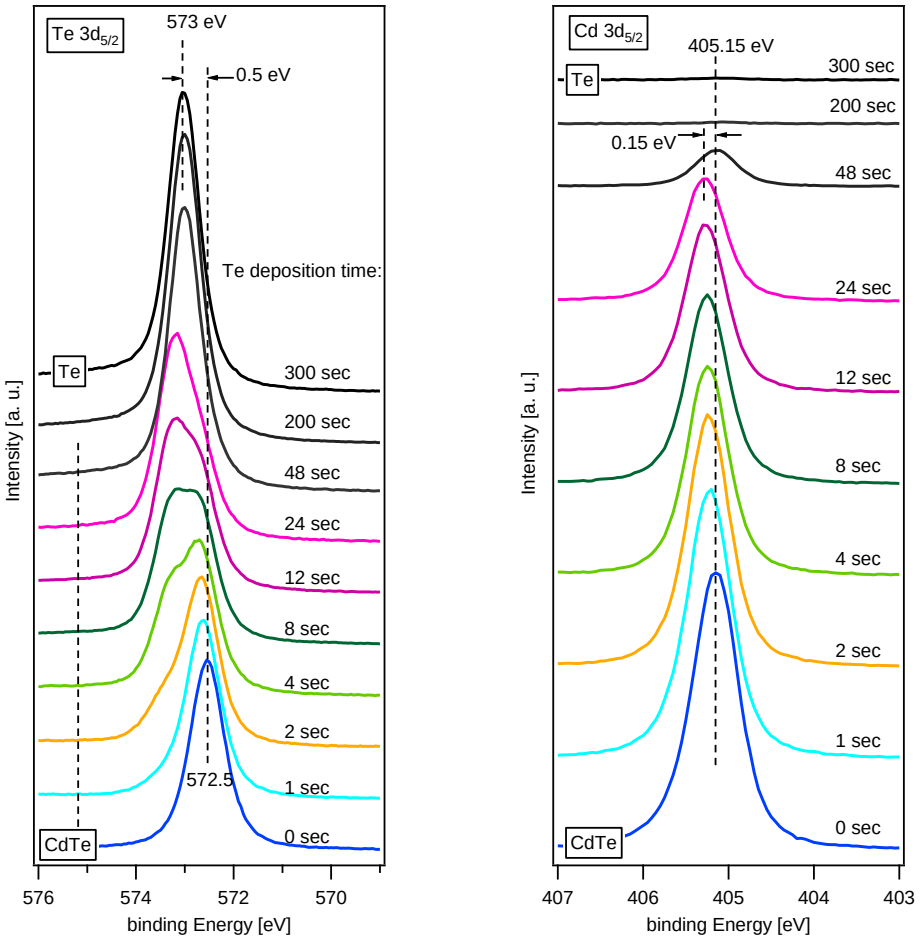

Fig. 7-26: Evaluation of XP core level spectra of Te $3d_{5/2}$ and Cd $3d_{5/2}$ during stepwise deposition po Te onto the CdTe surface.

UPS (He I) spectra during the stepwise deposition of Te onto the CdTe surface is shown in Fig. 7-27. From the secondary electrons (SE) cut-offs in Fig. 7-27(left), the work-function (ϕ) of CdTe and Te were determined to be 5.1 eV and 4.9 eV, respectively. From the UPS-VB spectra shown in Fig. 7-27(right), E_F-E_{VBM} was measured, which was 0.7 eV for the CdTe substrate and 0.1 eV for the Te layer.

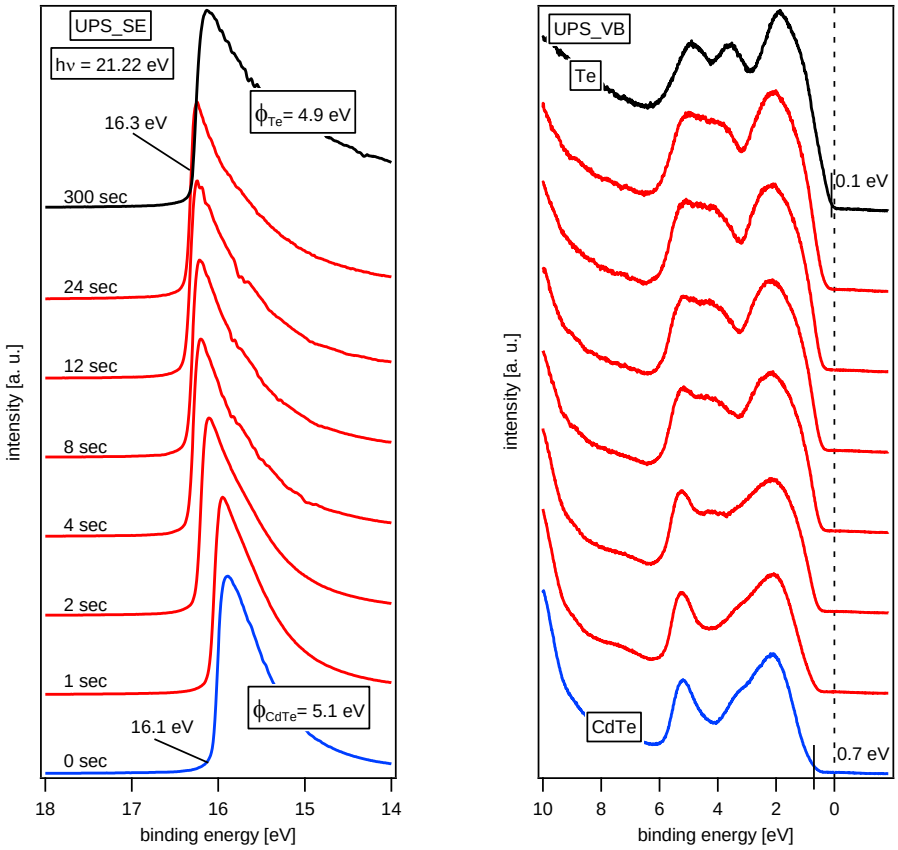

Fig. 7-27: UV photoelectron spectra of stepwise deposited Te onto CdTe surface.

From the measured values and the bandgaps of the CdTe and Te (i.e. 1.5 and 0.3 eV, respectively) the band energy diagram at the CdTe/Te interface was determined, as shown in Fig. 7-28.

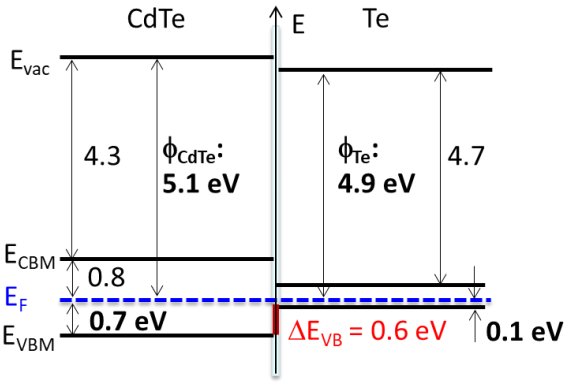

Fig. 7-28: band energy diagram at CdTe/Te interface.

A valence band offset of $\Delta E_{VB} = 0.6$ eV was measured, which indicates that the Te BC-interlayer cannot produce a low-barrier contact without a surface treatment or extra

doping. The rather high barrier for hole transport may lead to a large series resistance that limits the solar cell performance.

7.8 Te/Sb_2Te_3/Mo back contact

20 nm Te, 100 nm Sb_2Te_3 and 150 nm Mo were deposited onto an in-situ activated sample. The tellurium layer was deposited at a substrate temperature of 100 °C; while, the Sb_2Te_3 and Mo layers were deposited at 150 °C. Before starting the Sb_2Te_3 deposition, the sample was annealed at 150 °C for 20 min. After the Mo deposition, the sample was taken out of the vacuum chamber and the front contact was completed by gold sputtering.

J-V characteristics of this sample (in darkness and under AM 1.5 illumination) are shown in Fig. 7-29. As compared with the other copper-free BC-interlayers presented in this chapter, this contact had the lowest series resistance (R_s = 8 Ω.cm^2) with a rather high FF. However, the open-circuit voltage was rather low, limiting the cell efficiency to under 10 percent.

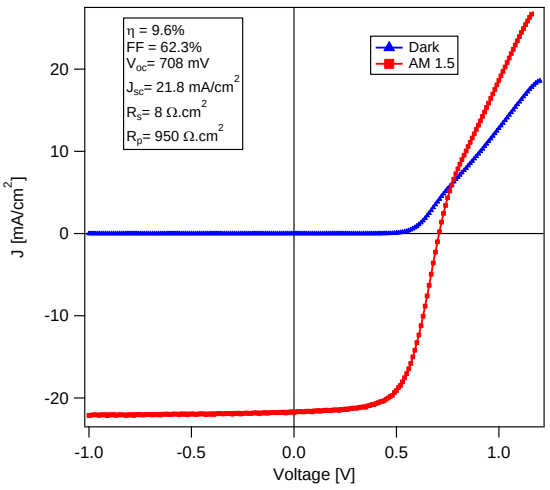

Fig. 7-29: J-V characteristics of CdTe solar cell with Te/Sb_2Te_3/Mo back contact.

An additional back contact strategy based on molybdenum oxide was investigated in this work, which will be discussed in next chapter along with a conclusion about all the investigated back contacts.

Chapter 8

MoO_x Back Contact

As explained in chapter 7, another method to overcome the back-contact barrier in CdTe solar cells is application of a high work-function transition metal-oxide (such as tungsten oxide, vanadium oxide and molybdenum oxide) as an interlayer or buffer layer between CdTe and the metal electrode. Previous investigations in our group on vanadium oxide and tungsten oxide interlayers showed presence of a high barrier height of $\Phi_B > 0.8$ eV due to the Fermi-level pinning in CdTe [97, 185].

There was a report on successful using of MoO_x as an interlayer between the CdTe and Ni to make ohmic back contacts to CdS/CdTe solar cells [152]. In that work, after a vapor $CdCl_2$ activation, the MoO_x layer was deposited onto CdTe surface (by thermal evaporation of MoO_3 powder) followed by deposition of a Ni metallic-contact (by sputtering). Solar cells with 12.2% efficiency (J_{sc}=21.3 mA/cm^2, V_{oc}=816 mV, FF=70.4%) and low series-resistance of 4.7 Ω.cm^2 were fabricated using a 40 nm thick MoO_x interlayer.

Therefore, the motivation for following line of work was to investigate the interface between CdTe and molybdenum oxide, as is shown schematically in Fig. 8-1.

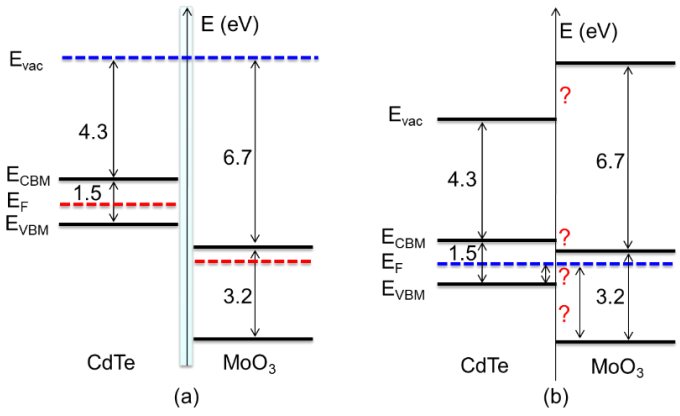

Fig. 8-1: Motivation to determine the band energy diagram at CdTe/MoO_3 interface, (a) before contact, and (b) after contact.

8.1 Deposition of MoO_x layers

Before applying the molybdenum oxide as back contact interlayer, different MoO_x layers were deposited onto FTO-coated glass-substrates (TEC 15) and were analyzed by XPS and UPS. MoO_x layers were prepared by reactive RF magnetron sputtering and physical vapor deposition (PVD) using the back-contact deposition chamber (see section 4.6.2).

A molybdenum source with 50.8 mm diameter and 3 mm thickness with purity of 99.99% was used as the sputtering target. Argon was used as the sputtering gas, and O_2 was introduced into the chamber as the reactive gas. The Ar and O_2 flow rates were adjusted using MKS controllers. In order to deposit Mo-oxide layers with suitable electronic properties, the sputtering was performed at various O_2/Ar ratios while the Ar+O_2 flow was kept constant. The sputtering parameters are listed in Table 8-1.

For the PVD experiment, an effusion cell filled with MoO_3 powder was used. The source temperature was 600-630 °C and the substrate temperature was at RT for the MoO_3 and 350 °C for reduced MoO_3 layers. During the PVD experiment, the chamber pressure was in the range of 1×10^{-8} to 5×10^{-8} mbar. The deposition rate on a substrate at RT at a distance of 10 cm from the source was 1.6 nm/min when the source temperature was 630 °C.

Table 8-1: Sputtering parameters used for MoO_x deposition.

parameter	range
substrate temperature	RT to 300 °C
substrate to target distance	6-7 cm
chamber base-pressure	10^{-8}-10^{-9} mbar
chamber pressure during sputtering	5×10^{-3}-9×10^{-3} mbar
total Ar+O_2 flow rate	5 SCCM[1]
O_2/Ar flow rate	0.5/4.5 to 2.5/2.5
RF power	20-25 W

[1] standard cubic centimeters per minute.

8.2 PES Study of MoO_x layers

MoO_x layers were deposited onto the FTO coated glass substrates by sputtering and PVD with different deposition parameters. The deposited layers were characterized by photoelectron spectroscopy to find the optimum deposition parameters. The purpose of optimization was to find the right deposition parameters in order to have MoO_x layers with high work-function and good conductivity.

8.2.1 Sputtered MoO_x layers

By changing the sputtering parameters given in Table 8-1, various Mo-oxide layers were deposited and investigated by XPS and UPS. Fig. 8-2(left) shows the Mo 3d core-level spectra of Mo and Mo oxides. The Mo $3d_{5/2}$ binding energy for metallic Mo shows the Mo^0 peak of the metal at 228.0 eV. For MoO_3, the Mo $3d_{5/2}$ binding energy shows a Mo^{6+} peak of the trioxide at 232.7 eV. The main peak of Mo $3d_{5/2}$ at 232.7 eV corresponds to Mo^{6+} and another small peak at ~231.5 eV is from Mo^{5+} oxidation state. In MoO_{2+x}, a mixture of Mo^{4+} and Mo^{5+} oxidation states with Mo $3d_{5/2}$ binding energies of 229.5 eV and ~231.5 eV was measured.

Valence-band spectra of the samples are shown in Fig. 8-2(middle). The Fermi level is located at zero binding energy and the valence-band maximum is determined from the cut-off of the spectra. For Mo, as expected, the valence band crosses the Fermi level. E_F - E_{VBM} is 2.8 eV for both MoO_3 and MoO_{3-x} samples; but the MoO_{3-x} has some defect-states with maximum intensity at 0.8 eV below the Fermi level. The valence band spectrum of the MoO_{2+x} crosses the Fermi level, which means that the sample should have a metallic behavior.

The work-function of all samples was determined from the secondary electron cut-off of the UP spectra as shown in Fig. 8-2(right). The measured work-functions range from 6.0 to 6.7 eV for the Mo-oxide layers and 4.5 eV for pure Mo, as given in Table 8-2. Therefore, by controlling the deposition parameters, Mo-oxide layers with high work-function and good conductivity could successfully be deposited. The electrical conductivity of the layers was confirmed with a simple resistance measurement using a multimeter.

Table 8-2: work-function of sputtered Mo oxide and Mo layers determined by UPS.

sample	O_2 flow (SCCM)	Ar flow (SCCM)	work-function (eV)
MoO_3	2.5	2.5	6.7
MoO_{3-x}	0.5	4.5	6.5
MoO_{2+x}	0.15	4.85	6.0
Mo	0	5	4.5

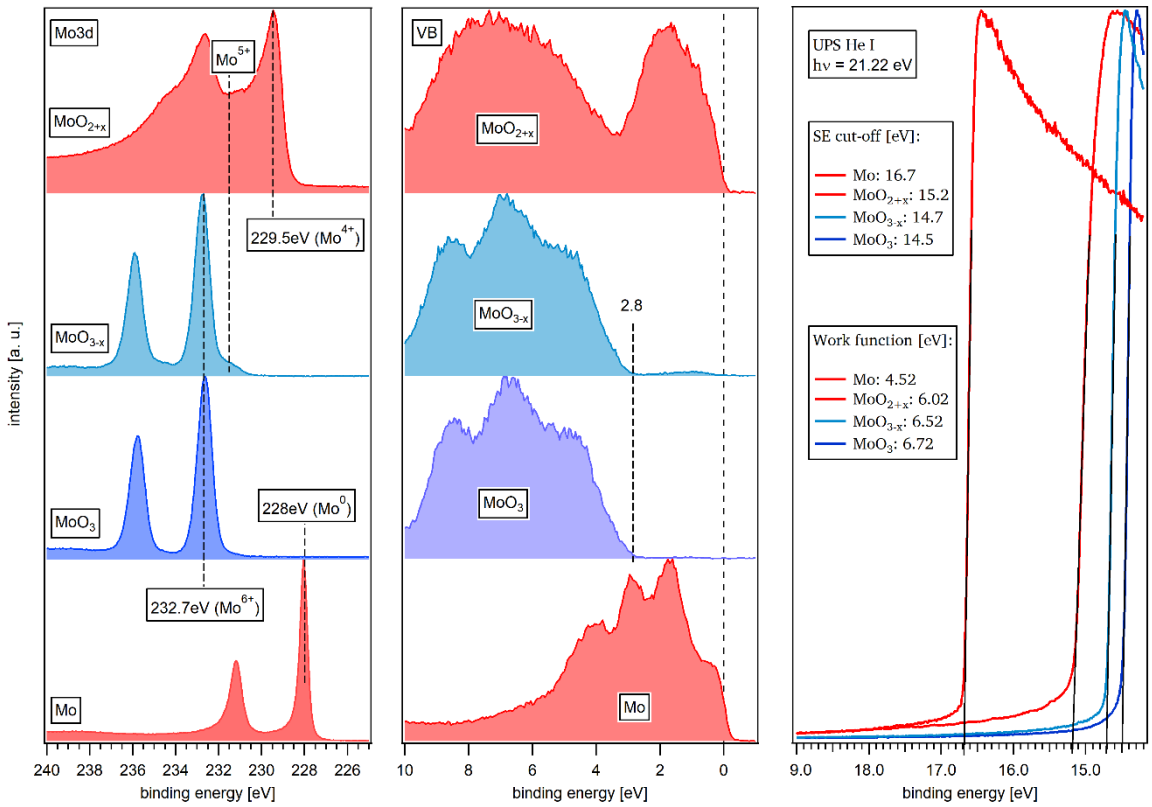

Fig. 8-2: Mo 3d spectra (left), valence band spectra (middle) and UP spectra (right) of Mo and Mo-oxide layers deposited on FTO-coated glass substrates by sputtering.

8.2.2 PVD-MoO_x layers

The Mo 3d core-level spectra of the MoO_3 and MoO_{3-x} layers prepared by PVD are compared in Fig. 8-3(left). For both layers, the Mo $3d_{5/2}$ peak at 232.5 eV corresponds to Mo^{6+}. The MoO_{3-x} showed another weak signal at lower binding energies, which is marked in the figure and is related to the oxygen deficiency.

XP valence-band spectra of the samples is shown in Fig. 8-3(middle). From this figure, the Fermi level of MoO_3 and MoO_{3-x} was determined to be at 2.5 and 2.7 eV above the valence

band maximum, respectively. Moreover, for MoO_{3-x} there were some defect states within the band gap, with maximum intensity at 1.1 eV below the Fermi level.

From the UP spectra shown in Fig. 8-3(right), the work-function of the samples were measured to be 6.8 and 6.6 eV for the MoO_3 and MoO_{3-x} layers, respectively.

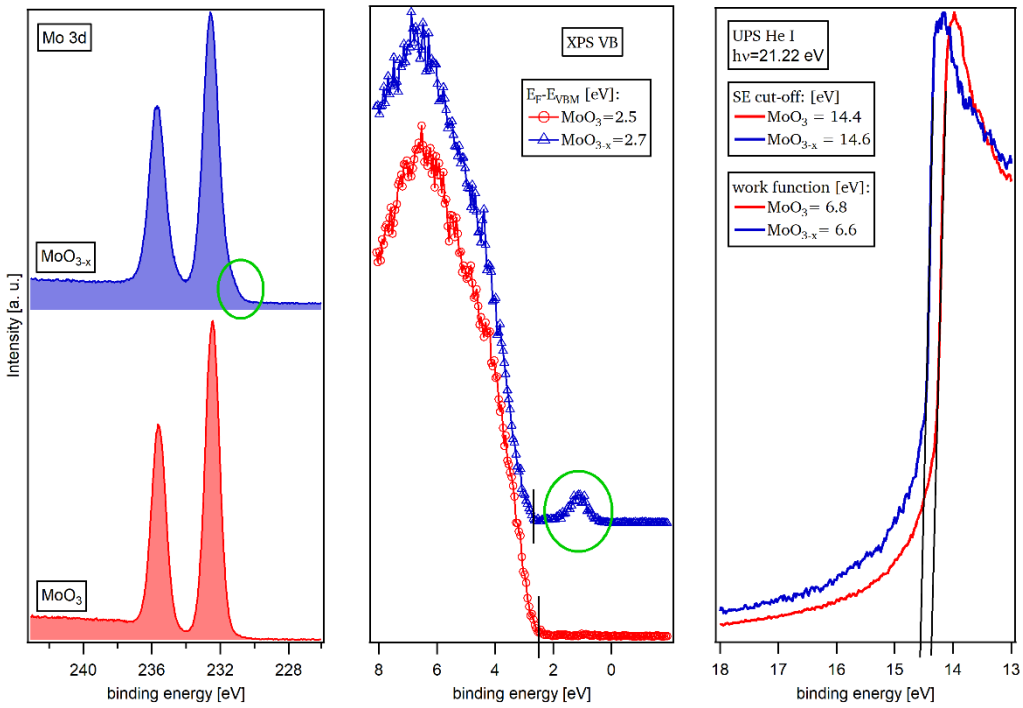

Fig. 8-3: Mo 3d spectra (left), valence-band spectra (middle) and UP valence-band spectra (right) of MoO_3 and MoO_{3-x} layers prepared by PVD at RT and 350 °C, respectively.

8.3 PES study of CdTe/MoO_x interface

Three sets of interface experiments were performed to study the interface between CdTe and different MoO_x layers deposited by sputtering and PVD methods. The interface experiments were performed by stepwise deposition of different MoO_x layers onto CSS CdTe layers deposited on glass/FTO substrates.

8.3.1 CdTe/Sputtered-MoO_3 interface

The high-resolution XP-spectra during the stepwise sputtering deposition of MoO_3 on a freshly deposited CdTe layer are shown in Fig. 8-4. As expected, with increasing the MoO_3 deposition time, the Cd and Te intensities gradually decreased; while the Mo and O signals increased. After 10 deposition and characterization steps, which corresponds to a total

deposition time of 1152 s, no Cd or Te emission was visible in the spectra. The valence band spectra showed a continuous increase from 0.81 eV for pure CdTe to 2.4 eV for MoO_3.
After starting the Mo-oxide deposition, the Te $3d_{5/2}$ core-level showed two components; the peak at lower binding energy (572.5 eV) corresponding to Te in CdTe and the one at higher binding energy (576.1 eV) corresponding to Te in $CdTeO_3$. The oxide component in the Cd $3d_{5/2}$ could not be distinguished clearly, since it had almost the same binding energy as Cd in CdTe, but it could be clearly seen in the Cd MNN Auger line (as marked by an arrow in Fig. 8-4).

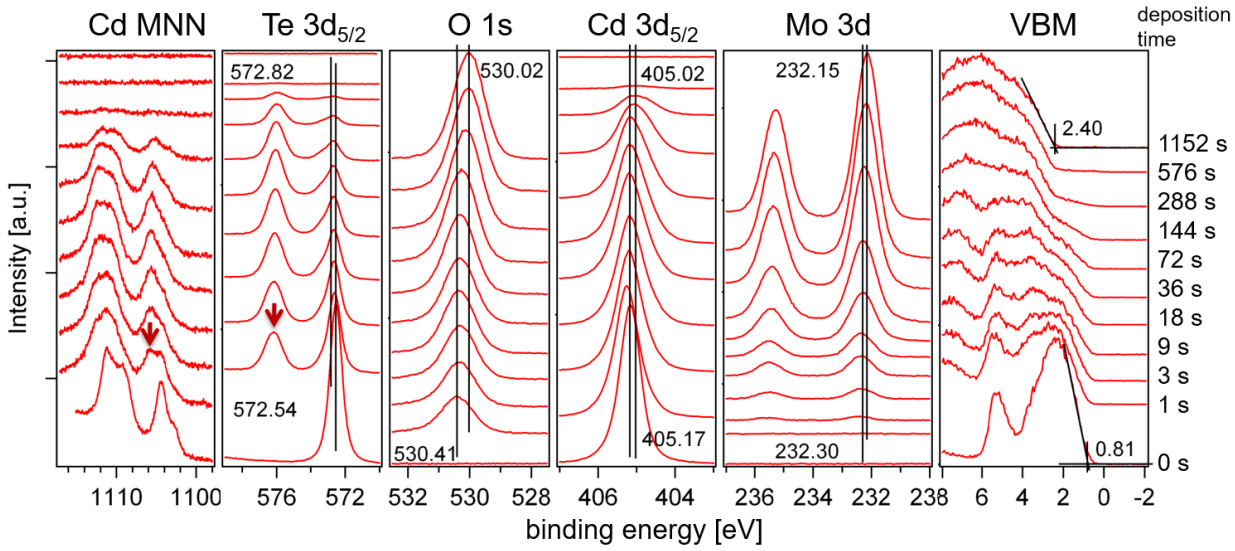

Fig. 8-4: Evaluation of XP spectra in stepwise deposition of MoO_3 on CdTe by reactive sputtering.

In order to determine the energy-band diagram at the CdTe/MoO_3 interface, UPS measurements were also performed on the CdTe substrate (i.e. before starting the MoO_3 deposition) and on the MoO_3 over-layer after it was deposited for 1152 sec. In the UPS spectra shown in Fig. 8-5, the secondary-electron cut-off positions are at 16.22 and 14.38 eV for CdTe and MoO_3, respectively. Therefore, the work-function of CdTe and MoO_3 were measured to be 5.0 and 6.8 eV, respectively.
Measured valence-band binding energies and the work-functions were used to draw the energy band-diagram of CdTe and MoO_3, as illustrated in Fig. 8-6. After the contact, a large valence-band offset of 1.5 eV and a small conduction band offset of 0.01 eV were formed, as can be seen in (b). The energy gap of CdTe (1.5 eV) and MoO_3 (3.0 eV) were used to determine these offsets.

From the difference in the work-functions of CdTe and MoO_3 (5.0 and 6.8 eV in this experiment, respectively) and 0.1 eV downward band-bending, the difference in vacuum levels corresponded to a very large interface dipole toward MoO_3 (ΔE_{vac} = 1.9 eV). The CdTe Fermi level was pinned at 0.9 eV above the valence band. This could be related to the chemical reaction at the interface.

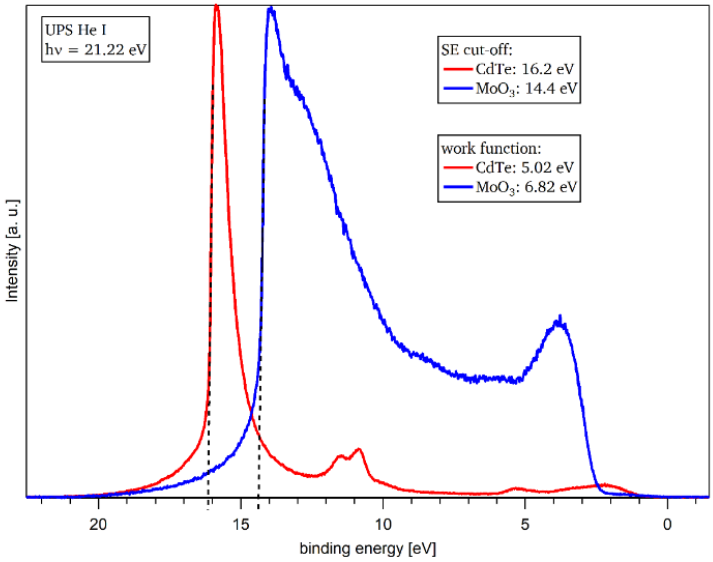

Fig. 8-5: UPS measurements of CdTe and sputtered MoO_3.

Despite the very large work-function, no small contact barrier to the CdTe can be realized by using sputtered MoO_3 interlayer. This could be due to oxidation of the CdTe surface during (deposition of the MoO_3 layer) and also pinning of the CdTe Fermi level at 0.9 eV above the valence band which leads to a large valence band offset of 1.9 eV.

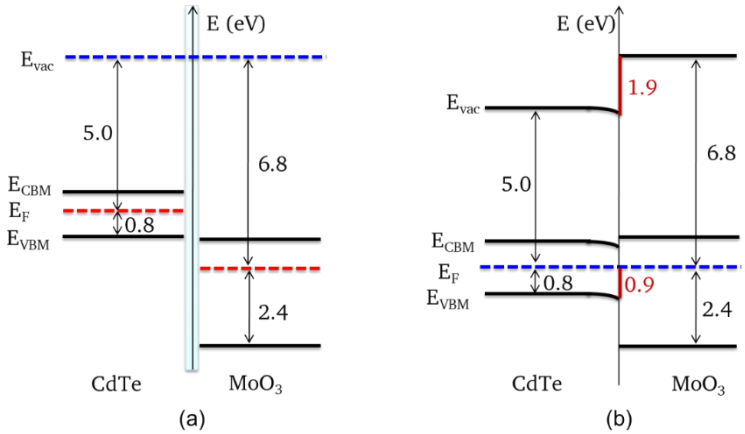

Fig. 8-6: Energy band diagram at the CdTe/MoO_3 interface, (a) before contact, and (b) after contact as determined from photoelectron spectroscopy. The Fermi level of CdTe is pinned at 0.9 eV above the valence band; therefore, a barrier height of E_F - E_{VBM} = 0.9 eV was measured at the interface.

8.3.2 CdTe/Sputtered MoO_{2+x} Interface

Besides the large barrier height which was measured at the CdTe/sputtered-MoO_3 interface, oxidation of the CdTe surface could be another reason for a bad performance of solar cells prepared with the stuttered MoO_3 back contact interlayer (see section 8.3.1). In order to reduce or prevent the CdTe surface oxidization, the MoO_{2+x} layer was investigated as the back-contact interlayer. This layer was prepared at much lower O_2 concentration during sputtering as given in Table 8-2.

The interface between CdTe and MoO_{2+x} was investigated by PES measurements during the stepwise-deposition of the oxide layer on CdTe. XPS core-level and valence-band spectra along with Cd MNN Auger spectra are shown in Fig. 8-7. One important result from these experiments was that the CdTe surface did not oxidize during the Mo-oxide deposition. This can clearly be seen by comparing the Te $3d_{5/2}$ emissions in Fig. 8-7 with those in Fig. 8-4. In addition, a parallel shift of ~0.2 eV in Cd, Te and O core levels to higher binding energies was observed. The Mo 3d core-level spectra showed an extra shift to higher binding energies by 0.7 eV, during the first 9 sec deposition of MoO_{2+x}. This could be due to extraction of some of the oxygen atoms by CdTe that could lead to further reduction of the MoO_{2+x}. However, no evidence for formation of an oxide layer ($CdTeO_3$) on the CdTe surface was observed.

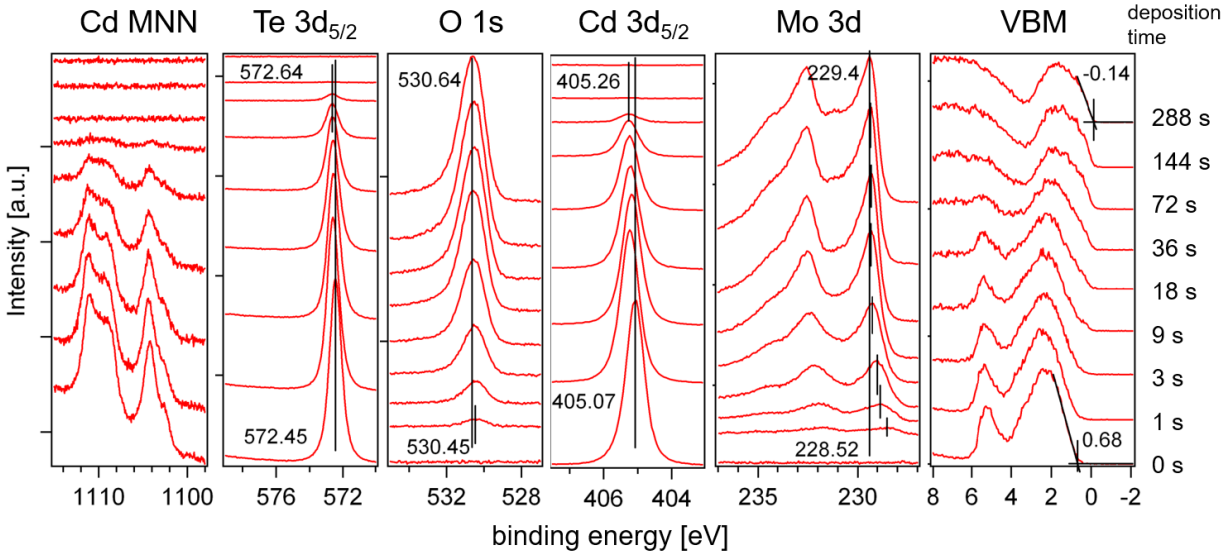

Fig. 8-7: Evaluation of XP spectra in the stepwise deposition of MoO_{2+x} on CdTe by reactive sputtering technique.

From the UPS measurement of CdTe substrate and the MoO_{2+x} over-layer, the work-functions of CdTe and MoO_{2+x} were determined to be 5.1 and 6.0 eV, respectively.

By using the results of the interface experiment and UPS measurements, the energy band diagram at the CdTe/MoO_{2+x} interface was drawn, as illustrated in Fig. 8-8. Similar to the CdTe/MoO_3 interface, a barrier height of E_F - E_{VBM} = 0.9 eV was formed due to pinning of the Fermi-level of CdTe. A large dipole of ΔE_{vac}= 1.1 eV is also formed at this interface.

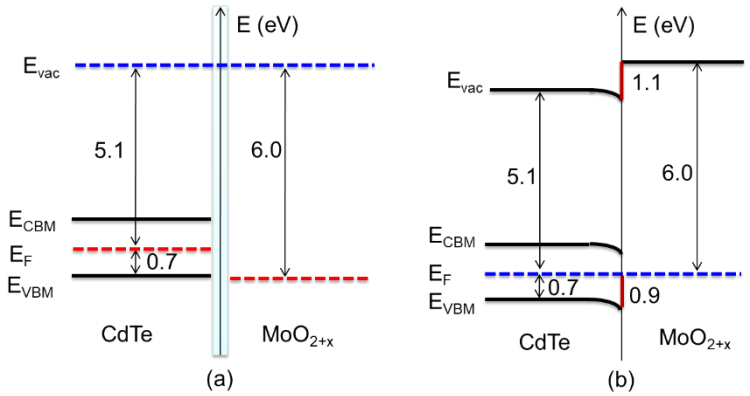

Fig. 8-8: Energy-band diagram at the CdTe/MoO_{2+x} interface as determined from photoelectron spectroscopy, (a) before and (b) after the contact formation.

8.3.3 CdTe/PVD-MoO_3 Interface

X-ray photoelectron spectra during stepwise-deposition of PVD-MoO_3 on CdTe are shown in Fig. 8-9. In contrast to the CdTe/sputtered-MoO_x interface experiment, XPS peaks of the CdTe substrate and MoO_3 adsorbates did not shift in parallel. Binding energy of the core level peaks as a function of MoO_3 deposition time is shown in Fig. 8-10. Cd $3d_{5/2}$ and Te $3d_{5/2}$ peaks shifted by 0.1 eV to higher binding energies, until a deposition time of 16 seconds and then stayed nearly constant.

The O 1s peak shifted by 0.4 eV to lower binding energies, while the Mo $3d_{5/2}$ shifted by 0.3 eV to the higher binding energies. This opposite binding-energy shifts can be explained by a chemical reaction near the interface. When an oxygen atom is extracted from MoO_3 and forms a chemical bound with the substrate, its binding energy shifts to lower values. Moreover, when oxygen atoms are extracted from the MoO_3 layer, binding energy of molybdenum shifts to higher values. Therefore, if we move from the MoO_3 side towards the CdTe substrate side, the MoO_3 layer gradually changes to MoO_{3-x}.

It should be noted that although the CdTe substrate extracted some oxygen atoms from the MoO_3 layer, the Te $3d_{5/2}$ spectra presented in Fig. 8-9 did not show any oxide component.

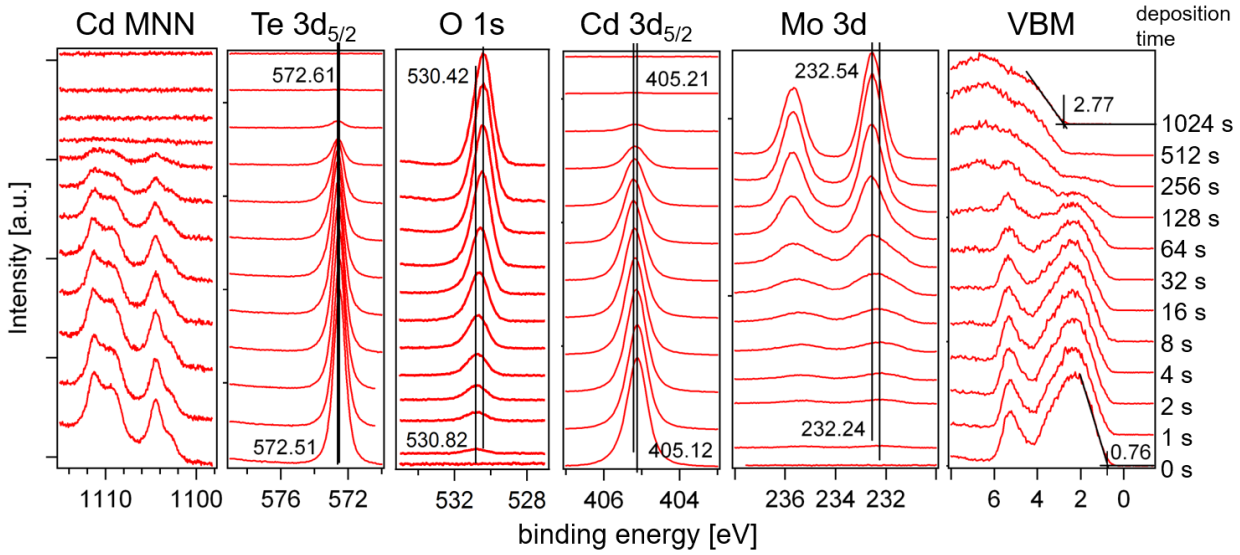

Fig. 8-9: Evaluation of XP core level spectra in the stepwise deposition MoO_3 layer on CdTe by PVD.

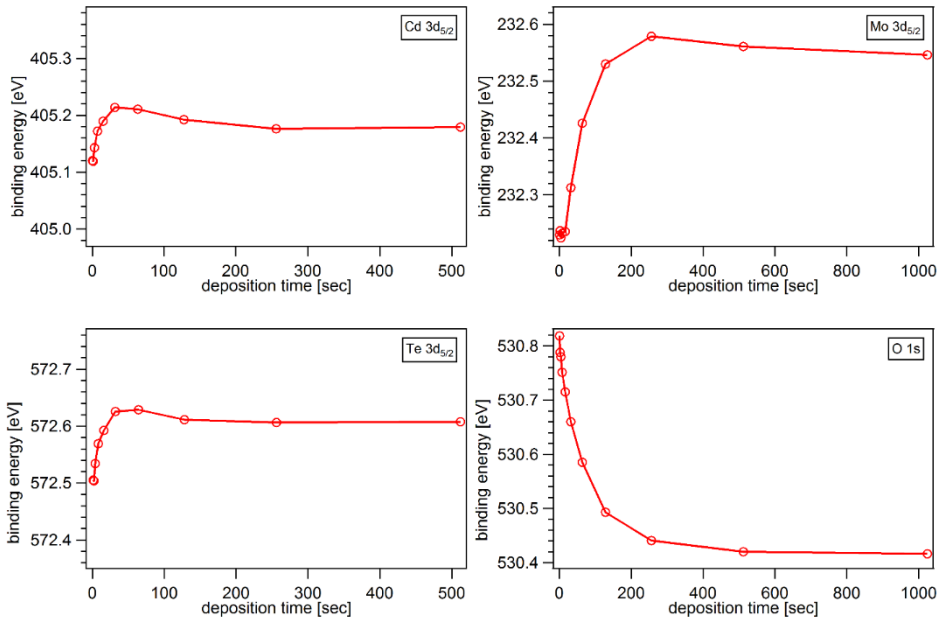

Fig. 8-10: Binding energy of CdTe and MoO_3 XPS core-level peaks as a function of MoO_3 deposition time.

Energy band diagrams of CdTe and PVD-MoO_3 before and after contact formation are shown in Fig. 8-11. Similar to the CdTe/sputtered-MoO_x interface experiments, the CdTe Fermi level was pinned at 0.9 eV above the valence band, and a large valence-band discontinuity of $\Delta E_{VB} = 2.0$ eV was formed at the interface. A very large vacuum level offset of $\Delta E_{VL} = 1.8$ eV was also measured which is related to the formation of an interface dipole. Therefore, it was expected that the PVD-MoO_3 layer would not provide an ohmic contact to CdTe. Another important result was that since the conduction band is perfectly aligned at

the interface, there is no barrier for electron transport to the back contact or injection of electrons from the back contact to CdTe conduction band. As a consequence, electron-hole pairs created near the back contact (by deeply-penetrated photons) would recombine at the back contact. This could lead to lower short-circuit currents, and therefore, lower efficiencies in solar cells with thin CdTe layer.

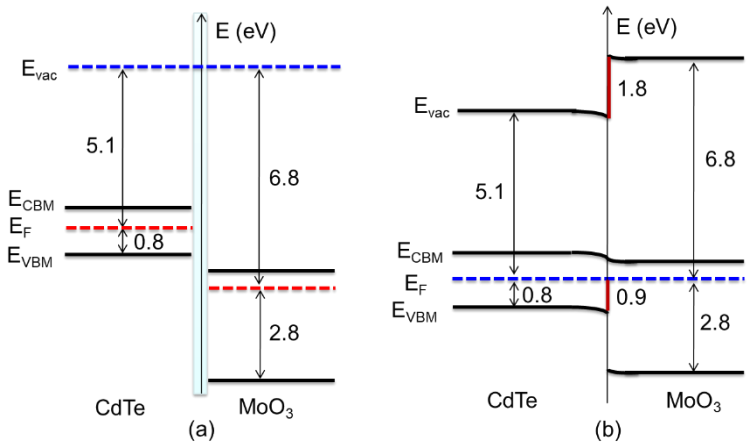

Fig. 8-11: Energy band diagram at the CdTe/PVD-MoO_3 interface as determined from the photoelectron spectroscopy.

8.4 CdTe Solar Cells with MoO_x Interlayer

CdTe solar cells with different MoO_x back contact interlayers were prepared with the following procedure:

- CSS deposition of CdS (~0.2 μm) and CdTe (~5μm) layers on FTO-coated glass substrates,
- CSS deposition of $CdCl_2$ (~0.2 μm) on CdTe,
- annealing of the samples at 380 °C in Ar atmosphere for 25 min to complete the $CdCl_2$ activation,
- washing of the samples in ultrasonic bath in water/methanol solution (1:1), to remove the $CdCl_2$ residue,
- deposition of the MoO_x layer on the activated sample, and
- deposition of the metallization contacts on MoO_x and FTO, followed by structuring of the samples, as explained in section 4.6. Mo, Au and Ni were used as the metallization contact.

Completed solar cells were characterized before and after an annealing step. The annealing was performed at 200 °C for 5, 10 and 20 minutes on a hotplate in air atmosphere.
It should be noted that during these experiments, the in-situ activation setup was not available therefore the activation process was performed with deposition of a thin $CdCl_2$ layer followed by annealing at 380 °C for 25 min in a nitrogen atmosphere.

8.4.1 Sputtered MoO_3/Mo back contact

J-V characteristics of the solar cells with sputtered MoO_3/Mo back contacts is shown in Fig. 8-12(left). Obviously, due to a very high series resistance, an ohmic contact is not present here. The reason for such a high series resistance could be due to formation of an oxide layer on the CdTe surface during the deposition of the MoO_3 layer, as illustrated in Fig. 8-12(right).

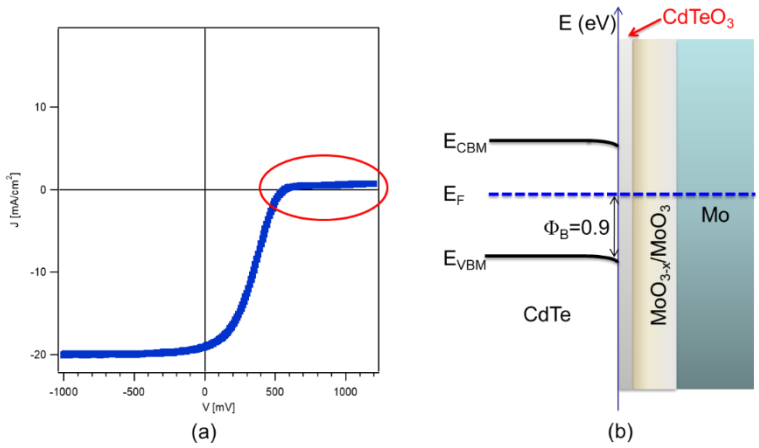

Fig. 8-12: J-V characteristics of CdTe solar cells with sputtered MoO_3/Mo back contact (a). The strong rollover at high voltages is related to a high barrier height at the interface, due to oxidation of the CdTe surface, as shown schematically in (b).

In order to reduce oxidation of the CdTe surface, solar cells with MoO_{3-x}/Mo back contacts in which the Mo-oxide layer was deposited at lower O_2/Ar flow were prepared (see Table 8-2). J-V curve of this solar cell before and after the back-contact annealing is shown in Fig. 8-13. Typical parameters of solar cell with sputtered MoO_{3-x}/Mo back contact are given in Table 8-3. This contact showed better performances (i.e., lower series resistance and therefore, less rollover and larger fill factors) compared with the sputtered MoO_3 back contact; however, the performance of these cells was still less than the solar cell with standard NP-etched/Mo back contact (see Table 8-5).

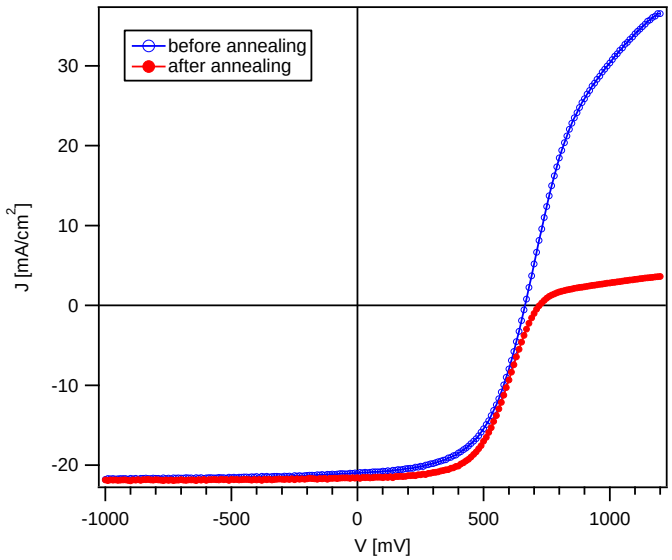

Fig. 8-13: J-V curve of solar cell with sputtered MoO_{3-x}/Mo back contact before and after the annealing.

Table 8-3: Typical parameters of the solar cells with sputtered MoO_{3-x}/Mo back contact.

	J_{sc} (mA/cm^2)	V_{oc} (mV)	FF (%)	η (%)	R_s (Ω/cm^2)
before annealing	21.06	664	56	7.8	8
after annealing	21.33	723	55.8	8.6	25.8

8.4.2 Sputtered MoO_{2+x} back contact

J-V characteristics of a CdTe solar cell with MoO_{2+x}/Mo back contact before and after the back contact annealing is shown in Fig. 8-14 and its typical parameters are given in Table 8-4.

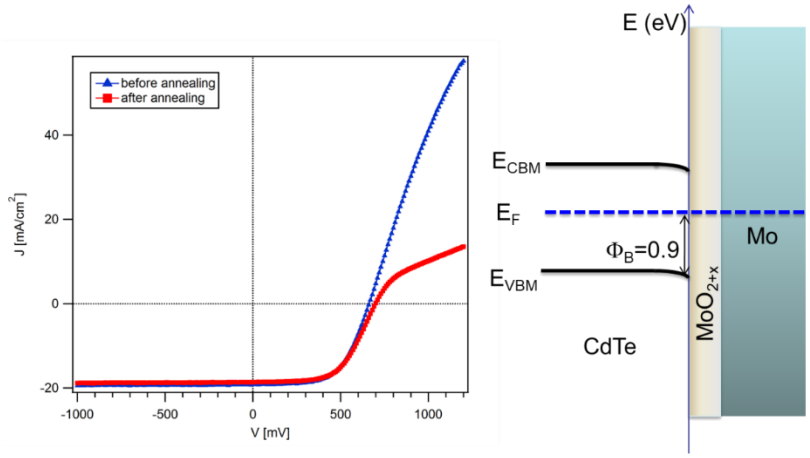

Fig. 8-14: J-V characteristics of a CdTe solar cell with MoO_{2+x}|Mo back contact.

This contact showed a lower series resistance (less rollover behavior) which was an advantage, but it had a lower open-circuit voltage (as compared with the cells with sputtered MoO_x/Mo back contacts). After annealing, the open-circuit voltage was slightly improved, but J_{SC} and FF were decreased and no change in the efficiency was observed.

Table 8-4: Typical parameters of the solar cell with MoO_{2+x}/Mo back contact.

MoO_{2+x}/Mo contact	J_{sc} (mA/cm^2)	V_{oc} (mV)	FF (%)	η (%)	R_s (Ω/cm^2)
before annealing	19.2	660	60	7.6	7.3
after annealing	18.9	723	52.8	7.6	22.1

8.4.3 PVD-MoO_3 back contact

CdTe solar cells with PVD-MoO_3/Ni back contacts were prepared with a similar procedure, as explained in section 8.4. J-V characteristics of these cells are presented in Fig. 8-15 and Table 8-5. A "standard cell" with NP-etch/Ni back contact is also given as a reference. Solar cells with PVD-MoO_3/Ni contacts did not have better performances, as compared with the NP-etch/Ni back contact cells. This was in contrast with the work done by Hao Lin et al. [186].

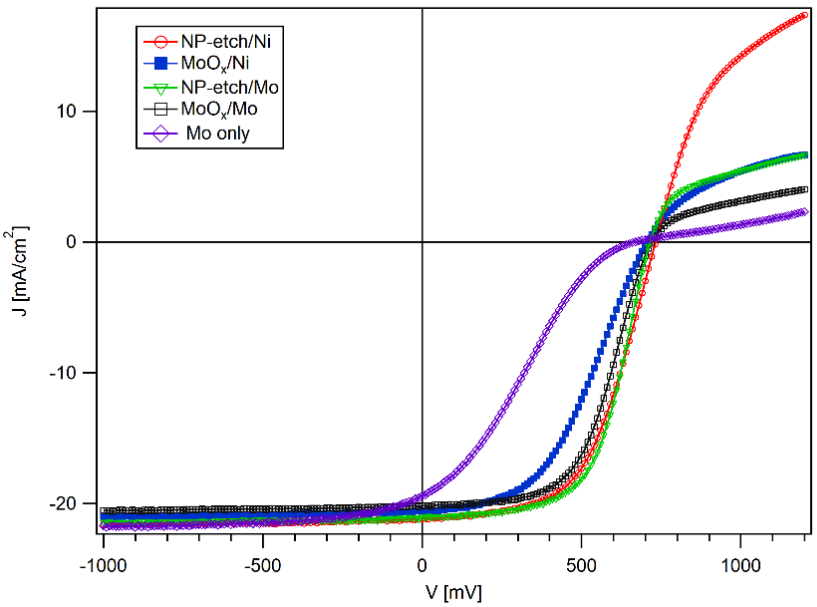

Fig. 8-15: J-V characteristics of solar cells with NP-Ni and PVD-MoO_3-Ni back contacts. As compared with the MoO_3-Mo contact, this contact delivered a better performance, i.e., higher fill factor and less series resistance.

Table 8-5: typical parameters of CdTe solar cells with NP/Ni and PVD-MoO_3/Ni back contact.

Contact	J_{sc} (mA/cm^2)	V_{oc} (mV)	FF (%)	η (%)	R_s (Ω/cm^2)
NP-etch/Ni	21.2	730	56	8.7	8.6
PVD-MoO_3/Ni	21	721	51	7.7	11
NP-etch/Mo	21	715	60.6	9.1	10.8
PVD-MoO_3/Mo	20.1	721	56.4	8.2	22.6
Mo only	19.4	668	25.4	3.29	136

Solar cells with PVD-MoO_3/Mo back contacts were also investigated, but their J-V characteristics were almost similar to those with the sputtered MoO_x/Mo back contacts, as presented in the previous section. In solar cells without etching, the cells with MoO_x inter-layer showed much better performances as compared with the cell without MoO_x; but their performances were not higher than the NP-etched samples (see Table 8-5). Solar cells with 5, 10, and 20 nm of MoO_x layers had almost similar efficiencies, while the cell with 2.5 and 40 nm had a poor performance, i.e. low FF and high series resistance (strong rollover).

8.5 Te/Sputtered-MoO_x/Mo back contact

In most of the solar cells with MoO_x/Mo back contacts, the open-circuit voltage was low. This could be due to either 1) imperfect $CdCl_2$ activation, or 2) low doping levels in CdTe and/or CdS. In order to increase the p-type doping of CdTe, a thin Te layer was deposited onto the CdTe surface before deposition of the MoO_x layer. The Te layer was deposited using a home-made PVD source. The source temperature (controlled by a Eurotherm controller) was 310 °C, and its distance to the substrate during deposition was 10 cm. With these parameters, the Te deposition rate (at room substrate temperature) was ~1 nm/min. In order to investigate the effect of the Te-layer thickness, two samples with Te thicknesses of 2 and 20 nm were prepared. After deposition of the Te layer, the MoO_x/Mo layers were deposited onto the samples, without breaking the vacuum. Then, the samples were annealed at 200 °C for 20 min in Ar. The chamber pressure during the annealing was 0.04 mbar. One more sample with 2 nm of Te layer was also prepared. For this sample, the only difference in the preparation procedure was an annealing at 200 °C for 20 min in Ar (before deposition of the MoO_x/Mo layers).

J-V characteristics of the completed solar cells with Te/MoO_x/Mo contacts are compared in Fig. 8-16. As a reference, J-V characteristics of a solar cell with a similar fabrication

procedure, except for deposition of the Te layer, was added to this figure. Typical parameters of the cells are given in Table 8-6.

The results of this experiment can be summarized as follows:

- Deposition of a tellurium layer on the CdTe surface improved the solar cell performance by increasing the open-circuit voltage.
- Higher V_{oc} could be due to p-type doping of the CdTe surface. However, the doping level was not high enough to provide a tunneling contact.
- The rollover effect was more pronounced in cells with tellurium. This was a consequence of the p-type doping of the CdTe surface.
- Solar cell with a thin Te layer (2 nm) had better performances, as compared with the cell with a rather thick (20 nm) Te layer.

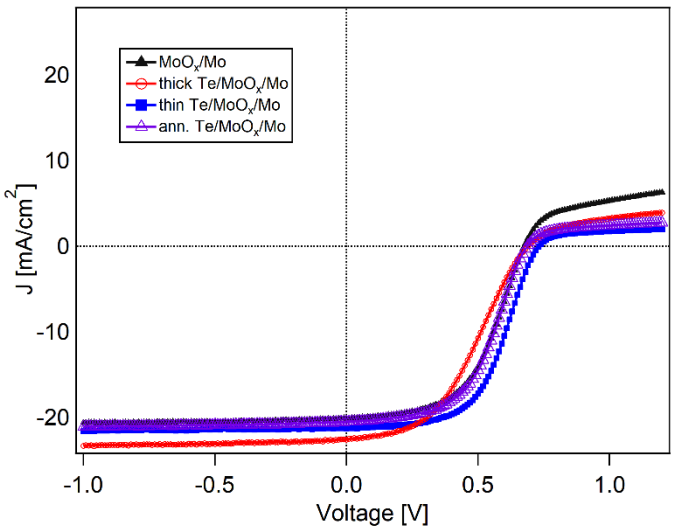

Fig. 8-16: J-V characteristics of solar cells with Te/MoO_x/Mo back contact.

Table 8-6: Typical parameters of solar cells with Te/MoO_x/Mo back contacts

Contact	Te (nm)	J_{sc} (mA/cm^2)	V_{oc} (mV)	FF (%)	η (%)	R_s (Ω/cm^2)
MoO_x/Mo	-	20.15	675	53.6	7.3	13
thick Te/MoO_x/Mo	20	22.13	703	43	6.69	23
thin Te/MoO_x/Mo	2	21.38	730	55.6	8.68	31
Te+ann./MoO_x/Mo	2	20.49	686	53.6	7.54	29

Chapter 9

Summary and Outlook

The main subject of this work was investigation of back contact in CdTe solar cells in superstrate configuration. After an introduction about the challenges in making a stable ohmic contact to p-CdTe in chapter 1, the structure of heterojunction CdS/CdTe solar cells and different layers and processing steps in fabrication of these cells were introduced in chapter 2. Then the operation details of p-n junction solar cells were explained and the two-diode model for CdTe solar cells was discussed. SCAPS simulation program was used to investigate and explain the important parameters (including R_s, R_p and film thicknesses) that affect the performance of CdS/CdTe solar cells.

Some characterization techniques, such as the Hall-effect and impedance measurements, were setup and used in this study. Most of the electrical and structural characterization techniques that were used in this work were introduced in chapter 3. The experimental procedures for preparation of CdTe solar cells were explained in chapter 4.

One of the primary goals in this work was to eliminate the chemical etching after the $CdCl_2$ activation treatment. In order to realize this, an in-situ activation treatment was developed to perform the activation process in a non-oxidizing environment. By optimization of the process, solar cell efficiencies as high as efficiency of the cells prepared with the standard wet $CdCl_2$ treatment were obtained. Since no oxide layer was formed on the CdTe surface after the $CdCl_2$ treatment, it was possible to study effects of the activation on glass/TCO/CdS/CdTe samples by photoelectron spectroscopy and conductive AFM. The results of these experiments were summarized in section 5.5 and 6.4, respectively. Impedance spectroscopy and capacitance-voltage measurements at room temperature were performed to investigate the effect of the $CdCl_2$ activation on defect levels in CdTe; however, for further investigations these measurements need to be performed at lower temperatures.

Different back contact strategies including interlayer deposition and CdTe surface doping have been investigated, which the important results were as following:

9.1 Back contact interlayers

Several back-contact interlayers based on ZnTe, Sb_2Te_3, Sb and Te were applied and the important parameters of each contact were optimized. Cell efficiencies close to the efficiencies obtained with our standard wet process (wet activation, NP etching and Au back contact) were obtained. This was achieved without any need for wet chemical etching or washing processes, and of course, without copper.

In the copper-free back contacts, the highest efficiency was obtained with $Sb/Sb_2Te_3/Mo$, but $Te/Sb_2Te_3/Mo$ produced the lowest series resistance and the highest fill factor. On the other hand, the easiest and more reproducible back contact was the Te/Mo bi-layer.

All the copper-free back contacts were stable for at least 6 months storage in the lab (some that were monitored for ~12 months were stable as well.

Few solar cells with a copper-doped ZnTe interlayer were also prepared. These cells showed the highest FF and lowest series-resistances with almost no rollover. Since the focus of this project was on copper-free back contacts, this contact was not optimized. However, the preliminary results showed that this contact has a high potential in fabrication of highly efficient CdTe solar cells.

9.2 Sb-doping

Previous investigations in our group showed that ZnTe was a good candidate to be used as the back-contact interlayer in CdTe solar cells; a valence band offset of 0.1 eV was measured between CdTe and ZnTe and ohmic contact to nitrogen-doped ZnTe was realized. However, performance of CdTe solar cells with ZnTe:N back contact was not high enough, therefore as an alternative Sb doped ZnTe layers were investigated. An efficient method was developed and ZnTe:Sb layers with p-type doping density of 3.1×10^{19} cm^{-3} and sheet resistance of 860 ohm per square were successfully deposited on glass substrates. Besides that, ohmic contacts to the ZnTe:Sb layers with Au and Mo contacts was possible. However, CdTe solar cells with ZnTe:Sb back contact interlayer were performed almost similar to those with the ZnTe/ZnTe:N interlayers (see Table 7-3 and Table 7-7).

Another successful experiment was Sb-doping of the CdTe surface to improve the solar cell performance. An efficient method, which was similar to the Sb doping of ZnTe, was used and the efficiency of CdTe solar cell was increased by 20%. With this method, solar cells with efficiency of 12.8 % and fill factor as high as 69.3 % with V_{oc} and J_{sc} of 770 mV and

24 mA/cm^2 were produced. This was the record efficiency in our group at the time when this project was performed.

9.3 MoO_x back contact

MoO_x layers were deposited by RF reactive sputtering and PVD. By changing the deposition parameters followed by photoelectron spectroscopy the optimum condition for deposition of MoO_x layers with high work-function and good electrical conductivity were determined. The interface between CdTe and different MoO_x layers (sputter and PVD deposited MoO_x layers and sputter deposited MoO_{2+x} layer) were investigated by photoelectron spectroscopy and energy band diagrams were resolved. The results of this work can be summarized as following:

- Despite the very high work-function and good conductivity of the MoO_x layers, small barrier heights to the CdTe could not be realized. The work-function difference was compensated by a large interface dipole and the Fermi level of CdTe was always pinned at 0.9 eV above the valence band.
- CdTe Solar cells prepared with the MoO_x back contact interlayers (without etching) had much better performance compared with the cells without MoO_x layer, but their performance was not higher than the NP-etched samples.
- The results of the PES experiments predicted that MoO_x layer cannot provide a low resistance contact to the CdTe but some solar cells with MoO_x back contact showed acceptable performance and series resistances as low as 7.3 Ω.cm^2 were realized. This can be explained with help of Fig. 9-1. CdTe solar cells prepared with sputtered MoO_3 or thick PVD-MoO_3 interlayer do not perform well as can be seen Fig. 9-1(a). This is due to formation an insulating layer than cannot be tunneled. In CdTe solar cells with a MoO_x interlayer, the carriers can reach to the metallic back contact via the defect states in MoO_x as shown in Fig. 9-1(b).
- In order to achieve a low resistance back contact with MoO_x buffer layer, the CdTe surface must be highly doped (e.g. by Cu) to facilitate carriers tunneling (tunneling of holes from the CdTe valence band through the interface barrier).

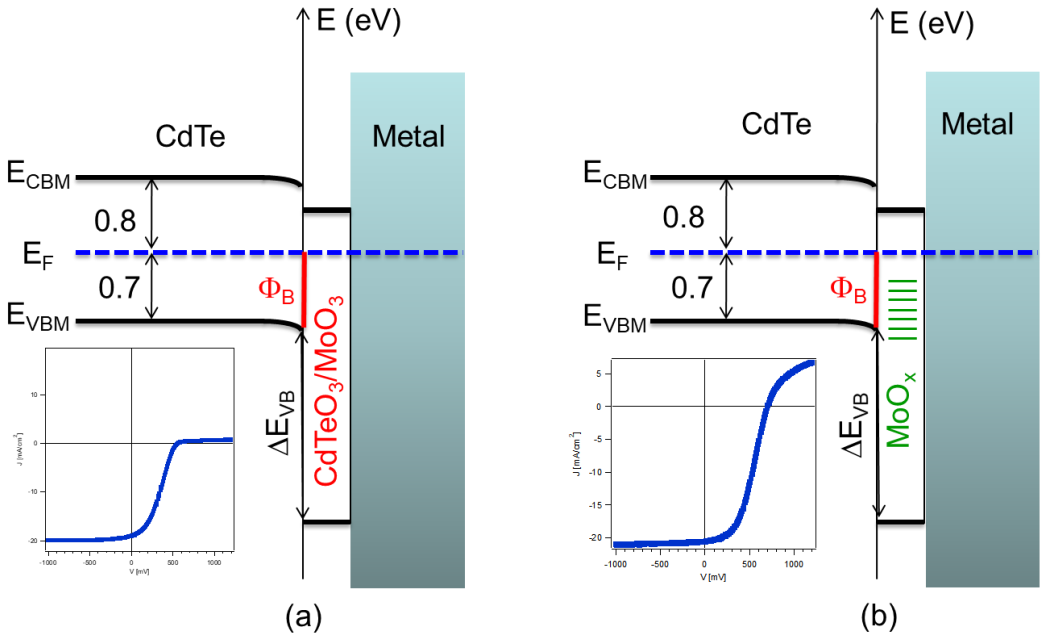

Fig. 9-1: Summary of the CdTe solar cells with MoO_x back contact interlayer.

- A very small conduction band offset was measured between MoO_x and CdTe; therefore, MoO_x buffer layers may be use in front contact to reduce or even replace the CdS layer. Another potential application could be using of a MoO_x interlayer in tandem solar cells to inject (or collect) electrons to (from) the CdTe conduction band.

9.4 Directions of further studies

Based on the results obtained in this PhD work, the chemical etching and Cu doping can be avoided when a non-oxidizing $CdCl_2$ activation is used; however, a washing with water in an ultrasonic bath before deposition of the BC-interlayer is highly recommended. In-situ p-type doping of the CdTe layer or deposition of Te-rich layers could be an alternative another subject for producing highly efficient cells in an all-dry process. Of all the intermediate layers examined, ZnTe has the highest potential to be used in cells with very thin absorber layer; however, deposition of p-type doped ZnTe layers on CdTe surface must be optimized. For this purpose, a more precise control of the substrate temperature during deposition of the layers is needed.

References

1. Green, M.A., et al., *Solar cell efficiency tables (Version 55)*. Progress in Photovoltaics: Research and Applications, 2020. **28**(1): p. 3-15.

2. Kraft, D., et al., *Alternative back contacts for CdTe solar cells: a photoemission study of the VSe2/CdTe and TiSe2/CdTe interface formation.* Thin Solid Films, 2003. **431**: p. 382-386.

3. Späth, B., et al., *Studies of sputtered ZnTe films as interlayer for the CdTe thin film solar cell.* Thin Solid Films, 2005. **480-481**: p. 204-207.

4. Tang, J., et al. *Properties of ZnTe:Cu thin films and CdS/CdTe/ZnTe solar cells*. in *Photovoltaic Specialists Conference, 1997., Conference Record of the Twenty-Sixth IEEE*. 1997.

5. Späth, B., et al., *Nitrogen doping of ZnTe and its influence on CdTe/ZnTe interfaces.* Applied Physics Letters, 2007. **90**(6): p. 062112-062112-3.

6. Späth, B., et al., *p-ZnTe for Back Contacts to CdTe Thin Film Solar Cells.* Materials Research Society Symposium Proceedings, 2005. **865**: p. F8.3.

7. Barati, A., A. Klein, and W. Jaegermann, *Deposition and characterization of highly p-type antimony doped ZnTe thin films.* Thin Solid Films, 2009. **517**(7): p. 2149-2152.

8. Kranz, L., S. Buecheler, and A.N. Tiwari, *Technological status of CdTe photovoltaics.* Solar Energy Materials and Solar Cells, 2013. **119**: p. 278-280.

9. Gessert, T.A., et al., *Research strategies toward improving thin-film CdTe photovoltaic devices beyond 20% conversion efficiency.* Solar Energy Materials and Solar Cells, 2013. **119**: p. 149-155.

10. Metzger, W.K., et al., *Exceeding 20% efficiency with in situ group V doping in polycrystalline CdTe solar cells.* Nature Energy, 2019. **4**(10): p. 837-845.

11. Kaminski, P.M., F. Lisco, and J.M. Walls, *Multilayer Broadband Antireflective Coatings for More Efficient Thin Film CdTe Solar Cells.* Ieee Journal of Photovoltaics, 2014. **4**(1): p. 452-456.

12. Chen, Q., et al., *Influence of SnO2 films with high resistance on the performance of CdTe solar cells.* Journal of Materials Science: Materials in Electronics, 2008. **20**(7): p. 661-665.

13. Paudel, N.R., et al. *CdTe cell stability vs. CdS thickness*. in *Photovoltaic Specialists Conference (PVSC), 2009 34th IEEE*. 2009.

14. Kephart, J.M., et al., *Band alignment of front contact layers for high-efficiency CdTe solar cells.* Solar Energy Materials and Solar Cells, 2016. **157**: p. 266-275.

15. Fuchs, A., et al., *Photoemission studies on undoped SnO2 buffer layers for CdTe thin film solar cells.* Energy Procedia, 2011. **10**: p. 149-154.

16. Han, J.F., et al., *Optimized chemical bath deposited CdS layers for the improvement of CdTe solar cells.* Solar Energy Materials and Solar Cells, 2011. **95**(3): p. 816-820.

17. Abou-Ras, D., et al., *Structural and chemical investigations of CBD- and PVD-CdS buffer layers and interfaces in Cu(In,Ga)Se2-based thin film solar cells.* Thin Solid Films, 2005. **480-481**: p. 118-123.

18. Feldmeier, E.M., et al., *Comparison between the structural, morphological and optical properties of CdS layers prepared by Close Space Sublimation and RF magnetron sputtering for CdTe solar cells.* Thin Solid Films, 2011. **519**(21): p. 7596-7599.

19. Romeo, N., et al., *Low resistivity CdS thin films grown by r.f. sputtering in an Ar-H2 atmosphere.* Solar Cells, 1987. **22**(1): p. 23-27.

20. Schaffner, J., et al., *12% efficient CdTe/CdS thin film solar cells deposited by low-temperature close space sublimation.* Journal of Applied Physics, 2011. **110**(6): p. 064508-064508-6.

21. Islam, M.A., et al., *Fabrication of high efficiency sputtered CdS:O/CdTe thin film solar cells from window/absorber layer growth optimization in magnetron sputtering.* Solar Energy Materials and Solar Cells, 2017. **172**: p. 384-393.

22. Gupta, A., et al., *Oxygenated CdS Window Layer for Sputtered CdS/CdTe Solar Cells.* MRS Proceedings, 2003. **763**: p. B8.9.

23. Islam, M.A., et al., *Investigation for Optimum Structure of CdS:O/CdTe Solar Cell from Numerical Analysis.* Advanced Materials Research, 2013. **622-623**: p. 1194-1198.

24. Powalla, M., et al., *Thin-film solar cells exceeding 22% solar cell efficiency: An overview on CdTe-, Cu(In,Ga)Se-2-, and perovskite-based materials.* Applied Physics Reviews, 2018. **5**(4).

25. Poplawsky, J.D., et al., *Structural and compositional dependence of the CdTexSe1 - x alloy layer photoactivity in CdTe-based solar cells (vol 7, pg 12537, 2016)*. Nature Communications, 2016. **7**.

26. Paudel, N.R., et al., *Current Enhancement of CdTe-Based Solar Cells.* IEEE Journal of Photovoltaics, 2015. **5**(5): p. 1492-1496.

27. Madelung, O., ed. *Semiconductors Basic Data (2nd ed.)*. 1996, Springer Verlag: Berlin.

28. Geisthardt, R.M., M. Topic, and J.R. Sites, *Status and Potential of CdTe Solar-Cell Efficiency*. Ieee Journal of Photovoltaics, 2015. **5**(4): p. 1217-1221.

29. Sze, S.M. and K.K. Ng, *Physics of semiconductor devices*. 2007. p. x, 815 pages.

30. Sites, B.E.M.a.J.R., *Cadmium Telluride Solar Cells.* book ch.14, 2003.

31. Amin, N., et al., *Prospects of Thickness Reduction of the CdTe Layer in Highly Efficient CdTe Solar Cells Towards 1 μm.* Japanese Journal of Applied Physics, 1999. **38**(Part 1, No. 8): p. 4666-4672.

32. Luschitz, J., et al., *Growth regimes of CdTe deposited by close-spaced sublimation for application in thin film solar cells.* Thin Solid Films, 2007. **515**(15): p. 5814-5818.

33. McCandless, B.E., R.W. Birkmire, and W.A. Buchanan. *Vapor transport deposition of cadmium telluride films*. in *Conference Record of the Twenty-Ninth IEEE Photovoltaic Specialists Conference, 2002.* 2002.

34. Romeo, A., et al., *High-efficiency flexible CdTe solar cells on polymer substrates.* Solar Energy Materials and Solar Cells, 2006. **90**(18-19): p. 3407-3415.

35. Moutinho, H.R., et al., *Investigation of Polycrystalline Cdte Thin-Films Deposited by Physical Vapor-Deposition, Close-Spaced Sublimation, and Sputtering.* Journal of Vacuum Science & Technology a-Vacuum Surfaces and Films, 1995. **13**(6): p. 2877-2883.

36. Soliman, M.M., M.M. Shabana, and F. Abulfotuh, *CdS/CdTe solar cell using sputtering technique.* Renewable Energy, 1996. **8**(1-4): p. 386-389.

37. Kartopu, G., et al., *Study of thin film poly-crystalline CdTe solar cells presenting high acceptor concentrations achieved by in-situ arsenic doping.* Solar Energy Materials and Solar Cells, 2019. **194**: p. 259-267.

38. Burst, J.M., et al., *CdTe solar cells with open-circuit voltage breaking the 1 V barrier (vol 1, 16015, 2016)*. Nature Energy, 2016. **1**.

39. McCandless, B.E., et al., *Overcoming Carrier Concentration Limits in Polycrystalline CdTe Thin Films with In Situ Doping.* Scientific Reports, 2018. **8**.

40. Burgelman, M., P. Nollet, and S. Degrave, *Modelling polycrystalline semiconductor solar cells.* Thin Solid Films, 2000. **361**: p. 527-532.

41. Sites, J.R. and P.H. Mauk, *Diode Quality Factor Determination for Thin-Film Solar-Cells.* Solar Cells, 1989. **27**(1-4): p. 411-417.

42. Oman, D.M., et al., *Reduction of Recombination Current in Cdte/Cds Solar-Cells.* Applied Physics Letters, 1995. **67**(13): p. 1896-1898.

43. Niemegeers, A. and M. Burgelman, *Effects of the Au/CdTe back contact on IV and CV characteristics of Au/CdTe/CdS/TCO solar cells.* Journal of Applied Physics, 1997. **81**(6): p. 2881-2886.

44. Kephart, J.M., et al., *Reduction of window layer optical losses in CdS/CdTe solar cells using a float-line manufacturable HRT layer.* 2013 Ieee 39th Photovoltaic Specialists Conference (Pvsc), 2013: p. 1653-1657.

45. Friesen, G., M.E. Ozsar, and E.D. Dunlop, *Impedance model for CdTe solar cells exhibiting constant phase element behaviour.* Thin Solid Films, 2000. **361**: p. 303-308.

46. Kaufmann, E.N., *Characterization of materials*. Second edition ed. 2003. 3 volumes.

47. Technologies, A., *Agilent Impedance Measurement Handbook 4th Edition.* 2009.

48. Klein, A. and F. Säuberlich, *Surfaces and Interfaces of Sputter-Deposited ZnO Films*, in *Transparent Conductive Zinc Oxide*, K. Ellmer, A. Klein, and B. Rech, Editors. 2008, Springer Berlin Heidelberg: Berlin, Heidelberg. p. 125-185.

49. Andreas Klein, T.M., Andreas Thissen, Wolfram Jaegermann, *Photoelectron Spectroscopy in Materials Science and Physical Chemistry.* BUNSEN-MAGAZIN, 2008. **10. JAHRGANG**: p. 124-139.

50. Sze, S.M. and K.K. Ng, *Physics of semiconductor devices*. 2007, Hoboken, N.J.: Wiley-Interscience.

51. Brandon, D.G. and W.D. Kaplan, *Microstructural characterization of materials*. 2008, Chichester, England: John Wiley.

52. Tendler, S.B.J. and P.M. Williams, *Atomic force microscopy*. 2003, Amsterdam; New York: Elsevier.

53. Lyman, C.E., *Scanning electron microscopy, X-ray microanalysis, and analytical electron microscopy : a laboratory workbook*. 1990, New York: Plenum Press.

54. Meyers P, L.C., Frey T, *Heterojunction p-i-n photovoltaic cell.* U. S. Patent, 1987. **4, 710, 589**.

55. McCandless, B.E., L.W. Moulton, and R.W. Birkmire, *Recrystallization and Sulfur Diffusion in $CdCl_2$ Treated CdTe/CdS Thin Film Solar Cells.* Progress in Photovoltaics: Research and Applications, 1997. **5**: p. 249-260.

56. Rimmaudo, I., A. Salavei, and A. Romeo, *Effects of activation treatment on the electrical properties of low temperature grown CdTe devices.* Thin Solid Films, 2013. **535**: p. 253-256.

57. Potlog, T., et al., *Influence of annealing in different chlorides on the photovoltaic parameters of CdS/CdTe solar cells.* Solar Energy Materials and Solar Cells, 2003. **80**(3): p. 327-334.

58. Romeo, A., et al., *Recrystallization in CdTe/CdS.* Thin Solid Films, 2000. **361**: p. 420-425.

59. Tiwari, A.N., et al., *CdTe solar cell in a novel configuration.* Progress in Photovoltaics, 2004. **12**(1): p. 33-38.

60. Jaehyung, L., et al. *Comparative study of CdTe thin film solar cells with wet and dry $CdCl_2$ treatment process*. in *Photovoltaic Specialists Conference (PVSC), 2010 35th IEEE*. 2010.

61. McCandless, B.E., I. Youm, and R.W. Birkmire, *Optimization of vapor post-deposition processing for evaporated CdS/CdTe solar cells.* Progress in Photovoltaics: Research and Applications, 1999. **7**: p. 21-30.

62. Moutinho, H.R., et al., *Alternative procedure for the fabrication of close-spaced sublimated CdTe solar cells.* Journal of Vacuum Science & Technology a-Vacuum Surfaces and Films, 2000. **18**(4): p. 1599-1603.

63. Yoxa Mahathongdy, D.S.A., Colin A. Wolden, and R.M. Baldwin, *Vapor CdCl2–Optimization and Screening Experiments for an All Dry Chloride Treatment of CdS/CdTe Solar Cells.* NREL/CP, 1998. **520**(25495).

64. Schulmeyer, T., et al., *Effect of in situ UHVCdCl2-activation on the electronic properties of CdTe thin film solar cells.* Thin Solid Films, 2003. **431**: p. 84-89.

65. Rios-Flores, A., et al., *A study of vapor CdCl2 treatment by CSS in CdS/CdTe solar cells.* Solar Energy, 2010. **84**(6): p. 1020-1026.

66. Hernández-Fenollosa, M.A., et al., *Photoluminescence studies of CdS/CdTe solar cells treated with oxygen.* Thin Solid Films, 2003. **431-432**: p. 176-180.

67. Edwards, P.R., et al., *A comparative EBIC study of CdTe solar cell activation using CdCl2 and Cl2.* Thin Solid Films, 2001. **387**(1-2): p. 189-191.

68. Mazzamuto, S., et al., *A study of the CdTe treatment with a Freon gas such as CHF2Cl.* Thin Solid Films, 2008. **516**(20): p. 7079-7083.

69. Vaillant, L., et al., *Interface properties of HCF2Cl annealed CdTe thin films for solar cells applications.* Thin Solid Films, 2008. **516**(20): p. 7075-7078.

70. Romeo, A., et al., *Study of CSS- and HVE-CdTe by different recrystallization processes.* Thin Solid Films, 2009. **517**(7): p. 2132-2135.

71. Salavei, A., et al., *Study of difluorochloromethane activation treatment on low substrate temperature deposited CdTe solar cells.* Solar Energy Materials and Solar Cells, 2013. **112**: p. 190-195.

72. Romeo, N., A. Bosio, and A. Romeo, *An innovative process suitable to produce high-efficiency CdTe/CdS thin-film modules.* Solar Energy Materials and Solar Cells, 2010. **94**(1): p. 2-7.

73. Kim, M.J., et al., *Study of CdTe/CdS heterostructure by CdCl2 heat treatment via in situ high temperature XRD.* Solar Energy Materials and Solar Cells, 2013. **109**: p. 209-214.

74. Kim, M., S. Sohn, and S. Lee, *Reaction kinetics study of CdTe thin films during CdCl2 heat treatment.* Solar Energy Materials and Solar Cells, 2011. **95**(8): p. 2295-2301.

75. Terheggen, M., et al., *Structural and chemical interface characterization of CdTe solar cells by transmission electron microscopy.* Thin Solid Films, 2003. **431**: p. 262-266.

76. Fritsche, J., A. Klein, and W. Jaegermann, *Thin film solar cells: Materials science at interfaces.* Advanced Engineering Materials, 2005. **7**(10): p. 914-920.

77. Pookpanratana, S., et al., *Effects of postdeposition treatments on surfaces of CdTe/CdS solar cells.* Applied Physics Letters, 2010. **97**(17): p. 172109-172109-3.

78. Huang, S., et al., *Effects of thermal annealing on the interface morphology of CdTe/CdS heterojunctions.* Journal of Vacuum Science & Technology a-Vacuum Surfaces and Films, 2001. **19**(5): p. 2181-2185.

79. Romeo, A., et al., *Influence of CdS growth process on structural and photovoltaic properties of CdTe/CdS solar cells.* Solar Energy Materials and Solar Cells, 2001. **67**(1-4): p. 311-321.

80. Luschitz, J., et al. *CdTe solar cells: Nucleation, structure, and performance*. in *Photovoltaic Specialists Conference, 2008. PVSC '08. 33rd IEEE*. 2008.

81. Luschitz, J., et al., *CdTe thin film solar cells: Interrelation of nucleation, structure, and performance.* Thin Solid Films, 2009. **517**(7): p. 2125-2131.

82. Fischer, A., et al. *Interdiffusion of CdS/CdTe in laser-deposited and RF sputtered alloys, bilayers and solar cells*. in *Photovoltaic Specialists Conference, 1996., Conference Record of the Twenty Fifth IEEE*. 1996.

83. Gomez-Barojas, E., R. Silva-Gonzalez, and J. Pantoja-Enriquez, *Determination of the interdiffusion coefficient for the CdS/CdTe heteroestructure by AES sputter depth profiling.* Solar Energy Materials and Solar Cells, 2006. **90**(15): p. 2235-2240.

84. Enriquez, J.P., et al., *S and Te inter-diffusion in CdTe/CdS hetero junction.* Solar Energy Materials and Solar Cells, 2007. **91**(15-16): p. 1392-1397.

85. Metzger, W.K., et al., *CdCl2 treatment, S diffusion, and recombination in polycrystalline CdTe.* Journal of Applied Physics, 2006. **99**(10): p. 103703.

86. Das, S.K., *Characterization of Cdcl2 Treated Electrodeposited Cds/Cdte Thin-Film Solar-Cell.* Solar Energy Materials and Solar Cells, 1993. **29**(3): p. 277-287.

87. Ringel, S.A., et al., *The effects of CdCl2on the electronic properties of molecular-beam epitaxially grown CdTe/CdS heterojunction solar cells.* Journal of Applied Physics, 1991. **70**(2): p. 881-889.

88. Grecu, D. and A.D. Compaan, *Rutherford backscattering study of sputtered CdTe/CdS bilayers.* Journal of Applied Physics, 2000. **87**(4): p. 1722-1726.

89. Krishna, K.V. and V. Dutta, *Effect ofin situCdCl2 treatment on spray deposited CdTe/CdS heterostructure.* Journal of Applied Physics, 2004. **96**(7): p. 3962-3971.

90. Fritsche, J., et al., *Interface modification of CdTe thin film solar cells by CdCl2-activation.* Thin Solid Films, 2003. **431**: p. 267-271.

91. Lourenco, M.A., et al., *Deep level transient spectroscopy of CdS/CdTe thin film solar cells.* Journal of Applied Physics, 1997. **82**(3): p. 1423-1426.

92. Castaldini, A., et al., *Deep energy levels in CdTe and CdZnTe.* Journal of Applied Physics, 1998. **83**(4): p. 2121-2126.

93. Balcioglu, A., R.K. Ahrenkiel, and F. Hasoon, *Deep-level impurities in CdTe/CdS thin-film solar cells.* Journal of Applied Physics, 2000. **88**(12): p. 7175-7178.

94. Ringel, S.A., et al., *The Effects of Cdcl2 on the Electronic-Properties of Molecular-Beam Epitaxially Grown Cdte/Cds Heterojunction Solar-Cells.* Journal of Applied Physics, 1991. **70**(2): p. 881-889.

95. Klein, A., et al., *A Photoemission-Study of Barrier and Transport-Properties of the Interfaces of Au and Cu with Wse2(0001) Surfaces.* Surface Science, 1994. **321**(1-2): p. 19-31.

96. Alonso, M., R. Cimino, and K. Horn, *Surface photovoltage effects in photoemission from metal-GaP(110) interfaces: Importance for band bending evaluation.* Phys Rev Lett, 1990. **64**(16): p. 1947-1950.

97. Kraft, D., *Präparation und Charakterisierung von Dunnschichtmaterialsystemen für die Ruckkontaktbildung bei Polykristallinen CdTe-Dunnschichtsolarzellen.* TU Darmstadt, 2004.

98. Kraft, D., et al., *Characterization of tellurium layers for back contact formation on close to technology treated CdTe surfaces.* Journal of Applied Physics, 2003. **94**(5): p. 3589-3598.

99. Komin, V., et al., *The effect of the CdCl2 treatment on CdTe/CdS thin film solar cells studied using deep level transient spectroscopy.* Thin Solid Films, 2003. **431**: p. 143-147.

100. B.E. McCandless, H.H., G. Hanket, R.W. Birkmire, *VAPOR PHASE TREATMENT OF CdTdCdS THIN FILMS WITH CdCl2:O2.* 25th PVSC, 1996: p. 781.

101. Nakamura, K., et al., *Influence of CdCl2Treatment on Structural and Electrical Properties of Highly Efficient 2-μm-Thick CdS/CdTe Thin Film Solar Cells.* Japanese Journal of Applied Physics, 2002. **41**(Part 1, No. 7A): p. 4474-4480.

102. Valdna, V., *Optoelectronic properties of chlorine- and oxygen-doped CdTe thin films.* Solar Energy Materials and Solar Cells, 2005. **87**(1-4): p. 369-373.

103. Emziane, M., et al., *In situ oxygen incorporation and related issues in CdTe/CdS photovoltaic devices.* Journal of Applied Physics, 2006. **100**(1): p. 013513-3.

104. Emziane, M., et al., *Efficiency improvement in thin-film solar cell devices with oxygen-containing absorber layer.* Applied Physics Letters, 2005. **87**(26): p. 261901-261901-2.

105. Komin, V., et al. *Identification of defect levels in CdTe/CdS solar cells using deep level transient spectroscopy*. in *Photovoltaic Specialists Conference, 2002. Conference Record of the Twenty-Ninth IEEE*. 2002.

106. Krishnakumar, V., Barati, A., Schimper,H. J., Klein, A., Jaegermann, W., *A possible way to reduce absorber layer thickness in thin film CdTe solar cells.* Thin Solid Films, 2013. **535**: p. 233-236.

107. Zhao, H., et al., *The effect of impurities on the doping and VOC of CdTe/CdS thin film solar cells.* Thin Solid Films, 2009. **517**(7): p. 2365-2369.

108. Lalitha, S., et al., *Influence of CdCl2 treatment on structural and optical properties of vacuum evaporated CdTe thin films.* Solar Energy Materials and Solar Cells, 2006. **90**(6): p. 694-703.

109. Emziane, M., et al., *A combined SIMS and ICPMS investigation of the origin and distribution of potentially electrically active impurities in CdTe/CdS solar cell structures.* Semiconductor Science and Technology, 2005. **20**(5): p. 434-442.

110. Emziane, M., et al., *Effect of CdCl2 activation on the impurity distribution in CdTe/CdS solar cell structures.* Thin Solid Films, 2005. **480**: p. 377-381.

111. Soo, J.L., et al., *Annealing effects and Te mixing in CdTe/CdS heterojunctions.* Applied Physics Letters, 1999. **74**(2): p. 218-220.

112. Hegedus, S.S. and W.N. Shafarman, *Thin-film solar cells: Device measurements and analysis.* Progress in Photovoltaics, 2004. **12**(2-3): p. 155-176.

113. Britt, J. and C. Ferekides, *Thin-Film Cds/Cdte Solar-Cell with 15.8-Percent Efficiency.* Applied Physics Letters, 1993. **62**(22): p. 2851-2852.

114. Burgelman, M., et al., *Analysis of CdTe solar cells in relation to materials issues.* Thin Solid Films, 2005. **480**: p. 392-398.

115. Degrave, S., M. Burgelman, and P. Nollet. *Modelling of polycrystalline thin film solar cells: new features in SCAPS version 2.3*. in *Photovoltaic Energy Conversion, 2003. Proceedings of 3rd World Conference on*. 2003.

116. Proskuryakov, Y.Y., et al., *Impedance spectroscopy of unetched CdTe/CdS solar cells-equivalent circuit analysis.* Journal of Applied Physics, 2007. **102**(2): p. -.

117. Cwil, M., et al., *Capacitance profiling in the CIGS solar cells.* Thin Solid Films, 2007. **515**(15): p. 6229-6232.

118. Proskuryakov, Y.Y., et al., *Impedance spectroscopy of thin-film CdTe/CdS solar cells under varied illumination.* Journal of Applied Physics, 2009. **106**(4): p. -.

119. Proskuryakov, Y.Y., et al., *Doping levels, trap density of states and the performance of co-doped CdTe(As,Cl) photovoltaic devices.* Solar Energy Materials and Solar Cells, 2009. **93**(9): p. 1572-1581.

120. Jun-feng, H., et al., *CdS annealing treatments in various atmospheres and effects on performances of CdTe/CdS solar cells.* Journal of Materials Science: Materials in Electronics, 2013. **24**(8): p. 2695-2700.

121. de Moure-Flores, F., et al., *Effect of the immersion in CdCl2 and annealing on physical properties of CdS:F films grown by CBD.* Journal of Physics and Chemistry of Solids, 2013. **74**(4): p. 611-615.

122. Kampmann, A. and D. Lincot, *Photoelectrochemical study of thin film semiconductor heterostructures: Junction formation processes in CdS vertical bar CdTe solar cells.* Journal of Electroanalytical Chemistry, 1996. **418**(1-2): p. 73-81.

123. Valdna, V., F. Buschmann, and E. Mellikov, *Conductivity conversion in CdTe layers.* Journal of Crystal Growth, 1996. **161**(1-4): p. 164-167.

124. Visoly-Fisher, I., et al., *How polycrystalline devices can outperform single-crystal ones: Thin film CdTe/CdS solar cells.* Advanced Materials, 2004. **16**(11): p. 879-883.

125. Li, C., et al., *Grain-Boundary-Enhanced Carrier Collection in CdTe Solar Cells.* Physical Review Letters, 2014. **112**(15).

126. Tuteja, M., et al., *Direct Observation of CdCl2 Treatment Induced Grain Boundary Carrier Depletion in CdTe Solar Cells Using Scanning Probe Microwave Reflectivity Based Capacitance Measurements.* Journal of Physical Chemistry C, 2016. **120**(13): p. 7020-7024.

127. Brooks, W.S.M., S.J.C. Irvine, and D.M. Taylor, *Scanning Kelvin probe measurements on As-doped CdTe solar cells.* Semiconductor Science and Technology, 2013. **28**(10).

128. Klein, A., et al., *Non-stoichiometry and electronic properties of interfaces.* Journal of Materials Science, 2007. **42**(6): p. 1890-1900.

129. Sarlund, J., et al., *Characterization of etching procedure in preparation of CdTe solar cells.* Solar Energy Materials and Solar Cells, 1996. **44**(2): p. 177-190.

130. Bätzner, D.L., et al., *A study of the back contacts on CdTe/CdS solar cells.* Thin Solid Films, 2000. **361-362**: p. 463-467.

131. Li, X.N., et al., *Effect of nitric-phosphoric acid etches on material properties and back-contact formation of CdTe-based solar cells.* Journal of Vacuum Science & Technology a-Vacuum Surfaces and Films, 1999. **17**(3): p. 805-809.

132. Han, J.F., et al., *Electrical properties of the CdTe back contact: A new chemically etching process based on nitric acid/acetic acid mixtures.* Applied Surface Science, 2010. **256**(20): p. 5803-5806.

133. Kraft, D., et al., *Electronic Properties of Chemically Etched CdTe Thin Films: Role of Te for Back-Contact Formation.* MRS Proceedings, 2001. **668**.

134. Amin, N., A. Yamada, and M. Konagai, *Effect of ZnTe and CdZnTe alloys at the back contact of 1-mu m-thick CdTe thin film solar cells.* Japanese Journal of Applied Physics Part 1-Regular Papers Short Notes & Review Papers, 2002. **41**(5a): p. 2834-2841.

135. Amin, N., A. Yamada, and M. Konagai. *ZnTe insertion at the back contact of 1 μm-CdTe thin film solar cells*. in *Photovoltaic Specialists Conference, 2000. Conference Record of the Twenty-Eighth IEEE*. 2000.

136. Avachat, U.S. and N.G. Dhere, *Preparation and characterization of transparent conducting ZnTe : Cu back contact interface layer for CdS/CdTe solar cell for photoelectrochemical application.* Journal of Vacuum Science & Technology A, 2006. **24**(4): p. 1664-1667.

137. B. Späth, J.F., F. S7uberlich, A. Klein, W. Jaegermann, *Studies of sputtered ZnTe films as interlayer for the CdTe thin film solar cell.* Thin Solid Films, 2005. **480–481**: p. 204–207.

138. Compaan, A.D., et al., *High efficiency, magnetron sputtered CdS/CdTe solar cells.* Solar Energy, 2004. **77**(6): p. 815-822.

139. Spath, B., et al., *Nitrogen doping of ZnTe and its influence on CdTe/ZnTe interfaces.* Applied Physics Letters, 2007. **90**(6): p. -.

140. Yun, J.H., et al., *Back contact formation usingCU(2)Te as a Cu-doping source and as an electrode in CdTe solar cells.* Solar Energy Materials and Solar Cells, 2003. **75**(1-2): p. 203-210.

141. Spath, B., et al., *Surface science studies of Cu containing back contacts for CdTe solar cells.* Thin Solid Films, 2007. **515**(15): p. 6172-6174.

142. Turck, J., et al., *Cu2S as ohmic back contact for CdTe solar cells.* Thin Solid Films, 2015. **582**: p. 336-339.

143. Turck, J., et al., *Copper (I) Oxide (Cu2O) based back contact for p-i-n CdTe solar cells.* Progress in Photovoltaics, 2016. **24**(9): p. 1229-1236.

144. Niles, D.W., et al., *Evaporated Te on CdTe: A vacuum-compatible approach to making back contact to CdTe solar cell devices.* Progress in Photovoltaics, 1996. **4**(3): p. 225-229.

145. Romeo, N., et al., *Back contacts to CSSCdS/CdTe solar cells and stability of performances.* Thin Solid Films, 2000. **361**: p. 327-329.

146. Schmidt, T., et al., *Chemical stability of Sb2Te3 back contacts to CdS/CdTe solar cells.* Thin Solid Films, 2000. **361**: p. 383-387.

147. Batzner, D.L., et al., *Development of efficient and stable back contacts on CdTe/CdS solar cells.* Thin Solid Films, 2001. **387**(1-2): p. 151-154.

148. Abken, A.E. and O.J. Bartelt, *Sputtered Mo/Sb2Te3 and Ni/Sb2Te3 layers as back contacts for CdTe/CdS solar cells.* Thin Solid Films, 2002. **403**: p. 216-222.

149. Du, M.H., *First-principles study of back-contact effects on CdTe thin-film solar cells.* Physical Review B, 2009. **80**(20).

150. Kraft, D., et al., *Chemical and Electronic Properties of Metal/Sb2Te3/ CdTe Contacts for CdTe Thin Film Solar Cells Studied by Photoelectron Spectroscopy.* Materials Research Society Symposium Proceedings, 2003. **763**: p. B3.3.

151. Du, S., et al., *Bilayered ZnTe/Cu1.4Te alloy thin films as a back contact for CdTe solar cells.* Solar Energy, 2019. **185**: p. 262-269.

152. Lin, H., et al., *CdS/CdTe solar cells with MoOx as back contact buffers.* Applied Physics Letters, 2010. **97**(12).

153. Lin, H., et al., *MoOx back contact for CdS/CdTe thin film solar cells: Preparation, device characteristics, and stability.* Solar Energy Materials and Solar Cells, 2012. **99**: p. 349-355.

154. Gretener, C., et al., *Development of MoOx thin films as back contact buffer for CdTe solar cells in substrate configuration.* Thin Solid Films, 2013. **535**: p. 193-197.

155. He, F., et al., *Characterization of sputtered MoOx thin films with different oxygen content and their application as back contact in CdTe solar cells.* Vacuum, 2020. **176**.

156. Kindvall, A., J. Kephart, and W. Sampath, *Molybdenum Oxide and Molybdenum Nitride Back Contacts for Thin-Film CdTe Solar Cells.* 2017 Ieee 44th Photovoltaic Specialist Conference (Pvsc), 2017: p. 785-790.

157. Rejon, V., et al., *The CdS/CdTe Solar Cells With Reactively Sputtered a-MoOx/Mo Back Contact.* 2015 Ieee 42nd Photovoltaic Specialist Conference (Pvsc), 2015.

158. Paudel, N.R., C.X. Xiao, and Y.F. Yan, *CdS/CdTe thin-film solar cells with Cu-free transition metal oxide/Au back contacts.* Progress in Photovoltaics, 2015. **23**(4): p. 437-442.

159. Drayton, J.A., et al., *Molybdenum oxide and molybdenum oxide-nitride back contacts for CdTe solar cells.* Journal of Vacuum Science & Technology A, 2015. **33**(4).

160. Paudel, N.R., A.D. Compaan, and Y.F. Yan, *Ultrathin CdTe Solar Cells with MoO3-x/Au Back Contacts.* Journal of Electronic Materials, 2014. **43**(8): p. 2783-2787.

161. Paudel, N.R., et al., *CdS/CdTe thin-film solar cells with Cu-free MoO3-x/Au back contacts.* 2013 Ieee 39th Photovoltaic Specialists Conference (Pvsc), 2013: p. 1161-1164.

162. Paudel, N.R., A.D. Compaan, and Y. Yan, *Sputtered CdS/CdTe solar cells with MoO3-x/Au back contacts.* Solar Energy Materials and Solar Cells, 2013. **113**: p. 26-30.

163. Xiao, D., et al., *CdTe thin film solar cell with NiO as a back contact buffer layer.* Solar Energy Materials and Solar Cells, 2017. **169**: p. 61-67.

164. Yang, J.Y., et al., *Optoelectrical Properties and Back Contact Characteristic of VSe2 Thin Films.* Journal of Inorganic Materials, 2013. **28**(3): p. 312-316.

165. Shu, T.Y., et al., *Determination of band alignment at the CdTe/SnTe heterojunction interface for CdTe thin-film solar cells.* Epl, 2019. **127**(3).

166. Li, X., et al., *CdTe thin film solar cells with copper iodide as a back contact buffer layer.* Solar Energy, 2019. **185**: p. 324-332.

167. Zakutayev, A., Tate, J., Platt, H. A. S., Keszler, D. A., Barati, A., and A. Klein, Jaegermann, W., *Band alignment at the BaCuSeF/ZnTe interface.* Applied Physics Letters, 2010. **96**(16): p. 162110-162110-3.

168. Zakutayev, A., Tate, J.,Xie, S. J.,Gibbons, B. J.,Platt, H. A. S.,Keszler, D. A.,Barati, A.,Klein, A.,Jaegermann, W., *Interdiffusion at the BaCuSeF/ZnTe interface.* Thin Solid Films, 2011. **519**(21): p. 7369-7373.

169. Chu, T.L., et al. *Mercury telluride as an ohmic contact to efficient thin film cadmium telluride solar cells*. in *Photovoltaic Specialists Conference, 1988., Conference Record of the Twentieth IEEE*. 1988.

170. Asa, G. and Y. Nemirovsky, *Properties of Metal Organic Chemical Vapour Deposition HgTe Contacts on p-type CdTe.* Journal of Applied Physics, 1995. **77**: p. 4417.

171. Hanafusa, A., T. Aramoto, and A. Morita, *Performance of Graphite Pastes Doped with Various Materials as Back Contact for CdS/CdTe Solar Cell.* Japanese Journal of Applied Physics, 2001. **40**(Part 1, No. 12): p. 6764-6769.

172. Yang, P., et al., *Study on graphite paste for back contact of CdTe thin film solar cells and modules.* Taiyangneng Xuebao/Acta Energiae Solaris Sinica, 2009. **30**: p. 137-140.

173. Bellakhder, H., A. Outzourhit, and E.L. Ameziane, *Study of ZnTe thin films deposited by r.f. sputtering.* Thin Solid Films, 2001. **382**(1-2): p. 30-33.

174. Kashyout, A.B., et al., *Influence of annealing temperature on the opto-electronic characteristics of ZnTe electrodeposited semiconductors.* Materials Chemistry and Physics, 1997. **51**(2): p. 130-134.

175. Sato, K. and S. Adachi, *Optical-Properties of Znte.* Journal of Applied Physics, 1993. **73**(2): p. 926-931.

176. Dennis Rioux1, D.W.N., and Hartmut Höchst1, *ZnTe: A potential interlayer to form low resistance back contacts in CdS/CdTe solar cells.* J. Appl. Phys. 73 (12), 1.5 June 1993, 1993.

177. Islam, A.B.M.O., et al., *Development of electrodeposited ZnTe layers as window materials in ZnTe/CdTe/CdHgTe multi-layer solar cells.* Materials Characterization, 2009. **60**(2): p. 160-163.

178. Späth, B., *Rückkontaktbildung von CdTe-Solarzellen.* TU Darmstadt, 2007.

179. Drayton, J., et al., *Properties of RF sputtered ZnTe:N films for back contact to CdS/CdTe solar cells.* Materials Research Society Symposium Proceedings, 2001. **668**: p. H5.9.

180. Spath, B., et al., *Nitrogen doping of ZnTe and its influence on CdTe/ZnTe interfaces.* Applied Physics Letters, 2007. **90**(6).

181. Luo, M., et al., *Photoluminescence of ZnTe and ZnTe : Cr grown by molecular-beam epitaxy.* Journal of Applied Physics, 2005. **97**(1).

182. Ibrahim, A.A., et al., *Structural and electrical properties of evaporated ZnTe thin films.* Vacuum, 2004. **75**(3): p. 189-194.

183. W. Jaegermann, A. Klein, K. Velappan, H. Schimper, A. Barati, *Bildung eines niederohmschen Kontaktes auf II-VI-Halbleitern durch Behandlung mit Metallhalogeniden.* UNIV TECH DARMSTADT 2014. **DE Patent Nr. DE102014101584-A1**.

184. *Vapor pressure data*. Available from: https://www.mbe-komponenten.de/selection-guide/vapor-pressure.php.

185. Herndon, M.K., et al., *Evidence for grain-boundary-assisted diffusion of sulfur in polycrystalline CdS/CdTe heterojunctions.* Applied Physics Letters, 1999. **75**(22): p. 3503-3505.

186. Lin, H., et al., *CdS/CdTe solar cells with MoOx as back contact buffers.* Applied Physics Letters, 2010. **97**(12): p. -.

Appendix A

SEM and EDX analysis of NP-etched sample

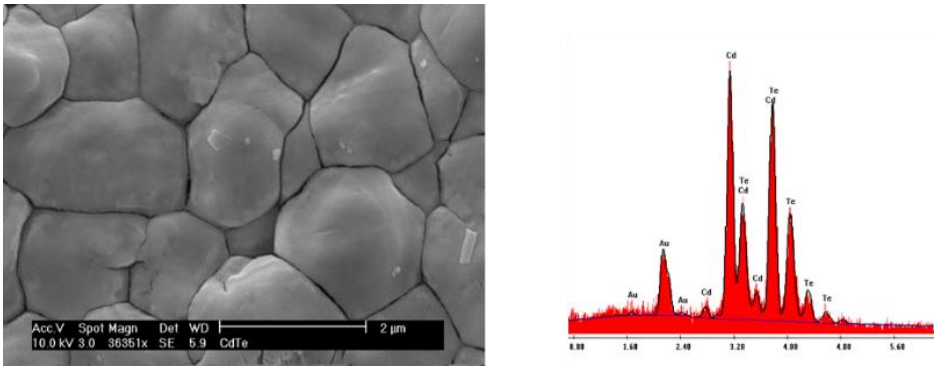

Fig. A.1: SEM image and EDX results of an NP-etched glass/ITO/SnO2/CdS/CdTe sample. The SEM image showed obvious preferential etching around grain boundaries. Formation of an elemental Te layer on top of the CdTe surface was confirmed by EDX.

XRD results of non-activated and activated samples

Table A.1: X-ray diffraction intensities and the texture coefficient of the non-activated and activated glass/FTO/CdS/CdTe samples from Fig. 5-11. Intensities of a powder sample (JCPDS file No. 65-880) are also added as a reference.

	Powder	Non-activated		Activated	
(hkl)	I_{ref}	$I_{non\text{-}act}$	C_{hkl}	I_{act}	C_{hkl}
(111)	100	100	1.10	100	1.00
(220)	65.73	39.68	0.66	45.14	0.69
(311)	37.98	88.89	2.57	94.85	2.49
(400)	9.12	3.64	0.44	4.36	0.48
(331)	12.93	5.57	0.47	6.1	0.47
(422)	15.53	14.5	1.03	17.03	1.09
(511)	7.92	8.06	1.12	9.3	1.17
(440)	4.11	2.09	0.56	2.33	0.57
(531)	6.81	6.48	1.05	7.14	1.05

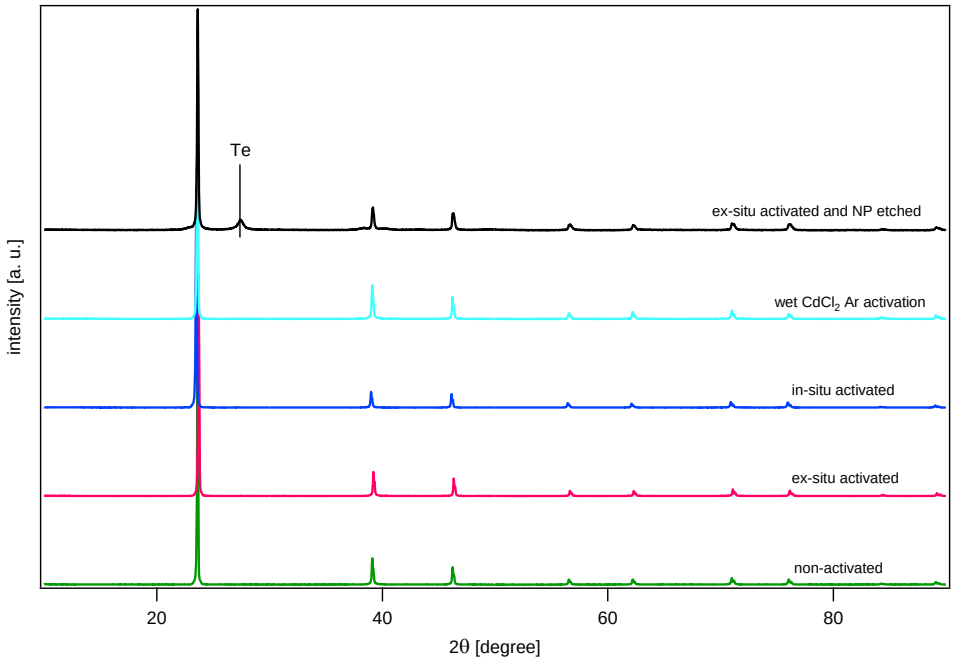

Fig. A.2: XRD patterns of non-activated, activated and NP-etched glass/ITO/SnO_2/CdS/CdTe samples. Since all samples were deposited by CSS at high substrate temperature, the non-activated and activated samples had almost similar structure. The NP-etched sample shows extra signal, which is related to the formation of an elemental Te layer.

XPS study of inter-diffusion at the CdS/CdTe interface

In order to investigate the effect of the in-situ activation on the CdS/CdTe interface, a sample was analyzed by XPS depth profiling before and after the in-situ activation. Survey and core levels spectra of the sample were measured after stepwise sputtering with 1 keV argon ions. The sample current and the raster size were 0.9 μA and 4 mm^2, respectively; this corresponds to a sputter rate of about 7 nm/min. For the XPS depth profile experiment the sample had to be thin and smooth therefore a CdS layer (~ 300 nm) and a CdTe layer (~ 300 nm) were deposited onto a glass/ITO/SnO_2 substrate at low substrate temperature of 350 °C.

Fig. A.3 shows the normalized peak area of the S 2p and Te $3d_{5/2}$ core levels versus the sputter time before and after the activation. The width of the inter-mixing region was increased from ~140 nm for the as-deposited sample to ~200 nm for the activated sample. The width of the region in which at least 1% of both the Te and S can be detected is broader and it reaches to about 350 nm after the activation. The inter-mixing

at the CdS/CdTe interface may decrease the interface defect states which can reduce the recombination rate and lead to an increase in the current density.

It was also found that the CdTe thickness was decreased after the activation. This reduction could be due to the evaporation/sublimation of CdTe during the activation and/or post activation annealing in vacuum. It should be note that this result might be different for the standard solar cell in which the layers are deposited at higher substrate temperature and the CdTe layer is much thicker.

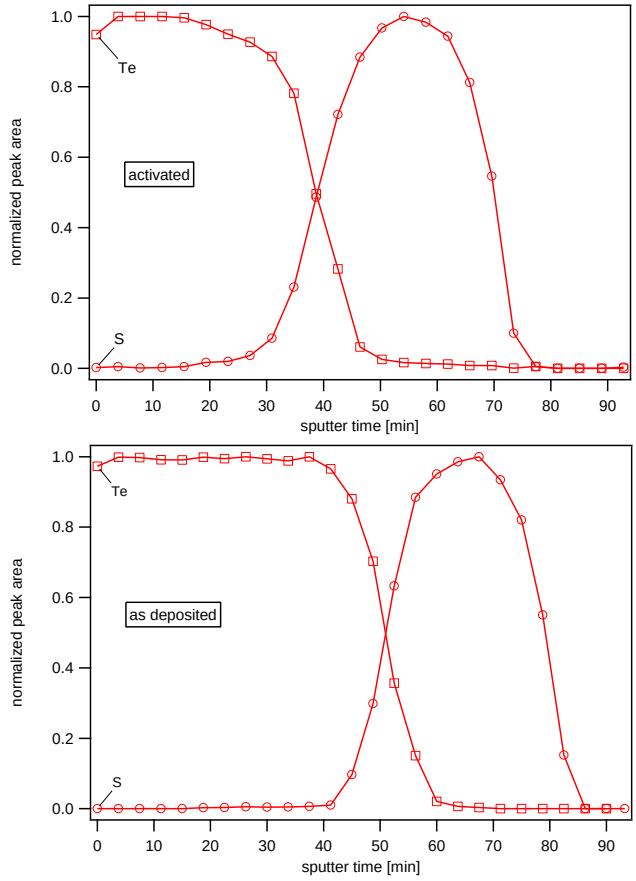

Fig. A.3: Normalized peak area of the S 2p and Te $3d_{5/2}$ emissions versus the argon sputter time. The in-situ activation leads to extending of the width of the inter-diffusion region at the CdS/CdTe interface and also reduction of the CdTe thickness.

Post deposition treatment of CdS layer

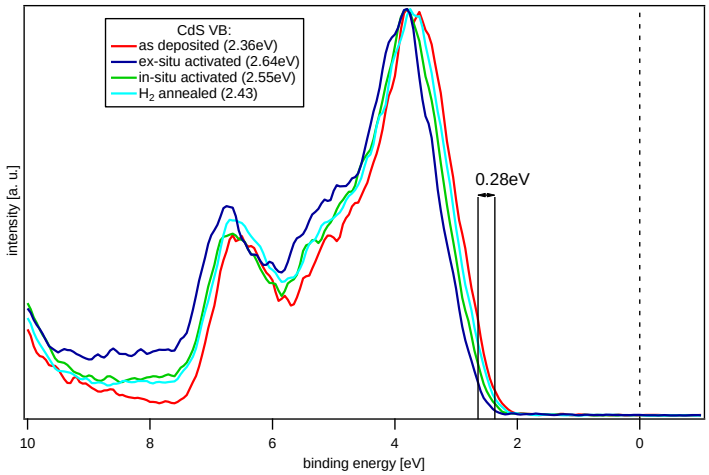

Fig. A.4: Impact of the $CdCl_2$ activation and/or annealing in H_2 atmosphere on the CdS layer. It was found that $E_F - E_{VBM}$ increased, which indicates an increase in the n-type doping of the CdS layer.

PES results of Mo/Te interface

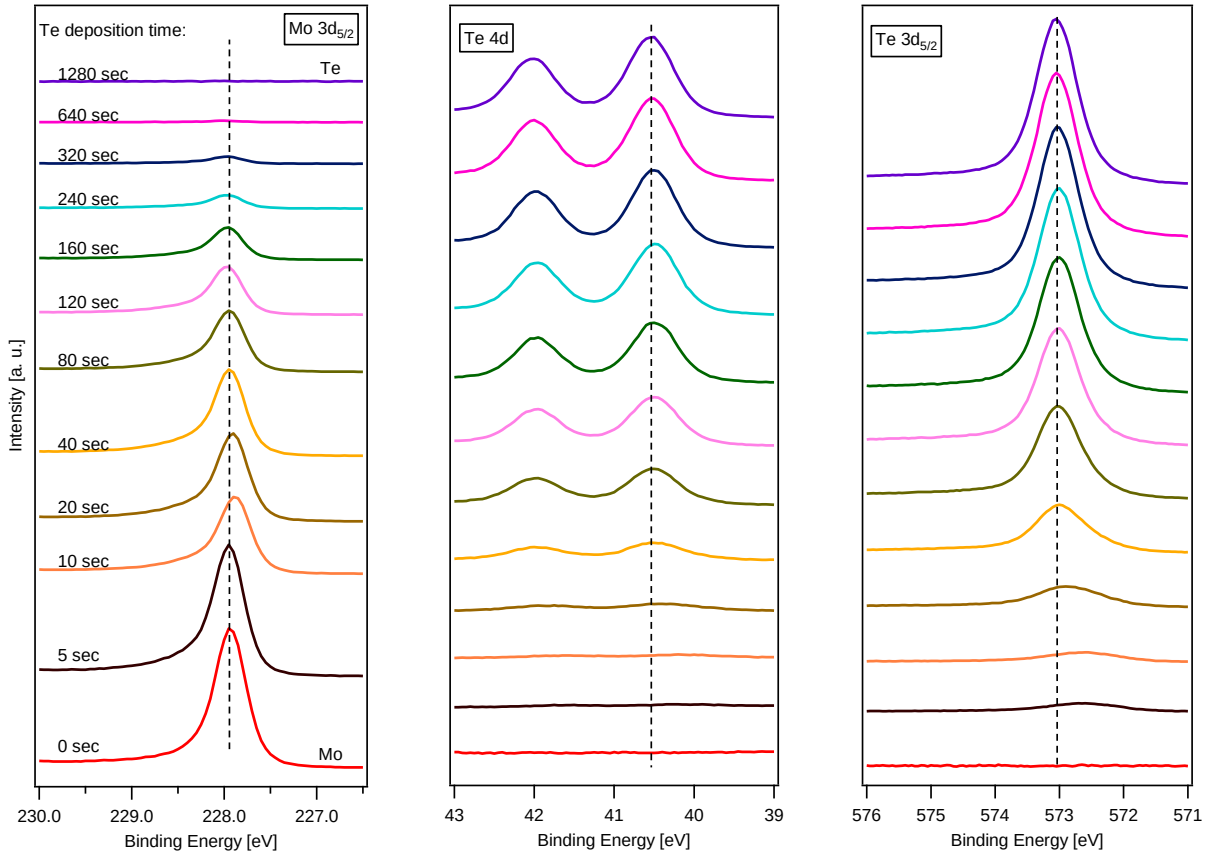

Fig. A.5: X-ray photoelectron spectra of Mo $3d_{5/2}$, Te 4d, and Te $3d_{5/2}$ core levels for stepwise deposition of Te onto a Mo substrate.

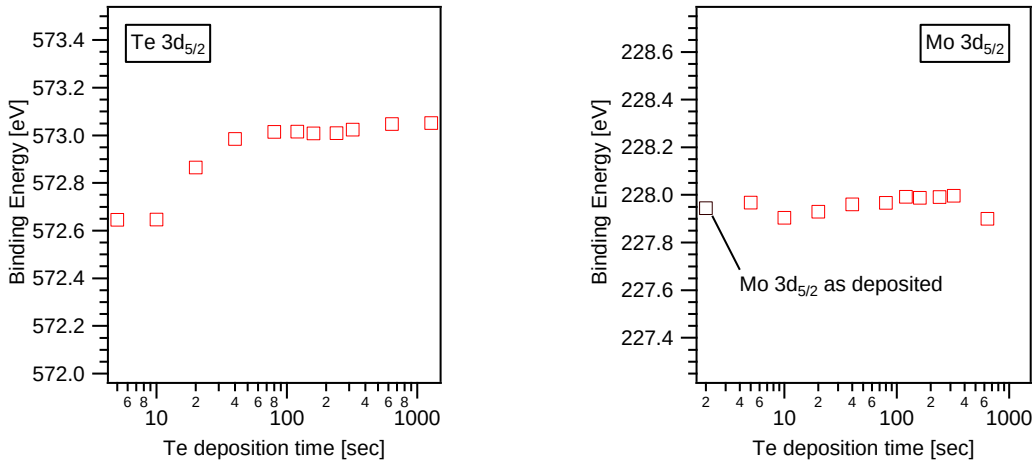

Fig. A.6: BEs of Te $3d_{5/2}$ and Mo $3d_{5/2}$ core levels as a function of the Te deposition time.

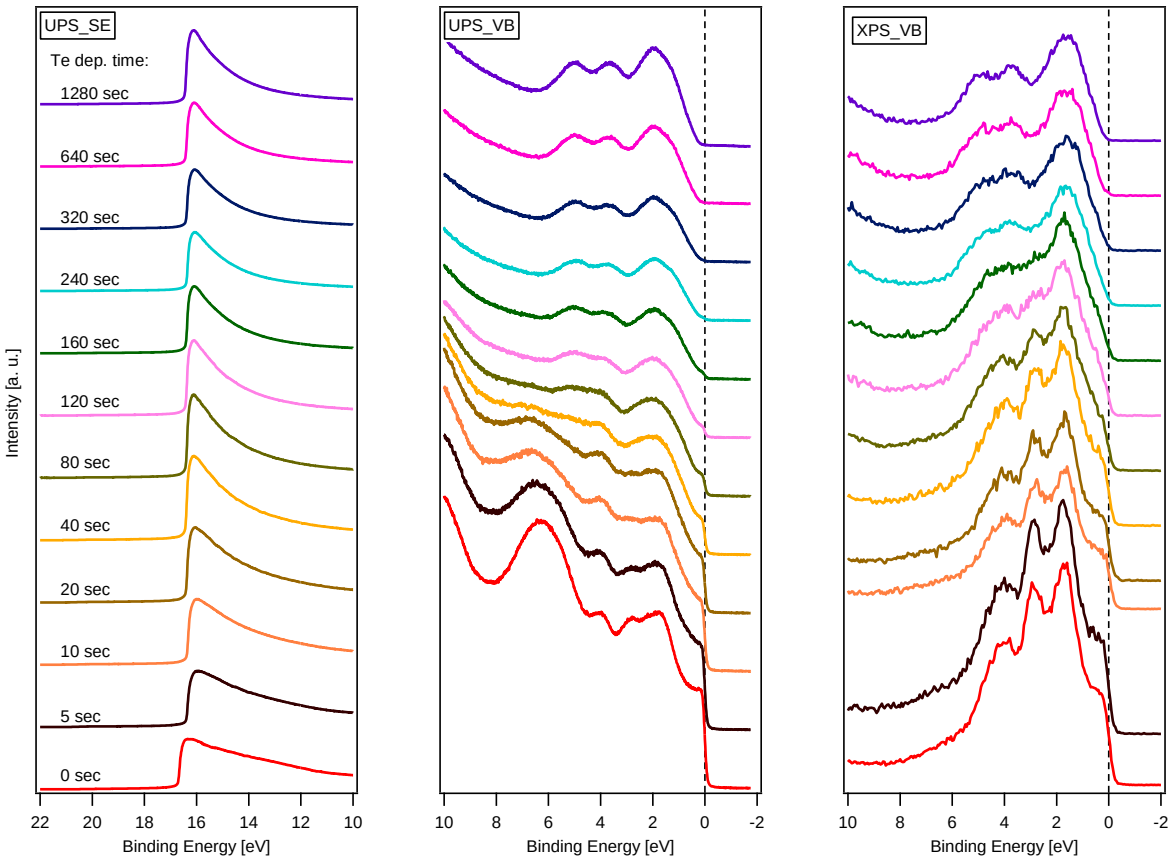

Fig. A.7: UV photoelectron and XBS VB spectra for stepwise deposition of Te onto Mo substrate.

Abstract

One of the key issues in manufacturing of CdTe solar cells is the formation of a stable and low-barrier ohmic contact to the CdTe layer. When typical metals are deposited onto the CdTe surface, a barrier is formed at the interface due to an unfavorable energy-band alignment. The alignment is determined by the work-function of the metal, interface states, and metal-induced gap states at the interface, which leads to pinning of the CdTe Fermi-level close to the middle of its energy gap.

The main subject of this PhD work was the fundamental investigation of the parameters involved in formation of reliable ohmic back contacts to the CdTe layer. For this purpose, a multifunction vacuum chamber, which was equipped with a plasma ion source and multiple sputtering targets and PVD sources, was integrated with the DAISY-SOL. Solar cells were prepared by sequential deposition of the CdS and CdTe layers onto TCO-coated glass substrates by close-space-sublimation (CSS). Then, the cells were completed by a $CdCl_2$ treatment followed by deposition of the back-contact layer(s). After any layer deposition or treatment, the sample could be transferred to an Escalab spectrometer for XPS/UPS characterization without breaking the ultra-high vacuum environment.

The goals of this project were to eliminate the use of copper (due to stability concerns), and to prepare back contact without etching. In order to meet these goals, the $CdCl_2$ activation had to be performed in a non-oxidizing atmosphere. Therefore, an in-situ $CdCl_2$ activation reactor was developed and integrated to the system to perform the treatment in vacuum. This facility, besides its benefits in fabrication of solar cells in an all-dry process, enabled us to study effects of the $CdCl_2$ activation on CdTe and CdS layers with photoelectron spectroscopy (PES). Moreover, since during the activation no oxide layer was formed, it was possible to study the electrical properties of the CdTe solar cells by conductive AFM (c-AFM) with nanoscale resolution. Effect of typical treatments, such as $CdCl_2$ activation and chemical etching, which usually must be performed before the back-contact deposition, were also investigated by this technique.

The electrical properties of the completed solar cells were characterized by current-voltage, external quantum efficiency (EQE), and capacitance-voltage (C-V) measurements. The surface morphology and structure of the layers were investigated by AFM, SEM and XRD.

The resistivity and carrier concentration of some thin films were also investigated by the four-point probe and Hall-effect measurements, respectively.

Three different back contact approaches were investigated in this work:

The first approach was application of an intermediate layer (or a combined layer structure) between the CdTe and metallic back contact. Several interlayers based on ZnTe, Sb_2Te_3, Sb and Te were applied and the important formation parameters of each contact were optimized. Cell efficiencies as high as the efficiencies obtained with our standard wet process were obtained. This was achieved without any need for chemical etching or washing processes, and of course, without copper. Based on our previous investigations, nitrogen doped ZnTe (ZnTe:N) was a good candidate to be used as the back-contact interlayer; because it could be doped p-type to high levels to realize ohmic contact and a negligible valence-band offset was measured at the CdTe/ZnTe interface. However, solar cells with ZnTe:N/Au back contact had rather low efficiencies, which could be related to the degradation of the cells during deposition of the ZnTe:N layers. As an alternative, antimony was selected to be used as the p-type dopant in ZnTe. After trying several methods, a 4-step procedure was developed and highly p-type antimony doped ZnTe (ZnTe:Sb) thin films with conductivity of 31 S/cm (resistivity of 0.03 Ω.cm) were successfully deposited. Although the contact between ZnTe:Sb and the metallization layer (Mo or Au) was ohmic, the efficiency of solar cells prepared with this interlayer was also low.

Another approach was Sb-doping of the CdTe surface to form a tunneling contact. For this purpose, an efficient method was developed, which was similar to the Sb doping of ZnTe layers with some modifications. Solar cells with Sb-doped CdTe surface showed a very low series resistance (3-5 Ω/cm^2) and efficiency of the cells was improved by 20%, as compared with our standard cell. With this method, solar cells with efficiency of 12.8% and fill factor as high as 69.3 % with V_{oc} and J_{sc} of 770 mV and 24 mA/cm^2 were produced. This was our record efficiency at the time when this project was performed.

The last approach was investigation of reduced molybdenum oxide (MoO_x) as the back-contact interlayer. MoO_x layers were deposited by RF reactive sputtering and PVD methods. By changing the deposition parameters followed by XPS and UPS characterization, the optimum condition for depositing conductive MoOx layers with work-function larger than 6 eV were determined.

CdTe solar cells prepared with MoOx back contact interlayer had better performance compared with the cells without this layer, but their performance was not higher than those

prepared with our standard back contact (i.e. NP-etching followed by gold sputtering). Three sets of interface experiments were performed to study the contact between the CdTe surface and MoOx layers deposited by sputtering and PVD methods. The interface investigations were performed by stepwise deposition of MoOx layers onto the CdTe surface followed by XPS and UPS measurement after each step. The resulting energy band diagrams showed that the MoO_x interlayers cannot provide a low resistance contact to the CdTe, despite the high work-function and good conductivity of these layers. It was also found that, the work-function difference was compensated by a large interface dipole and the Fermi-level of the CdTe was always pinned at 0.9 eV above the valence band. Therefore, in order to achieve a low resistance back contact with MoO_x buffer layer, the CdTe surface must be highly doped to facilitate carriers tunneling, otherwise a large barrier height is formed at the interface.

Most of the copper-free back contacts investigated in this work did not show any degradation after at least one-year storage in the lab.

Publications

- A. Barati, A. Klein, and W. Jaegermann, Deposition and characterization of highly p-type antimony doped ZnTe thin films. *Thin Solid Films*, 2009. 517(7): p. 2149-2152.
- A. Zakutayev, J. Tate, H. Platt, D. Keszler, A. Barati, A. Klein, W. Jaegermann, *Band alignment at the BaCuSeF/ZnTe interface. Applied Physics Letters*, 2010. **96**(16): p. 162110-162110-3.
- A. Zakutayev, J. Tate, S. Xie, B. Gibbons, H. Platt, D. Keszler, A. Barati, A. Klein, W. Jaegermann, *Interdiffusion at the BaCuSeF/ZnTe interface. Thin Solid Films*, 2011. **519**(21): p. 7369-7373.
- V. Krishnakumar, A. Barati, H. J. Schimper, A. Klein, W. Jaegermann, A possible way to reduce absorber layer thickness in thin film CdTe solar cells. Thin Solid Films, 2013. **535**: p. 233-236.

Patent

- W. Jaegermann, A. Klein, K. Velappan, H. J. Schimper, A. Barati, Bildung eines niederohmschen Kontaktes auf II-VI-Halbleitern durch Behandlung mit Metallhalogeniden, UNIV TECH DARMSTADT, DE Patent: DE 10 2014 101 584.3

Conference Presentations

- A. Barati, A. Klein, and W. Jaegermann, *EMRS[1] Spring Meeting, 2008, Strasburg, France:* highly p-type antimony doping of ZnTe thin films, Oral presentation.
- A. Barati, B. Kaiser, S. H. Keshmiri, A. Klein, and W. Jaegermann, EMRS *Spring Meeting, 2009, Strasburg, France:* Conductive Atomic Force Microscopy analysis of CdS/CdTe solar cells prepared by close-space sublimation, Poster presentation.
- A. Barati, A. Tüschen, A. Klein, and W. Jaegermann, *EMRS Spring Meeting, 2010, Strasburg, France:* All dry and copper-free back contacts to CdTe solar cells, Poster presentation.

[1] European Materials Research Society

- Alireza Barati, Bastian Siepchen, Azad J. Darbandi, Andreas Klein, and Wolfram Jaegermann, *First International Conference on Materials for Energy, 2010, Karlsruhe, Germany*: Advanced characterization methods for CdTe solar cells, Poster presentation.
- J. Schaffner, A. Barati, V. Krishnakumar, J. Luschitz, G. Fu, H.-J. Schimper, G. Haindl, A. Swirschuk, E. Feldmeier, A. Schneikart, A. Tueschen, A. Klein, W. Jaegermann, *First International Conference on Materials for Energy, 2010, Karlsruhe, Germany*: CdTe thin film solar cells: optimization of material, morphology and device preparation, Oral presentation.

1. A. Barati, B. Siepchen, J. Schaffner, H.-J. Schimper, A. Klein, W. Jaegermann, S. H. Keshmiri, H. Schulz, D. Kraft, *EU-PVSEC*[1] *2010, Valencia, Spain*: Electrical and *morphological* studies of CdTe solar cells, Oral presentation.

- A. Barati, J. Türck, H.-J. Schimper, A. Klein, W. Jaegermann, *EU-PVSEC 2011, Hamburg, Germany*: Investigation of MoOx as back contact for CdTe thin film solar cells, Oral presentation.
- A. Barati, J. Türck, V. Krishnakumar, H.-J. Schimper, A. Klein, W. Jaegermann, *EU-PVSEC 2012, Frankfurt, Germany:* Non-oxidizing vacuum based $CdCl_2$ activation of CdS/CdTe solar cells, Poster presentation.

[1] European Photovoltaic Solar Energy Conference

Curriculum Vitae

Personal data

Name **Alireza Barati**

Study

06.2008 – 09.2012 **PhD Study in Materials Science**
Surface Science Division, Department of Materials Science, Darmstadt University of Technology, Germany

09.1993 – 12.1996: **Master of Science in Solid State Physics**
Ferdowsi University of Mashhad, Iran

09.1988 – 06.1993: **Bachelor of Science in Physics**
Birjand University, Iran

06.1988: **Diploma in Mathematics and Physics**
Mashhad High School, Iran

Acknowledgements

First and foremost, I would like to express my sincere appreciation and gratitude to my supervisor Prof. Wolfram Jaegermann for his encouragements, trust and insight. The long journey that has led to the writing of this dissertation would not have been possible without his continuous support along the way. I am also thankful to Prof. Lambert Alff for accepting to be my co-supervisor.
I extend many thanks to Prof. S. H. Keshmiri and Prof. Andreas Klein for their inputs and valuable suggestions. In addition, I thank Prof. Ralf Riedel and Prof. Wolfgang Elsäßer for accepting to be on my committee.

Thanks to everyone who has helped me throughout all these years, especially to:

- Mrs. Marga Lang for her kind assistance with administrative tasks.
- Drs. Jochen Fritsche, Bettina Späth and Johannes Luschitz for familiarizing me with DAISY-SOL and Escalab when I joined the group.
- Dr. Bernhard Kaiser for introducing AFM setup at the Center of Smart Interfaces.
- Dr. Azad Darbandi for his support in XRD characterization.
- Dr. Krishnakumar Velappan for great collaboration and fruitful discussions.
- Dr. Daniel Kraft for EBSD measurements.
- Johannes Türck for adjusting MoO_x back contacts.
- Kerstin Lakus-Wollny for fine-tuning SEM.
- Gabi Haindl and Michael Weber for their technical supports.
- Dr. Andriy Zakutayev for the joint effort in studying interfaces in chalcogenide PVs.

I owe a lot to my parents for all their encouragements at every step of my personal and academic life. I deeply miss them. Last but not least, I would like to thank my wife Mona, and children Amin and Matin, for their love and cheers. This work is for them.